

中国科学技术大学
博士学位论文



基于 ATLAS 探测器上 ZZ 玻色子到全轻子
通道的衰变事例对标准模型 ZZ 过程和寻找
重共振态衰变到双 Z 玻色子过程的研究

作者姓名：祝鹤龄
学科专业：粒子与原子核物理
导师姓名：赵政国 马宏
完成时间：二〇二〇年九月二十四日

University of Science and Technology of China
A dissertation for doctor's degree



**Studies of Standard Model ZZ
Production and Search for heavy ZZ
resonances in Purely Leptonic
Decay with ATLAS Detector**

Author: Heling Zhu

Speciality: Particle and Nuclear Physics

Supervisors: Zhengguo Zhao, Hong Ma

Finished time: September 24, 2020

摘要

论文介绍了本人在粒子物理领域基于大型强子对撞机 (LHC) 上 ATLAS 实验做的研究工作。大型强子对撞机是当今世界上最大的、能量最高的对撞机，是建立在理论和实验之间的重要桥梁。而 ATLAS 实验是 LHC 上的一个通用粒子探测器实验，同时也是体积最大的探测器。基于 ATLAS 实验在 LHC 上收集到的亮度为 139 fb^{-1} 能量为 13 TeV 的质子-质子对撞数据，本文重点介绍了两个 Z 玻色子衰变到四轻子末态过程的一系列研究。包括，标准模型 (SM) 下 ZZ 到四轻子过程截面的测量、矢量玻色子散射 (VBS) 过程在 ZZ 到四轻子末态的观测，和寻找重共振态衰变到 ZZ 到四轻子末态的过程。

ZZ 到四轻子过程截面的测量结果为 $\sigma_{ZZjj}^{tot} = 1.27 \pm 0.12(\text{stat}) \pm 0.02(\text{theo}) \pm 0.07(\text{exp}) \pm 0.01(\text{bkg}) \pm 0.03(\text{lumi})$ ，总体相对误差为 11%。在误差范围内，该结果和标准模型预言值 $1.14 \pm 0.04(\text{stat}) \pm 0.20(\text{theo})$ 相吻合。同时，在两个 Z 玻色子伴随着两个喷注 (jets) 末态的电弱相互作用过程的寻找中，我们观测到偏离本底假说超过 5 倍标准差 (5.5σ) 的明显偏差。在此基础上，本文也介绍了对于下一代高亮度大型强子对撞机 (HL-LHC) 在两个 Z 玻色子伴随着两个喷注 (jets) 末态的电弱相互作用过程的模拟预言。

另一方面，本文介绍了在一对 Z 玻色子衰变至四轻子末态过程中寻找重共振态的实验。根据不同的信号模型，寻找的粒子质量区间设置在 200 GeV 到 2000 GeV 之间。基于该测量结果，没有证据可以证明重共振态的存在。因此，研究给出了基于不同信号模型的截面上限，包括在不同衰变宽度假说下自旋为 0 的共振态，以及基于 Randall–Sundrum 模型的自旋为 2 的引力子 (graviton)。在该分析中，我们认为，信号主要可通过 gluon-gluon Fusion (ggF) 和 Vector Boson Fusion (VBF) 过程产生。在自旋为 0 的窄衰变宽度模型下，我们对 ggF 和 VBF 两个过程都进行了研究。而对于大宽度模型，由于在质量很高的区间分辨率很差以及 VBF 过程的统计量太小等客观原因，只对 ggF 过程进行了研究。对于自旋为 2 的模型，实验给出了 Randall–Sundrum 模型的引力子的理论质量下限，为 1500 GeV 。

28

ABSTRACT

29 This dissertation presents my research in the field of Particle Physics with the ATLAS
30 experiment at the Large Hadron Collider (LHC). The LHC is the world's largest and most
31 powerful collider, and it was built as a bridge between the theories and the experiment.
32 The ATLAS experiment is a general-purpose particle detector experiment with the largest
33 volume at the LHC. This dissertation focus on the studies with two Z bosons production
34 decaying into $\ell\ell\ell'\ell'$ final state, where ℓ stands for electron or muon, using 139 fb^{-1} of
35 13 TeV proton-proton (pp) collision data collected by ATLAS experiment at the LHC.
36 The ZZ production in $\ell\ell\ell'\ell'$ channel provides a most clean and sensitive tool to test
37 the Standard Model (SM) at the energy frontier and to study the *Higgs* physics. Studies
38 including the measurement on SM $ZZjj$ production cross section, the observation of
39 Vector Boson Scattering (VBS) process as well as the searches of heavy resonances in
40 ZZ production decaying into $\ell\ell\ell'\ell'$ final state are reported in this dissertation.

41 The fiducial cross section for SM $ZZjj$ production is measured to be $\sigma_{ZZjj}^{tot} = 1.27 \pm$
42 $0.12(\text{stat}) \pm 0.02(\text{theo}) \pm 0.07(\text{exp}) \pm 0.01(\text{bkg}) \pm 0.03(\text{lumi})[\text{pb}]$ with a total relative
43 uncertainty of 11% for the $\ell\ell\ell'\ell'$ final state, and found to be compatible with the SM
44 prediction of $1.14 \pm 0.04(\text{stat}) \pm 0.20(\text{theo})[\text{pb}]$. The electroweak production of two jets
45 in association with a Z -boson pair (EW- $ZZjj$) is observed with a significant deviation
46 from the background-only hypothesis corresponding to a statistical significance of 5.5σ .
47 Following with the observation, the prospect study for the EW- $ZZjj$ production at the
48 High luminosity LHC (HL-LHC) using 3000 fb^{-1} simulated pp collision data at a centre-
49 of-mass energy of 14 TeV is presented, with a expected significance of around 7σ .

50 A search for heavy resonances decaying into a pair of Z bosons to $\ell\ell\ell'\ell'$ final state is
51 also conducted in this dissertation. Different mass ranges for the hypothetical resonances
52 are considered, depending on the signal models and spanning between 200 GeV and
53 2000 GeV. Data is found to agree with a background-only hypothesis, thus, the results
54 are interpreted as upper limits on production cross section for sevaral different models,
55 including heavy Higgs like (spin-0) narrow-width approximation (NWA) and large-width
56 approximation (LWA), as well as the Randall–Sundrum model with a graviton excitation
57 spin-2 resonance (RSG). The signal is assumed to generate dominatly via gluon-gluon
58 Fusion (ggF) production mode and Vector Boson Fusion (VBF) production mode. Both
59 ggF and VBF channels are studied in NWA, while for LWA, only ggF channel is studied
60 due to worse resolution in higher mass region and the lack of statistic for VBF process. In

Abstract

- 61 addition, mass of RS Graviton is constrained, $m(G_{KK}) < 1500$ GeV is excluded at 95%
- 62 CL by $ZZ \rightarrow \ell\ell\ell'\ell'$ analysis.

63

64

Acknowledgments

65 First of all, I would like to express my great gratitude to my supervisors Prof. Zhao
66 Zhengguo and Dr. Ma Hong, for their guidance and patience during my Ph.D years. It's
67 Zhengguo, who inspire me with his deep physics insight when I was an undergraduate
68 student and led me enter the field of Particle Physics. I will never forget how I was attracted
69 by his broad knowledge and the amazing picture of particles he showed me, which became
70 the reason I choose the Particle Physics as my major. It's always relaxed and beneficial
71 greatly when chating with him, which broads my version, makes me to be more confident
72 and helps me step out of so many difficulties.

73 Thanks to Hong, for giving me the oppotunity to study in Brookhaven National Lab
74 (BNL) that I can work with so many senior and brilliant physicists, and teaching me a lot in
75 the details of physics. As the chair of physics department at BNL, can you imagine that he
76 managed to take time sitting with me every week, teaching me the details and techniques
77 of my analysis as well as helping me to parepre my talks at conference.

78 Thank you both for leading me to the field of physics, showing me how beautiful the
79 science and the world are. And thank you for providing me so many oppotunities and
80 tremendous supports to work at physics frontier and work with people all over the world.
81 It's my greatest honor to be your student. Your strong personalitis will definitely influence
82 my future life and career.

83 I would like to give my large gratitude to Prof. Zhou Bing. It's Bing who introduced
84 me to ATLAS experiment when I was a junior. As a professor and group leader of ATLAS
85 group in University of Michigan with busy schedule, Bing still took time to teach me in
86 physics start from simple formulas and help me to prepare my first academic presentation
87 patiently when I was a undergraduate student. Also it's my great fortune that I can have
88 opportunities to work with you and learn from you in so many analyses during these years.
89 Your kind and patience, your high standard influence me deeply in all these years.

90 Moreover, I really want to give my sincere gratitude to Dr. Xu Lailin. Thank you,
91 Lailin, for all your helps during the passing five years. Thanks for teaching me in all the
92 analysis details, coding techniques, presentation skills hand by hand. You are really a
93 very good and patient teacher and give me as many knowledges as you can. Your broad
94 knowledge, your perseverance in science and your very hard working indeed affect me a
95 lot.

96 In the meantime, I want to give my special thanks to Dr. Li Bing, who helped me a lot

97 in several different analyses (low-mass 4μ resonance search, VBSZZ analysis, Z' search),
98 he never hesitated to give his hand to me when I faced difficulties.

99 I would like to express my gratitude to many colleagues in both USTC and BNL team.
100 Thanks to Prof. Sun Yongjie, who is the supervisor of my undergraduate thesis, helped
101 me start my first detector project on MRPC. Also thanks Dr. Liu Zhen who taught me
102 in details in this project, and helped me a lot for my life at BNL too. Thanks to Prof.
103 Peng Haiping, Prof. Zhu Yingchun and Dr. Hu Qipeng for helping me all the details
104 and techniques in HWW analysis when I was a beginner. Thanks to Dr. Dai Tiesheng,
105 I have learnt quite a lot in the project of Monitored Drift Tubes (MDT) when working
106 with you at CERN and also thank you for all the help in regular life since that was my
107 first time to Europe. Thanks to Dr. Chen Hucheng, who is the supervisor of my ATLAS
108 qualification task on LAr Trigger Digitizer Boards (LTDB) and the person lead me into
109 this interesting electronic project. And my appreciation to Dr. Xu Hao, Dr. Chen Kai and
110 Dr. Liu Hongbin who taught me in patience for this project as I was really a freshman on
111 electronics. Thanks to Prof. Yuji Enari and Dr. Georges Aad for the help in LAr software
112 tasks when I moved from BNL to CERN. In the meantime, I would really like to give
113 my gratitude to Dr. Michael Begal, Dr. Marc-Andre Pleier, Dr. Alessandro Tricoli, Dr.
114 George Redlinger, Dr. Viviana Cavalieri, Dr. Gaetano Barone and many senior physicists
115 in BNL omaga group. I have learnt a lot from every chat with you and every seminar
116 you hosted. Also I want to thanks to Prof. Wu Yusheng, Prof. Qian Jianming, Prof. Liu
117 Yanwen, Dr. Ju Xiangyang for teaching me in lots of details in different physics analyses.

118 Moreover, I want to give my thanks to friends I met at USTC, BNL and CERN during
119 my Ph.D years. Thanks to Dr. Yang Qian, Dr. Chu Xiaoxuan, Dr. Tu Biao, Dr. Gao
120 Shanshan, Dr. Liu Feng, Dr. Yuan Guangyuan, and many other friends I met at BNL.
121 Thanks to Prof. Geng Cong, Dr. Li Peilian, Dr. Zhang Liqing, Dr. Guo Yicheng, Dr.
122 Xu Tairan, Dr. Wang Rongkun, Chen Jing, He Fudong, Guo Qianying, Chen Ye, Xu Hao,
123 Wang Tao, Xie Xiangyu, Liu Xiangtian and all friends I met at USTC and CERN. Thank
124 you all my friends! I will always remember all the happiness with you, and best wishes
125 to you in the future!

126 Last but not least, I would give my greatest gratitude to my families. Thanks my
127 parents for giving me all your endless loves and supports in my whole life. My deep
128 appreciation to my three aunts for loving and caring me so much since I was born and
129 help me to accompany with my mother when I was thousands miles far away from home.
130 And my husband, Lin, thank you for your understanding and walk through all difficulties
131 with me in these years especially when we were in a foreign country.

Contents

132	Acknowledgments	IV
134	Chapter 1 Introduction	1
135	Chapter 2 Theory	3
136	2.1 The Standard Model of Particle Physics	3
137	2.1.1 Elementary particles in the Standard Model	3
138	2.1.2 Electroweak theory	4
139	2.1.3 Higgs mechanism and Electroweak symmetry breaking	6
140	2.1.4 Beyond the SM Higgs sector	9
141	2.2 Phenomenology of Large Hadron Collider	10
142	2.2.1 Physics at hadronic collision	11
143	2.2.2 Higgs physics at the LHC	13
144	2.2.3 Diboson physics at the LHC	15
145	Chapter 3 The Large Hadron Collider and the ATLAS Detector	19
146	3.1 The Large Hadron Collider	19
147	3.1.1 Operation history and machine layout	19
148	3.1.2 Luminosity and pile-up	22
149	3.2 ATLAS detector	24
150	3.2.1 Detector overview	24
151	3.2.2 Physics requirement	26
152	3.2.3 Magnet system	26
153	3.2.4 Inner detector	27
154	3.2.5 Calorimeters	30
155	3.2.6 Muon spectrometer	31
156	3.2.7 Trigger system	33
157	Chapter 4 Simulation and Event Reconstruction for the ATLAS Experiment	37
158	4.1 Event simulation	37
159	4.2 Event reconstruction	40
160	4.2.1 Track	40
161	4.2.2 Primary vertex	42
162	4.2.3 Electron	43

164	4.2.4 Muon	48
165	4.2.5 Jets	52
166	4.2.6 Missing transverse energy	56
167	Chapter 5 Statistical treatment of searching for new particles or processes	59
168	5.1 The likelihood function	59
170	5.2 Test statistic	60
171	5.3 The CLs upper limit	61
172	Chapter 6 Studies of SM $Z Z$ production in $\ell \ell \ell' \ell'$ final state using pp collision data collected by ATLAS detector from 2015 to 2018	62
175	6.1 Introduction	62
176	6.2 Data and MC samples	63
177	6.2.1 Data samples	63
178	6.2.2 MC simulations	64
179	6.3 Objects and Event selection	65
180	6.3.1 Objects selection	65
181	6.3.2 Event selection	66
182	6.4 Background estimation	67
183	6.4.1 QCD backgrounds	67
184	6.4.2 Reducible backgrounds	68
185	6.5 Systematics	72
186	6.5.1 Theoretical systematics	72
187	6.5.2 Experimental systematics	74
188	6.6 Measurement of fiducial cross section	77
189	6.6.1 Calculation of C-factor	77
190	6.6.2 Result of fiducial cross section	78
191	6.7 Search for EW- $Z Z jj$	78
192	6.7.1 MD discriminant	78
193	6.7.2 Fitting procedure	78
194	6.7.3 Result of fit	80
195	6.8 Prospect study of EW- $Z Z jj$ production in HL-LHC	82
196	6.8.1 The ATLAS detector at HL-LHC	83
197	6.8.2 Simulation	83

198	6.8.3 Event selection	83
199	6.8.4 Systematics	84
200	6.8.5 Results	86
201	6.9 Conclusion	89
202	Chapter 7 Search for heavy resonances decaying into a pair of Z bosons in $\ell\ell\ell'\ell'$ final state using pp collision data collected by ATLAS detector from 2015 to 2018	90
205	7.1 Introduction	90
206	7.2 Data and MC samples	91
207	7.2.1 Data samples	91
208	7.2.2 Background MC simulations	91
209	7.2.3 Signal MC simulations	92
210	7.3 Analysis selections	93
211	7.3.1 Objects selection	93
212	7.3.2 Event selection	94
213	7.3.3 Event categorizations	96
214	7.3.4 Signal acceptance	104
215	7.4 Background estimation	105
216	7.4.1 Irreducible backgrounds	106
217	7.4.2 Reducible backgrounds	110
218	7.5 Signal modelling	111
219	7.5.1 Modelling of narrow-width signal	112
220	7.5.2 Modelling of large-width signal	112
221	7.5.3 Modelling of interference	116
222	7.5.4 Modelling of spin-2 RS Graviton signal	120
223	7.6 Systematic uncertainties	121
224	7.6.1 Theoretical uncertainties	122
225	7.6.2 Experimental systematics	124
226	7.7 Results in $\ell\ell\ell'\ell'$ channel	124
227	7.7.1 Statistical procedure	125
228	7.7.2 For to likelihood function under background-only hypothesis for MVA-based analysis	126
230	7.7.3 Interpretations	126
231	7.8 Conclusion	136

Contents

232	Chapter 8 Summary	137
233	Bibliography	140

234	List of Figures	
235	2.1 The elementary particles of the Standard Model.	3
236	2.2 The Feynman diagrams of interactions that form the basis of the standard model.	5
238	2.3 The Higgs potential $V(\phi)$ with $\mu^2 > 0$ (left) and $\mu^2 < 0$ (right).	7
239	2.4 Schematic view of a hadron-hadron collision ^[8]	11
240	2.5 The PDF4LHC15 NLO PDFs at a low scale $\mu^2 = Q^2 = 4GeV^2$ (left) and at $\mu^2 = Q^2 = 100GeV^2$ (right) as a function of x.	12
242	2.6 Feynman diagrams of the Higgs production modes: (a) ggF; (b) VBF; (c) VH; (d) ttH.	14
244	2.7 The SM Higgs boson production cross sections for various production modes as a function of the centre-of-mass energy for pp collision.	14
246	2.8 Higgs boson production cross section for various production modes as a function of the Higgs mass for $\sqrt{s} = 13$ TeV (left) and 14 TeV (right) for pp collision.	14
249	2.9 SM Higgs decay channels.	15
250	2.10 Branching ratio of Higgs decays in various channels as a function of Higgs mass ^[14]	16
252	2.11 The tree-level Feynman diagrams of diboson production at the LHC.	16
253	2.12 Total production cross-section presented by ATLAS as a function of centre-of-mass energy \sqrt{s} from 7 to 13 TeV for some selected processes, the diboson measurements are scaled by a factor 0.1 to allow a presentation without overlaps.	17
257	2.13 Feynman diagrams of the vector boson scattering.	17
258	2.14 Feynman diagrams of vertexes involving QGC, TGC and Higgs.	18
259	3.1 Cumulative luminosity as a function of time in years from 2011 to 2018 for ATLAS detector.	20
261	3.2 CERN accelerator complex ^[20]	21
262	3.3 Integrated luminosity in ATLAS.	23
263	3.4 Number of Interactions per Crossing from 2015-2018 in ATLAS.	23
264	3.5 Coordinate system used by the ATLAS experiment at the LHC ^[22]	24
265	3.6 Cut-away view of the ATLAS detector ^[23]	25

266	3.7	Schematic diagram of the ATLAS magnet system.	27
267	3.8	Schematic diagram of the ATLAS inner detector ^[25]	28
268	3.9	Schematic diagram of the ATLAS 4-Layer Pixel Detector.	28
269	3.10	SCT (a) barrel module and (b) end-cap ^[29]	29
270	3.11	Cut-away view of the ATLAS calorimeters. The LAr calorimeters are seen 271 inside the scintillator-based tile hadronic calorimeters ^[31]	30
272	3.12	Schematic diagram of a LAr EM calorimeter barrel module.	31
273	3.13	Schematic diagram of tile calorimeter module ^[33]	32
274	3.14	Cut-away view of the ATLAS muon spectrometer ^[35]	32
275	3.15	Schematic diagram of the ATLAS trigger and data acquisition system in run- 276 2.	34
277	3.16	An examples of L1 calorimeter trigger tower for electron and photon trig- 278 gers ^[37]	35
279	3.17	The HLT trigger algorithm sequence ^[37]	36
280	4.1	The flow of the ATLAS simulation software.	37
281	4.2	Sketch of a hardon-hardon collision simulated by MC event generator. The 282 red blob in center denotes the hard collision, surrounded by tree-like structures 283 representing Bremsstrahlung which is simulated by Parton Showers. The pur- 284 ple blob stands for a secondary hard scattering event. The light green blobs 285 indicate the parton-to-hardon transitions and the dark green blobs represents 286 hardon decays. The yellow lines are soft photon radiations.	39
287	4.3	The flowchart of the ATLAS data processing.	40
288	4.4	Schematic view of the ATLAS inner detector showing all the corresponding 289 components.	41
290	4.5	Schematic of the impact parameters of a track in the transverse plane (left) 291 and RZ-plane (right), as defined in the global ATLAS tracking frame ^[59]	46
292	4.6	The efficiencies of three electron identification WPs from $Z \rightarrow ee$ (left) 293 events and hadrons misidentified as electrons estimated using di-jet MC sam- 294 ples (right).	47
295	4.7	Distributions of $E_T^{cone0.2}$ (left) and $p_T^{varcone0.2}$ (right) for electrons from $ZZ \rightarrow$ 296 ee events in data and MC simulation. The simulated events (full histograms) 297 are normalized to data.	48
298	4.8	Muon reconstruction efficiency as a function of η for: Medium (and Loose), 299 Tight and High- p_T working points.	51

300	4.9	Muon reconstruction efficiency for Low- p_T working point as a function of η .	52
301	4.10	Distributions of the calorimeter-based (right) and the track-based (left) relative isolation variables measured in $Z \rightarrow \mu\mu$ events.	53
302			
303	4.11	A overview schematic of ATLAS jet reconstruction ^[65] .	53
304	4.12	A overview schematic of ATLAS jet calibration ^[66] .	54
305	4.13	MV2c10 BDT output for b- (solid blue), c- (dashed green) and light-flavour (dotted red) jets in $t\bar{t}$ events ^[67] .	56
306			
307	4.14	Measured E_T^{miss} distribution for $Z \rightarrow \mu\mu$ events (left) and $W \rightarrow e\nu$ events (right).	57
308			
309	6.1	Typical diagrams for the production of $ZZjj$, including the relevant EW VBS diagrams (first row) and QCD diagrams (second row).	63
310			
311	6.2	Pre-fit m_{ZZ} and m_{jj} distribution in QCD-enriched CR.	69
312	6.3	Fake factor for $Z+jets$ background, constructed with additional electron, as a function of p_T (left) and η (right).	70
313			
314	6.4	Fake factor for $Z+jets$ background, constructed with additional muon, as a function of p_T (left) and η (right).	70
315			
316	6.5	Fake factor for $t\bar{t}$ background, constructed with additional electron, as a function of p_T (left) and η (right).	71
317			
318	6.6	Fake factor for $t\bar{t}$ background, constructed with additional muon, as a function of p_T (left) and η (right).	71
319			
320	6.7	The theoretical uncertainties for $gg \rightarrow ZZ$ background in particle-level SR (left) and CR (right).	74
321			
322	6.8	MD distribution for QCD- $ZZjj$ process in low and high pile-up events for SR (left) and CR (right).	76
323			
324	6.9	MD shape difference for QCD $q\bar{q} \rightarrow ZZ$ background between different SHERPA theoretical uncertainties and sample from MADGRAPH5_aMC@NLO on SR (left) and CR (right).	76
325			
326	6.10	Observed and post-fit expected multivariate discriminant distributions after the statistical fit in the $\ell\ell\ell'\ell'$ SR (left) and QCD CR (right). The error bands include the experimental and theoretical uncertainties, as well as the uncertainties in μ_{EW} and $\mu_{\text{QCD}}^{\ell\ell\ell'jj}$. The error bars on the data points show the statistical uncertainty on data.	80
327			
328			
329			
330			
331			

332	6.11 Observed and post-fit expected m_{jj} distributions in SR (left) and QCD CR (right). The error bands include the expected experimental and theoretical uncertainties. The error bars on the data points show the statistical uncertainty. The contributions from the QCD and EW production of $ZZjj$ events are scaled by 0.96 and 1.35, respectively, corresponding to the observed normalization factors in the statistical fit. The last bin includes the overflow events.	
333		
334		
335		
336		
337		
338	81	
339	6.12 Observed and post-fit expected m_{ZZ} spectrum in SR. The error bands include the expected experimental and theoretical uncertainties. The error bars on the data points show the statistical uncertainty. The contributions from the QCD and EW production of $ZZjj$ events are scaled by 0.96 and 1.35, respectively, corresponding to the observed normalization factors in the statistical fit. The last bin includes the overflow events.	81
340		
341		
342		
343		
344		
345	6.13 Display of an event candidate of EW- $ZZjj$ production in $2e2\mu$ channel in last MD bin ($0.875 < \text{MD} < 1.0$). The invariant mass of the di-jet (four-lepton) system is 2228 (605) GeV.	82
346		
347		
348	6.14 Detector-level distributions of EW- and QCD- $ZZjj$ processes with selected events in defined phase space at 14 TeV of (a) m_{jj} , (b) m_{ZZ} , (c) $ \Delta\phi(ZZ) $, (d) ZZ centrality, normalized to 3000 fb^{-1} .	85
349		
350		
351	6.15 Jet variations on m_{jj} distribution for EW- $ZZjj$ (left) and QCD- $ZZjj$ (right) processes with luminosity of 3000 fb^{-1} at 14 TeV. <i>Upgrade Performance Function</i> is used to extract the uncertainties with <i>baseline</i> setting.	86
352		
353		
354	6.16 The expected significance of EW- $ZZjj$ processes as a function of different m_{jj} cut with 3000 fb^{-1} , under conditions of different sizes of theoretical uncertainties on the QCD- $ZZjj$ background modelling. The statistical uncertainty is estimated from expected data yield at 14 TeV with 3000 fb^{-1} . Different uncertainties are summed up quadratically.	87
355		
356		
357		
358		
359	6.17 The projected differential cross-sections at 14 TeV for the EW- $ZZjj$ processes as a function of m_{jj} (left) and m_{ZZ} (right). The top panel shows measurement with statistical only case, where statistical uncertainty is estimated from expected data yield at 14 TeV with 3000 fb^{-1} . The bottom panel shows impact of different sizes of systematic uncertainties.	87
360		
361		
362		
363		
364	7.1 (a) VBF DNN architecture diagram. (b) ggF DNN architecture.	100

365	7.2	(a) $m_{4\ell}$ distribution of raw (unweighted) training events for VBF signal (blue)		
366		and background (black); (b) $m_{4\ell}$ distribution of weighted VBF signal (blue)		
367		and background (black) used at training time.	101	
368	7.3	(a) $m_{4\ell}$ distribution of raw (unweighted) training events for ggF signal (blue)		
369		and background (black); (b) $m_{4\ell}$ distribution of weighted ggF signal (blue)		
370		and background (black) used at training time.	101	
371	7.4	The output score of “ggF-classifier” (a) and “VBF-classifier” (b) with the		
372		events passing the common event selections for the data, the SM backgrounds		
373		and an example of a NWA signal with a mass of 600 GeV. For the “VBF-		
374		classifier”, an additional requirement of at least two jets in the event is ap-		
375		plied. The signals cross section are set to one hundred times of the observed		
376		limit for the “ggF-classifier” and fifty times of the observed limit for the		
377		“VBF -classifier”. The $Z Z$ backgrounds are scaled by the normalisation fac-		
378		tors shown in Table 7.15. The lower panels show the ratio of data to prediction.		
379		Only statistical and experimental systematic uncertainties are included.	103	
380	7.5	Significance improvements of the MVA-based over the cut-based categoriza-		
381		tion of the VBF (ggF) category for VBF (ggF) signal samples from 300 to		
382		2000 GeV for seven different cuts on the VBF (ggF) output score. The op-		
383		timal cut of 0.8 (0.5) for VBF (ggF) score is chosen as the solid line, while		
384		other alternative cuts are plotted with dashed lines. For VBF category, results		
385		at 2000 GeV for cuts of 0.8 and 0.9 are missing due to a lack of background		
386		events passing this tight selection.	103	
387	7.6	Illustration of the MVA-based VBF and ggF event classification for events		
388		with (a) $N_{\text{jets}} < 2$ and (b) $N_{\text{jets}} \geq 2$	105	
389	7.7	NWA acceptance as a function of m_H for the MVA-based categorization for		
390		the samples of (a) ggF production; (b) VBF production.	105	
391	7.8	NWA acceptance as a function of m_H for the Cut-based categorization for the		
392		samples of (a) ggF production mode; (b) VBF production mode.	106	
393	7.9	Distributions of the $m_{4\ell}$ invariant mass fit projections of the $q\bar{q} \rightarrow ZZ$ back-		
394		ground samples for the 4μ , $4e$ and $2\mu 2e$ final states in the ggF-CBA-enriched		
395		category, and the 4ℓ inclusive VBF-CBA-enriched category. Cut-based cat-		
396		egorization is used.	107	

397	7.10	Distributions of the $m_{4\ell}$ invariant mass fit projections of the $gg \rightarrow ZZ$ background samples for the 4μ , $4e$ and $2\mu2e$ final states in the ggF-CBA-enriched category, and the 4ℓ inclusive VBF-CBA-enriched category. Cut-based categorization is used.	108
401	7.11	Distributions of the $m_{4\ell}$ invariant mass fit projections of the $q\bar{q} \rightarrow ZZ$ (EW) background samples for the 4μ , $4e$ and $2\mu2e$ final states in the ggF-CBA-enriched category, and the 4ℓ inclusive VBF-CBA-enriched category. Cut-based categorization is used.	108
405	7.12	Distributions of the $m_{4\ell}$ invariant mass fit projections of the $q\bar{q} \rightarrow ZZ$ background samples for the 4μ , $4e$ and $2\mu2e$ final states in the ggF-MVA-high category, the 4ℓ inclusive ggF-MVA-low category and VBF-MVA-enriched category. DNN-based categorization is used.	109
409	7.13	Distributions of the $m_{4\ell}$ invariant mass fit projections of the $gg \rightarrow ZZ$ background samples for the 4μ , $4e$ and $2\mu2e$ final states in the ggF-MVA-high category, the 4ℓ inclusive ggF-MVA-low category and VBF-MVA-enriched category. DNN-based categorization is used.	109
413	7.14	Distributions of the $m_{4\ell}$ invariant mass fit projections of the $q\bar{q} \rightarrow ZZ$ (EW) background samples for the 4μ , $4e$ and $2\mu2e$ final states in the ggF-MVA-high category, the 4ℓ inclusive ggF-MVA-low category and VBF-MVA-enriched category. DNN-based categorization is used.	110
417	7.15	Distributions of the $m_{2\mu2e}$ and fit projection for signal samples between 200 to 3000 GeV for ggF production mode. Three MC campaigns, mc16a, mc16d and mc16e, are combined. The lower panel in each plot shows the pull distribution.	113
421	7.16	Polynomial fits of the parameters μ , f_C , σ_G , σ_C , n_C and α_C for the signal $C + G$ model in the $2\mu2e$ channel as a function of m_H for the ggF production mode. The combination of the mc16a, mc16d and mc16e MC campaigns is used.	114
424	7.17	The difference between MC simulation and parameterization of 4μ (left), $4e$ (middle) and $2\mu2e$ (right) for the ggF production mode. The combination of the mc16a, mc16d and mc16e MC campaigns is used.	114
427	7.18	The final signal shapes for the ggF production mode, interpolated from the polynomial fit parameters.	114
429	7.19	Comparison of the analytical shape to a truth $m_{4\ell}$ distribution of gg2VV MC samples for $m_H = 450$ GeV (top), 700 GeV (bottom) and width equal to 5% (left), 10% (middle), 15% (right) of the mass.	116

432	7.20	Comparison between the analytical shape convoluted with detector effects and the reconstructed $m_{2\mu 2e}$ MC distribution for mass points ranging from 400 to 1800 GeV and width equal to 15% of the mass.	117
433			
434			
435	7.21	The interference (H-B) model fitted to the truth $m_{4\ell}$ MC distribution after signal region selection for $2\mu 2e$ channel.	119
436			
437	7.22	The signal modelling for the large-width scenario at m_H of 400 GeV (top), 600 GeV (middle) and 800 GeV (bottom), as well as three different signal width: 5% (left), 10% (middle) and 15% (right). The contribution of the interference between heavy Higgs and SM Higgs (H-h) is shown together with the one between heavy Higgs and SM $gg \rightarrow ZZ$ background (H-b).	121
438			
439			
440			
441			
442	7.23	Fitted parameters of the graviton RBW, m_{RBW} and Γ_{RBW} , as a function of the graviton resonance mass, m_G	122
443			
444	7.24	Reconstructed $m_{4\ell}$ distributions in the $2\mu 2e$ channel with the final signal model superimposed for each RS graviton signal sample at masses of 600 GeV, 1600 GeV and 2000 GeV. The lower panel in each plot shows the pull distribution. The dashed green lines show the truth-level graviton signal models for reference.	122
445			
446			
447			
448			
449	7.25	Distribution of the four-lepton invariant mass $m_{4\ell}$ in the $\ell\ell\ell'\ell'$ search for (a), (b), (c) the ggF-MVA-high categories, (d) the ggF-MVA-low category and (e) the VBF-MVA-enriched category. The backgrounds are determined from a combined likelihood fit to the data under the background-only hypothesis. The simulated signal at 600 GeV is normalized to a cross section corresponding to one hundred times the observed upper limit given in section 7.7.3. The error bars on the data points indicate the statistical uncertainty, while the systematic uncertainty in the prediction is shown by the hatched band. The lower panels show the ratio of data to prediction.	127
450			
451			
452			
453			
454			
455			
456			
457			
458	7.26	Pulls and constraints of nuisance parameters after a background only fit to (a) Asimov data and (b) observed data in the $\ell\ell\ell'\ell'$ channel. The Asimov data is generated with background data only, and the observed data includes datasets from 2015 to 2018.	128
459			
460			
461			
462	7.27	Correlation of nuisance parameters after a background only fit to Asimov data in the $\ell\ell\ell'\ell'$ channel. The Asimov data is generated with background data only.	129
463			
464			

465	7.28	The expected and observed upper limits at 95% CL on $\sigma \times BR(H \rightarrow ZZ)$ using the MVA-based analysis for ggF (left) and VBF (right) production. The green and yellow bands represent the $\pm 1\sigma$ and $\pm 2\sigma$ uncertainties in the ex- pected limits.	129
466			
467			
468			
469	7.29	The expected and observed upper limits at 95% CL on $\sigma \times BR(H \rightarrow ZZ)$ using the cut-based analysis for ggF (left) and VBF (right) production. The green and yellow bands represent the $\pm 1\sigma$ and $\pm 2\sigma$ uncertainties in the ex- pected limits.	130
470			
471			
472			
473	7.30	The upper limits at 95% confidence level on $\sigma_{ggF} \times BR(H \rightarrow ZZ)$ as a function of the heavy resonance mass m_H for the ggF production mode with an intrinsic width of 1% (top left), 5% (top right), 10% (bottom left) and 15% (bottom right) for both the case where interference with Standard Model processes is considered. The green and yellow bands represent the $\pm 1\sigma$ and $\pm 2\sigma$ uncertainties in the expected limits.	131
474			
475			
476			
477			
478			
479	7.31	The upper limits at 95% confidence level on $\sigma_{ggF} \times BR(G_{KK} \rightarrow ZZ)$ as a function of the heavy resonance mass $m(G_{KK})$ for the ggF production mode in RS Graviton model. The green and yellow bands represent the $\pm 1\sigma$ and $\pm 2\sigma$ uncertainties in the expected limits.	131
480			
481			
482			
483	7.32	The expected (left) and observed (right) upper limits at 95% confidence level on $\sigma \times BR(S \rightarrow ZZ)$ for ggF production mode at different assumptions.	133
484			
485	7.33	Comparisons of the expected upper limits at 95% CL on the cross section times branching ratio as a function of the heavy resonance mass m_H for the ggF production mode (left) and for the VBF production mode (right) in the case of the NWA. The expected limits from the previous publication are shown in the green dashed line and are projected to the 139 fb^{-1} as shown in the blue dashed line. In addition, the current results based on either cut-based categorisation or the multivariate-based categorisation are shown in red and black lines.	135
486			
487			
488			
489			
490			
491			
492			
493	7.34	Display of one candidate event in 4μ final state with the mass of 1.35 TeV.	135
494			

List of Tables

494	3.1	Summary of design parameters of the LHC for pp collisions.	20
496	4.1	Overview of the contributions to E_T^{miss} .	58
497	6.1	Overlap removal criteria between pre-selection objects for the $\ell\ell\ell'\ell'$ channel. The overlap removal follows the order shown in this table. Once an object has been marked as removed, it does not participate in the subsequent stages of the overlap removal procedure.	66
501	6.2	Summary of selection of physics objects and candidate events at detector level in the $\ell\ell\ell'\ell'jj$ signal region.	67
503	6.3	Observed data and expected signal and background yields in 139 fb^{-1} of luminosity. Minor backgrounds are summed together as ‘Others’. Uncertainties on the predictions include both statistical and systematic components.	67
506	6.4	Observed data and expected signal and background yields in 139 fb^{-1} of luminosity. Diboson background in table includes all the other diboson processes discussed in section 6.2.2, except those with four-lepton final state. Uncertainties include only MC statistic. No events from $Z+jets$ and $t\bar{t}$ MC samples pass the selection, and are indicated as 0 in the table.	68
511	6.5	Fake background estimations in the SR. For nominal value, the 2D fake factor together with the $Z+jets$ and $t\bar{t}$ combination applied. The other lines show the estimations with different uncertainty variations.	72
514	6.6	Summary of different variations for EW- and QCD- $ZZjj$ theoretical uncertainties measurement.	73
516	6.7	Summary of theoretical uncertainties for the fiducial volume (SR) for both EW and QCD qq -initial processes.	73
518	6.8	Summary of theoretical uncertainties for the control region for EW and $qqQCD$ processes.	73
520	6.9	Experimental systematic uncertainties in $\ell\ell\ell'\ell'$ channel with the luminosity of 139 fb^{-1} . The “Electron Exp.”, “Muon Exp.” and “Jet Exp.” represent the quadrature of the respective sources from electron, muon, and jets.	75
523	6.10	C Factor of different $ZZjj$ processes.	77
524	6.11	Measured and predicted fiducial cross-sections in $\ell\ell\ell'\ell'jj$ final-state. Uncertainties due to different sources are presented.	78

526	6.12	Input features for the training of MD.	79
527	6.13	Observed μ_{EW} and $\mu_{\text{QCD}}^{\ell\ell\ell'jj}$, as well as the observed and expected significance from the individual $\ell\ell\ell'\ell'$ channel. The full set of systematic uncertainties are included.	80
530	6.14	Comparison of event yields for signal ($N_{\text{EW-ZZjj}}$) and background ($N_{\text{QCD-ZZjj}}$) processes, and expected significance of EW- $Z Z jj$ processes, normalized to 3000 fb^{-1} data at 14 TeV, with baseline and alternative selections. Uncertainties in the table refer to expected data statistical uncertainty at 14 TeV with 3000 fb^{-1}	84
535	6.15	Summary of expected cross-section measured with different theoretical uncertainties. The statistical uncertainty is computed from expected data yield with 3000 fb^{-1} at 14 TeV. Different uncertainties are treated as uncorrelated and summed quadratically.	88
539	7.1	Summary of the recorded integrated luminosity (lumi), average and peak pile-up (PU) of data from 2015 to 2018.	91
541	7.2	Summary of the p_T (E_T) trigger thresholds (in GeV) employed for the muon (electron) trigger selection in the year of 2015, 2016, 2017, and 2018.	94
543	7.3	Summary of the object and event selection requirements.	97
544	7.4	Cutflow table for a narrow-width ggF signal sample at $m_H = 600 \text{ GeV}$. N_{event} denotes the number of events selected after each cut is applied, normalized to 139 fb^{-1} , according to the expected upper limit on the cross section. The acceptances (the proportion of events selected relative to the initial number of events) are also included.	98
549	7.5	Cutflow table for a narrow-width ggF signal sample at $m_H = 1000 \text{ GeV}$. N_{event} denotes the number of events selected after each cut is applied, normalized to 139 fb^{-1} , according to the expected upper limit on the cross section. The acceptances (the proportion of events selected relative to the initial number of events) are also included.	98
554	7.6	Cutflow table for a narrow-width VBF signal sample at $m_H = 600 \text{ GeV}$. N_{event} denotes the number of events selected after each cut is applied, normalized to 139 fb^{-1} , according to the expected upper limit on the cross section. The acceptances (the proportion of events selected relative to the initial number of events) are also included.	99

559	7.7	Cutflow table for a narrow-width VBF signal sample at $m_H = 1000$ GeV.	99
560		N_{event} denotes the number of events selected after each cut is applied, nor-	
561		malized to 139 fb^{-1} , according to the expected upper limit on the cross sec-	
562		tion. The acceptances (the proportion of events selected relative to the initial	
563		number of events) are also included.	99
564	7.8	Input features used in the “VBF-classifier” for the $\ell\ell\ell'\ell'$ analysis. The RNN	
565		stands for the recurrent neural network and MLP for the multilayer perceptron.	
566		102
567	7.9	Input features used in the “ggF-classifier” for the $\ell\ell\ell'\ell'$ analysis. The RNN	
568		stands for the recurrent neural network and MLP for the multilayer perceptron.	
569		104
570	7.10	Summary of acceptance uncertainties of PDF, QCD scale and parton shower	
571		variations for ggF production. The MVA-based categorization is used.	123
572	7.11	Summary of acceptance uncertainties of PDF, QCD scale and parton shower	
573		variations for VBF production. The MVA-based categorization is used.	123
574	7.12	Summary of acceptance uncertainties of PDF, scale, and parton showering	
575		variations for QCD $q\bar{q} \rightarrow ZZ$ background. The MVA-based categorization	
576		is used.	124
577	7.13	A list of the experimental systematics considered in this analysis. The NPs	
578		have been separated by whether they only affect the normalisation (left col-	
579		umn) or if they affect the shape (right column) of the $m_{4\ell}$ distribution. They	
580		are further subdivided into the primary objects that they affect.	132
581	7.14	Expected and observed numbers of events for $m_{4\ell} > 200$ GeV, together with	
582		their systematic uncertainties, for three MVA-based categories. The expected	
583		number of events, as well as their uncertainties, are obtained from a likelihood	
584		fit to the data under the background-only hypothesis. The uncertainties of the	
585		ZZ normalisation factors, presented in table 7.15, are also taken into account.	
586		133
587	7.15	ZZ normalization factor in each category, obtained from a likelihood fit to	
588		the data under the background-only hypothesis.	133

589	7.16 Impact of the leading systematic uncertainties, the data statistic uncertainties,	
590	as well as the total uncertainties on the predicted signal event yield with the	
591	cross section times branching ratio being set to the expected upper limit, ex-	
592	pressed as a percentage of the signal yield for the ggF (left) and VBF (right)	
593	production modes at $m_H = 400$ and 1000 GeV.	134

594

Dedicated to my mother!

595

献给我的母亲！

596

597

598

Chapter 1 Introduction

599 The goal of particle physics is to understand how our universe works at its most fundamental level. It can be accomplished by pursuing the mysteries of the basic construction of
600 matter and energy, probing the interactions between elementary particles, and exploring
601 the basic nature of space and time itself.

603 **Elementary particles**

604 From around the 6th century BC, ancient Greek philosophers Leucippus, Democritus, and Epicurus brought up a philosophical idea that everything is composed of “uncuttable” elementary particles. In the 19th century, John Dalton, through his work
605 on stoichiometry, concluded that each element of nature was composed of a single, unique
606 type of particle. The particle was named as “atom” after the Greek word atomos, with
607 the meaning of “indivisible”. However this Dalton’s atom theory was strongly chal-
608 lenged later. Near the end of 19th century, physicists discovered that Dalton’s atoms
609 are not, in fact, the fundamental particles of nature, but conglomerates of even smaller
610 particles. Electron was discovered by J. J. Thomson in 1897, and then its charge was
611 carefully measured by Robert Andrews Millikan and Harvey Fletcher in their “oil drop
612 experiment” of 1909. In early 20th-century, Rutherford’s “gold foil experiment” showed
613 that the atom is mainly empty space, with almost all its mass concentrated in a tiny posi-
614 tively charge atomic nucleus. Then the discoveries of anti-particles (the positron in 1932)
615 and other particles (e.g. the muon in 1936) show that more discoveries could be expected
616 in future experiments.

619 Starting from 1950s, more accelerator facilities were put into service. Throughout
620 the 1950s and 1960s, a bewildering variety of particles were found in collisions of parti-
621 cles from increasingly high-energy beams. It was referred to informally as the “particle
622 zoo”. In 1964, the quark model was independently proposed by physicists Murray Gell-
623 Mann and George Zweig, and experimentally confirmed of their existence in mid-1970s.
624 In 1970s, the establishment of quantum chromodynamics (QCD) postulated the funda-
625 mental strong interaction, experienced by quarks and mediated by gluons.

626 The well-known Standard model (SM) was developed in stages throughout the latter
627 half of the 20th century. Since then, confirmation of the top quark (1995), the tau neu-
628 trino (2000), and the Higgs boson (2012) have added further credence to the Standard
629 Model. Now, the quarks, leptons and gauge bosons are the elementary constituents in a
630 framework of Standard Model of particle physics, which theoretically describes three of

631 the four known fundamental forces (the electromagnetic, weak, and strong interactions,
632 and not including the gravitational force) in the universe, as well as classifies all
633 known elementary particles.

634 **Higgs mechanics and electroweak symmetry breaking**

635 In 1961, Sheldon Glashow, Steven Weinberg and Abdus Salam together brought for-
636 ward a unified electroweak theory to combine the electromagnetic and weak interactions.
637 In the standard model, if under the condition that the energy is high enough but elec-
638 troweak symmetry is unbroken, all elementary particles are massless. But measurements
639 show the fact that the W and Z bosons actually have masses. Later on, the Higgs mechan-
640 ics resolves this conundrum. The simplest description of the mechanism adds a Higgs
641 field that permeates all space to the Standard Model. Below some extremely high energy,
642 the field causes spontaneous symmetry breaking during interactions. All massive parti-
643 cles in the Standard Model, including the W and Z bosons, interact with Higgs boson to
644 acquire their mass.

645 Over the past few decades, with the combination of electroweak theory, Higgs me-
646 chanics and strong interactions has been widely accepted. But the Higgs boson, which is
647 essential to explain the mechanics of the property “mass” for gauge bosons and fermions,
648 had been the final missing piece in the Standard Model of particle physics at that time. The
649 mass of Higgs boson was not specifically predicted, and it has been searched in several
650 large experiments (eg. LEP at CERN, Tevatron at Fermilab, and LHC at CERN) with
651 different energy. In 2012, the discovery of Higgs boson was finally announced by the
652 ATLAS and CMS collaborations at the Large Hadron Collider (LHC) with its mass round
653 125 GeV. Peter Higgs and Francois Englert were award the 2013’s Nobel Prize in Physics
654 for their theoretical discovery of a mechanism that contributes to our understanding of the
655 origin of mass of subatomic particles.

656 **Contents of this thesis**

657 This dissertation is organized as follows. Section 2 briefly introduces the Standard
658 Model of particle physics, the Higgs mechanism related to the dissertation and the LHC
659 phenomenology. Section 3 gives an overview of the LHC and the ATLAS detector. The
660 detector simulation and the reconstruction of physics objects are described in section 4.
661 And then section 5 focuses on the Standard model ZZ production cross section measure-
662 ment in $ZZ \rightarrow \ell\ell\ell'\ell'$ channel, where ℓ stands for electron or muon, and the observation
663 of its electroweak component as well as its further prospects in High luminosity LHC
664 (HL-LHC). Section 6 present the search of possible heavy resonances in $ZZ \rightarrow \ell\ell\ell'\ell'$
665 channel. In the end, section 7 gives the summary and outlook for future physics in LHC.

666

Chapter 2 Theory

667 2.1 The Standard Model of Particle Physics

668 The standard model (SM) reflects our current understanding of elementary particles
 669 and several basic interactions. It is a gauge quantum field theory containing the internal symmetries of the unitary product group $SU(3) \times SU(2) \times U(1)$, in which the color
 670 group $SU(3)$ presents the strong interaction, and $SU(2) \times U(1)$ describes the electroweak
 671 interactions. Over the past decades, the SM has been widely tested through various ex-
 672 periments with extremely high precision.

674 2.1.1 Elementary particles in the Standard Model

675 The elementary particles in SM can be classified into 3 class: *fermions*, *gauge bosons* and the *Higgs boson* as shown in Figure 2.1.

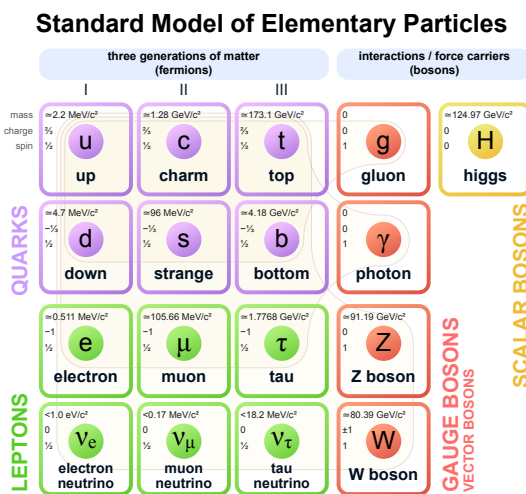


Fig. 2.1 The elementary particles of the Standard Model.

676

677 **Fermions** The Standard Model includes 12 elementary particles of spin- $\frac{1}{2}$ obeying the
 678 Fermi-Dirac statistics, known as fermions. They are classified into two types: *leptons* and
 679 *quarks* according to their interactions. The *leptons* include three generations: electron
 680 (e) and electron neutrino (ν_e); muon (μ) and muon neutrino (ν_μ); tau (τ) and tau neutrino
 681 (ν_τ). The e , μ and τ carry electric charge of -1 and three neutrinos are electrically neutral.
 682 All the leptons can participate in electroweak interactions. Also there are three generations
 683 of *quarks*: up (u) and down (d); charm (c) and strange (s); top (t) and bottom (b). The
 684 defining property of the quarks is that they carry color charge (while leptons don't), and
 685 hence interact via the strong interaction, letting them to be strongly bound from one to

another, forming color-neutral composite particles (known as hadrons) containing either a quark and an antiquark (mesons) or three quarks (baryons). In the meantime, u , c and t -quark carry electric charge of $2/3$, and d , s and b -quark carry electric charge of $-1/3$. Hence they interact via all three interactions described in SM. Each fermion also has a corresponding antiparticles.

Gauge bosons act as force carriers that mediate the strong, weak, and electromagnetic interactions in SM. They are spin-1 particles obeying the Bose-Einstein statistics. There are three types of gauge bosons:

- The eight massless *gluons* mediate the strong interactions between color charged particles (quarks).
- The massless *photons* mediate the electromagnetic force between electrically charged particles.
- The W^+ , W^- and Z bosons mediate the weak interactions between particles of different flavors (all quarks and leptons). All these three bosons are massive, the W^\pm carries an electric charge of $+1$ and -1 and couples to the electromagnetic interaction while Z boson is electrically neutral.

Figure 2.2 shows the Feynman diagrams of corresponding interactions in SM.

Higgs boson is a massive scalar elementary particle with spin-0. It plays a unique role in the SM by explaining the origin of masses of massive gauge bosons (W^\pm and Z) and fermions. And it is the last discovered particle in SM.

2.1.2 Electroweak theory

The electroweak interaction is the unified description of two of the four known fundamental interactions of nature: electromagnetism and the weak interaction. It is based on the gauge group of $SU(2)_L \times SU(1)_Y$, in which L is the left-handed fields and Y is the weak hypercharge^[1]. It follows the Lagrangian of

$$L_{EW} = L_{gauge} + L_{Higgs} + L_{fermion} + L_{Yukawa} \quad (2.1)$$

L_{gauge} is the **gauge term** part

$$L_{gauge} = -\frac{1}{4} W_{\mu\nu}^i W^{\mu\nu i} - \frac{1}{4} B_{\mu\nu} B^{\mu\nu} \quad (2.2)$$

where W_μ^i and B_μ present the $SU(2)_L$ and $SU(1)_Y$ gauge fields respectively, with the

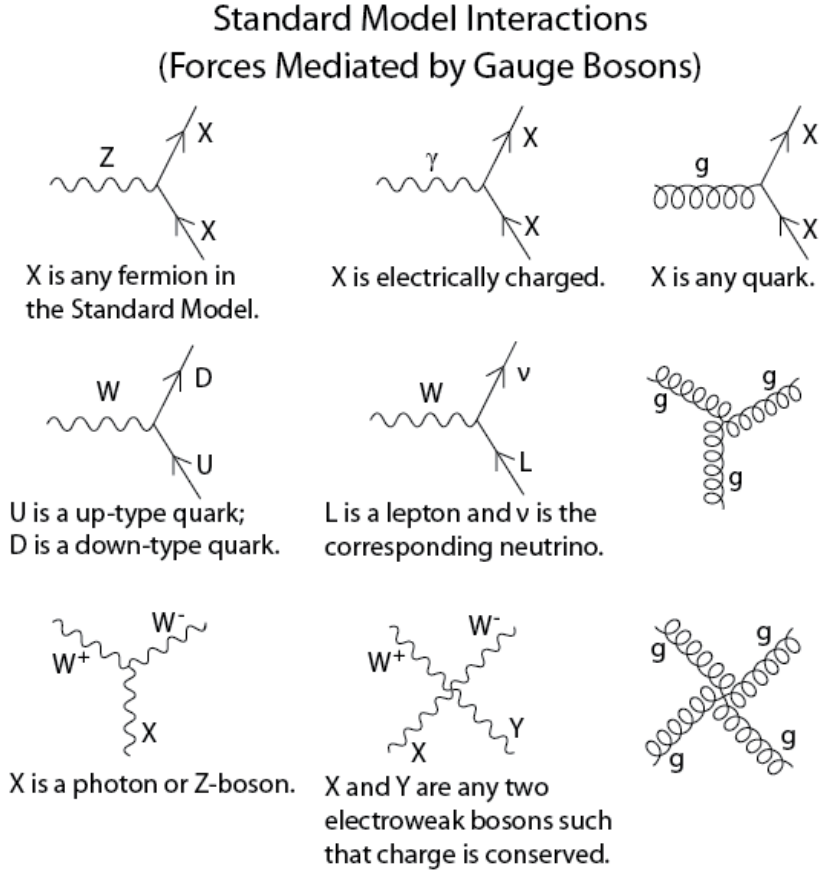


Fig. 2.2 The Feynman diagrams of interactions that form the basis of the standard model.

⁷¹³ corresponding field strength tensors of

$$\begin{aligned} B_{\mu\nu} &= \partial_\mu B_\nu - \partial_\nu B_\mu \\ W_{\mu\nu}^i &= \partial_\mu W_\nu^i - \partial_\nu W_\mu^i - g \epsilon_{ijk} W_\mu^j W_\nu^k \end{aligned} \quad (2.3)$$

⁷¹⁴ In the equations above, g is the $SU(2)_L$ gauge coupling and ϵ_{ijk} is the totally antisymmetric tensor. The gauge Lagrangian has three and four-point self interactions of W^i , which result in triple and quartic gauge boson couplings.

⁷¹⁷ The second term of the Lagrangian is the **scalar part**:

$$L_{Higgs} = (D^\mu \phi)^\dagger D_\mu \phi - V(\phi) \quad (2.4)$$

⁷¹⁸ where $\phi = \begin{pmatrix} \phi^+ \\ \phi^0 \end{pmatrix}$ is a complex Higgs scalar, and $V(\phi)$ is the Higgs potential which is ⁷¹⁹ restricted into the form of

$$V(\phi) = +\mu^2 \phi^\dagger \phi + \lambda (\phi^\dagger \phi)^2 \quad (2.5)$$

⁷²⁰ due to the combination of $SU(2)_L \times SU(1)_Y$ invariance and renormalizability. In Eq. 2.5,

721 μ is a mass-dependent parameter and λ is the quartic Higgs scalar coupling, which rep-
 722 resents a quartic self-interaction between the scalar fields. When $\mu^2 < 0$, there will be
 723 spontaneous symmetry breaking (more details in section 2.1.3). To maintain vacuum sta-
 724 bility, $\lambda > 0$ is required. And in Eq. 2.4, the gauge covariant derivative is defined as

$$D_\mu \phi = \left(\partial_\mu + ig \frac{\tau^i}{2} W_\mu^i + \frac{ig'}{2} B_\mu \right) \phi \quad (2.6)$$

725 in which τ^i represents the Pauli matrices, and g' is the $U(1)_Y$ gauge coupling. The square
 726 of the covariant derivative results in three and four -point interactions between the gauge
 727 and scalar fields.

728 The third term of the Lagrangian is the **fermion part**

$$\begin{aligned} L_{fermion} = & \sum_{m=1}^F (\bar{q}_{mL}^0 \gamma_\mu D_\mu q_{mL}^0 + \bar{l}_{mL}^0 \gamma_\mu D_\mu l_{mL}^0 + \bar{u}_{mR}^0 \gamma_\mu D_\mu u_{mR}^0 \\ & + \bar{d}_{mR}^0 \gamma_\mu D_\mu d_{mR}^0 + \bar{e}_{mR}^0 \gamma_\mu D_\mu e_{mR}^0 + \bar{v}_{mR}^0 \gamma_\mu D_\mu v_{mR}^0) \end{aligned} \quad (2.7)$$

729 In Eq. 2.7, m is the family index of fermions, F is the number of families. The subscripts
 730 $L(R)$ stand for the left (right) chiral projection $\psi_{L(R)} \equiv (1 \mp \gamma_5) \psi / 2$.

$$q_{mL}^0 = \begin{pmatrix} u_m^0 \\ d_m^0 \end{pmatrix}_L \quad l_{mL}^0 = \begin{pmatrix} v_m^0 \\ e_m^{-0} \end{pmatrix}_L \quad (2.8)$$

731 are the $SU(2)$ doublets of left-hand quarks and leptons, while u_{mR}^0 , d_{mR}^0 , e_{mR}^{-0} and v_{mR}^0 are
 732 the right-hand singlets.

733 The last term in Eq. 2.1 is **Yukawa term**

$$\begin{aligned} L_{Yukawa} = & - \sum_{m,n=1}^F [\Gamma_{mn}^u \bar{q}_{mL}^0 \tilde{\phi} u_{nR}^0 + \Gamma_{mn}^d \bar{q}_{mL}^0 \phi d_{nR}^0 \\ & + \Gamma_{mn}^e \bar{l}_{mL}^0 \phi e_{nR}^0 + \Gamma_{mn}^v \bar{l}_{mL}^0 \tilde{\phi} v_{nR}^0] + h.c. \end{aligned} \quad (2.9)$$

734 the matrices Γ_{mn} refer to the Yukawa couplings between single Higgs doublet (ϕ) and the
 735 various flavors of quarks (m) and leptons (n).

736 2.1.3 Higgs mechanism and Electroweak symmetry breaking

737 As shown in previous subsection, the Lagrangian L_{gauge} does not involve any mass
 738 term due to the requirement of gauge invariance. So all the W and B bosons should be
 739 massless. But experimental observations show that the gauge bosons are massive. There-
 740 fore, the gauge invariance must be broken spontaneously. The Higgs field is introduced
 741 to break the $SU(2)_L \times U(1)_Y$ symmetry and gauge bosons and fermions can interact with

742 Higgs filed to acquire their masses. And this specific process is named *Higgs mechanism*
 743 in SM.

744 The Higgs field ϕ is a doublet and can be written in a Hermitian basis as

$$\phi = \begin{pmatrix} \phi^+ \\ \phi^0 \end{pmatrix} = \frac{1}{\sqrt{2}} \begin{pmatrix} \phi_1 - i\phi_2 \\ \phi_3 - i\phi_4 \end{pmatrix} \quad (2.10)$$

745 where $\phi_i = \phi_i^+$ stand for four Hermitian field. In this new basis, the Higgs potential in
 746 Eq. 2.5 can be expressed as:

$$V(\phi) = \frac{1}{2}\mu^2 \left(\sum_{i=1}^4 \phi_i^2 \right) + \frac{1}{4}\lambda \left(\sum_{i=1}^4 \phi_i^2 \right)^2 \quad (2.11)$$

747 To simplify the situation, the axis in this four-dimensional space can be chosen to satisfied
 748 $\langle 0 | \phi_i | 0 \rangle = 0$ for $i = 1, 2, 4$, and $\langle 0 | \phi_3 | 0 \rangle = v$. Thus,

$$V(\phi) \rightarrow V(v) = \frac{1}{2}\mu^2 v^2 + \frac{1}{4}\lambda v^4 \quad (2.12)$$

749 The minimization of this potential depends on the sign of μ^2 as shown in figure 2.3. When
 750 $\mu^2 > 0$ the minimum occurs at $v = 0$, namely the vacuum is empty space and $SU(2)_L \times$
 751 $U(1)_Y$ symmetry is unbroken. In the case of $\mu^2 < 0$, the $v = 0$ symmetric point is no
 752 longer stable and the minimum occurs at nonzero value of $v = (-\mu^2/\lambda)^{1/2}$ which breaks
 the $SU(2)_L \times U(1)_Y$ symmetry. Thus, the classical vacuum ϕ_0 of Higgs doublet can be

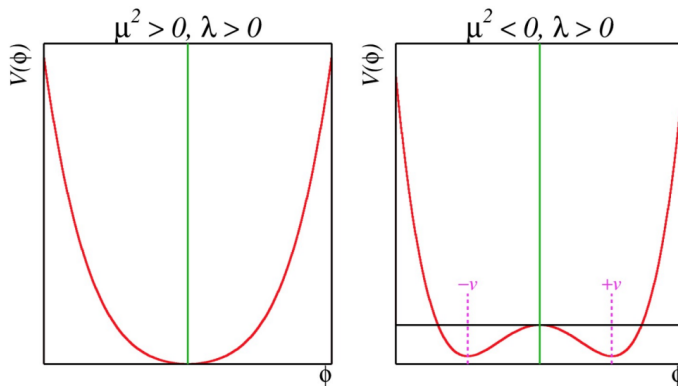


Fig. 2.3 The Higgs potential $V(\phi)$ with $\mu^2 > 0$ (left) and $\mu^2 < 0$ (right).

753

754 expressed by

$$\phi_0 = \frac{1}{\sqrt{2}} \begin{pmatrix} 0 \\ v \end{pmatrix} \quad (2.13)$$

755 And to quantize around the classical vacuum in a general form:

$$\phi = \frac{1}{\sqrt{2}} \begin{pmatrix} 0 \\ v + H \end{pmatrix} \quad (2.14)$$

756 Where H is a Hermitian field for physical Higgs scalar. In this gauge, the Lagrangian

757 L_{Higgs} in Eq. 2.4 takes a simple form

$$\begin{aligned} L_{Higgs} &= (D^\mu \phi)^\dagger D_\mu \phi - V(\phi) \\ &= M_W^2 W^{\mu+} W_\mu^- \left(1 + \frac{H}{v}\right)^2 + \frac{1}{2} M_Z^2 Z^\mu Z_\mu \left(1 + \frac{H}{v}\right)^2 \\ &\quad + \frac{1}{2} (\partial_\mu H)^2 - V(\phi) \end{aligned} \quad (2.15)$$

758 where the W and Z fields are

$$\begin{aligned} W^\pm &= \frac{1}{\sqrt{2}} (W^1 \mp iW^2) \\ Z &= -\sin\theta_W B + \cos\theta_W W^3 \end{aligned} \quad (2.16)$$

759 Therefore, in Eq. 2.15 spontaneous symmetry breaking brings out masses for the W and

760 Z gauge bosons

$$\begin{aligned} M_W &= \frac{gv}{2} \\ M_Z &= \sqrt{g^2 + g'^2} \frac{v}{2} = \frac{M_W}{\cos\theta_W} \end{aligned} \quad (2.17)$$

761 where θ_W is the weak angle defined as

$$\sin\theta_W = \frac{g'}{\sqrt{g^2 + g'^2}} \quad \cos\theta_W = \frac{g}{\sqrt{g^2 + g'^2}} \quad \tan\theta_W = \frac{g'}{g} \quad (2.18)$$

762 Then another gauge boson photon remains massless with the field of

$$A = \cos\theta_W B + \sin\theta_W W^3 \quad (2.19)$$

763 After the symmetry breaking, the Higgs potential in unitary gauge can be written into

$$V(\phi) = -\frac{\mu^4}{4\lambda} - \mu^4 H^2 + \lambda v H^3 + \frac{\lambda}{4} H^4 \quad (2.20)$$

764 The first term in V is a constant, while the second term denotes a (tree-level) mass of

765 Higgs boson

$$M_H = \sqrt{-2\mu^2} = \sqrt{2\lambda} v \quad (2.21)$$

766 Due to the unknown of quartic Higgs coupling λ , the Higgs mass is not predicted. The

767 third and fourth terms in the Higgs potential V denote the induced cubic and quartic in-
 768 teractions of the Higgs scalar.

769 Through the Higgs mechanism, fermions can also acquire their masses. In the unitary
 770 gauge, Yukawa Lagrangian (L_{Yukawa}) can be written as a simple form of^[2]

$$L_{Yukawa} = - \left(1 + \frac{H}{v} \right) (m_d \bar{d}d + m_u \bar{u}u + m_l \bar{l}l) \quad (2.22)$$

771 in which $m_f = \frac{y_f v}{\sqrt{2}}$ for $f = d, u, l$.

772 2.1.4 Beyond the SM Higgs sector

773 After the discovery of the Higgs boson by the ATLAS and CMS Collaborations at the
 774 LHC^[3-4] in 2012, one question comes out: if this Higgs boson at around 125 GeV is fully
 775 responsible for the unitarization of the scattering amplitudes? The possibility that this
 776 discovered particle is just a part of the extended Higgs sector by various extensions cannot
 777 be ruled out. Many models, motivated by hierarchy and naturalness arguments, predicted
 778 the extended Higgs sector, such as the electroweak-singlet model^[5] and the two-Higgs-
 779 doublet models (2HDM)^[6].

780 Singlet scalar extension of the SM

781 The electroweak singlet model can be considered as the minimal extension of the SM
 782 Higgs sector, encompassing a single gauge singlet real scalar field S . In this model, a
 783 heavy, real singlet is introduced in addition to the SM one. The associated zero tempera-
 784 ture, tree-level scalar potential can be written as:

$$V = V_{SM} + V_{HS} + V_S \quad (2.23)$$

785 where

$$\begin{aligned} V_{SM} &= \mu^2 (H^\dagger H) + \bar{\lambda}_0 (H^\dagger H) \\ V_{HS} &= \frac{a_1}{2} (H^\dagger H) S + \frac{a_2}{2} (H^\dagger H) S^2 \\ V_S &= \frac{b_2}{2} S^2 + \frac{b_3}{3} S^3 + \frac{b_4}{4} S^4 \end{aligned} \quad (2.24)$$

786 where H stands for the SM scalar field of the original Higgs mechanism. After elec-
 787 troweak symmetry breaking, this model gives rise to two CP -even Higgs bosons, in which
 788 the lighter one is the Higgs boson that has been discovered at around 125 GeV. And the new
 789 heavy scalar (S) is allowed to have both SM and non-SM decays. One would expect to
 790 see suppressions of the branching ratio to SM Higgs decay modes, as the branching ratio
 791 to the pair of singlet-like scalars would be considerable.

792 **Two Higgs Doublet Model**

793 The two-Higgs-doublet model (2HDM) is another extension of SM Higgs sector carried
794 by an additional scalar doublet. In this model, through electroweak symmetry breaking,
795 there are five physical Higgs bosons: two CP-even, one CP-odd, and two charged ones.

796 The most general CP-conserving 2HDM has seven free parameters:

- 797 • The Higgs boson masses: m_h , m_H , m_A and $m_{H^{pm}}$.
798 • $\tan\beta$: the ratio of the vacuum expectation values of the two doublets.
799 • α : the mixing angle between the CP-even Higgs bosons.
800 • m_{12}^2 : the potential parameter that mixes the two Higgs doublets.

801 where the m_h can be identified as the mass of observed Higgs boson at around 125 GeV,
802 and m_H is another heavy scalar with similar properties as h boson. The coupling of the
803 neutral Higgs bosons to the W and Z are the same:

- 804 1. The coupling of the light Higgs, h , to either WW or ZZ is the same as the Standard
805 Model coupling times $\sin(\beta - \alpha)$
806 2. The coupling of the heavier Higgs, H , is the same as the Standard Model coupling
807 times $\cos(\alpha - \beta)$.
808 3. The coupling of the pseudoscalar, A , to vector bosons vanishes.

809 The two Higgs doublets, Φ_1 and Φ_2 , can couple to fermions (leptons and up- and down-
810 type quarks) in several ways, which leads to several types of 2HDM models:

- 811 • Type-I model: all quarks and leptons couple only to Φ_2 .
812 • Type-II model: down-type quarks and leptons couple to Φ_1 , and up-type quarks
813 couple to Φ_2 .
814 • The “lepton-specific” model: leptons couple to Φ_1 , while all quarks couple to Φ_2 .
815 • The “flipped” model: down-type quarks couple to Φ_1 , while up-type quarks and
816 leptons couple to Φ_2 .

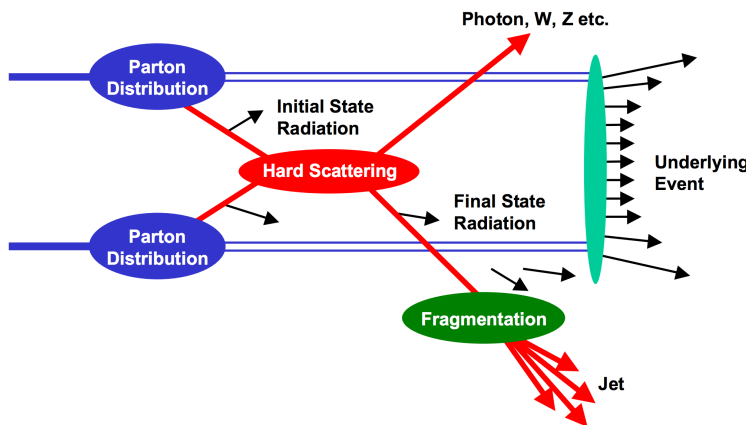
817 **2.2 Phenomenology of Large Hadron Collider**

818 The Large Hadron Collider (LHC) was built as a bridge between the theories and the
819 experiment. Physicists hope that the LHC can help to answer some of the fundamental
820 open questions in physics, concerning the basic laws of interactions and forces among the
821 elementary particles, the deep structure of space and time, and in particular the interrela-
822 tion between quantum mechanics and general relativity. This section will talk about firstly
823 the general introduction of Physics inside hadronic collision, then followed by two impor-
824 tant LHC phenomenologies of the Higgs physics and Diboson physics that are related

825 closely to this dissertation.

826 2.2.1 Physics at hadronic collision

827 Protons are not the elementary particle, which actually are composed of quarks and
 828 gluons. So in proton-proton (pp) collision at the LHC, it is not protons themselves interact
 829 but quarks and gluons. Scattering processes can then be further classified into either *hard*
 830 or *soft* processes according to the momentum transfer during the interaction^[7]. QCD, as
 831 an underlying theory for both processes, its approach and level of understandings in two
 832 cases are quite different. For hard process, eg. Higgs, vector bosons and jets production,
 833 the rates and event properties can be precisely predicted based on perturbation theory.
 834 However, for soft processes like total cross-section, the underlying events, the rates and
 835 properties are dominated by non-perturbative QCD effects that are less understood. For
 836 many hard processes, the hard interactions are accompanied by soft ones. An example of
 the hadronic collision is illustrated in figure 2.4. and the typical features are summarized



837
 838 **Fig. 2.4 Schematic view of a hadron-hadron collision^[8].**

839 as below:

- 840 • **Parton Distribution Function (PDF):** $f_i(x, Q^2)$ gives the probability of finding a
 841 parton with flavor i (quark or gluon), carrying a momentum fraction of x and with
 842 the scale of momentum transfer Q in a proton. Parton distribution function cannot
 843 be fully calculated by perturbative QCD because of the inherent non-perturbative
 844 nature of partons. There are many different sets of PDFs that are determined by
 845 fits to data from experimental observables in various processes. As an example,
 846 figure 2.5 shows the *PDF4LHC15 NLO PDFs*, which are based on the combination
 847 of the *CT14*, *MMHT14* and *NNPDF3.1 NNLO* PDF sets^[9].
- 848 • **Fragmentation and hadronization:** The processes to produce final state particles

(or jets) from the partons produced in hard scattering.

- **Initial/Final state radiation:** The incoming and outgoing partons that carry color charge can emit QCD radiation, which gives rise to additional jets. Also the charged incoming and outgoing particles can emit Quantum Electrodynamics (QED) radiations with photons.
- **Underlying events:** Products from soft processes (not come from the primary hard scattering) as the remnants of scattering interactions.

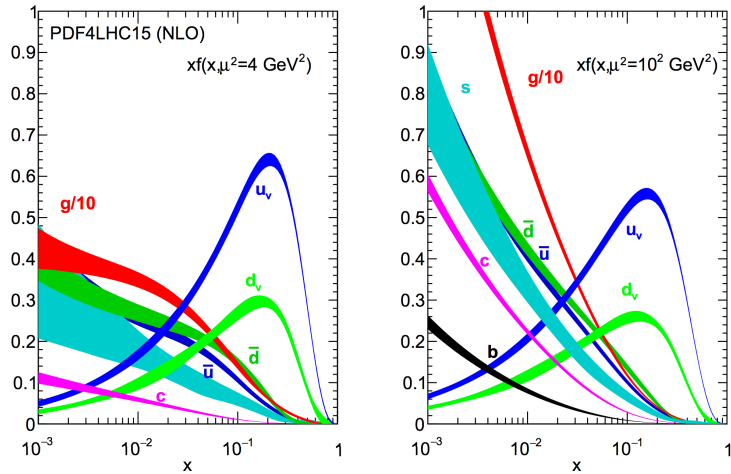


Fig. 2.5 The PDF4LHC15 NLO PDFs at a low scale $\mu^2 = Q^2 = 4\text{GeV}^2$ (left) and at $\mu^2 = Q^2 = 100\text{GeV}^2$ (right) as a function of x .

855 Cross section of hard scattering

856 According to *QCD factorization theorems*^[10], the perturbative calculations can be ap-
857 plied to many important hard processes involving hadrons. The basic problem addressed
858 by factorization theorems is how to calculate high energy cross sections. Consider the
859 process of scattering between two hardons A and B to produce a final state X, the cross
860 section σ can be obtained by summing over all the subprocess cross section $\hat{\sigma}$ ^[11]

$$\sigma_{AB} = \int dx_a dx_b f_{q/A}(x_a) f_{q/B}(x_b) \hat{\sigma}_{ab \rightarrow X} \quad (2.25)$$

861 where $f_{q/A}(x_q)$ is the parton distribution functions of parton q . Taking into account the
862 leading order correction:

$$\sigma_{AB} = \int dx_a dx_b f_{q/A}(x_a Q^2) f_{q/B}(x_b Q^2) \hat{\sigma}_{ab \rightarrow X} \quad (2.26)$$

863 where Q^2 represents large momentum scale that characterizes the hard scattering. Later
864 on, since the finite corrections were not universal and had to be calculated separately for
865 each process, the perturbative $O(\alpha_S^n)$ corrections to the leading logarithm cross section

866 in Eq. 2.26 need to be applied, one can get:

$$\sigma_{AB} = \int dx_a dx_b f_{a/A}(x_a \mu_F^2) f_{b/B}(x_b \mu_F^2) \hat{\sigma}_{ab \rightarrow X}(\alpha_S, \mu_R, \mu_F) \quad (2.27)$$

867 in which μ_F is *factorization scale* which can represent the scale that separates the long-
 868 and short-distance physics, and μ_R is the *renormalization scale* for QCD running coupling.
 869 $\hat{\sigma}_{ab \rightarrow X}$ is the parton-level hard scattering cross section that can be calculated perturbatively
 870 in QCD with the form of

$$\hat{\sigma}_{ab \rightarrow X}(\alpha_S, \mu_R, \mu_F) = (\alpha_S)^n \left[\hat{\sigma}^{(0)} + (\alpha_S/2\pi) \hat{\sigma}^{(1)}(\mu_R, \mu_F) + (\alpha_S/2\pi)^2 \hat{\sigma}^{(2)}(\mu_R, \mu_F) + \dots \right] \quad (2.28)$$

871 where $\hat{\sigma}^{(0)}$ stands for the leading-order (LO) partonic cross section, while $\hat{\sigma}^{(1)}$ and $\hat{\sigma}^{(2)}$ are
 872 the next-to-leading-order (NLO) and next-to-next-to-leading-order (NNLO) cross section.

873 μ_R and μ_F depend on the order of truncation in Eq. 2.28. In principle, if cross section is
 874 calculated to all orders, it is invariant under changes in these parameters. The choices of μ_R
 875 and μ_F are arbitrary. To avoid unnaturally large logarithms reappearing in the perturbation
 876 series, it is sensible to choose μ_R and μ_F values of the order of the typical momentum
 877 scales of the hard scattering process and $\mu_R = \mu_F$ is also often assumed. Take Drell–Yan
 878 process as an example, the standard choice is $\mu_R = \mu_F = m_{ll}$, where m_{ll} is the invariant
 879 mass of di-lepton pair.

880 2.2.2 Higgs physics at the LHC

881 One important physics purpose of the LHC is searching for the Higgs boson, which
 882 was the last missing part in the SM. This section will discuss both the production and
 883 decay modes of the SM Higgs boson in proton-proton collision.

884 Higgs productions

885 The Higgs boson can be produced through several processes. There are 4 main produc-
 886 tion modes at the LHC: gluon-gluon Fusion (ggF), vector boson Fusion (VBF), associated
 887 production with vector-bosons (VH) (also called the Higgs Strahlung) and associated pro-
 888 duction with a pair of top/anti-top quarks ($t\bar{t}H$)^[12]. Figure 2.6 shows the corresponding
 889 Feynman diagrams of each process (at LO). For pp collisions, the cross section of pro-
 890 duction of Higgs boson is a function of centre-of-mass energy \sqrt{s} . Figure 2.7 depicts the
 891 cross section of SM Higgs, whose mass is 125 GeV, for several different production modes
 892 when centre-of-mass energy varying from 6 to 15 TeV. Figure 2.8 shows the prospect of
 893 production cross section as a function of Higgs mass from 10 to 2000 GeV for pp collision
 894 at the centre-of-mass energy of 13 TeV and 14 TeV^[13].

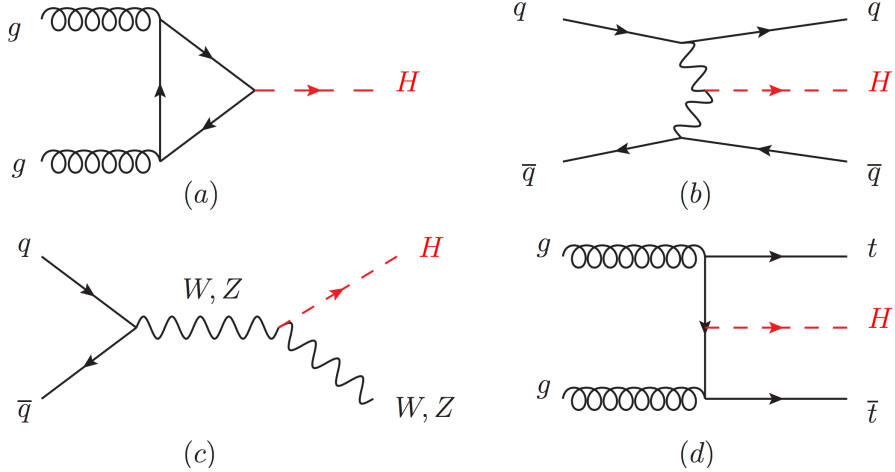


Fig. 2.6 Feynman diagrams of the Higgs production modes: (a) ggF; (b) VBF; (c) VH; (d) ttH.

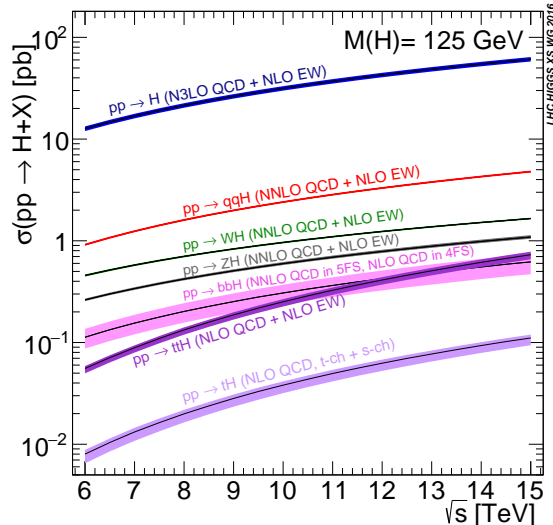


Fig. 2.7 The SM Higgs boson production cross sections for various production modes as a function of the centre-of-mass energy for pp collision.

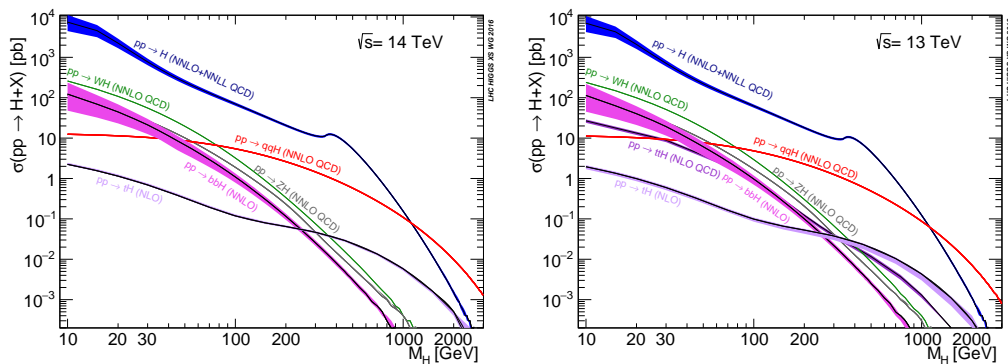


Fig. 2.8 Higgs boson production cross section for various production modes as a function of the Higgs mass for $\sqrt{s} = 13$ TeV (left) and 14 TeV (right) for pp collision.

Higgs decays

The Higgs boson can interact with gauge bosons and fermions through gauge coupling

897 and the Yukawa coupling as introduced in section 2.1.3. Figure 2.9 depicts the Feynman
diagrams of various possible Higgs decay channels. The branching ratio of Higgs boson

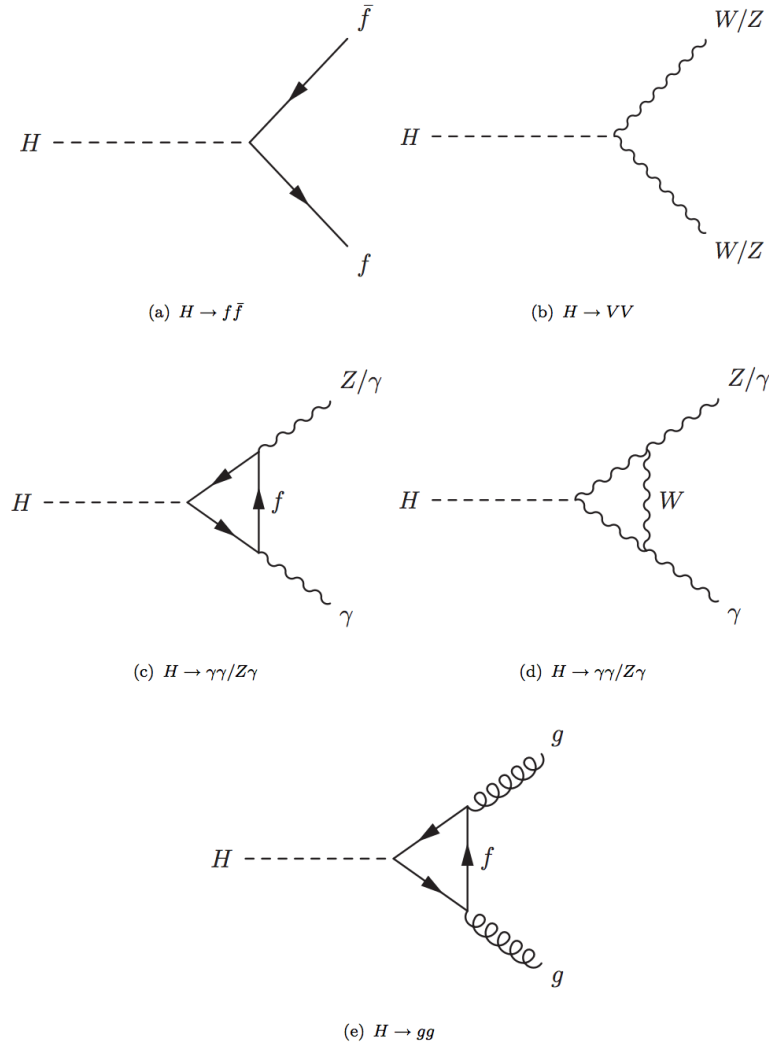


Fig. 2.9 SM Higgs decay channels.

898

899 decaying into different final states as a function of Higgs mass is shown in figure 2.10.

900 2.2.3 Diboson physics at the LHC

901 The study of diboson physics is another important test for SM of particle physics in
902 electroweak sector, while the Vector Boson Scattering (VBS) is a key process for probing
903 the mechanism of the electroweak symmetry breaking (EWSB). In the meantime, the non-
904 resonant diboson productions are crucial backgrounds for Higgs studies at the LHC, which
905 make the precise measurement of their cross section becomes very important.

906 **Diboson productions**

907 About 90% of diboson productions at hadron collider is from quark-antiquark anni-
908 hilation, while others are from gluon initiated process. Figure 2.11 shows the tree-level

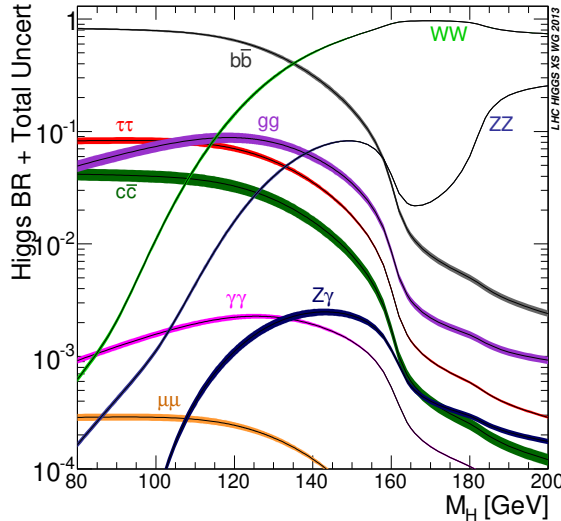


Fig. 2.10 Branching ratio of Higgs decays in various channels as a function of Higgs mass^[14].

Feynman diagrams of diboson production. Then figure 2.12 illuminates the total produc-

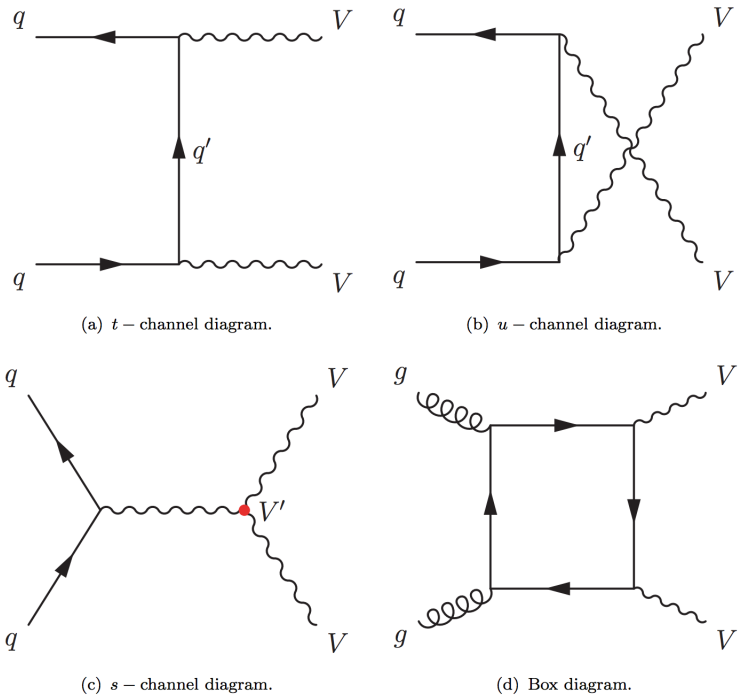


Fig. 2.11 The tree-level Feynman diagrams of diboson production at the LHC.

909

910 tion cross-section presented by ATLAS as a function of centre-of-mass energy \sqrt{s} from
 911 7 to 13 TeV for several diboson processes compared to some other major processes in
 912 hadron collision. The cross section for diboson processes are calculated at next-to-next
 913 leading order (NNLO).

914

Vector boson scattering

915 The $SU(2)_L \times U(1)_Y$ structure in SM predicts self-interactions between electroweak
 916 gauge bosons. Those self-couplings can involve either three or four gauge bosons at a sin-

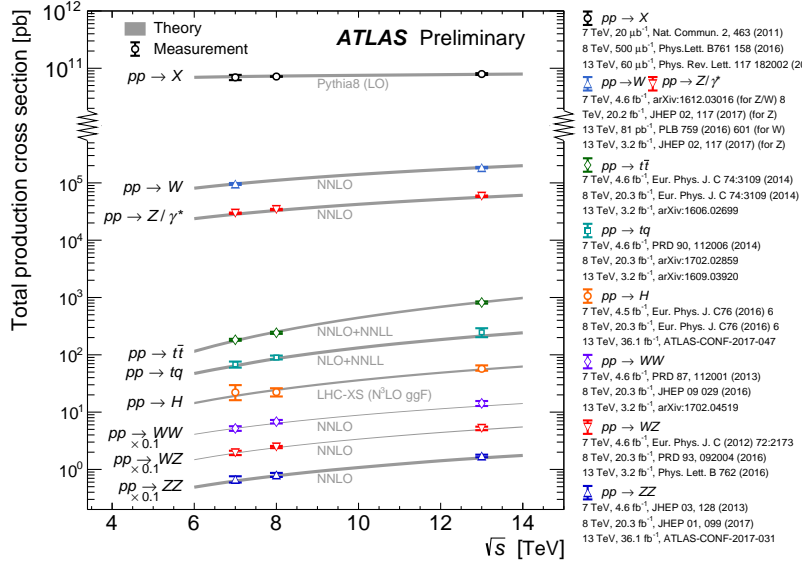


Fig. 2.12 Total production cross-section presented by ATLAS as a function of centre-of-mass energy \sqrt{s} from 7 to 13 TeV for some selected processes, the diboson measurements are scaled by a factor 0.1 to allow a presentation without overlaps.

gle vertex, known as triple gauge coupling (*TGC*) or quartic gauge couplings (*QGC*), respectively. Vector boson scattering (*VBS*) is carried out by four electroweak vector bosons, namely Z , W^\pm and photon (γ) as the Feynman diagrams shown in figure 2.13. And the vertexes include either those self-interactions or the interactions with the Higgs boson are described in figure 2.14.

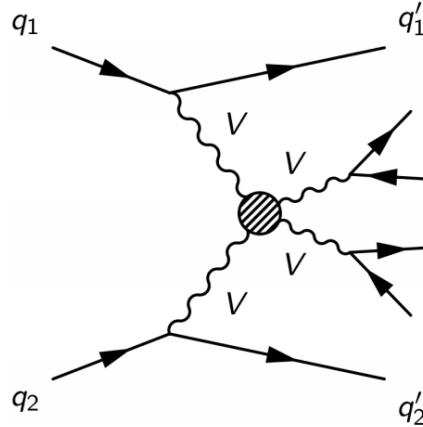


Fig. 2.13 Feynman diagrams of the vector boson scattering.

921

922 The amplitudes of leading-order (LO) VBS can be expressed as^[15]:

$$iM_{TGC}^{s-channel} = -i \frac{g_1^2}{4m_W^4} [s(t-u) - 3m_W^2(t-u)] \quad (2.29)$$

$$iM_{TGC}^{t-channel} = -i \frac{g_1^2}{4m_W^4} \left[(s-u)t - 3m_W^2(s-u) + \frac{8m_W^2}{s} u^2 \right]$$

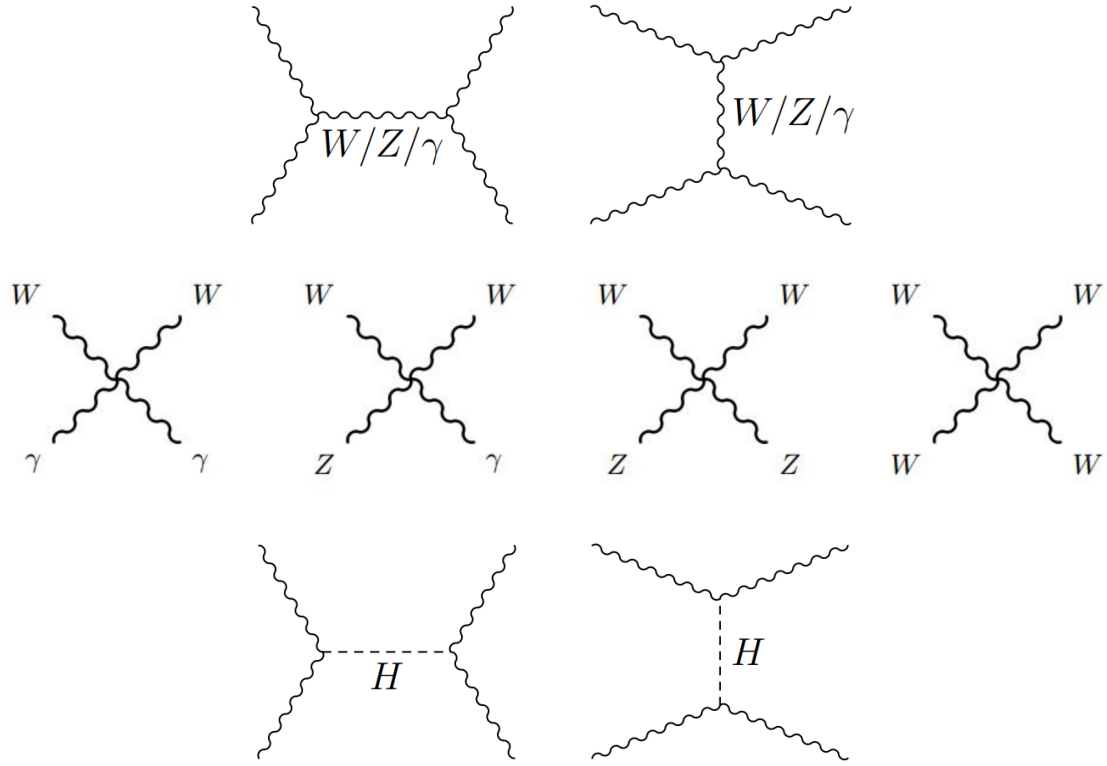


Fig. 2.14 Feynman diagrams of vertexes involving QGC, TGC and Higgs.

$$iM_{QGC} = i \frac{g_1^2}{4m_W^4} \left[s^2 + 4st + t^2 - 4m_W^2(s+t) - \frac{8m_W^2 ut}{s} \right] \quad (2.30)$$

923

$$\begin{aligned} iM_{Higgs} &= -i \frac{C_v g_1^2}{4m_W^2} \left[\frac{(s-2m_W^2)^2}{s-m_H^2} + \frac{(t-2m_W^2)^2}{t-m_H^2} \right] \\ &\simeq -i \frac{C_v g_1^2}{4m_W^2} (s+t) \end{aligned} \quad (2.31)$$

924 Combining s- and t-channel of TGC in Eq. 2.29 and the QGC term in Eq. 2.30:

$$iM_{TGC} + iM_{QGC} = i \frac{g_1^2}{4m_W^2} (s+t) + O((s/m_W^2)^0) \quad (2.32)$$

925 In Eq. 2.32, the amplitude grows as a function of centre-of-mass energy (\sqrt{s}), which
 926 violates the unitarity in the TeV region. Considering the Higgs term in Eq. 2.31 can
 927 perfectly cancel out this growing, and the remaining term $O((s/m_W^2)^0)$ only depends on
 928 the total amplitude in SM.

929 In conclusion, the Higgs boson acts as "moderator" to unitarize high-energy longitudi-
 930 dinal vector boson scattering as introducing the Higgs restores the unitarity of total am-
 931 plitude in high energy region.

932 **Chapter 3 The Large Hadron Collider and the ATLAS** 933 **Detector**

934 3.1 The Large Hadron Collider

935 Located near the French-Swiss border at the European Organization for Nuclear Re-
936 search (CERN), the Large Hadron Collider (LHC) is the world's largest and most pow-
937 erful particle collider. It's the proton-proton collider with the centre-of-mass energy up
938 to 14 TeV. The beams inside the LHC are made to collide at four locations around its
939 27-kilometer accelerator ring, corresponding to the positions of four particle detectors -
940 ATLAS, CMS, ALICE and LHCb. With its unprecedented energy, the LHC is designed
941 to observe physics that involve highly massive particles, which have never been observed
942 in previous accelerators with lower energies.

943 3.1.1 Operation history and machine layout

944 **Operation history**

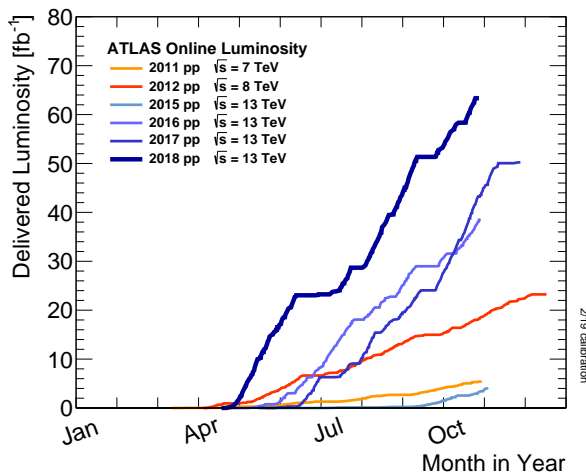
945 The LHC^[16-19] is a two-ring-superconducting-hadron accelerator and collider lies in
946 a tunnel 27 kilometres in circumference and as deep as 175 metres underground. It's
947 designed to provide proton-proton (pp) collisions at the centre-of-mass energy (\sqrt{s}) up
948 to 14 TeV with a unprecedented luminosity of $10^{34} \text{ cm}^{-2} \text{ s}^{-1}$. In the meantime, it can also
949 collide heavy (Pb) ions with an energy of 2.8 TeV per nucleon and a peak luminosity of
950 $10^{27} \text{ cm}^{-2} \text{ s}^{-1}$. Table 3.1 shows the main design parameters of the LHC for proton-proton
951 collisions.

952 The LHC was built from 1998 to 2008. It started its first beam in September 2008, but
953 then was interrupted by a quench incident only after a few days running. Then it resumed
954 the operation in November 2009 with a low energy beams. From March 2010, physics runs
955 took place at the centre-of-mass energy of 7 TeV. Later on, this energy was increased in
956 2012 to $\sqrt{s} = 8 \text{ TeV}$, with an integrated luminosity of 20.3 fb^{-1} , and this period is called
957 “run-1”. After run-1, the LHC was shut down for two years for hardware maintenance and
958 upgrade, starting from February 2013.

959 The second operation period with higher centre-of-mass energy at 13 TeV started
960 from 2015 called “run-2”. And it continued to the end of 2018 with total integrated lumi-
961 nosity reaching about 147 fb^{-1} for ATLAS experiment. Figure 3.1 shows the cumulative
962 luminosity as a function of time in month delivered to ATLAS experiment during stable
963 beams in years from 2011 to 2018.

Table 3.1 Summary of design parameters of the LHC for pp collisions.

Circumference	26.7 km
Beam energy at collision	7 TeV
Beam energy at injection	0.45 TeV
Dipole field at 7 TeV	8.33 T
Luminosity	$10^{34} \text{ cm}^{-2} \text{ s}^{-1}$
Beam current	0.56 A
Protons per bunch	1.1×10^{11}
Number of bunches	2808
Nominal bunch spacing	24.95 ns
Normalized emittance	3.75 μm
Total crossing angle	300 μrad
Energy loss per turn	6.7 keV
Critical synchrotron energy	44.1 eV
Radiated power per beam	3.8 kW
Stored energy per beam	350 MJ
Stored energy in magnets	11 GJ
Operating temperature	1.9 K

**Fig. 3.1 Cumulative luminosity as a function of time in years from 2011 to 2018 for ATLAS detector.**

964

Machine layout

965

The layout of CERN accelerator complex is shown in figure 3.2. The protons are accelerated by a series of machines before being injected into the main ring. At beginning, the 50 MeV protons are produced in the linear particle accelerator LINAC2, and further accelerated to 1.4 GeV in Proton Synchrotron Booster (PSB). The protons are then injected

966

967

968

969 into the Proton Synchrotron (PS) to gain the energy of 26 GeV and further accelerated to
 970 450 GeV in Super Proton Synchrotron (SPS). At the end, they are injected into the main
 971 ring, and can reach a maximum energy of 7 TeV.

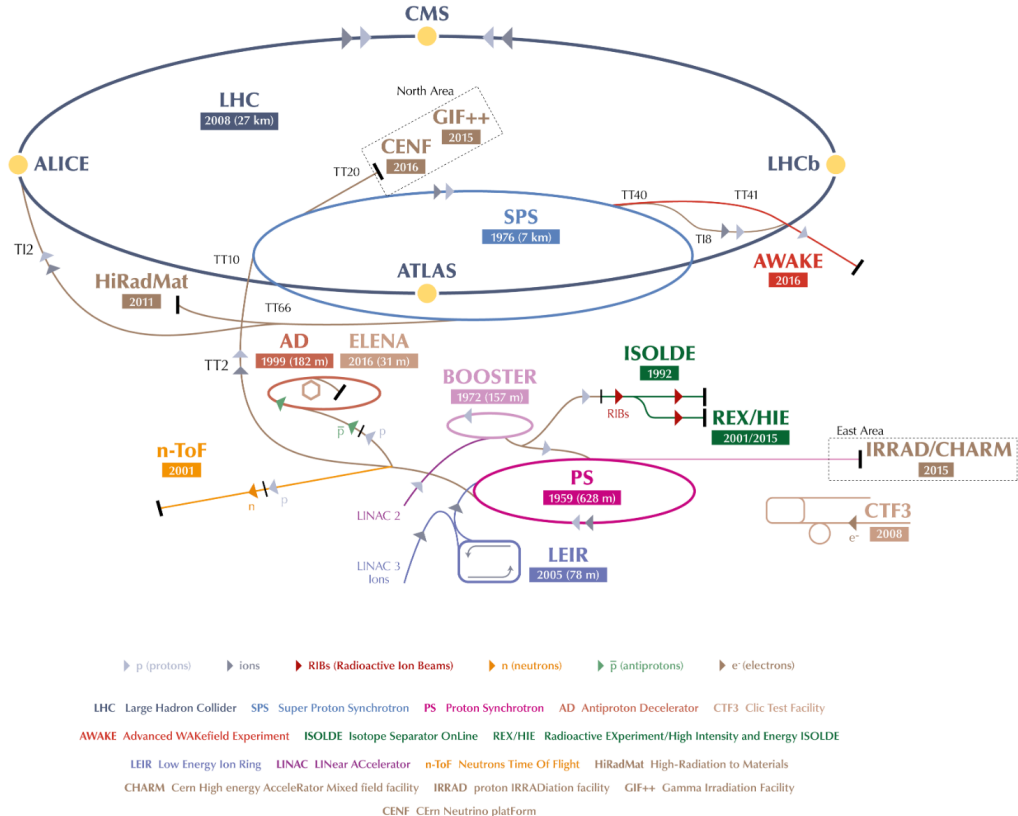


Fig. 3.2 CERN accelerator complex^[20].

922 The collisions can occur in 4 points, with corresponding 4 major detector experiments
 923 that are briefly described as follows:

- 924 • **ATLAS:** A Toroidal LHC ApparatuS, one of the two general-purpose particle de-
 925 tector experiments and detector with largest volume at the LHC. It is designed to
 926 search for the Higgs boson, test the stardand model of particle physics and search
 927 for possible beyond SM physics.
- 928 • **CMS:** Compact Muon Solenoid, another large general-purpose particle physics de-
 929 tector, with the same physics goal (also cross check) as ATLAS.
- 930 • **ALICE:** A Large Ion Collider Experiment, it is optimized to study heavy-ion (Pb-
 931 Pb nuclei) collisions at a centre-of-mass energy of 2.76 TeV per nucleon pair.
- 932 • **LHCb:** Large Hadron Collider beauty, it is a specialized b-physics experiment,
 933 designed primarily to measure the parameters of CP violation in the interactions of
 934 b-hadrons.

3.1.2 Luminosity and pile-up

Luminosity

In beam-beam collisions, the event rate for a process is given by^[19]:

$$N = \mathcal{L}\sigma \quad (3.1)$$

where σ is the cross section of the process, and \mathcal{L} is the luminosity. For the studies of rare events, \mathcal{L} must be as high as possible. The luminosity only depends on the beam parameters, and can be written as:

$$\mathcal{L} = \frac{N_b^2 n f_r \gamma}{4\pi \epsilon_n \beta^*} \quad (3.2)$$

where N_b denotes the number of particles per bunch, n is the number of bunches per beam, f_r is the revolution frequency, γ represents relativistic γ factor, ϵ_n is the normalized transverse emittance and β^* denotes the β function at the collision point. To reduce the beam-beam interaction effects, the bunches must have a crossing angle, which produces a geometrical luminosity reduction factor F :

$$F = 1/\sqrt{1 + \left(\frac{\theta_c \sigma_Z}{2\sigma^*}\right)} \quad (3.3)$$

where θ_c denotes the crossing angle at the interaction point, σ_Z is the root mean square (RMS) bunch length and σ^* is the transverse RMS beam size at crossing point.

The luminosity expressed in Eq. 3.2 is normally the instantaneous luminosity. In fact the running conditions usually vary with time, so the luminosity can change as well. To take into account the time dependence, integrated luminosity is invited, by integraling the instantaneous luminosity over time:

$$L = \int \mathcal{L}(t) dt \quad (3.4)$$

The unit of integrated luminosity we commonly use is b^{-1} that satisfying $1b^{-1} = 10^{24} cm^{-2}$. Figure 3.3 shows integrated luminosity as a function of time delivered to ATLAS (green), recorded by ATLAS (yellow), and certified to be good quality data (blue) during run-2 pp collisions. For most physics analysis, the data with good quality (require to satisfy *Good Run List*) is used.

Pile-up

In collisions, multiple interactions can happen in one single bunch crossing, which is called “pile-up”. The variable $\langle \mu \rangle$, representing the average number of interactions per

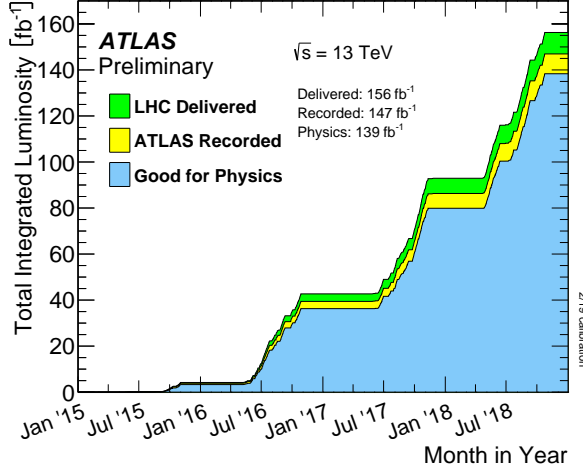


Fig. 3.3 Integrated luminosity in ATLAS.

bunch crossing, is defined to describe pile-up effect:

$$\langle \mu \rangle = \frac{L_{tot}\sigma}{f_r n_{bunch}} \quad (3.5)$$

where L_{tot} is the instantaneous luminosity, σ is the inelastic cross section, f_r is the LHC revolution frequency and n_{bunch} is the number of colliding bunches. Normally, with increasing luminosity, the pile-up becomes more significant. Figure 3.4 shows the luminosity-weighted distribution of the mean number of interactions per crossing for pp collision data from 2015 to 2018 (full run-2), the challenge of pile-up increased in each year.

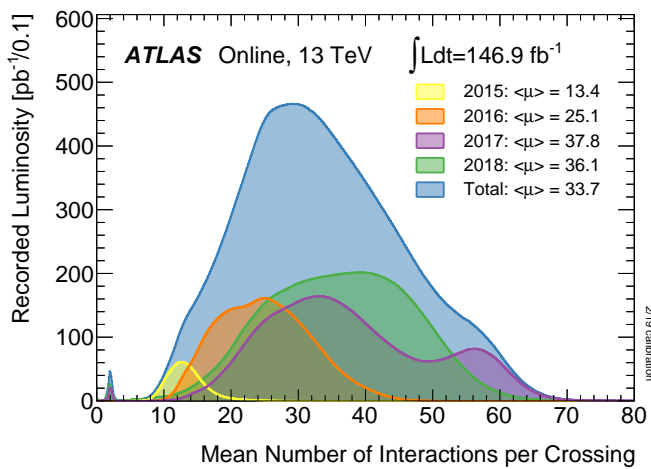


Fig. 3.4 Number of Interactions per Crossing from 2015-2018 in ATLAS.

1016

3.2 ATLAS detector

3.2.1 Detector overview

ATLAS (A Toroidal LHC ApparatuS) is the largest volume detector ever constructed for a particle collider. It is a cylinder with 46 meters long, 25 meters in diameter, and sits in a cavern 100 meters below ground. The detector contains about 3000 km of cables and it weights 7000 tonnes.

This paragraph briefly summarizes the coordinate system and nomenclature used to describe the ATLAS detector^[21]. As depicted in figure 3.5, we define the nominal interaction point as the origin of the coordinate system, the beam direction as the z -axis and the x - y plane is transverse to the beam direction. The positive x -axis is defined to be the direction pointing to the center of the LHC ring, while the positive y -axis is pointing upwards. There are two sides of detector A and C, in which A (C) -side is in the positive

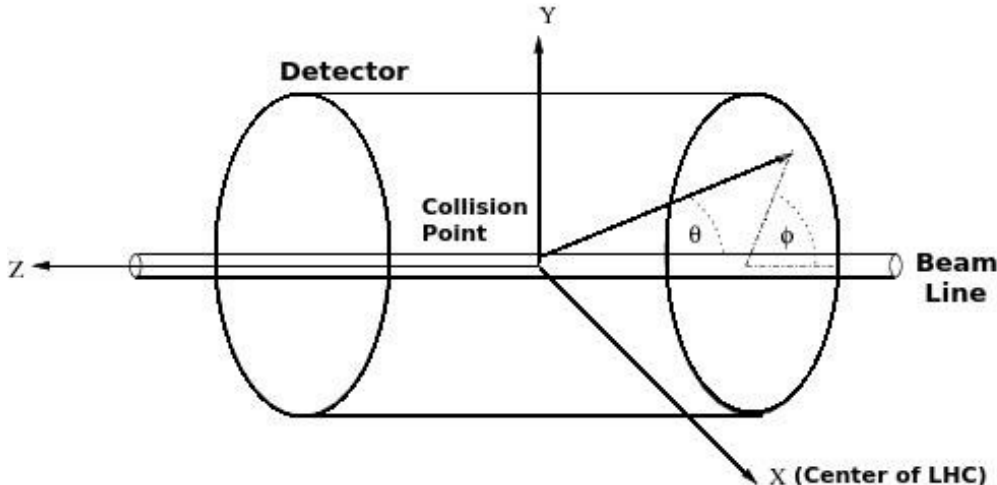


Fig. 3.5 Coordinate system used by the ATLAS experiment at the LHC^[22].

(negative) z direction. The azimuthal angle ϕ is measured as usual around the beam axis, while the polar angle θ is the angle from the beam axis. In physics analysis, we usually use the pseudorapidity instead of θ angle, which is designed as $\eta = -\ln \left[\tan \left(\frac{\theta}{2} \right) \right]$.

For massive objects (eg. jets), the rapidity $y = \frac{1}{2} \ln \left[\frac{E+p_z}{E-p_z} \right]$ is used. In addition, the transverse momentum p_T , transverse energy E_T and the missing transverse energy E_T^{miss} are defined in x - y plane. The ΔR , a commonly used distance measurement, is defined in the pseudorapidity-azimuthal angle space as $\Delta R = \sqrt{\Delta\eta^2 + \Delta\phi^2}$.

The overall ATLAS layout is shown in figure 3.6, which is forward-backward symmetric with respect to the interaction point. The magnet configuration comprises a thin superconducting solenoid surrounding the inner-detector cavity, and three large superconducting toroids (one barrel and two end-caps) arranged with an eight-fold azimuthal

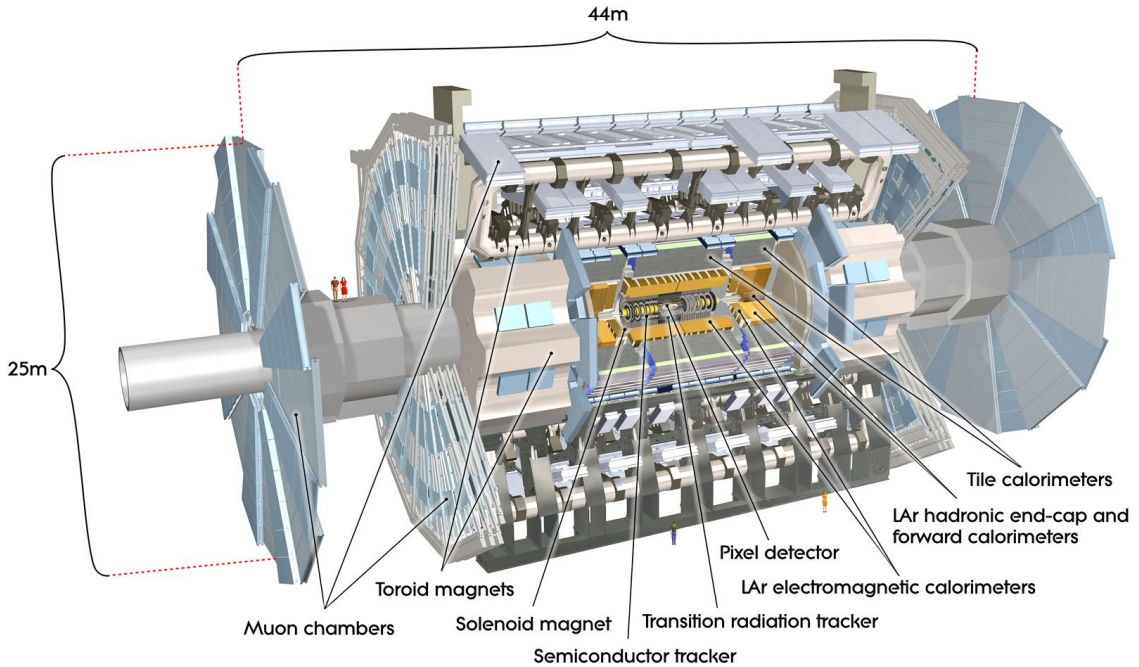


Fig. 3.6 Cut-away view of the ATLAS detector^[23].

1040 symmetry around the calorimeters.

1041 **The inner detector**, which is the innermost part of ATLAS, is immersed in a 2 T
 1042 solenoidal magnetic field. It's used for pattern recognition, momentum and vertex mea-
 1043 surements and electron identification, with the combination of tracking system.

1044 **The calorimeter** is outside the solenoid, for electromagnetic and hadronic en-
 1045 ergy measurements. The high granularity liquid-argon (LAr) electromagnetic sampling
 1046 calorimeters is used to measure energy and position with range up to $|\eta| < 3.2$ for electrons
 1047 and photons. For hadron, a scintillator-tile calorimeter is used in the range of $|\eta| < 1.7$,
 1048 and the liquid-argon hadronic endcap calorimeters (HEC) is used in end-cap region. And
 1049 then the LAr forward calorimeters provide both electromagnetic and hadronic energy mea-
 1050 surements with the coverage in forward region up to $|\eta| = 4.9$.

1051 **The muon spectrometer** is the outermost layer. It's a air-core toroid system, with
 1052 a long barrel and two inserted end-cap magnets that provides strong bending power in a
 1053 large volume within a light and open structure. A set of chambers measuring the tracks
 1054 of muons with high spatial precision and accurate time-resolution are used. Multiple-
 1055 scattering effects are minor, and excellent muon momentum resolution can be achieved.

3.2.2 Physics requirement

As mentioned previously, ATLAS is one of two general-purpose particle detector experiment at the LHC. It's designed to take advantage of the unprecedented energy at the LHC, as the discovery of Higgs boson is one of its benchmark. Lots of precise tests and measurements of SM physics are ongoing with ATLAS experiment. while, in the meantime, ATLAS is also designed to observe the phenomena that involve highly massive particles, which can also explore the possibility of extra dimensions proposed by several models in TeV region. To fulfil many diverse physics goals, a set of general requirements are needed:

- The high-speed and radiation-hard electronics are required due to the experimental conditions at the LHC.
- High detector granularity is needed to reduce the overlapping events and handle the particle fluxes.
- Large acceptance in pseudorapidity and azimuthal angle coverage is needed.
- For inner detector, good charged-particle momentum resolution and reconstruction efficiency are crucial. And the vertex detectors close to the interaction region are required to be able to observe secondary vertices for offline tagging of τ -lepton and b -jets.
- Good electromagnetic (EM) calorimetry for electron and photon, as well as full-coverage hadronic calorimetry for accurate jet and missing transverse energy measurements, are essentially required, since these measurements form the basis of many studies.
- Good muon spectrometer is also required for muon identification and momentum measurement over a wide range of momenta.
- Highly efficient but with sufficient background rejection triggers are also needed and extremely important for objects with low transverse-momentum.

More detailed descriptions of each sub-system will be given in the following subsec-

tions.

3.2.3 Magnet system

A strong magnetic field is required for precise measurement of charged particle momenta. The ATLAS detector uses two large superconducting magnet systems, a hybrid system of a central superconducting solenoid and three outer superconducting toroids, to bend charged particles^[24]. The total magnet system is 22 m in diameter and 26 m in length as shown in figure 3.7.

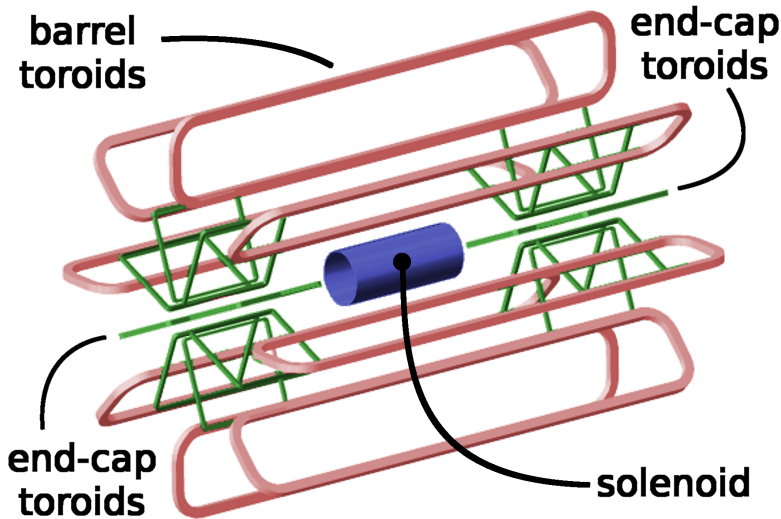


Fig. 3.7 Schematic diagram of the ATLAS magnet system.

1090 The central solenoid produces two Tesla (T) magnetic field surrounding the inner De-
 1091 tector. When obtaining such high field strength, at the same time, the solenoid needs to
 1092 be thin in order to reduce the material in front of the calorimeter.

1093 The outer toroid system comprises one barrel superconducting toroid and two end-
 1094 caps. The barrel one is composed of eight coils encased in individual racetrack-shaped,
 1095 stainless-steel vacuum vessels and produces the magnetic field in the cylindrical volume
 1096 surrounding the calorimeters. Each end-cap toroid consists of a single cold mass built up
 1097 from eight flat, square coil units and eight keystone wedges and provides a magnetic field
 1098 of approximately 1 T for the muon detectors in the end-cap regions.

1099 3.2.4 Inner detector

1100 The inner detector, as shown in figure 3.8, is the detector closest to beam pipe. It's
 1101 used to measure the position of charged particle tracks in high precision together with
 1102 good momentum resolution, among which the measurement of primary and secondary
 1103 vertices and electron identification are especially important. Due to the extremely high
 1104 luminosity produced by the LHC, the precise measurements of vertex and momentum
 1105 becomes tough and fine-granularity detectors are crucial. The inner detector consists of
 1106 three subdetectors described as below:

1107 **Pixel detector**

1108 The pixel detector^[26] is the innermost part of ATLAS tracking system. With finest
 1109 granularity of materials, it has the best spatial resolution and 3-dimensional space-point
 1110 measurement in inner detector. ATLAS Pixel Detector for the LHC run-2 is composed of
 1111 4 layers of barrel pixel detector and two end-caps with three pixel disks each, as shown in

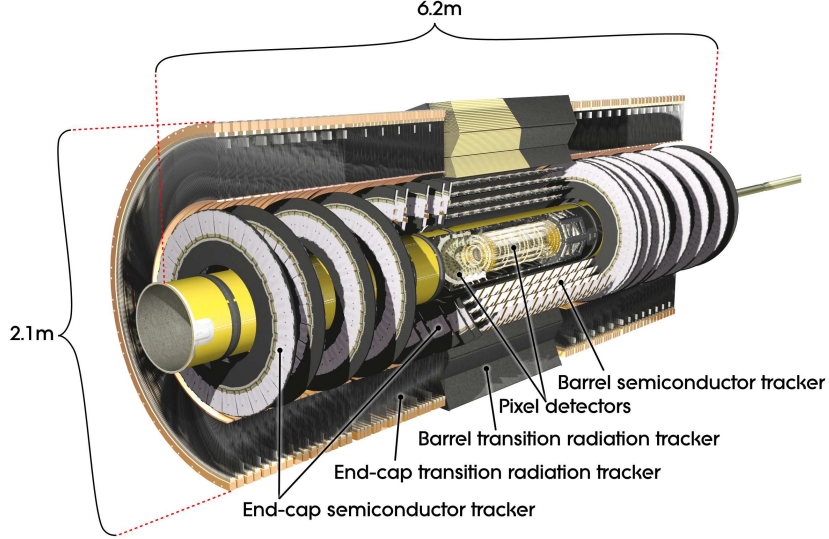


Fig. 3.8 Schematic diagram of the ATLAS inner detector^[25].

figure 3.9. There are three outer layers that originally installed for run-1 and one additional layer called Insertable B-Layer (IBL) that newly constructed in run-2^[27]. Now the 4-layer pixel detector has very good reconstruction of primary and secondary vertices, which is even crucial for long-lived particles like τ -lepton and b-quark.

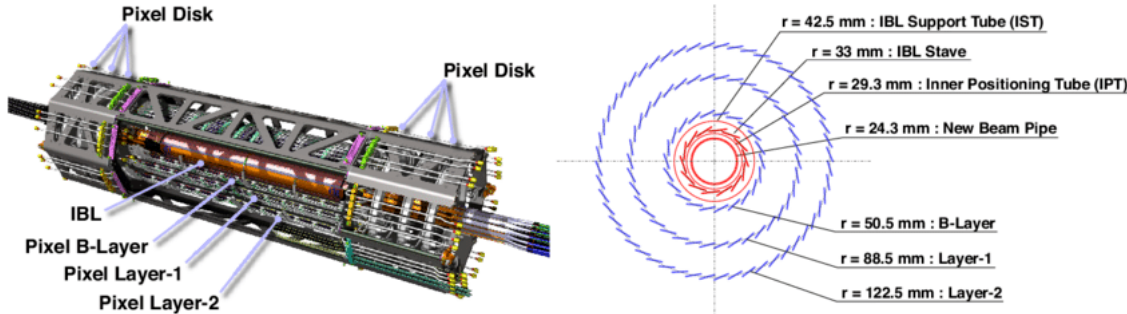


Fig. 3.9 Schematic diagram of the ATLAS 4-Layer Pixel Detector.

1115

1116

Semiconductor Tracker

1117

1118

1119

1120

1121

1122

1123

1124

1125

1126

The Semiconductor Tracker (SCT)^[28] installed outside the pixel detector is the middle component of the inner detector. It has similar function as pixel detector but with long and narrow strips instead of small pixels, which makes a much larger coverage than pixel detector. The SCT consists of 4088 modules, and contains four concentric layers in barrel (2112 modules) and nine disks in each of the two end-caps (1976 modules) as shown in figure 3.10. And it measures particles over a large area with 6.3 million readout channels and a total area of 61 square meters. The SCT is the most critical part of the inner detector for 2D track hit reconstruction. In barrel, the hit precision is $17 \mu\text{m}$ in the $r\phi$ coordinate and $580 \mu\text{m}$ in z coordinate. In end-caps, the precision is $17 \mu\text{m}$ in the $z\phi$ coordinate and $580 \mu\text{m}$ in r coordinate.

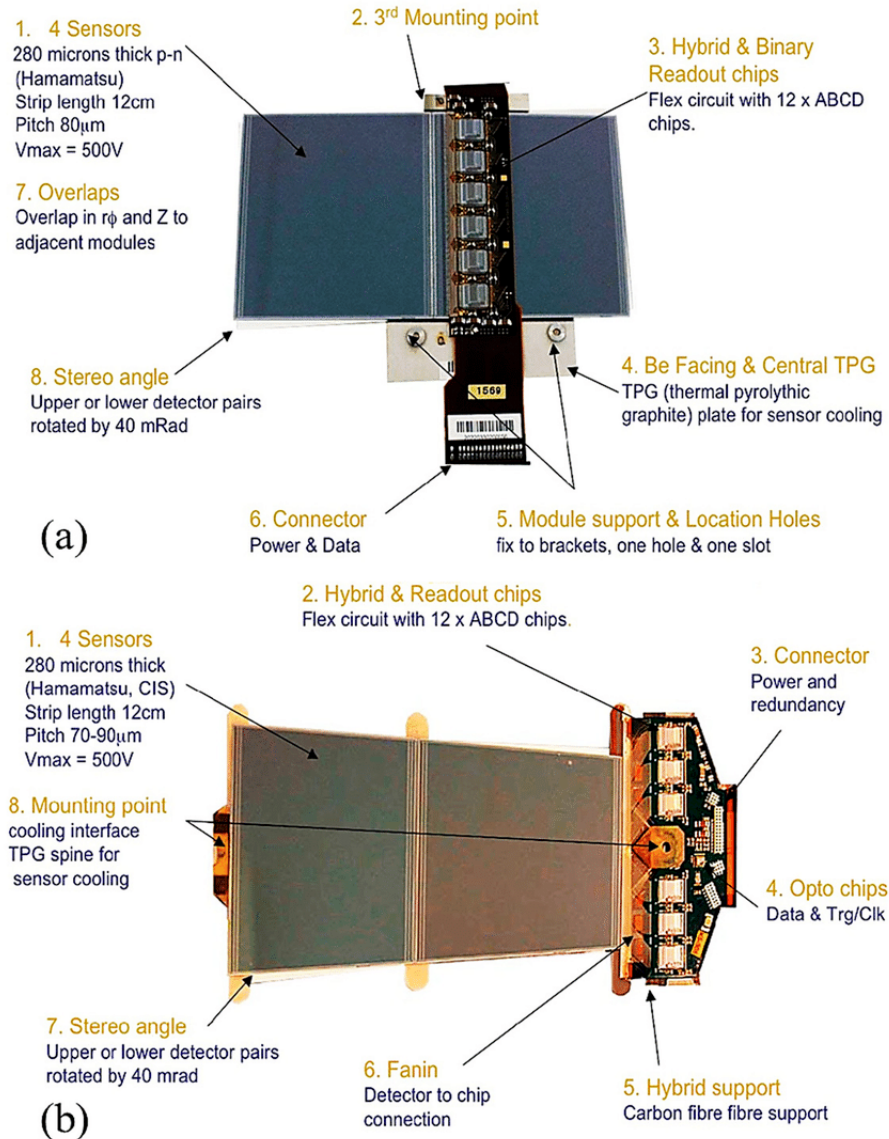


Fig. 3.10 SCT (a) barrel module and (b) end-cap^[29].

Transition radiation tracker

The transition radiation tracker (TRT)^[30] is the outermost part of inner detector, which has a very different design comparing to the two previously described sub-detectors. It can be separated into three parts: one barrel and two end-cap regions with the $|\eta|$ coverage up to 2.0. There are 73 barrel layers and 224 end-cap layers (112 in each) with 372000 straws in total, and about 351000 readout channels for TRT. The TRT provides better z resolution but much worse $r\phi$ resolution (about $130 \mu\text{m}$) comparing to the pixel detector and SCT per straw. But the straw hits still make significant contributions to momentum measurement, since its lower precision per point (compared to silicon) can be compensated by the large number of measurements and long track length.

3.2.5 Calorimeters

The calorimeters are designed to measure the energy from particles by absorbing them. They are located outside the solenoidal magnet that surrounds the inner detector. The ATLAS calorimeters are comprised of a number of sampling calorimeters with full ϕ -symmetry and the pseudorapidity range of $|\eta| < 4.9$. Figure 3.11 shows the layout of the ATLAS calorimeter system. There are two basic calorimeter systems: an inner electromagnetic (EM) calorimeter and an outer hadronic calorimeter. The EM calorimeter is designed for precise measurements of electrons and photons with fine granularity; while the hadronic one has relative coarser granularity but satisfies the physics requirements for jets reconstructions and E_T^{miss} measurements. Two different sampling techniques are used, the EM calorimeter is purely based on liquid-argon (LAr) technology, while the hadronic one use both LAr and scintillating tiles calorimeters. More details are described as below:

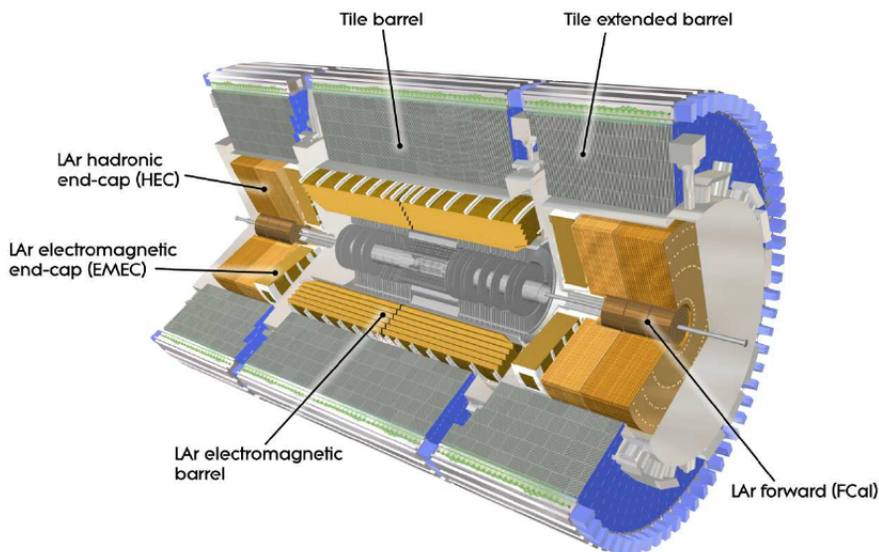


Fig. 3.11 Cut-away view of the ATLAS calorimeters. The LAr calorimeters are seen inside the scintillator-based tile hadronic calorimeters^[31].

1149

Liquid Argon calorimeter

The LAr calorimeter uses liquid-argon as active medium. The LAr sampling calorimeter technique with “accordion-shaped” electrodes is used for all electromagnetic calorimetry covering the pseudorapidity range of $|\eta| < 3.2$; and for hadronic calorimetry with range from $|\eta| = 1.4$ to the acceptance limit $|\eta| = 4.9$ ^[32]. Figure 3.12 depicts a segment of the barrel calorimeter, which had “accordion-shaped” electrodes and absorber. For barrel EM calorimeter, the absorbing material is lead-liquid argon, while the hadronic end-cap calorimeter uses copper plates. In addition, the forward calorimeter is split into

1158 three parts, an EM sector in which copper is used as absorbing material and two hadronic sectors using tungsten outside the EM sector.

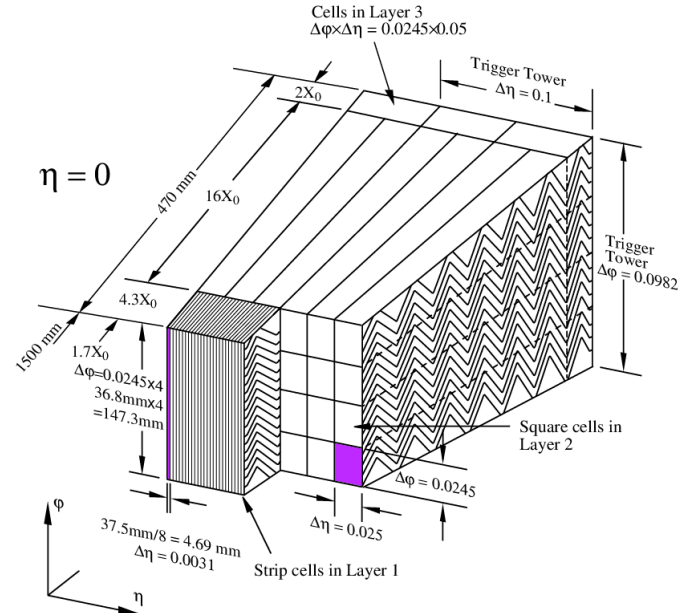


Fig. 3.12 Schematic diagram of a LAr EM calorimeter barrel module.

1159

1160 Tile calorimeter

1161 Tile calorimeter is a sampling calorimeter using scintillating plates as active medium
 1162 and steel as absorber. It consists of three sections: the central barrel with the pseudorapidity range of $|\eta| < 1.0$ and two extended barrels with $0.8 < |\eta| < 1.7$. Figure 3.13 shows
 1163 the design of one tile calorimeter module. It's used for energy reconstruction of jets and
 1164 E_T^{miss} measurement by combining the measurements with the end-cap and forward LAr
 1165 hadronic calorimeter.
 1166

1167

3.2.6 Muon spectrometer

1168 Muon spectrometer^[34] is the outermost part of the ATLAS detector with an extremely
 1169 large tracking system. It measures a large range of muon momentum, and the accuracy is
 1170 about 3% at 100 GeV and 10% at 1 TeV. The muon spectrometer comprises three main
 1171 parts: a magnetic field produced by three toroidal magnets; a set of chambers measur-
 1172 ing the tracks of muons with high spatial precision; and triggering chambers with accu-
 1173 rate time-resolution. Figure 3.14 shows the schematic of ATLAS muon spectrometer that
 1174 consists of four types of muon chambers (*MDT*, *CSC*, *RPC*, *TGC*) as well as the magnet
 1175 systems (barrel and end-cap toroid).

1176

More details of four chambers are given as below:

1177

- **Monitored Drift Tubes (MDT).** MDTs provide the precise momentum measure-

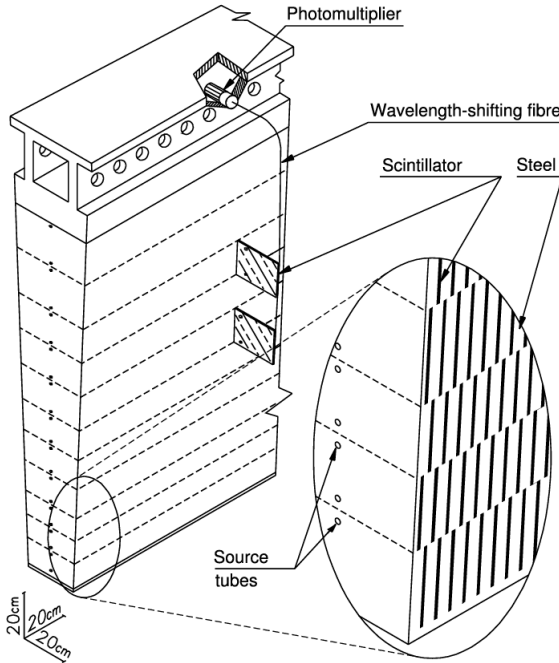


Fig. 3.13 Schematic diagram of tile calorimeter module^[33].

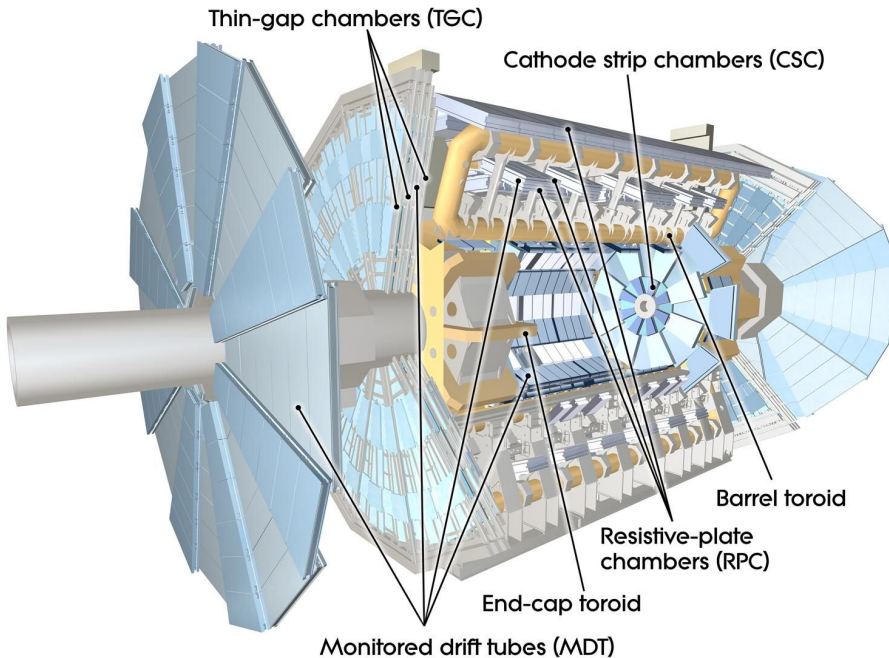


Fig. 3.14 Cut-away view of the ATLAS muon spectrometer^[35].

ment with the $|\eta|$ range up to 2.7, except in the innermost end-cap layer where the coverage is limited to $|\eta| < 2.0$. The chambers comprises three or four layers of drift tubes, with a diameter of 29.970 mm, operated with Ar/CO₂ gas (93/7) at 3 bar. The average resolution can reach 80 μm per tube and 30 μm per chamber.

- **Cathode strip chambers (CSC).** CSCs are used in the forward region of $2 < |\eta| < 2.7$ in the innermost tracking layers, due to their good time resolution and high

rate capability. The CSCs are multi-wire proportional chambers (MWPC) with the cathode planes segmented into strips in orthogonal directions, which allows both coordinates to be measured from the induced-charge distribution. The resolution of a chamber is about $40 \mu\text{m}$ for bending plane and 5 mm for the transverse plane.

- **Resistive plate chambers (RPC).** The RPCs serve as fast triggers in the barrel region of $|\eta| < 1.05$ due to the high rate capability and good spatial and time resolution. It is a gaseous parallel electrode-plate detector without any wires. There are three concentric cylindrical layers around the beam axis, as three trigger stations. Each station consists of two independent layers to measure the transverse coordinates of η and ϕ .
- **Thin gap chambers (TGC).** TGCs are used as trigger system for the end-cap region of $1.5 < |\eta| < 2.4$, and works based on the same principle as multi-wire proportional chambers. In addition, they can also provide the second azimuthal coordinate to complement the measurement of MDT in bending direction.

3.2.7 Trigger system

Trigger system in ATLAS is a very essential component, which is responsible for deciding whether to keep a given collision event for later study or not. In the LHC run-2, higher energy, luminosity and pile-up lead to a large increase of event rate by up to a factor of five, which causes to a even larger challenge and more strict requirement of trigger system.

The trigger system in run-2 consists of a hardware-based first level trigger (Level-1) and a software-based high level trigger (HLT)^[36]. As depicted in figure 3.15, in Level-1, the inputs from coarse granularity calorimeter and muon detector information together with some other subsystems are sent to the Central Trigger Processor to determine Regions-of-Interest (RoIs) in the detector. The event rate can be reduced by Level-1 triggers from 30 MHz to 100 kHz. After that, the RoI information from Level-1 is sent to HLT, in which more sophisticated selection algorithms are run for regional reconstruction. The HLT reduces the rate from Level-1 from 100 kHz to about 1 kHz on average. At the end, the events that accepted by HLT are transferred to local storage at experimental site for offline reconstruction. Details about Level-1 and HLT trigger systems are described as below:

1215 **Level-1 trigger**

Substantial upgrades have been delivered in ATLAS Level-1 trigger system for run-2 data taking. The upgrades took place in both hardware and detector readout, allow the

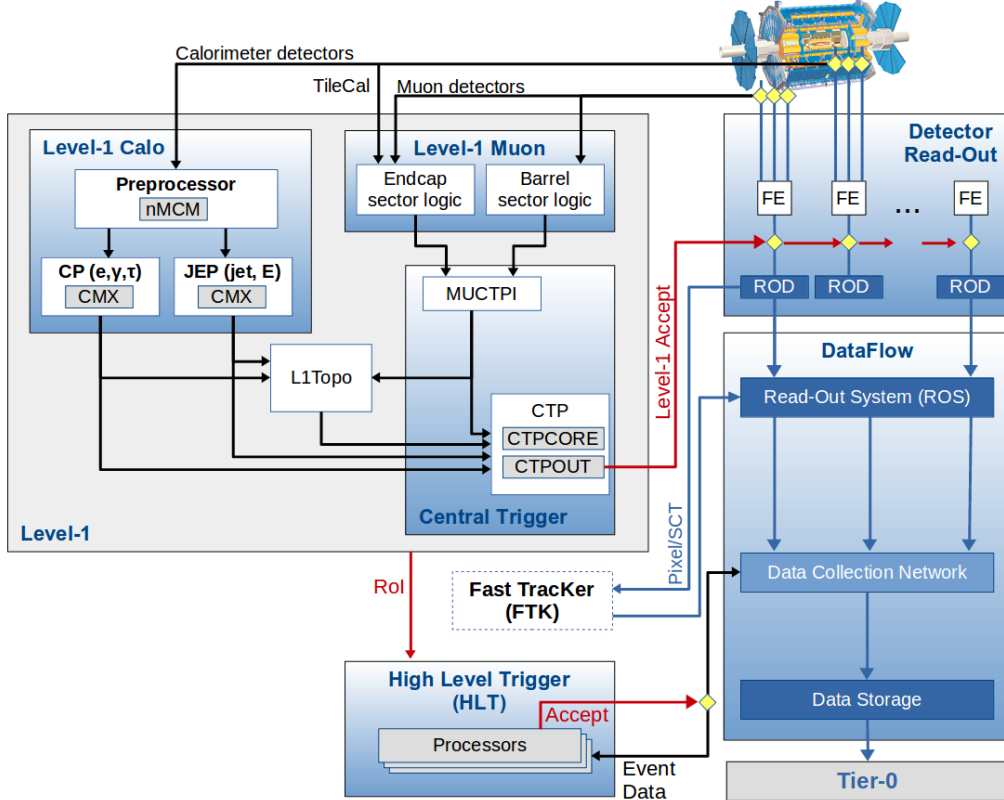


Fig. 3.15 Schematic diagram of the ATLAS trigger and data acquisition system in run-2.

trigger rate increasing from 70 kHz (in run-1) to 100 kHz (in run-2). There are two major parts of Level-1 triggers, including Level-1 calorimeter (L1calo) trigger and Level-1 muon (L1mu) trigger.

Level-1 Calorimeter trigger uses the reduced granularity information from the electromagnetic and hadronic calorimeters to search for electrons, photons, taus and jets and missing transverse energy (E_T^{miss}). It can identify an Region-of-Interest (RoI) as a 2×2 trigger tower cluster in the EM calorimeter as shown in figure 3.16, and 4×4 or 8×8 trigger tower for Jet RoIs. One important upgrade was that, the new FPGA-based (field-programmable gate array) Multi-Chip Modules are used to replace the ASICs (application-specific integrated circuits) included in the modules used in run-1, which allows the use of auto-correlation filters to suppress pile-up.

The Level-1 Muon trigger system includes one barrel section (RPC) and two end-cap section (TGC), which provides fast trigger signals from the muon detectors for the Level-1 trigger decision. By requiring a coincidence with hits from the innermost muon chambers, it can reduce the L1_MU15 rate by about 50% in the region of $1.3 < |\eta| < 1.9$ with only a loss of around 2% signal efficiency. In addition, the coverage was extended by around 4% due to installing new chambers in the feet region of the muon detector.

1235 High Level Trigger

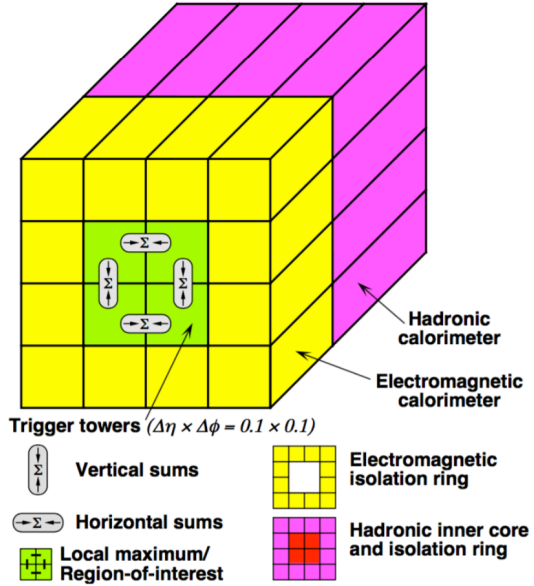


Fig. 3.16 An examples of L1 calorimeter trigger tower for electron and photon triggers^[37].

1236 In run-1, the Event Filter computer clusters and Level-2 trigger system were separated,
 1237 while now in run-2, they have been merged into a single HLT event processing. The new
 1238 arrangement helps to reduce the complexity and duplication of algorithm, which leads to
 1239 a more flexible high level trigger system. During the long-shutdown between the LHC
 1240 run-1 and run-2, lots of reoptimizations have been done for trigger reconstruction algo-
 1241 rithms as well as the offline analysis selections, which can improve the efficiency by more
 1242 than a factor of two in some cases like hadronic tau triggers. For some triggers, the HLT
 1243 processing performed within RoIs also allows to aggregate from RoIs to single objects.
 1244 This improvement reduces the CPU processing for events with overlapping RoIs, and the
 1245 average output rate has been increased from 400 Hz to 1 kHz.

1246 The HLT reconstruction algorithm can be divided into fast and precision online recon-
 1247 struction steps. As illuminated by figure 3.17, the initial fast reconstruction helps to reduce
 1248 the event rate, and to seed into precision reconstruction. Then the final online precision
 1249 reconstruction is improved and uses offline-like algorithms as much as possible. In partic-
 1250 ular, multivariate analysis techniques (based on machine learning) have been introduced
 1251 online in many aspects.

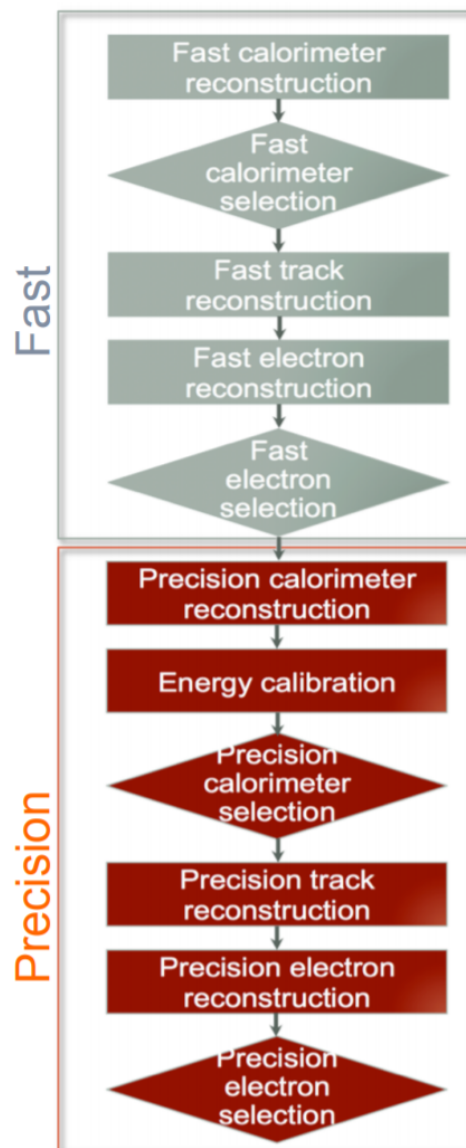


Fig. 3.17 The HLT trigger algorithm sequence^[37].

1252 Chapter 4 Simulation and Event Reconstruction for 1253 the ATLAS Experiment

1254 In current LHC pp collision, bunches of protons collide every 25 nanoseconds (ns),
1255 which gives a large challenge to event reconstruction and selections. To predict and model
1256 each process, Monte Carlo simulations of physics events are essential for high-energy
1257 physics experiments. This section will briefly discuss the event simulation and recon-
1258 struction programs based on the ATLAS software framework.

1259 4.1 Event simulation

1260 The ATLAS simulation program is integrated into the ATLAS software framework
1261 called *Athena*^[38], which uses Python as an object-oriented scripting and interpreter lan-
1262 guage to configure and load C++ algorithms and objects. Figure 4.1 shows the overview
1263 of ATLAS simulation data flow^[39]. In the diagrams, the square-cornered boxes represents
algorithms and applications to be run and round-cornered boxes denote data objects.

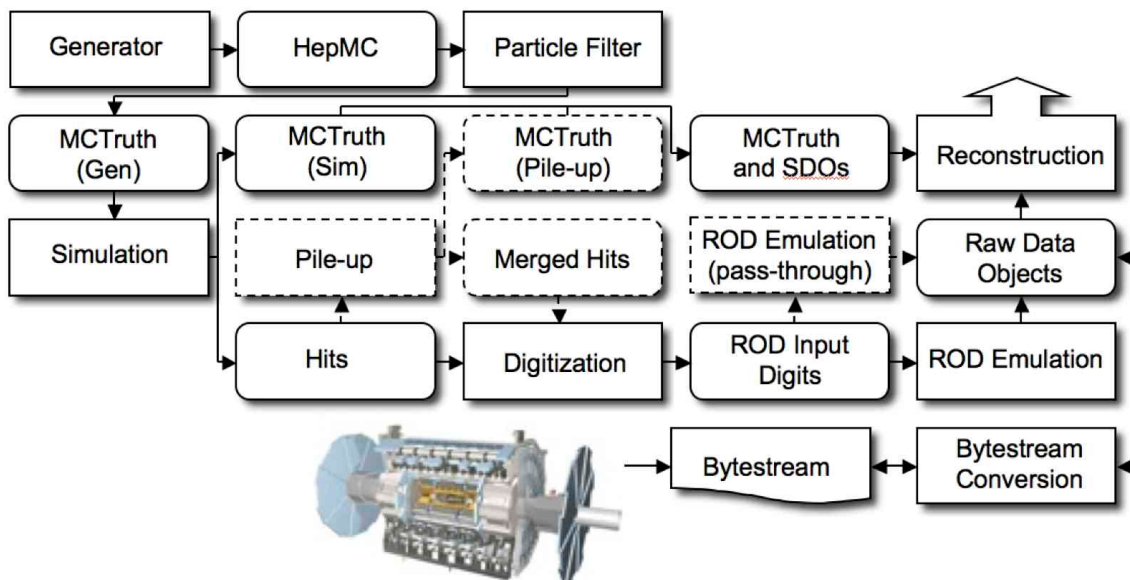


Fig. 4.1 The flow of the ATLAS simulation software.

1264
1265 First of all, events are produced by MC generators in standard HepMC format and
1266 then read into the simulation. During the simulation, particles are propagated through the
1267 full ATLAS detector whose configurations can be set by users via GEANT4 toolkit. The
1268 energies deposited in the sensitive regions of the detector are recorded as *hits* that contains
1269 the total energy deposition, position and time, and are written to a simulation hit file. In

1270 the meantime, the events in “truth” format are also recorded to contain the history of the
1271 interactions from the generator, including incoming and outgoing particles. Simulated
1272 Data Objects (SDOs) are created from truth, which are maps between hits in sensitive
1273 portions of the detector and truth information of particles in simulation. The files are then
1274 sent to digitization, with constructs “digits” inputs and be written into Raw Data Object
1275 (RDO) file used for reconstruction.

1276 In conclusion, there are three main parts of framework: *Generation*, *Simulation* and
1277 *Digitization*. More details are given as below:

1278 **Event generation**

1279 As shown in figure 4.2^[40], at hardon colliders, multiple scattering and rescattering
1280 effects arise, which needs to be simulated by Monte Carlo (MC) event generators to reflect
1281 the full complexity of those event structures. Several MC event generators can be used to
1282 generate events in HepMC format. The events can be filtered at generation time with some
1283 certain requirements (eg. decay channel or missing energy above a certain threshold). The
1284 generator is responsible for any prompt decays (e.g. W or Z bosons) and stores any “stable”
1285 particle expected to propagate through a part of the detector. During the generation steps,
1286 any interactions with detector are ignored and only immediate decays are considered.

1287 There are several MC generators that have been widely used with general purpose,
1288 including SHERPA^[41], HERWIG++^[42], POWHEGBox^[43], MC@NLO^[44] and PYTHIA8^[45].

1289 **Simulation**

1290 GEANT4 is used as standard simulation toolkit for the ATLAS experiment, which
1291 transports physics particles through the detector’s geometry. During the generation level,
1292 the entire connected chain of the HepMC event is stored as the Monte Carlo truth. Only the
1293 stable particles are read into GEANT4 for further simulation and selection, and transfor-
1294 mations can be applied to these events to select certain processes. During the simulation,
1295 many secondary tracks can be produced, therefore only information from the interactions
1296 of interest are stored, including the incoming particles, step sequence, vertex as well as
1297 outgoing particles. The output of GEANT4 is called *hit file*, which contains metadata de-
1298 scribing the configuration of the simulation during the run, all requested truth information
1299 and a collection of hits for each subdetector.

1300 Since the standard ATLAS detector simulation cost very large computing resources
1301 to accurately model the complex detector geometry and physics descriptions, some fast
1302 simulation programss are developed according to different user purpose. Some popular
1303 fast-sim toolkits include *Fast G4 Simulation*^[46], *ATLFAST-I*^[47] and *ATLFAST-II*^[48].

1304 **Digitization**

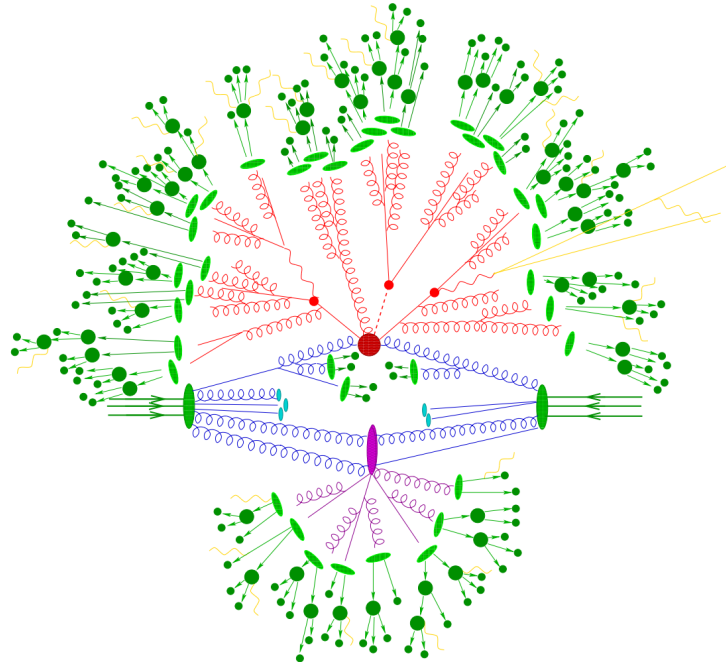


Fig. 4.2 Sketch of a hardon-hardon collision simulated by MC event generator. The red blob in center denotes the hard collision, surrounded by tree-like structures representing Bremsstrahlung which is simulated by Parton Showers. The purple blob stands for a secondary hard scattering event. The light green blobs indicate the parton-to-hardon transitions and the dark green blobs represents hardon decays. The yellow lines are soft photon radiations.

1305 The hit outputs from simulated events, including hard scattering signal, minimum
 1306 bias, beam halo, beam gas and cavern background events, are then sent into digitization
 1307 procedure, converted into detector response called “digits”. Before converted into detector
 1308 signal as “digits” formart, each type of event can be overlaid at a user-specified rate. Those
 1309 overlay, called “pile-up”, can be done during digitization to save the CPU time. At this
 1310 stage, the detector noise and the first level trigger that implemented with hardware on
 1311 the real detector are added into events. The digitization firstly constructs “digits” inputs
 1312 to the readout drivers (RODs) in the detector electronics. Then the ROD functionality
 1313 is emulated, and the output digits are written out as Raw Data Object (RDO) file. In
 1314 addition, the digitization algorithms can also produce Simulated Data Objects (SDOs),
 1315 which contain information about all the particles, noise and the amount of energy that
 1316 contributed to the signal. Then all information are sent into reconstruction level described
 1317 in next subsection.

4.2 Event reconstruction

The data flow of ATLAS data processing is sketched in figure 4.3^[49]. Data from detector is firstly filtered by online trigger system before sending to the *Tier-0* (*T0*) for initial processing by offline reconstruction software based on Athena. A small amount of data named “express stream” is processed in almost real time in *T0* for online data quality monitoring. In addition, some other dedicated data streams are sent out at trigger level for detector alignment and calibration. These calibration and alignment information are then used for bulk reconstruction in *T0*. At the end of the reconstruction chain, the data are delivered into *Tier-1* (*T1*) and *Tier-2* (*T2*) centers around the world for further analysis and production of simulated data. *T1* centers are also responsible for data reprocessing by re-running data reconstruction with improved calibration and alignment constants and with improved reconstruction algorithms.

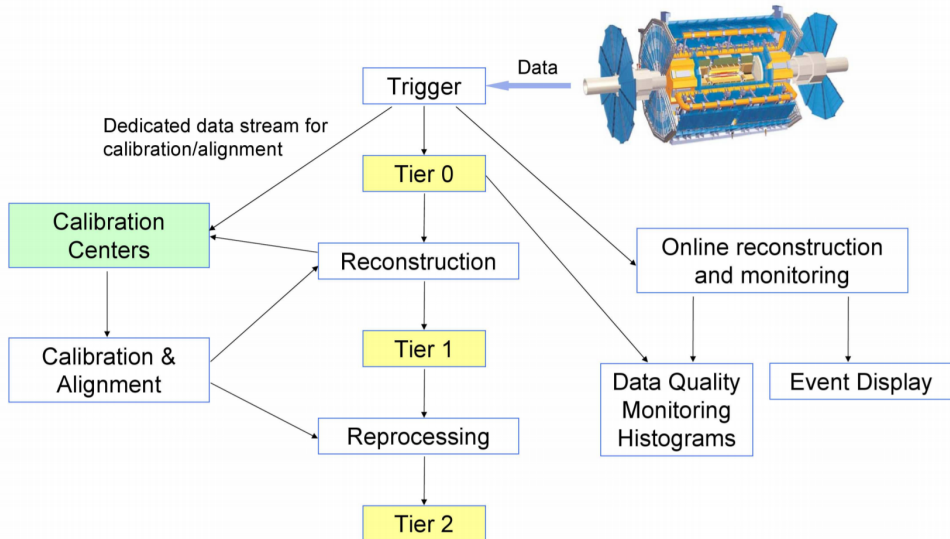


Fig. 4.3 The flowchart of the ATLAS data processing.

This section describes the reconstruction of some important physics objects in ATLAS experiment: tracks, vertices, electrons, muons, jets, and missing energies.

4.2.1 Track

The ATLAS detector is composed of two independent tracking systems: the Inner Detector (ID) close to the interaction point, and the Muon Spectrometer (MS) located in the outermost region. The reconstructed charged-particle trajectories in the ID and MS are referred to as ID tracks and MS tracks respectively. The challenge of ID reconstruction is that it needs to handle high track density that imposes a large number of combinatorial track candidates, while the MS reconstruction is however largely limited by the huge

amount of inert material, the large background and the highly inhomogeneous magnetic field^[50]. More details of these two types of track are given as below:

1341 **Inner detector track**

1342 Figure 4.4 sketches the ID system used for detecting charge-particle tracks. The ID
1343 track reconstructions contains two sequences: *inside-out* track reconstruction and *outside-in* one.

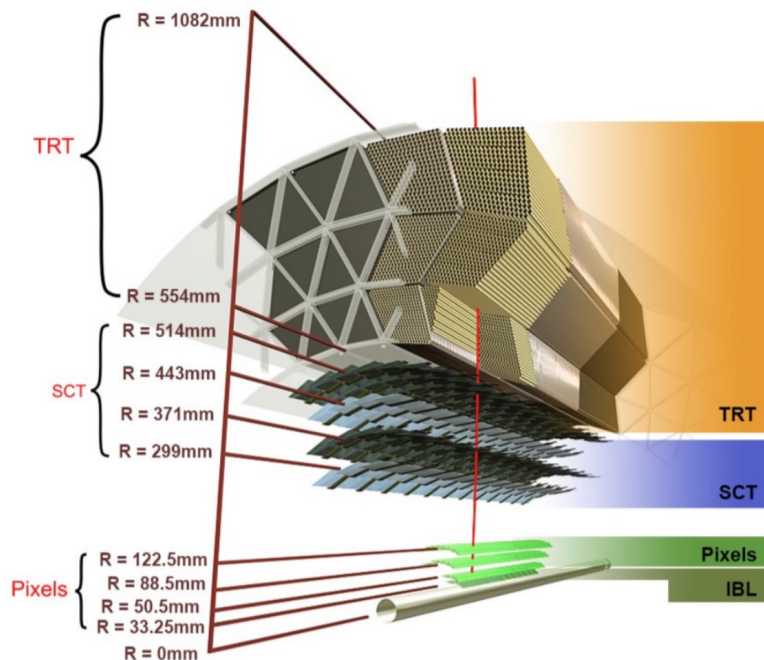


Fig. 4.4 Schematic view of the ATLAS inner detector showing all the corresponding components.

1344
 1345 For inside-out tracking, it exploits the high granularity of the pixel and SCT detectors
1346 to discover prompt tracks originating from the interaction point. In first step, the track
1347 seeds are formed by combining the information of space-points in the three pixel layers
1348 and the first SCT layer. Then, these seeds are extended throughout the SCT to build track
1349 candidates. After that, these candidates are fitted with some quality cuts applied to remove
1350 the outlier clusters, reject the fake tracks and resolve ambiguities in the cluster-to-track
1351 association. The selected tracks are then further extended to TRT, and refitted with the
1352 full information from pixel, SCT and TRT detectors.

1353 Another complementary approach, outside-in, searches for unused track segments
1354 start from TRT instead. These segments are then extended into the SCT and pixel de-
1355 tectors to improve the tracking efficiency for secondary tracks from conversions or decays
1356 of long-lived particles.

1357 **Muon spectrometer track**

1358 The MS track reconstruction^[51] starts from searching hit patterns inside each muon
 1359 chamber to form segments. In each MDT chamber and nearby trigger chamber, a Hough
 1360 transform^[52] is used to search the hits lie on a certain trajectory in the bending plane of the
 1361 detector. The MDT segments are reconstructed by performing a linear fit to the hits found
 1362 in each layer. The RPC or TGC hits can be built by measuring the coordinate orthogonal to
 1363 the bending plane. And the segments of CSC can be built using a separate combinatorial
 1364 search in the η and ϕ detector planes.

1365 Then muon track candidates are built by fitting hits from segments in different layers
 1366 together. This task makes use of the algorithm by performing a segment-seeded combi-
 1367 natorial search, which starts by using the segments generated in the middle layers of the
 1368 detector where more trigger hits are available as seeds. The search is then extended to use
 1369 the segments as seeds from the inner and outer layers. The segments are selected based
 1370 on criteria of hit multiplicity and fit quality, and are matched using their relative positions
 1371 and angles. To build a track, at least two matching segments are required, except in the
 1372 barrel-endcap transition region where a single high-quality segment with η and ϕ infor-
 1373 mation can be used to build a track. At beginning, the same segment can be used to build
 1374 more than one track candidates. Later on, an overlap removal algorithm is performed to
 1375 select the best assignment to a single track, or decide whether allows the certain segment
 1376 to be shared between two tracks.

1377 The hits associated with each track candidate are then fitted using a global χ^2 fit. The
 1378 algorithm accepts the track candidate if its fitting χ^2 passes the selection criteria. Hits
 1379 with large contribution to χ^2 are removed and the track fit is repeated. In addition, the
 1380 algorithm performs a hit recovery procedure looking for additional hits consistent with
 1381 the candidate trajectory, and the track candidate is refit if additional hits are found.

1382 4.2.2 Primary vertex

1383 The reconstruction of primary vertex (PV) uses the reconstructed tracks introduced in
 1384 previous section as inputs. The tracks must satisfy the following criteria^[53]:

- 1385 • $p_T > 400$ MeV
- 1386 • $|\eta| < 2.5$
- 1387 • Number of silicon hits $\geq \begin{cases} 9 & \text{if } |\eta| \leq 1.65 \\ 11 & \text{if } |\eta| > 1.65 \end{cases}$
- 1388 • IBL hits + B-layer hits ≥ 1
- 1389 • A maximum of 1 shared module (1 shared pixel hit or 2 shared SCT hits)
- 1390 • Pixel holes = 0

1391 • SCT holes ≤ 1

1392 A candidate vertex is formed by requiring two tracks passing these selection criteria.

1393 The reconstruction of PV can be divided into two steps^[54]: vertex finding and vertex
1394 fitting. The first step is the pattern recognition process, namely the association of recon-
1395 structed tracks to vertex candidates. The latter one works on the reconstruction of the
1396 actual vertex position and its covariance matrix. More details are described as below:

1397 First of all, a set of tracks passing the selection criteria mentioned above is selected.
1398 Then a seed position for the first vertex is chosen. This seed position is determined by beam
1399 spot in the transverse plane. The starting point for x- and y- coordinates are directly from
1400 the centre of the beam spot, while the one for z-coordinate is calculated as the mode of
1401 z-coordinates of tracks at their respective points with closest approach to the reconstructed
1402 centre of the beam spot.

1403 After determining the seed position, the iterative primary vertex finding procedure
1404 starts. An vertex fitting algorithm is adopted to find the optimal vertex position by per-
1405 forming an iterative χ^2 minimization, in which the seed position is used as the start point
1406 and the reconstructed tracks are used as input measurements. For this fitting procedure, the
1407 input tracks are assigned weights to reflect their compatibility with the vertex estimation,
1408 and the vertex position is re-calculated based on these weighted tracks. Then the iterative
1409 procedure is repeated by re-calculating the track weight according to the new vertex posi-
1410 tion. After the last iteration, the final weight of each track used in vertex fit is estimated.
1411 And those incompatible tracks ($> 7 \sigma$) are then rejected from this vertex candidate and
1412 moved back to the unused pool for next vertex finding. Then iteration procedure describes
1413 above are repeated again by using the remaining tracks, until no un-associated tracks are
1414 left or no additional vertex can be found in remaining tracks.

1415 At the end, the vertices with at least two associated tracks passing through are treated
1416 as possible PV candidates. And the output of this vertex reconstruction algorithm is the in-
1417 formation of three dimensional vertex positions and their covariance matrices. In physics
1418 analysis, it's most often to choose the one with highest sum of transverse momentum
1419 ($\sum p_T^2$) as PV.

1420 4.2.3 Electron

1421 Many interesting physical processes are with the involvement of one or more elec-
1422 trons (or positrons) at the LHC. But these electrons can be subjected to large amount of
1423 backgrounds such as hadrons, non-prompt electrons from photon conversions and non-
1424 isolated electrons from heavy flavor hadon decays. It is therefore essential to efficiently

1425 reconstruct and identify electrons as well as, in the meantime, to keep high background
1426 rejection.

1427 In ATLAS, in central region, the electrons leave tracks in inner detector (ID) and
1428 deposit the energies in the electromagnetic (EM) calorimeter. Firstly the signals from
1429 calorimeter are used for L1 trigger system, and then combined with the information from
1430 ID tracks to reconstruct electron candidates that will be used for the high level trigger
1431 (HLT) decision algorithms^[55]. The backgrounds mentioned above can then be further
1432 suppressed by using several identification criteria. In addition, electrons are required to
1433 be isolated from other activities to be further distinguished from background.

1434 More details of electron *reconstruction*, *identification* and *isolation* are described as
1435 below.

1436 **Electron reconstruction**

1437 Several steps are proceeded for electron reconstruction in the central region of ATLAS
1438 detector ($|\eta| < 2.47$):

1439 1. **Seed-cluster reconstruction:** A sliding window with size of 3×5 in unit of
1440 $\Delta\eta^{tower} \times \Delta\phi^{tower} = 0.025 \times 0.025$ in $\eta \times \phi$ space is utilized to search for elec-
1441 tron cluster seeds with total cluster transverse energy greater than 2.5 GeV. Then
1442 a clustering algorithm^[56] is applied to form the clusters around the seeds, which
1443 can take advantage of removing the duplications. The kinematics of clusters are
1444 then reconstructed by using an extended window depending on the cluster posi-
1445 tion. The efficiency of cluster search is from about 95% at $E_T = 7GeV$ to 99% for
1446 $E_T \geq 15GeV$.

1447 2. **Track reconstruction:** The track reconstruction can be divided into two steps: pat-
1448 tern recognition and track fit. The standard pattern recognition in ATLAS uses pion
1449 hypothesis for energy loss caused by interactions with detector material. If a track
1450 seed with $p_T > 1$ GeV cannot be successfully extended to a full track required at
1451 least seven hits using this pion hypothesis, but still falls inside one of the EM clus-
1452 ter region of interest, as a second attempt, the pattern recognition using electron
1453 hypothesis is then used to allow larger energy loss. Depending on the pattern used
1454 in previous stage, the track candidates are then fitted with either the pion hypothesis
1455 or the electron hypothesis by using ATLAS Global χ^2 Track Fitter^[57]. If a track
1456 candidate fails the fit by using pion hypothesis, it can be refit with the electron hy-
1457 pothesis again. In this method, a specific electron-oriented algorithm is integrated
1458 into the ATLAS standard track reconstruction, which improves the performance for
1459 electron and as well as maintain minimal interference with the main track recon-

1460 struc-

1461 **3. Electron specific track fit:** Once the tracks are obtained, they are loosely matched
1462 to EM cluster using the distance in η and ϕ between the position of track (after ex-
1463 trapolation) in calorimeter's middle layer and the cluster barycentre. The matching
1464 conditions take into account the energy loss of bremsstrahlung and the number of
1465 precise hits in silicon detector.

1466 **4. Electron candidate reconstruction:** The electron candidate is reconstructed by
1467 matching the track candidate to EM cluster seed to eventually completes the electron
1468 reconstruction procedure. If more than one track satisfy the matching condition,
1469 one track is chosen as primary track based on the information of the cluster-track
1470 distance R, the number of pixel hits and the presence of a hit in the first silicon
1471 layer^[58]. In addition, the electron candidates are removed from electron pool if it's
1472 without any associated precise hit tracks, and moved into photon candidates pool.
1473 Then we reformed the electron clusters by using 3×7 (5×5) longitudinal towers
1474 of cells in barrel (end-caps) in EM calorimeter. The measured energy is calibrated
1475 to original electron energy based on MC simulated samples by using multivariate
1476 techniques (MVA).

1477 In addition, in physics analysis, to reduce the background from photon conversions
1478 and secondary particles, the track associated with electron is required to be compatible
1479 with the primary vertex of the hard collision. Practically, the impact parameters cuts such
1480 as $d_0/\sigma_{d_0} < 5$ and $z_0 \sin\theta < 0.5$ mm are usually applied, where d_0 is the closest distance
1481 of the track to the measured beam-line, z_0 is the distance along the beam-line between the
1482 point where d_0 is measured and the beam-spot position, and θ is polar angle of the track,
1483 σ_{d_0} denotes the estimated uncertainty of d_0 parameter. Figure 4.5 depicts the definition of
1484 each track impact parameter.

1485 **Electron identification**

1486 The electron identifications are applied to determine whether the reconstructed elec-
1487 tron candidate is more signal-like or background-like object. The identification algorithms
1488 make use of quantities of related variables from electron cluster and track measurements
1489 including calorimeter shower shapes, track properties, as well as variables measuring
1490 bremsstrahlung effects for distinguishing signal from background. Taking the advantage
1491 of new IBL in run-2, the number of hits in this innermost pixel layer is utilized for discrim-
1492 inating between electrons and converted photons. In addition, a likelihood method based
1493 on the TRT high-threshold hits is adopted to compensate the lower transition radiation
1494 absorption probability of the argon.

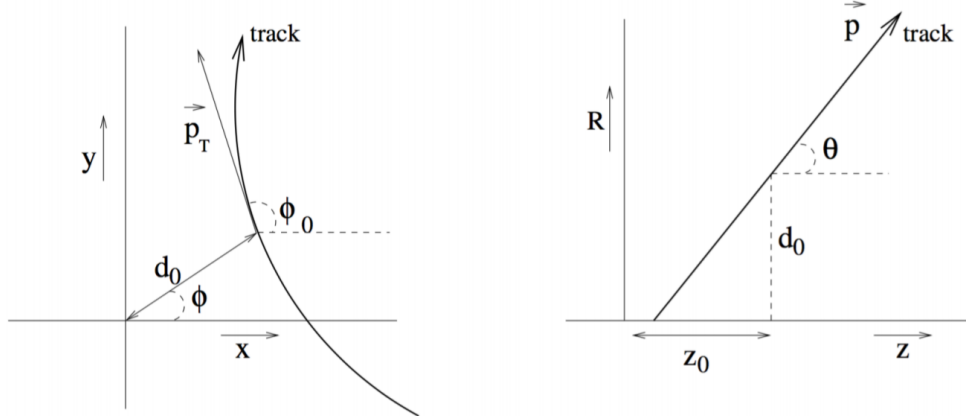


Fig. 4.5 Schematic of the impact parameters of a track in the transverse plane (left) and RZ-plane (right), as defined in the global ATLAS tracking frame^[59].

1495 The baseline identification algorithm introduced for ATLAS run-2 data analysis is the
 1496 likelihood-based (LH) method, which uses a MVA technique to simultaneously evaluate
 1497 several properties of electron candidates when making a decision. The LH method utilizes
 1498 the probability density functions (PDFs) of signal and background as the input discrimi-
 1499 nating variables. Based on these PDFs, it can calculate overall probabilities of the object
 1500 to be signal or background. Then the probabilities of signal and background are combined
 1501 together into a discriminant $d_{\mathcal{L}}$:

$$d_{\mathcal{L}} = \frac{\mathcal{L}_S}{\mathcal{L}_S + \mathcal{L}_B}, \quad \mathcal{L}_{S(B)}(\mathbf{x}) = \prod_{i=1}^n P_{s(b),i}(x_i) \quad (4.1)$$

1502 where \mathbf{x} denotes the vector of discriminating variables and $P_{s(b),i}(x_i)$ represents the value
 1503 of signal (background) PDF of the i^{th} variable as x_i .

1504 Three levels of working points (WPs) for electron identification are provided: *Loose*,
 1505 *Medium* and *Tight*, in order of increasing background rejection. Samples selected by a
 1506 looser WP are subsets of a tighter one, for example, the electrons passing Medium can
 1507 all be selected by Loose. The identification efficiency varies as function of transverse
 1508 energy (E_T) as shown in figure 4.6. For evaluations, the electron candidates from MC
 1509 simulation of $Z \rightarrow ee$ decays (di-jet) are used as signal (background). Depending on the
 1510 working point, the signal (background) efficiencies for reconstructed electron candidates
 1511 at $E_T = 25 GeV$ are in the range of 78 to 90% (0.3 to 0.8%), and increase (decrease) with
 1512 E_T .

1513 Electron isolation

1514 In addition to the identification criteria, most analyses have electron isolation require-
 1515 ment to further distinguish signal from background. To quantify the energy of particles

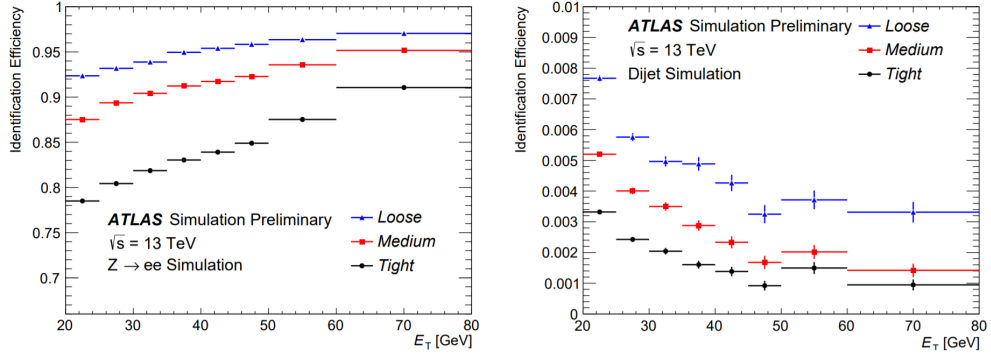


Fig. 4.6 The efficiencies of three electron identification WPs from $Z \rightarrow ee$ (left) events and hadrons misidentified as electrons estimated using di-jet MC samples (right).

around the electron candidate, the isolation variables can help to separate the prompt electron from other non-isolated electrons, like the electrons from converted photons or from heavy flavour hadron decays. There are two kinds of discriminating variables that have been designed:

- **Calorimeter-based variable:** $E_T^{topocone20}$. It's defined as the sum of transverse energies of topological clusters^[60], calibrated at EM scale within a cone of $\Delta R = 0.2$ around the candidate electron cluster. It only considers the clusters with positive reconstructed energy. In addition, a correction as a function of (E_T, η) values is applied to account for the electron energy leakage outside the cluster.
- **Track-based variable:** $p_T^{varcone20}$. It's calculated as the sum of transverse momentum of all satisfied tracks within a cone of $\Delta R = \min(0.2, 10\text{GeV}/E_T)$ around the candidate electron track. To calculate the sum, it requires the tracks are originating from the reconstruction PV of hard collision, and exclude the associated tracks of electron itself.

Based on the values of $E_T^{topocone20}/p_T$ and $p_T^{varcone20}/p_T$, a series of working points with different selection requirements are defined. The resulting WPs are divided into two kinds:

- Efficiency targeted working points: varying requirements to obtain a certain isolation efficiency, which can either be a constant or as a function of E_T .
- Fixed requirement working points: set the constant upper thresholds on isolation variables.

The distribution of two discriminating variables are shown in figure 4.7 for $ZZ \rightarrow ee$ events with $E_T > 27\text{GeV}$ and satisfying *Tight* requirement.

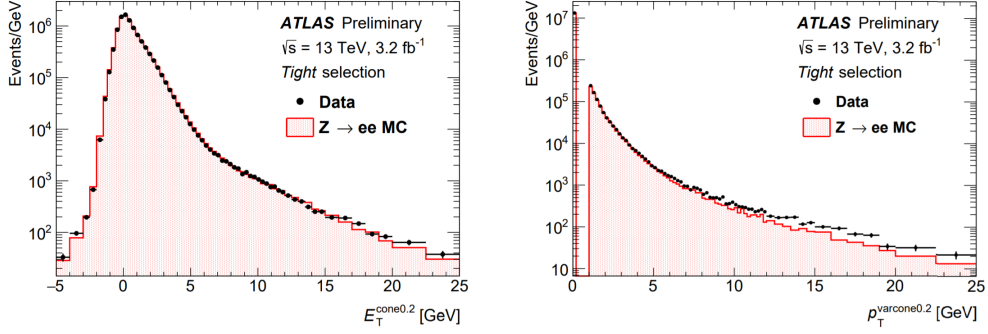


Fig. 4.7 Distributions of $E_T^{cone0.2}$ (left) and $p_T^{varcone0.2}$ (right) for electrons from $Z Z \rightarrow ee$ events in data and MC simulation. The simulated events (full histograms) are normalized to data.

4.2.4 Muon

Muons are distinctive signatures in final states of many physics analyses at the LHC including the Higgs analyses, SM measurements, BSM searches and so on. High performance of muon reconstruction and identifications are crucial. This section briefly describes some more details of the *reconstruction, identification and isolation* of muon.

Muon reconstruction

Muon reconstruction is firstly performed in inner detector (ID) and muon spectrometer (MS) independently as given in section 4.2.1. The information from each individual detector is then combined together to form the muon tracks for physics analyses. The combined ID-MS reconstruction is developed according to several algorithm based on the information from ID, MS and calorimeters. Four different muon types are defined^[51]:

- **Combined (CB) muons:** a combined track is formed by using the reconstructed tracks performed independently in ID and MS with a global refit. To improve the fit quality, the hits from MS may be added to or removed from the track. The outside-in pattern recognition is utilized for the reconstruction of most muons, in which the muons are first reconstructed in MS and then extrapolated inward to match the ID track. In the meantime, the inside-out pattern is also used as a complementary method.
- **Segment-tagged (ST) muons:** a reconstructed track in ID is defined as muon, if it can be associated with at least one track segment in MDT or CSC chambers. These ST muons are used when they can only pass across one layer of MS chambers due to their low p_T or falling into regions with less MS acceptance.
- **Calorimeter-tagged (CT) muons:** a reconstructed track in ID is categorized as muon if it's matched to the energy deposit in calorimeter which is recognized with

1562 a minimum-ionizing particle. This CT muons have lowest purity amount all types
1563 of muons, but it covers the region where ATLAS muon spectrometer is only par-
1564 tially constructed. For the region of $|\eta| < 0.1$ and $15GeV < p_T < 100GeV$, the
1565 identification of CT muons are optimal.

- 1566 • **Extrapolated (ME) muons:** the muon is reconstructed based only on the MS track
1567 and a loose requirement of originating from the interaction point. In general, this
1568 type of muon needs to pass at least two (three) layers of MS chambers to provide
1569 a track measurement in barrel (forward) region. ME muons are designed to extend
1570 the acceptance for muon reconstruction into the region $2.5 < |\eta| < 2.7$ where ID
1571 doesn't cover.

1572 Before collecting those muons for physics analyses, overlap removals are performed
1573 between different muon types with the priority of CB > ST > CT, when two types of muons
1574 share the same ID track. Besides, the overlaps with ME muons are resolved by analyzing
1575 the track hit content, and selecting the track with better fit quality and larger number of
1576 hits.

1577 **Muon identification**

1578 After reconstruction, the muon identification is then performed to further discrimi-
1579 nate between signal and background, especially to suppress backgrounds from pion and
1580 kaon decays by requiring prompt muons with high efficiency and guaranteeing a robust
1581 momentum measurement. The muon identification is defined by using the fit quality of
1582 combined track. The variables utilized in judgement for CB tracks include:

- 1583 • *q/p significance*, the absolute difference between q/g (charge over momentum) of
1584 muons measured in ID and MS divided quadratic sum of their corresponding un-
1585 certainties;
- 1586 • ρ' , the absolute value of difference between the p_T (transverse momentum) mea-
1587 sured in ID and MS, divided by the p_T of combined track;
- 1588 • *Nomalized χ^2* of the combined track fit;
- 1589 • *Number of hits in ID and MS*

1590 In addition, some new variables used for *LowPt* muon working point what will be de-
1591 scribed later^[61]:

- 1592 • *Momentum balance significance (MBS)* is computed as momentum difference be-
1593 tween the ID and MS standalone measurements with respect to the uncertainty σ on
1594 energy lost in the calorimeter system.
- 1595 • *Scattering neighbor significance (SNS)* is defined to estimated the significance of a
1596 change in trajectory along the track, expected in the presence of a hadron decaying

1597 to a muon.

- 1598 • *Scattering curvature significance (SCS)* is defined as the normalized integral of the
1599 scattering angle significances, corrected for large kinks along the trajectory.

1600 Five selection working points are developed to satisfy the different needs for different
1601 physics goals: *LowPt*, *Loose*, *Medium*, *Tight* and *HighPt*. The *Tight*, *Medium*, *Loose* are
1602 subsets from the tighter one to looser one. More detailed definition of each working point
1603 is given as follow:

- 1604 • *Loose*: this working point is designed to maximize the reconstruction efficiency
1605 while keeping good-quality of muon tracks. And they are specifically developed
1606 for reconstructing the Higgs boson candidates from four-lepton final states. All
1607 four muon types are used for this selection level. The CB and ME muons passing
1608 Medium WP that will mentioned below are all included into Loose category. In
1609 addition, the CT and ST muons are restricted to $|\eta| < 0.1$ region. In the range of
1610 $|\eta| < 2.5$, around 97.5% Loose muons are CB muons, and about 1.5% are CT while
1611 remaining 1% are ST muons.

- 1612 • *Medium*: this working point is the default criteria of muon identification in ATLAS.
1613 This selection minimizes the systematic uncertainties of muon reconstruction and
1614 calibration. In this category, we only use CB and ME muons. For CB muons, at least
1615 3 hits in at least two layers of MDT are required, except $|\eta| < 0.1$ region, in which
1616 tracks with ≥ 1 MDT layer but ≤ 1 MDT hole layer are allowed. For ME muons, at
1617 least 3 MDT/CSC layers are required. Furthermore, a loose cut on the compatibility
1618 between measured momentum in ID and MS is applied to reduce the fake muons
1619 from hadrons misidentification. Besides, the q/p-significance is required to be less
1620 than 7.

- 1621 • *Tight*: this working point is used to maximize the purity of muons but with sacrifice
1622 of some selection efficiency. Only CB muons with hits in ≥ 2 stations of MS and
1623 passing Medium criteria are selected. In addition, the normalized χ^2 of combined
1624 track fit should be smaller than 8. Then, a two-dimensional cut of q/p-significance
1625 and ρ' is adopted as a function of muon p_T to ensure tighter background rejection
1626 for momentum below 20 GeV, in which the fake rate is usually higher.

- 1627 • *High- p_T* : this set of selections aims to maximize the momentum resolution for
1628 tracks with $p_T > 100\text{GeV}$ region. The selection is especially optimized for searching
1629 high-mass Z' and W' resonances. CB muons satisfying Medium selection and
1630 with ≥ 3 hits in 3 MS stations are chosen. The specific region in MS where alignment
1631 is suboptimal are removed as a precaution.

- 1632 • *Low- p_T* : this type of muon is newly designed for physics analyses with ATLAS
 1633 software release version 21. It's designed to obtain a optimal muon identification
 1634 with very low transverse momentum of $3GeV < p_T < 5GeV$, which is crucial
 1635 for B-physics measurement in ATLAS. In this muon requirement, only CB muons
 1636 are used. In the range of $|\eta| < 1.3$, it requests muons hit at least one MS station; in
 1637 $1.3 < |\eta| < 1.55$, a least two MS stations are required; while in region of $|\eta| > 1.55$,
 1638 *Medium WP* is required. In addition, cuts are applied to suppress fakes as: $|MBS| <$
 1639 3.0 , $|SNS| < 3.0$ and $|SCS| < 3.0$.

1640 Figure 4.8 and 4.9 show the selection efficiency of different muon identification work-
 1641 ing points. For *Medium (Loose)*, *Tight* and *High- p_T* : $Z \rightarrow \mu\mu$ events with $p_T > 10GeV$
 1642 are used for measurement. In the top figure of figure 4.8, the efficiency of the Loose se-
 1643 lection (squares) is shown comparing to Medium one, where significant difference can be
 1644 observed in region of $|\eta| < 0.1$. For *LowPt*, $J/\Psi \rightarrow \mu\mu$ events with $3GeV < p_T < 10GeV$
 are used for measurement.

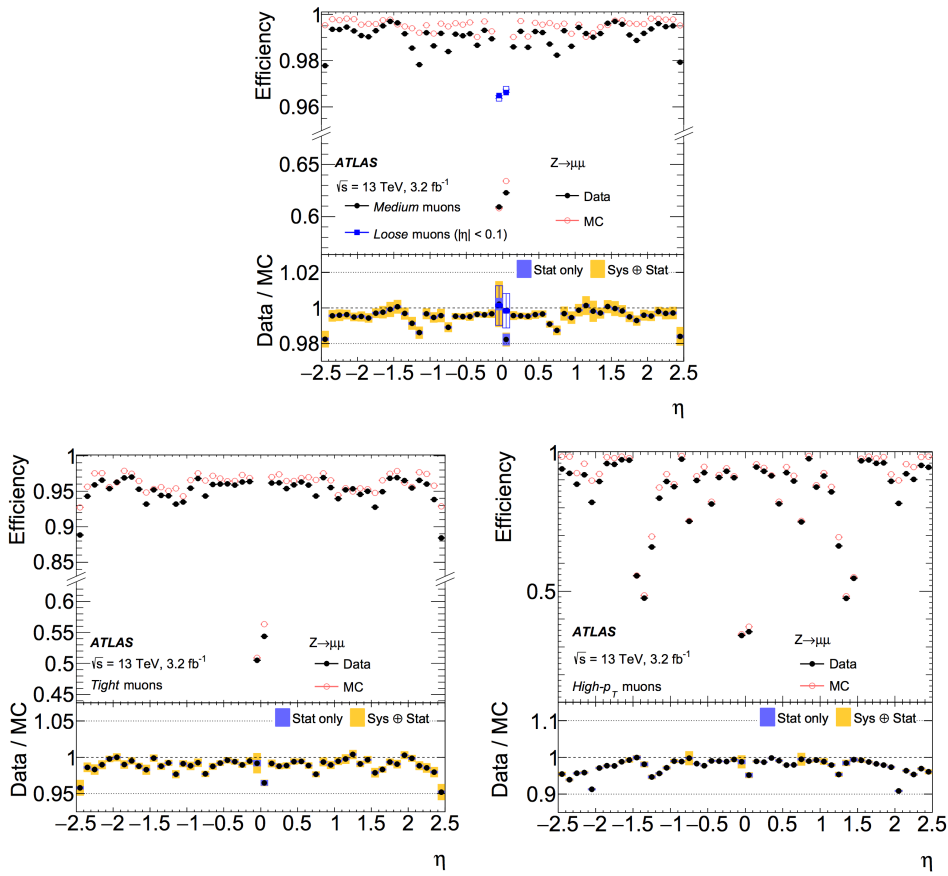


Fig. 4.8 Muon reconstruction efficiency as a function of η for: Medium (and Loose), Tight and High- p_T working points.

1645

1646

Muon isolation

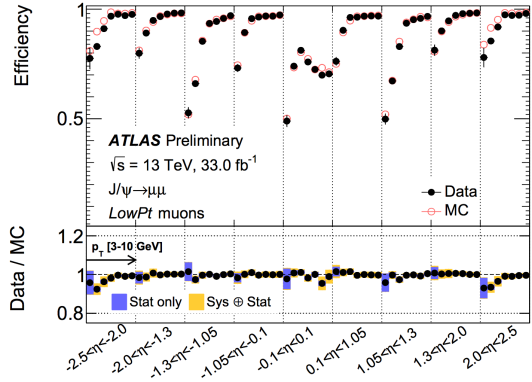


Fig. 4.9 Muon reconstruction efficiency for Low- p_T working point as a function of η .

Similar to electron, the muon isolation is used to further distinguish the prompt muon from non-prompt backgrounds. There are also two types of isolation variables for muon:

- **Calorimeter-based variable:** $E_T^{topocone20}$. It's defined as the sum of the transverse energy of topological clusters within a cone of size $\Delta R = 0.2$ around the candidate muon, after subtracting the contribution from the energy deposit of the muon itself and correcting for pile-up effects. The contributions from pile-up and underlying events are computed using the ambient energy-density technique^[62] and are corrected on an event-by-event basis.
- **Tracked-based variable:** $p_T^{varcone30}$. It's computed as the scalar sum of the transverse momenta of the tracks with $p_T > 1 GeV$ in a cone size of $\Delta R = \min(10 GeV/p_T^\mu, 0.3)$ around the candidate muon whose transverse momenta is p_T^μ after excluding the muon track itself. This p_T -dependent cone size can help to improve the performance for muons produced in the decay of particles with a large transverse momentum.

Then the isolation selections are applied based on *relative isolation variables*, which are computed as the ratio of the track- or calorimeter-based isolation variables to the transverse momentum of the muon. Figure 4.10 shows the distribution of those relative isolation variables by using $Z \rightarrow \mu\mu$ events for muons passing *Medium* identification criteria.

4.2.5 Jets

Jets are another important features for many physics analyses at the LHC, and especially the key signatures for vector boson fusion/scattering (VBF/VBS) processes. In ATLAS detector, jets are reconstructed as groups of topologically associated energy deposits in the calorimeters, tracks associated with charged particles measured in the inner

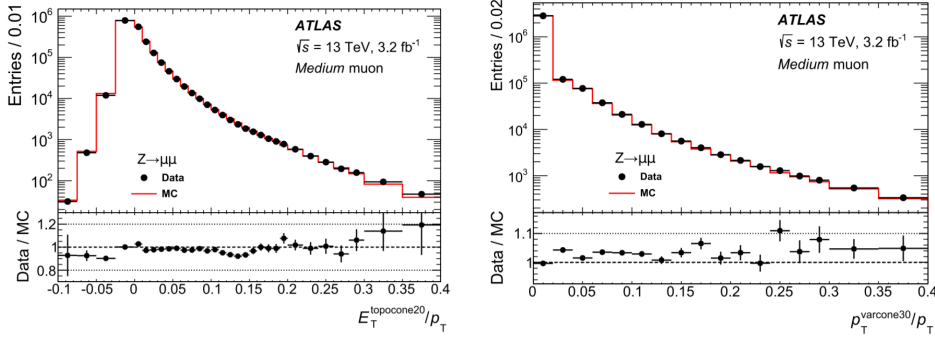


Fig. 4.10 Distributions of the calorimeter-based (right) and the track-based (left) relative isolation variables measured in $Z \rightarrow \mu\mu$ events.

tacking detector, or simulated particles. This section introduces the jet reconstruction, jet energy scale (JES) calibration and the b-jet tagging techniques.

Jet reconstruction

Jets are reconstructed using anti- k_t algorithm^[63] and with radius parameter of $R = 0.4$ in most cases. The FASTJET software package^[64] is utilized for jet finding and reconstruction. A collection of four-vectors are used as inputs at each combination step in jet clustering, the total four-momentum is therefore computed as the sum of four-vector of all its constituents. There are three types of jets in ATLAS:

- *Truth jets*: the inputs to jet algorithm are simulated particles.
- *Track jets*: the inputs are charged tracks measured from inner detector.
- *Calorimeter jets*: the inputs are energy deposits in calorimeters.

Figure 4.11 shows the schematic of ATLAS jet reconstruction.

Jet reconstruction

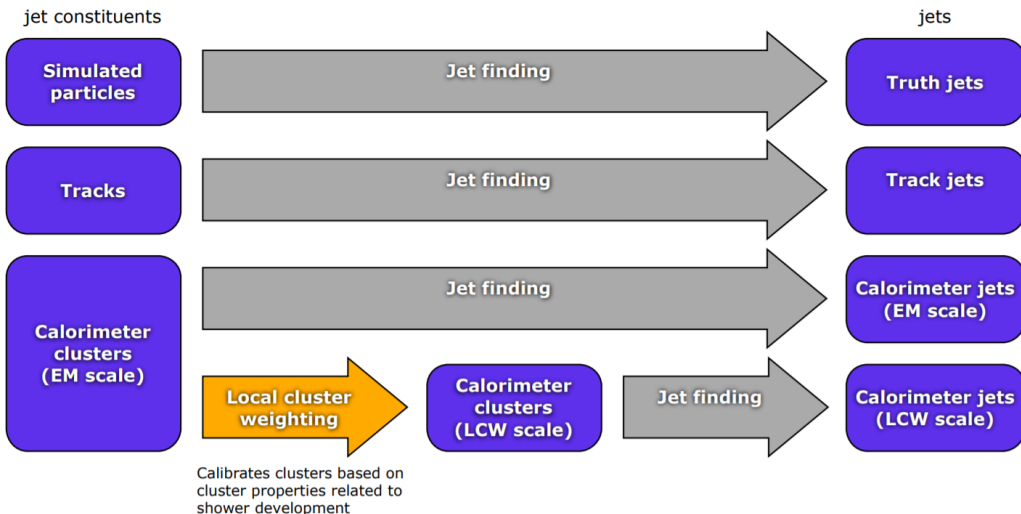


Fig. 4.11 A overview schematic of ATLAS jet reconstruction^[65].

1682

1683 The *truth jets* are reconstructed using anti- k_t algorithm with $R = 0.4$ by using final-

state, stable particles from MC simulation as inputs. It requires the candidate particles with lifetime $c_\tau > 10$ mm and excludes the particles from pile-up. Truth jets with $p_T > 7\text{GeV}$ and $|\eta| < 4.5$ are then used for jets calibration described later.

The *track jets* are reconstructed from charged particles within the full acceptance of inner detector ($|\eta| < 2.5$). The track reconstruction has been introduced in section 4.2.1. Reconstructed jets with $p_T > 500\text{MeV}$ and associated with primary vertex are then selected. Tracks are assigned to jets using ghost association^[62], a procedure that treats selected tracks as four-vectors of infinitesimal magnitude during the jet reconstruction and assigns them to the jet which they are clustered with. In addition, muon track segments are used as a compensation for those uncaptured jet energy carried by energetic particles passing through the calorimeters without being completely absorbed. Similar to the ID track, muon segments are assigned to jets using the method of ghost association mentioned above as well.

The *calorimeter jets* are reconstructed using a set of three-dimensional, positive-energy topological clusters (topo-clusters) made of calorimeter cell energies as input to the anti- k_t algorithm^[66]. Topo-clusters are built from near-by calorimeter cells that contains a significant energy above a noise threshold, which is estimated from measurements of calorimeter electronic noise and simulated pile-up noise. Those calorimeter cell energies are measured at electromagnetic energy scale (EM scale) corresponding to the energy deposited by electromagnetically interacting particles. And jets passing a p_T threshold of 7 GeV are reconstructed with the anti- k_t algorithm.

1705 Jet energy scale calibration

Figure 4.12 depicts an overview of ATLAS jet calibration scheme for EM-scale calorimeter jets. In this procedure, the jet energies are scaled to truth jets, which is reconstructed at the particle-level. Each step of the calibration corrects the full four-momentum unless otherwise stated, scaling the jet p_T , energy, and mass.

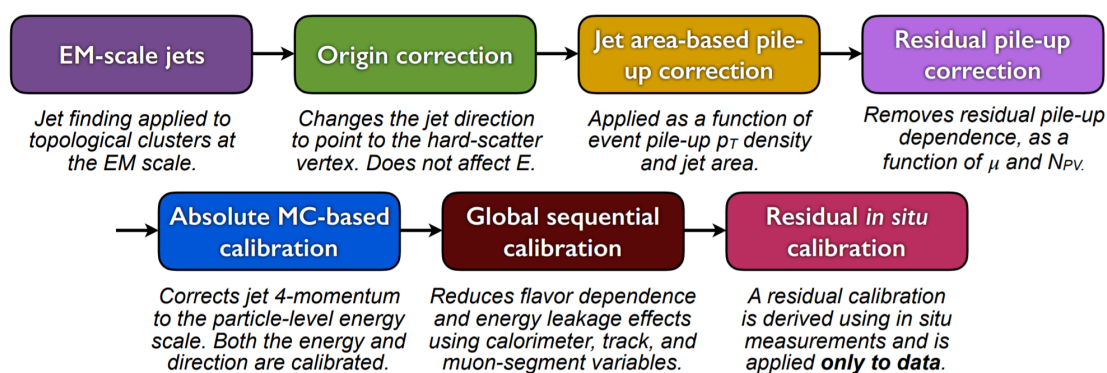


Fig. 4.12 A overview schematic of ATLAS jet calibration^[66].

1709 First of all, the origin correction recompute the four-momentum of jets to point them to
1710 the hard-scatter primary vertex instead of the centre of detector, and in the meantime keep
1711 the jet energy unchanged. This correction improves the η resolution of jets by roughly
1712 25% at a jet p_T of 20 GeV and > 5 times improvement for jet with p_T above 200 GeV,
1713 as measured from the difference between reconstructed jets and truth jets in MC simu-
1714 lation. Secondly, the pile-up correction is adopted to remove the excess energy due to
1715 in-time and out-of-time pile-up, which consists of two processes: an area-based p_T den-
1716 sity subtraction applied on the top of each event; and a residual correction derived from
1717 the simulation. Thirdly, the absolute JES calibration corrects the jet four-momentum to
1718 the particle-level energy scale, using truth jets in di-jet MC events. Furthermore, the step
1719 of global sequential calibration uses calorimeter, track and MS-based variables to reduce
1720 the flavor dependence and energy leakage effects. Finally, the residual in situ calibration
1721 is adopted to correct jets in data by using well-measured objects eg. photons, Z bosons
1722 and calibrated jets.

1723 **B-jet tagging**

1724 Tagging of b-jets plays a important role in many physics analyses involving b- or t-
1725 quark. In the meantime, lots of analyses need to apply b-jet veto to suppress $t\bar{t}$ process.
1726 There are three major types of algorithms that have been developed to distinguish b-quark
1727 jets from light-quark (u,d,s) jets^[67]:

- 1728 • **Impact parameter based algorithms (IP2D and IP3D):** b-hadrons usually have
1729 long lifetime (~ 1.5 ps, $c_\tau \sim 450$ μm), which leads to large impact parameter for
1730 tracks produced from b-hadron decay. The impact parameter taggers are devel-
1731 oped based on these variables. The IP2D tagger makes use of the transverse im-
1732 pact parameter significance $d_0/\sigma(d_0)$ as discriminant, while IP3D tagger uses two-
1733 dimensional discriminant of both transverse and longitudinal impact parameter sig-
1734 nificances: $d_0/\sigma(d_0)$ and $z_0 \sin\theta/\sigma(z_0)$.
- 1735 • **Secondary vertex finding algorithm (SV1)** makes use of the secondary vertex
1736 formed by decay products of b-hadron within the jet. All track pairs within a jet are
1737 tested for a two-track vertex hypothesis, and removed if they are likely to originate
1738 from a long-live particle decay (eg. K_s or Λ), hadronic interactions or photon con-
1739 versions. After that, a new vertex is fitted with all tracks from remaining two-track
1740 vertices, and the outliers are removed from this set of tracks.
- 1741 • **Decay chain multi-vertex algorithm (JetFitter)**^[68] exploits the topological struc-
1742 ture of weak b- and c- hadron decays inside the jet and tries to reconstruct the full

1743 b-hadron decay chain. A Kalman filter is adopted to find a common line between
 1744 primary vertex and b/c- vertices, as well as their position in this line, which gives
 1745 a approximated flight path for the b-hadron. In this approach, the b- and c-hadron
 1746 vertices, whenever resolution allows, can be resolved, even when there is only a
 1747 single track associated to them.

1748 The final discrimination commonly used in many physics analyses is called **Multivariate**
 1749 **Algorithm (MV2)**, which is based on Boosted Decision Tree (BDT) implemented in the
 1750 TMVA package^[69] by combining the outputs from underlying taggers mentioned above.
 1751 The MV2 was trained using jets in $t\bar{t}$ sample, where the b-jets are treated as signal while
 1752 the c- and light-flavor jets are treated as backgrounds. There are three kinds of MV2
 1753 depending on the fraction of c-jets in background for training: *MV2c00*, *MV2c10* and
 1754 *MV2c20*. Figure 4.13 presents the output score of MV2c10 for different flavor jets.

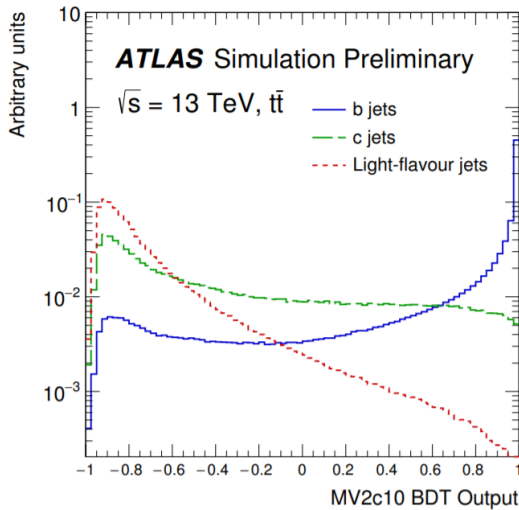


Fig. 4.13 MV2c10 BDT output for b- (solid blue), c- (dashed green) and light-flavour (dotted red) jets in $t\bar{t}$ events^[67].

1754

1755 4.2.6 Missing transverse energy

1756 Many interesting physics processes are with the involvement of neutrinos. Since they
 1757 do not interact with any materials in the detector, neutrinos cannot be detected directly;
 1758 but instead, they can result in imbalance in the plane transverse to the beam axis, where
 1759 momentum conservation is assumed. It is known as the missing transverse momentum
 1760 denoted as E_T^{miss} , which is obtained from the negative vector sum of the momenta of all
 1761 particles detected in a proton-proton collision event.

1762 The E_T^{miss} is measured using selected, reconstructed and calibrated hard objects in an

1763 event. Its x- and y- components can be calculated as follow^[70]:

$$E_{x(y)}^{miss} = E_{x(y)}^{miss,e} + E_{x(y)}^{miss,\gamma} + E_{x(y)}^{miss,\tau} + E_{x(y)}^{miss,jets} + E_{x(y)}^{miss,\mu} + E_{x(y)}^{miss,soft} \quad (4.2)$$

1764 where each object term is given by the negative vectorial sum of the momenta of the re-
 1765 spective calibrated objects. The calorimeter signals are associated with the reconstructed
 1766 objects in the following order: electrons, photons, hadronically decaying taus, jets, muons.
 1767 The soft term is reconstructed from detected objects not match any hard object passing
 1768 the selections, but associated with the primary vertex. Details of applied selections for
 1769 each term are summarized in table 4.1.

1770 Based on $E_{x(y)}^{miss}$, the magnitude of E_T^{miss} and the azimuthal angle ϕ^{miss} are computed:

$$\begin{aligned} E_T^{miss} &= \sqrt{(E_x^{miss})^2 + (E_y^{miss})^2} \\ \phi^{miss} &= \arctan(E_y^{miss}/E_x^{miss}) \end{aligned} \quad (4.3)$$

1771 In equation 4.2, each objects are required to pass certain reconstruction and calibrated
 1772 criteria and selections mentioned above before taken as inputs.

1773 In figure 4.14, left plot shows the observed E_T^{miss} distribution for data and MC of $Z \rightarrow$
 1774 $\mu\mu$ events without genuine missing transverse momentum; and right plot shows the E_T^{miss}
 1775 distribution for $W \rightarrow ev$ events that has genuine (true) missing transverse momentum due
 to real neutrino.

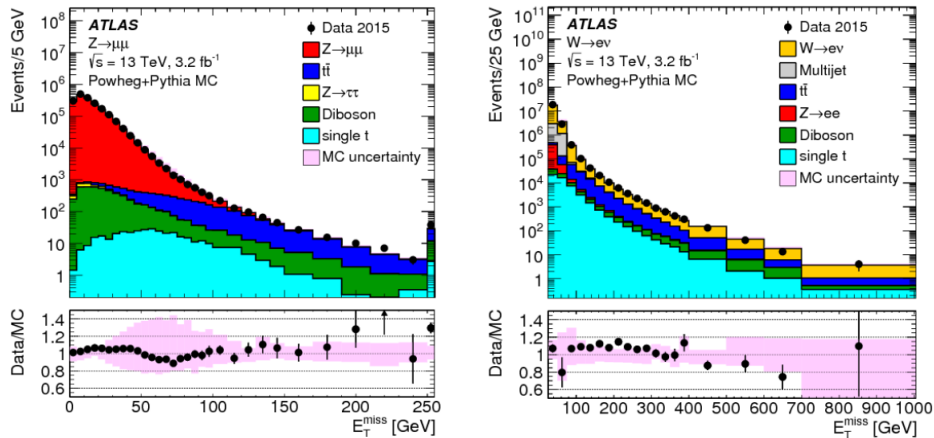


Fig. 4.14 Measured E_T^{miss} distribution for $Z \rightarrow \mu\mu$ events (left) and $W \rightarrow ev$ events (right).

1776

Table 4.1 Overview of the contributions to E_T^{miss} .

Objects contributing to E_T^{miss}				
Priority	Type	Selections	Variables	Comments
(1)	e	$ \eta < 1.37 \text{ or } 1.52 < \eta < 2.47$ $p_T > 10GeV$	$E_T^{miss,e}$	all e^\pm passing kinematic selections and medium reconstruction quality
(2)	γ	$ \eta < 1.37 \text{ or } 1.52 < \eta < 2.47$ $p_T > 25GeV$	$E_T^{miss,\gamma}$	all γ passing kinematic selections and tight reconstruction quality, and without overlapping with (1)
(3)	τ_{had}	$ \eta < 1.37 \text{ or } 1.52 < \eta < 2.47$ $p_T > 20GeV$	$E_T^{miss,\tau}$	all τ_{had} passing kinematic selections and medium reconstruction quality, and without overlapping with (1) and (2)
(4)	μ	$ \eta < 2.7$ $p_T > 10GeV$	$E_T^{miss,\mu}$	all μ passing kinematic selections and medium reconstruction quality
(5)	jet	$ \eta < 4.5$ $p_T > 60GeV$ --- or --- $2.4 < \eta < 4.5$ $20GeV < p_T < 60GeV$ --- or --- $ \eta < 2.4$ $20GeV < p_T < 60GeV$ $JVT > 0.59$	$E_T^{miss,jet}$	all jets passing kinematic selections and reconstruction quality (jet cleaning), and without overlap with (1)–(4)
(6)	ID track	$p_T > 400MeV$ $ d_0 < 1.5mm$ $ z_0 \sin\theta < 1.5mm$ $\Delta R(track, e/\gamma cluster) > 0.05$ $\Delta R(track, \tau_{had}) > 0.2$	$E_T^{miss,soft}$	all ID tracks from the hard-scattering vertex passing kinematic selections and reconstruction quality, and not associated with any particle from (1), (3) or (4), or associated with a jet from (5)

1777 **Chapter 5 Statistical treatment of searching for new 1778 particles or processes**

1779 In the experiments of particle physics, one often searches for particles or processes
1780 that have been predicted but not yet observed, such as the two analysis presented in this
1781 dissertation: searching for the vector boson scattering process and searching for the heavy
1782 resonance(s). Usually two hypotheses are defined:

- 1783 • H_0 : null hypothesis, in most cases are designated as background-only hypothesis.
1784 • H_1 : signal plus background hypothesis, where signal is a new model one would like
1785 to search for.

1786 For the purpose of discovering a new signal process, the H_0 hypothesis is tested against
1787 the alternative H_1 . When setting limits, the H_1 hypotheses with different signal strengths
1788 are tested against the H_0 .

1789 The level of agreement between observed data and a given hypothesis can be quantified
1790 by computing the p -value, the probability under this hypothesis assumption, or its equiv-
1791 alent Gaussian significance. This section describes the statistical treatment for searches
1792 related to this dissertation.

1793 5.1 The likelihood function

1794 The likelihood function is defined as the product of a set of the probability density
1795 functions (pdfs) of variables x , that used to evaluate the probability of the observed dataset:

$$\mathcal{L}(x_1, \dots, x_N; \theta_1, \dots, \theta_M) = \prod_i^N f(x_i; \theta_1, \dots, \theta_M) \quad (5.1)$$

1796 where $\theta_1, \dots, \theta_M$ are the nuisance parameters that can be written as $\boldsymbol{\theta}$, and x_1, \dots, x_N
1797 denote the observables of dataset. Usually one measures the variable x by constructing a
1798 histogram $\mathbf{n} = (n_1, \dots, n_N)^\top$. The expectation value of the i th bin n_i can be written as:

$$E[n_i] = \mu s_i + b_i \quad (5.2)$$

1799 where μ is the signal strength, s_i and b_i are the number of signal and background events
1800 in that bin. In addition to the histogram \mathbf{n} , in some cases, one would like to use subsidiary
1801 measurements to help further constrain the nuisance parameters. For instance, due to the
1802 lack of background simulation or the mismodelling issue of one MC sample, one can

choose a control region and construct another histogram $\mathbf{m} = (m_1, \dots, m_M)$ to constrain the contribution of one certain background in data. For this measurement, the expectation value of the i th bin m_i can be written as:

$$E[m_i] = u_i(\boldsymbol{\theta}) \quad (5.3)$$

In most particle experiments, the number of these events observed in one bin follows the Poisson distribution, by combining the equation 5.2 and 5.3, one can get the likelihood function for all bins as:

$$\mathcal{L}(\mu, \boldsymbol{\theta}) = \prod_i^N \frac{(\mu s_i + b_i)^{n_j}}{n_j!} e^{-(\mu s_i + b_i)} \prod_i^M \frac{u_k^{m_k}}{m_k!} e^{-u_k} \quad (5.4)$$

Then to test the hypothesized value of μ , the profile likelihood ratio is defined as:

$$\lambda(\mu) = \frac{\mathcal{L}(\mu, \hat{\boldsymbol{\theta}})}{\mathcal{L}(\hat{\mu}, \hat{\boldsymbol{\theta}})} \quad (5.5)$$

where numerator denotes to a local maximum-likelihood for a specific μ , $\hat{\boldsymbol{\theta}}$ is the value of $\boldsymbol{\theta}$ that maximizes the numerator. And the denominator is the global maximum-likelihood with best $\hat{\mu}$ and $\hat{\boldsymbol{\theta}}$ as their best fit value.

5.2 Test statistic

To test the level of agreement between the data and the hypothesized value μ , a test statistic t_μ can be defined:

$$t_\mu = -2 \ln \lambda(\mu) \quad (5.6)$$

From the definition of $\lambda(\mu)$ in equation 5.5, one can see that $0 \leq \lambda \leq 1$, and a λ with value close to 1 implies good agreement between data and μ . Thus, larger value of t_μ means the increase of incompatibility between data and μ . To quantify the level of disagreement, one can calculate the p -value as:

$$p_\mu = \int_{t_{\mu,obs}}^{\infty} f(t_\mu | \mu) dt_\mu \quad (5.7)$$

in which $t_{\mu,obs}$ is the value of test statistic from observed data, and $f(t_\mu | \mu)$ is the pdf of t_μ under the assumption of hypothesized value μ . This is a one-side p -value with its

1822 corresponding observed significance, Z , can be defined as:

$$Z = \Phi^{-1}(1 - 2p_\mu) \quad (5.8)$$

1823 The relationship between the t_μ , p -value and significance Z are depicted in figure ??.

1824 In most cases, one assumes that the presence of a new signal can only increase the
 1825 event rate comparing to the background only model, then the signal strength $\mu \geq 0$. And
 1826 for the case of discovery, the hypothesis of a positive signal strength should be tested
 1827 against to the background-only (null) hypothesis by using the test statistic called p_0 :

$$p_0 = \begin{cases} -2\ln(\lambda(0)) & \hat{\mu} \geq 0 \\ 0 & \hat{\mu} < 0 \end{cases} \quad (5.9)$$

1828 which corresponds to the p -value called p_0 :

$$p_0 = \int_{q_{0,obs}}^{\infty} f(q_0|0) dq_0 \quad (5.10)$$

1829 to quantify the level of disagreement between the data and the null hypothesis ($\mu = 0$).

1830 5.3 The CLs upper limit

1831 For a signal hypothesized value μ , one can compute the probability that this hypothesis
 1832 (called S+B hypothesis) gives a **greater** test statistic value than the observed one q_{obs} :

$$P_{s+b} = \int_{q_{obs}}^{\infty} f(q_\mu|\mu) dq_\mu \quad (5.11)$$

1833 In the meantime, the probability that the background-only hypothesis gives a **smaller** test
 1834 statistic than observed data can be calculated as:

$$1 - P_b = \int_{-\infty}^{q_{obs}} f(q_\mu|0) dq_\mu \quad (5.12)$$

1835 Then we define the CLs of a hypothesized value μ as:

$$CLs = \frac{p_{s+b}}{1 - p_b} \quad (5.13)$$

1836

1837 **Chapter 6 Studies of SM ZZ production in $\ell\ell\ell'\ell'$ final** 1838 **state using pp collision data collected by ATLAS** 1839 **detector from 2015 to 2018**

1840 6.1 Introduction

1841 After the discovery of Higgs boson^[3-4], the examination of electroweak symmetry
1842 breaking (EWSB) becomes a main focus at the LHC. In addition to measuring the prop-
1843 erties of Higgs boson directly, the vector boson scattering (VBS) process is another key
1844 avenue to probe EWSB^[71-73]. As introduced in section 2.1.3, in Standard Model (SM),
1845 the Higgs boson acts as “moderator” to unitarize high-energy longitudinal VBS ampli-
1846 tudes at the TeV scale. Therefore, studying high-energy behaviours of VBS is crucial to
1847 understand the mechanism of EWSB.

1848 Since no VBS process was observed prior to the LHC era, LHC provides an exception-
1849 able opportunity to study them due to its unprecedented high energy and luminosity. At
1850 the LHC, the VBS process is typically studied through the measurements of electroweak
1851 (EW) production of two vector bosons radiated from quark-quark initial state, plus a pair
1852 of hadronic jets with high energy in the back and forward regions (denoted as EW- $VVjj$).
1853 The quantum chromodynamics (QCD) production of $VVjj$ containing two QCD vertices
1854 at the lowest order (denoted as QCD- $VVjj$) is an irreducible background to the search
1855 of EW- $VVjj$ production. The features of EW- $VVjj$ production including a large invari-
1856 ant mass of jet pair (m_{jj}) and a significant separation of rapidity between two jets (Δy_{jj}).
1857 Figure 6.1 presents some typical Feynman diagrams of EW- and QCD- $ZZjj$ processes.
1858

1859 The first evidence of the EW- $VVjj$ process was seen in same-sign WW channel (EW-
1860 $W^\pm W^\pm jj$) by ATLAS collaboration with 20.3 fb^{-1} 8 TeV data^[74], in which a 3.6σ excess
1861 was observed in data over the background-only prediction. In the LHC run-2, the obser-
1862 vation (with $> 5 \sigma$ statistical significance) of EW- $W^\pm W^\pm jj$ process has been reported
1863 in both ATLAS and CMS collaboration with 36 fb^{-1} 13 TeV data^[75-76]. In WZ channel
1864 (EW- $WZjj$), an observation with 5.3σ excess was also reported by the ATLAS col-
1865 laboration recently^[77]. As for the EW- $ZZjj$ production, it was searched by CMS using
1866 35.9 fb^{-1} 13 TeV data but no evidence was found^[78]. The EW production in ZZ final state
1867 (EW- $ZZjj$) is typically rare, whose fiducial cross section has an order of $O(0.1) \text{ fb}^{-1}$ in the
1868 final state where both Z bosons decay leptonically. But in the meantime, $ZZ \rightarrow \ell\ell\ell'\ell'$

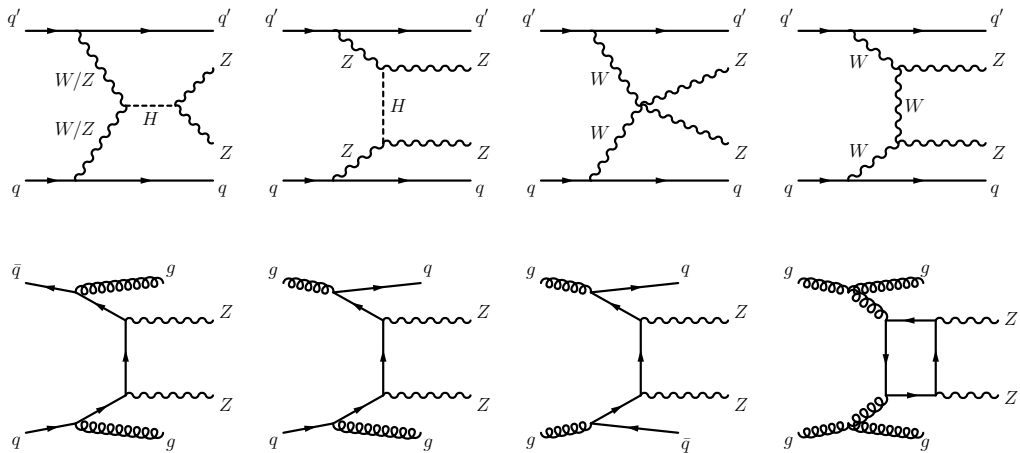


Fig. 6.1 Typical diagrams for the production of $ZZjj$, including the relevant EW VBS diagrams (first row) and QCD diagrams (second row).

process offers an extremely clean channel than all the others. So with more data collected in the LHC, the observation of EW- $ZZjj$ becomes possible.

This section presents the first observation of EW- $ZZjj$ production decaying to four charged leptons with two jets ($\ell\ell\ell'\ell' jj$) by ATLAS collaboration using the complete set of the LHC run-2 data with 139 fb^{-1} luminosity. It is a new milestone in the study of EWSB at the LHC, and completes the last missing part of observation of weak boson scattering for massive bosons. In the meantime, the measurement of fiducial cross-sections for SM ZZ production including both EW and QCD processes is also reported. The $ZZjj$ production involving intermediate τ -leptons from Z decays is considered as signal but has a negligible contribution to the selected events. Reducible backgrounds give minor contributions in the $\ell\ell\ell'\ell' jj$ channel are also studied. To further separate the EW signal and the QCD background, multivariate discriminant (MD) is trained using event kinematic information from simulated samples. The MD distribution is then used as discriminant in statistical fit to evaluate the signal strength of EW process.

6.2 Data and MC samples

6.2.1 Data samples

The datasets for this analysis include the full run-2 pp collision data collected by the ATLAS experiment during the years from 2015 to 2018. Data event is only used if it passed the latest Good Run List (GRL) released by the Data Quality group from ATLAS experiment, corresponding to an integrated luminosity of $139.0 \pm 2.4 \text{ fb}^{-1}$.

1889 6.2.2 MC simulations

1890 The EW- $Z Z jj$ production is modelled using **MADGRAPH5_aMC@NLO** 2.6.1^[79]
1891 with the matrix elements (ME) calculated in the leading-order (LO) approximation in
1892 perturbative QCD (pQCD) and with the NNPDF2.3LO^[80] parton distribution functions
1893 (PDF). The VBF Higgs process is also included.

1894 The QCD- $Z Z jj$ production is modelled using **SHERPA** 2.2.2^[81] with the
1895 NNPDF3.0NNLO^[82] PDF, where events with up to one (three) outgoing partons are gen-
1896 erated at NLO (LO) in pQCD. The production of $Z Z jj$ from the gluon-gluon initial state
1897 with a four-fermion loop or with an exchange of the Higgs boson has an order of α_S^4 in
1898 QCD, and is not included in the **SHERPA** simulation. A separate gg induced $Z Z + 2\text{jets}$
1899 sample is modelled using **SHERPA** 2.2.2 with the NNPDF3.0NNLO PDF and with an addi-
1900 tional 1.7 k-factor^[83] being applied. Then the interference between EW- and QCD- $Z Z jj$
1901 is modelled with **MADGRAPH5_aMC@NLO** 2.6.1 calculated at LO.

1902 The diboson productions from QCD $WW \rightarrow \ell\nu qq$ as well as QCD and EW $WZ \rightarrow$
1903 $\ell\ell qq$ are modelled using **SHERPA** 2.2.2 with the NNPDF3.0NNLO PDF. The produc-
1904 tions of semileptonic decays ($WW \rightarrow \ell\nu qq$ and $WZ \rightarrow qq\ell\ell$) are modelled using **POWHEG-**
1905 **Box v2**^[84] with the CT10 PDF^[85]. The triboson production is modelled using **SHERPA**
1906 2.2.2 with the NNPDF3.0NNLO PDF.

1907 For top-quark pair ($t\bar{t}$) production, the **POWHEG-Box v2** is used with the CT10 PDF.
1908 The single top-quark production in t -channel, s -channel and Wt -channel are simulated
1909 using the **POWHEG-Box v1** event generator^[86-88]. The productions of $t\bar{t}$ in association with
1910 vector boson(s) ($t\bar{t}V$) are modelled with **MADGRAPH5_aMC@NLO** 2.3.3 for $t\bar{t}W$ and $t\bar{t}Z$
1911 with $Z \rightarrow \nu\nu/qq$ decays, with **SHERPA** 2.2.1 for $t\bar{t}Z$ where the Z decays to dilepton, and
1912 with **MADGRAPH5_aMC@NLO** 2.2.2 for $t\bar{t}WW$ respectively.

1913 The $Z+jets$ processes are modelled using **SHERPA** 2.2.1 with the NNPDF3.0NNLO
1914 PDF, in which the ME is calculated for up to two partons with next-to-leading-order (NLO)
1915 accuracy in pQCD and up to four partons with LO accuracy.

1916 For all the samples except those from **SHERPA**, the parton showering is modelled with
1917 **PYTHIA8**^[45] using the NNPDF2.3^[80] PDF set, and the A14 set of tuned parameters^[89].
1918 While for **SHERPA** samples, the parton showering is simulated within the programme.

1919 All simulated events are processed with detector response simulation based on **GEANT4**
1920 described in section 4.1. In addition, simulated inelastic pp collisions are overlaid to
1921 model additional pp collision in the same and neighbouring bunch crossings (pile-up),
1922 and reweighted to match the pile-up conditions in data. Moreover, all simulated events
1923 are processed using the same reconstruction algorithms as data. And the leptons and jets

1924 reconstruction, energy scale and resolution, and the leptons identification, isolation, trig-
1925 ger efficiencies for simulated events, as described in section 4.2, are all corrected to match
1926 the data measurements.

1927

6.3 Objects and Event selection

1928

6.3.1 Objects selection

1929 The selection of analysis relies on the definition of multiple objects: *electrons*, *Muons*,
1930 and *jets*. Details of definition for each object are described as below:

1931 **Muon:** To increase the acceptance range in reconstruction (reco) -level for $\ell\ell\ell'\ell'$
1932 channel, all four types of muons (CB, ST, CT, ME muons, described in section 4.2.4)
1933 are used. The identified muons are then required to pass $p_T > 7$ GeV and $|\eta| < 2.7$,
1934 and satisfy the *Loose* identification criterion (see definition in sec 4.2.4). The impact
1935 parameter cuts are further applied to suppress the contribution from cosmic muons and
1936 non-prompt muons, with the value of: $|d_0/\sigma(d_0)| < 3.0$ and $|z_0 \sin\theta| < 0.5$ mm, where d_0
1937 is the transverse impact parameter relative to the beam line, $\sigma(d_0)$ is its uncertainty, and
1938 z_0 is the longitudinal impact parameter relative to the primary vertex. In order to avoid
1939 muons associated with jets, all muons are required to be isolated and pass *FixedCutLoose*
1940 isolation criteria of $E_T^{\text{topocone}20}/p_T < 0.3$ and $p_T^{\text{varcone}30}/p_T < 0.15$.

1941 **Electron:** As described in section 4.2.3, electrons are reconstructed from energy de-
1942 posits in the EM calorimeter matched to a track in the inner detector. The electron candi-
1943 dates must satisfy the *Loose* criterion defined by the likelihood-based (LH) method. And
1944 electrons are required to have $p_T > 7$ GeV and $|\eta| < 2.47$. Moreover, the impact parame-
1945 ter requirements of $|d_0/\sigma(d_0)| < 5.0$ and $|z_0 \sin\theta| < 0.5$ mm are applied. Same as muon,
1946 all electrons are required to satisfy *FixedCutLoose* isolation criteria, which, for electrons,
1947 is $E_T^{\text{topocone}20}/p_T < 0.2$ and $p_T^{\text{varcone}20}/p_T < 0.15$.

1948 **Jets:** Jet are key signatures for VBS processes. This analysis use the jets clustered
1949 using the anti- k_t algorithm with radius parameter $R = 0.4$, more details of jets' reconstruc-
1950 tion can be found in section 4.2.5. The jets are required to satisfy $p_T > 30$ (40) GeV in
1951 the $|\eta| < 2.4$ ($2.4 < |\eta| < 4.5$) region. To further reduce the effects of pile-up jets, a jet
1952 vertex tagger (JVT) is applied to jets with $p_T < 60$ GeV and $|\eta| < 2.4$ to select jets from
1953 hard-scattering vertex^[90].

1954 **Overlap removal:** An overlap-removal procedure is applied to selected leptons and
1955 jets. To enhance the selection efficiency, leptons are given higher priority to be kept when
1956 overlapping with jets. More details of the strategy is summarized in table 6.1.

	Reference objects	Criteria
Remove electrons	electrons	Share a track or have overlapping calorimeter cluster. Keep higher p_T electron
Remove muons	electrons	Share track and muon is calo-tagged
Remove electrons	muons	Share track
Remove jets	electrons	$\Delta R_{e-jet} < 0.2$
	muons	$\Delta R_{\mu-jet} < 0.2$ OR muon track is ghost-associated to jet AND ($N_{Trk}(jet) < 3$ OR ($p_T^{jet}/p_T^{\mu} < 2$ and $p_T^{\mu}/\sum_{Trk} p_t > 0.7$))

Table 6.1 Overlap removal criteria between pre-selection objects for the $\ell\ell\ell'\ell'$ channel. The overlap removal follows the order shown in this table. Once an object has been marked as removed, it does not participate in the subsequent stages of the overlap removal procedure.

6.3.2 Event selection

The events are required to additionally be recorded by single or multi-lepton triggers, with transverse momentum (p_T) thresholds varying from 8 to 26 GeV. The overall trigger efficiency for selected inclusive $\ell\ell\ell'\ell' jj$ signal events in the analysis region are from 95 to 99%.

The $\ell\ell\ell'\ell'$ quadruplets are formed by two opposite-sign, same-flavour (OSSF) lepton pairs ($\ell^+\ell^-$), in which leptons are required to be separated by $\Delta R > 0.2$ in table 6.1. At most one muon is allowed to be ME or CT muon. The p_T threshold of first three leading leptons are 20, 20 and 10 GeV. If more than one quadruplets are found, the one with minimum sum of difference between two dilepton pair masses and Z boson mass ($|m_{l_1^+ l_1^-} - m_Z| + |m_{l_2^+ l_2^-} - m_Z|$) is selected. Both two dilepton pair masses are required to be between 66 to 116 GeV. In addition, the invariant masses of all possible OSSF pairs are required to be greater than 10 GeV to reject events from J/ψ or Υ decay.

For VBS topology, the two most energetic jets in different detector side ($y_{j1} \times y_{j2} < 0$) are selected. Furthermore, the invariant mass of two jets (m_{jj}) is required to be greater than 300 GeV, while Δy_{jj} is required to be larger than 2. Table 6.2 summarizes the above selection requirements, which is defined as signal region (SR).

Electrons	$p_T > 7 \text{ GeV}, \eta < 2.47$ $ d_0/\sigma_{d_0} < 5 \text{ and } z_0 \times \sin \theta < 0.5 \text{ mm}$
Muons	$p_T > 7 \text{ GeV}, \eta < 2.7$ $ d_0/\sigma_{d_0} < 3 \text{ and } z_0 \times \sin \theta < 0.5 \text{ mm}$
Jets	$p_T > 30 (40) \text{ GeV}$ for $ \eta < 2.4$ ($2.4 < \eta < 4.5$)
ZZ selection	$p_T > 20, 20, 10 \text{ GeV}$ for the leading, sub-leading and third leptons Two OSSF lepton pairs with smallest $ m_{\ell^+\ell^-} - m_Z + m_{\ell'^+\ell'^-} - m_Z $ $m_{\ell^+\ell^-} > 10 \text{ GeV}$ for all OSSF lepton pairs $\Delta R(\ell, \ell') > 0.2$ $66 < m_{\ell^+\ell^-} < 116 \text{ GeV}$
Dijet selection	Two most energetic jets with $y_{j_1} \times y_{j_2} < 0$ $m_{jj} > 300 \text{ GeV}$ and $\Delta y_{jj} > 2$

Table 6.2 Summary of selection of physics objects and candidate events at detector level in the $\ell\ell\ell'\ell' jj$ signal region.

6.4 Background estimation

Table 6.3 summarizes the background yields for $ZZjj \rightarrow \ell\ell\ell'\ell' jj$ process in 139 fb^{-1} . Uncertainties on the predictions include both statistical and systematic components. ‘‘Others’’ includes minor contributions from non- ZZ processes including $Z+jets$, top-quark, triboson and $t\bar{t}V$ processes. Details of estimation for each source are described as below.

Process	$\ell\ell\ell'\ell' jj$
EW- $ZZjj$	20.6 ± 2.5
QCD- $q\bar{q} \rightarrow ZZ$	77 ± 25
QCD- $gg \rightarrow ZZ$	13.1 ± 4.4
Others	3.2 ± 2.1
Total	114 ± 26
Data	127

Table 6.3 Observed data and expected signal and background yields in 139 fb^{-1} of luminosity. Minor backgrounds are summed together as ‘‘Others’’. Uncertainties on the predictions include both statistical and systematic components.

6.4.1 QCD backgrounds

The QCD- $ZZjj$ production, which include both qq and gg initial processes, is the irreducible background in the search of EW- $ZZjj$ production. A QCD-enriched control region, named as QCD CR, is defined to constrain the normalization of ZZ background

1984 by reverting either the m_{jj} or Δy_{jj} requirements as:

$$m_{jj} < 300 \text{ GeV} \text{ AND } \Delta y_{jj} < 2 \quad (6.1)$$

1985 Then this normalization factor is included into statistical fit as a free parameter to properly
 1986 treat the uncertainty correlations between SR and CR, while the shapes are taken from MC
 1987 simulation. Table 6.4 shows the event yields of each background components in this CR.
 Uncertainties are statistical one only. The distributions of invariant mass of $\ell\ell\ell'\ell'$ and

Process	$\ell\ell\ell'\ell' jj$
EW-ZZjj	3.9 ± 0
QCD-ZZjj	136.9 ± 0.6
QCD-ggZZjj	16.8 ± 0.1
Diboson	0.3 ± 0.1
Triboson	1.6 ± 0.1
Z+jets	0
t̄t	0
Total	159.5 ± 0.62
Data	152

Table 6.4 Observed data and expected signal and background yields in 139 fb^{-1} of luminosity.

Diboson background in table includes all the other diboson processes discussed in section 6.2.2, except those with four-lepton final state. Uncertainties include only MC statistic. No events from Z+jets and t̄t MC samples pass the selection, and are indicated as 0 in the table.

1988

1989 dijet in QCD CR are shown in figure 6.2.

1990 6.4.2 Reducible backgrounds

1991 Backgrounds from Z+jets, top-quark and WZ processes called reducible back-
 1992 grounds can be estimated by data-driven method. These events usually contain two or
 1993 three leptons from Z/W decays, together with heavy-flavor jets or misidentified compo-
 1994 nents of jets reconstructed as leptons called “fake leptons”. A *fake factor* method is used
 1995 to estimate these backgrounds, where the lepton misidentification is measured in data with
 1996 the region enhances contributions from Z+jets and top-quark processes. The method is
 1997 described as below:

1998 1. Define a dedicated background dominant region to derive the fake factor for this

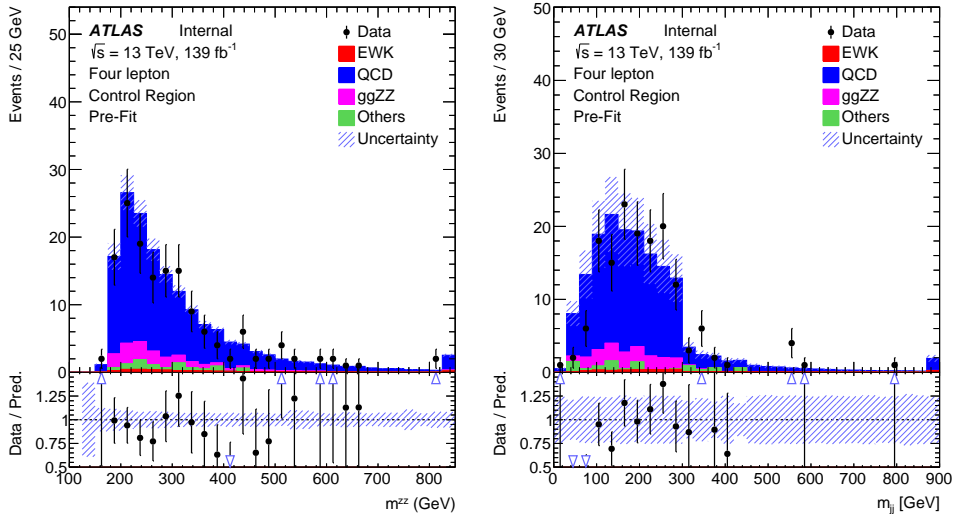


Fig. 6.2 Pre-fit m_{ZZ} and m_{jj} distribution in QCD-enriched CR.

background. The *fake factor* is defined as:

$$\mathcal{F} = \mathcal{N}_{good}/\mathcal{N}_{pool} \quad (6.2)$$

where \mathcal{N}_{good} refers to the number of good leptons passing all SR selection, while \mathcal{N}_{pool} denotes the number of poor leptons passing most SR selection but fail one certain requirement.

2. Define a fake control region, where one or two lepton(s) pass *poor* requirement while all the other leptons are required to pass SR selection.
3. The number of fake events are calculated as:

$$\mathcal{N}_{fake} = (N_{gggp} - N_{ggp}) \times \mathcal{F} - (N_{gppg} - N_{gpp}) \times \mathcal{F}^2 \quad (6.3)$$

with the subtraction of ZZ contribution, and the double counting between N_{gggp} and N_{gppg} .

For the definition of *poor* leptons: The poor electrons are defined as failing “Fixed-CutLoose” isolation requirement, or failing “LooseLH” electron ID requirement but satisfying “VeryLooseLH” WP. The poor muons are required to fail the “FixedCutLoose” isolation requirement or invert the impact parameter cut to be $3 < d_0/\sigma(d_0) < 10$. The dedicated $Z+jets$ and $t\bar{t}$ dominant regions are defined to calculate the fake factor respectively in the following subsections.

1. Fake factor for $Z+jets$

Fake factor for $Z+jets$ background is calculated in $Z+jets$ enriched region, where events with one OSSF lepton pair around Z mass associated with two jets are selected. The value of fake factor is driven from data, and is a function of p_T and η as shown in

2018 figure 6.3 for electrons and figure 6.4 for muons. During calculation, the contributions
 2019 from non- $Z+jets$ backgrounds ($t\bar{t}$, ZZ , WZ) have been subtracted from data. The values
 calculated directly from $Z+jets$ MC are also shown in plots for comparison.

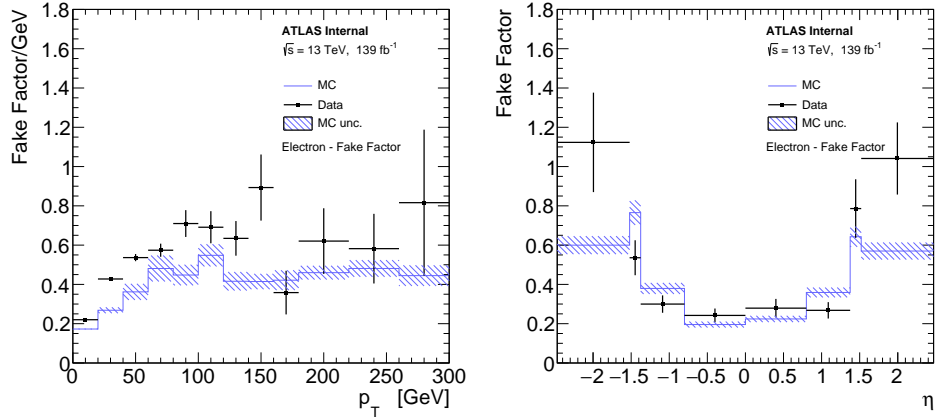


Fig. 6.3 Fake factor for $Z+jets$ background, constructed with additional electron, as a function of p_T (left) and η (right).

2020

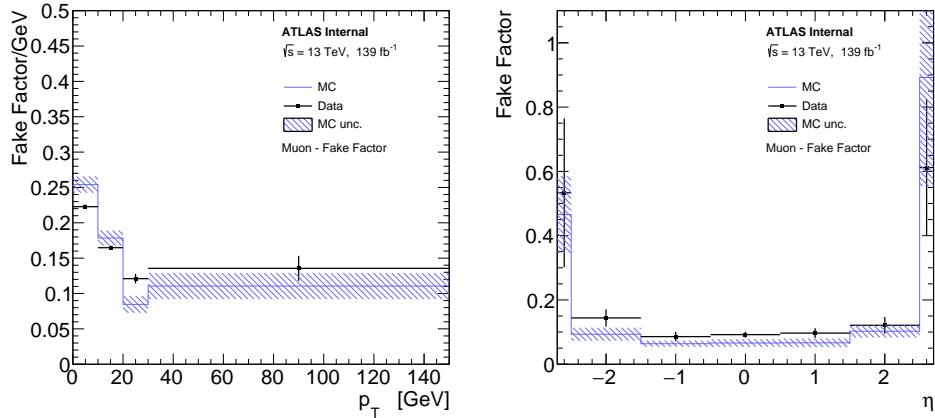


Fig. 6.4 Fake factor for $Z+jets$ background, constructed with additional muon, as a function of p_T (left) and η (right).

2021

2. Fake factor for $t\bar{t}$

2022 The fake factor for $t\bar{t}$ are calculated in $t\bar{t}$ dominant region by selecting the events that
 2023 have one $e\mu$ -pair with additional two jets. For events with three leptons, $m_T^W < 60 \text{ GeV}$ cut
 2024 is applied to reject the contribution from $t\bar{t} + W$ events. The m_T^W is defined as below:

$$m_T^W = \sqrt{2p_T^{l_3}E_T^{\text{miss}} \left[1 - \cos(\Delta\phi(p_T^{l_3}, E_T^{\text{miss}})) \right]} \quad (6.4)$$

2025 In addition, at least one b-jet is required to enhance the top component. The fake factors of
 2026 $t\bar{t}$ calculated from data as the function of p_T and η are shown in figure 6.5 for electrons and
 2027 6.6 for muons. The non- $t\bar{t}$ contributions including $Z+jets$, ZZ and WZ , are subtracted

from data.

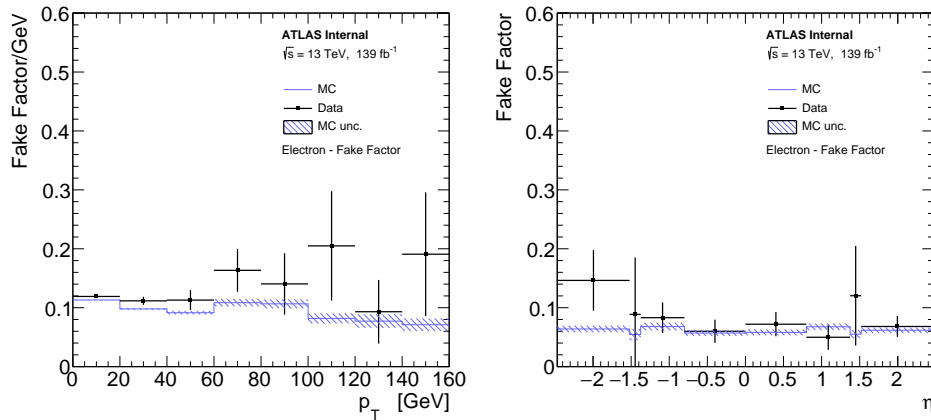


Fig. 6.5 Fake factor for $t\bar{t}$ background, constructed with additional electron, as a function of p_T (left) and η (right).

2028

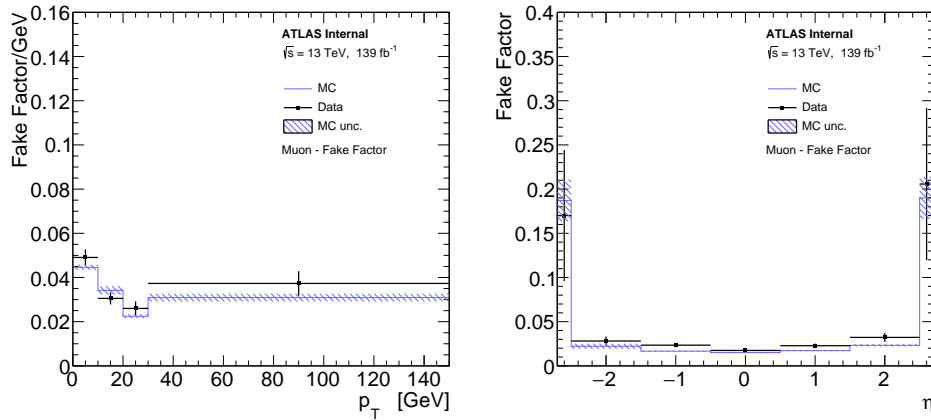


Fig. 6.6 Fake factor for $t\bar{t}$ background, constructed with additional muon, as a function of p_T (left) and η (right).

2029

3. Systematics of fake estimation and results

2030 The systematics of fake factor method can be measured by varying the parameters and
 2031 selection requirements in fake factor calculation. In addition, due to the very limited data
 2032 statistic in $\ell\ell\ell'\ell'$ channel, to be more conservative, the difference between data measure-
 2033 ment and MC simulation are also considered as additional systematics component. The
 2034 sources of systematics that have been included are listed as below:

- 2035 • Variations of isolation cut for the poor lepton definition up and down scaled by a
 2036 factor of two.
- 2037 • Variations of the yields of those subtracted MC in fake control region scaled by 30%
 2038 up and down.
- 2039 • The difference of fake factors between driven from data and from MC simulation.

- The difference of fake factors when changing to one bin measurement (instead of p_T or η dependent).
- The statistical uncertainties on fake factor in fake control region.

Table 6.5 summarizes the contribution of fake backgrounds in signal region under different systematic conditions mentioned above as well as the nominal one, together with their statistical uncertainties.

channel	4e	2e2 μ	4 μ	inclusive
Nominal estimate	0.678 ± 0.652	1.023 ± 0.740	0.566 ± 0.240	2.268 ± 1.015
F stat. uncertainty varied down	0.698 ± 0.622	0.872 ± 0.652	0.509 ± 0.214	2.079 ± 0.926
F stat. uncertainty varied up	0.657 ± 0.685	1.173 ± 0.840	0.622 ± 0.267	2.452 ± 1.116
One bin F	0.653 ± 0.590	0.594 ± 0.558	0.646 ± 0.313	1.892 ± 0.870
MC F	0.534 ± 0.471	1.415 ± 0.993	0.439 ± 0.184	2.389 ± 1.114
Isolation varied down	0.938 ± 0.686	0.552 ± 0.466	0.215 ± 0.107	1.704 ± 0.837
Isolation varied up	0.723 ± 0.646	1.104 ± 0.739	0.559 ± 0.237	2.386 ± 1.010
MC corr. varied down	0.697 ± 0.695	1.048 ± 0.811	0.832 ± 0.385	2.577 ± 1.136
MC corr. varied up	0.660 ± 0.614	0.984 ± 0.687	0.316 ± 0.159	1.961 ± 0.935

Table 6.5 Fake background estimations in the SR. For nominal value, the 2D fake factor together with the $Z+jets$ and $t\bar{t}$ combination applied. The other lines show the estimations with different uncertainty variations.

2045

2046 6.5 Systematics

2047 The analysis includes both the statistical fit to MD distribution to search the EW- $ZZjj$
 2048 process, as well as the cross section measurement of inclusive EW and QCD $ZZjj$ pro-
 2049 cess in fiducial volume. Therefore, theoretical and experimental uncertainties may affect
 2050 the predicted background yields and shapes, the correction factors from detector-level to
 2051 particle-level measurement, as well as the $ZZjj$ MD shapes and so on. Moreover, the ex-
 2052 statistical uncertainties of simulated samples are also taken into account. Due to the ex-
 2053 tremely low cross section of $\ell\ell\ell'\ell'$ channel, the analysis is still data statistic dominant.
 2054 This section describes the measurement of both theoretical and experimental systematics
 2055 for $ZZjj$ productions. The systematics for fake backgrounds have been elaborated in
 2056 section 3.

2057 6.5.1 Theoretical systematics

2058 The theoretical systematics on EW- and QCD- $ZZjj$ processes including the uncer-
 2059 tainties from PDF, QCD scale, α_S and parton showering variations are summarized in ta-

ble 6.6. The PDF uncertainty is estimated from the envelop of NNPDF internal variations and the difference between nominal and alternative PDF sets, following the PDF4LHC as introduced in section 2.2.1. The QCD scale uncertainty is estimated by varying the nominal renormalization scale (μ_R) and factorisation scale (μ_F) by a factor of 0.5 or 2.0. There are seven different configurations being considered, where the maximum of variations is chosen as final uncertainty. The parton showering uncertainty is estimated by comparing events with different parton showering setting between the nominal PYTHIA8 and the alternative HERWIG^[91-92] algorithm. The α_S uncertainty is estimated by varying the value of α_S within ± 0.001 . Due to the lack of simulation sample for alternative parton showering on QCD- $Z Z jj$ process, the value of parton showering component is taken from the measurement of EW process.

Process	EW- $Z Z jj$	QCD- $Z Z jj$
PDFs	NNPDF30lo (nominal), CT14lo	NNPDF30nnlo (nominal), MMHT2014nnlo68cl, CT14nnlo
α_S	0.118	0.117, 0.118 (nominal), 0.119
QCD scale ($[\mu_R, \mu_F]$)	[0.5,0.5], [0.5,1], [1,0.5], [1,1], [1,2], [2,1], [2,2]	[0.5,0.5], [0.5,1], [1,0.5], [1,1], [1,2], [2,1], [2,2]
Parton showering algorithm	PYTHIA8, HERWIG7	-

Table 6.6 Summary of different variations for EW- and QCD- $Z Z jj$ theoretical uncertainties measurement.

Table 6.7 summarizes the uncertainties of each theoretical components in fiducial volume of SR, while table 6.8 shows the numbers in QCD-enriched CR region. For QCD process, the uncertainty is QCD scale dominant. Both of them are taken as inputs for statistical fit.

Process	PDF (%)	α_S (%)	QCD scale (%)	Parton shower (%)
EW	+5.9 -5.9		+6.1 -5.6	+3.3 -3.3
qqQCD	+2.0 -1.0	+2.6 -2.6	+34.2 -22.8	

Table 6.7 Summary of theoretical uncertainties for the fiducial volume (SR) for both EW and QCD qq -initial processes.

Process	PDF (%)	α_S (%)	QCD scale (%)	Parton shower (%)
EW $\ell\ell\ell'\ell'$	+6.1 -6.1		+0.8 -1.1	+10.1 -10.1
qqQCD $\ell\ell\ell'\ell'$	+2.0 -1.0	+2.6 -2.6	+31.5 -22.0	

Table 6.8 Summary of theoretical uncertainties for the control region for EW and qqQCD processes.

2075 The uncertainties of QCD gg-induced process ($gg \rightarrow ZZ$) as the function of MD discriminant is shown in figure 6.7 for both fiducial volume (SR) and QCD CR.

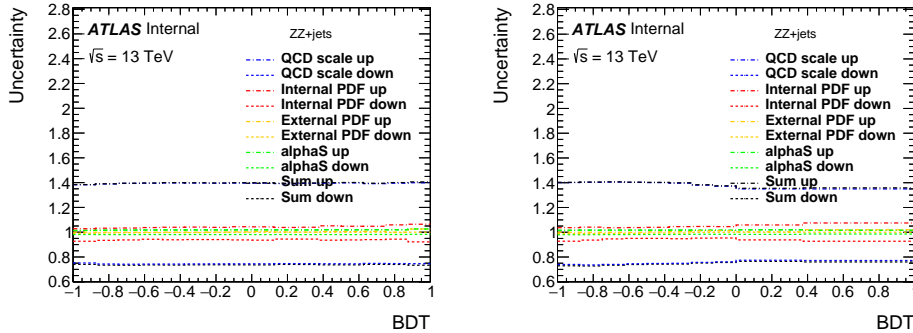


Fig. 6.7 The theoretical uncertainties for $gg \rightarrow ZZ$ background in particle-level SR (left) and CR (right).

2077 6.5.2 Experimental systematics

2078 The dominant experimental uncertainties are from the luminosity uncertainty, the mo-
 2079 mentum scale and resolution of leptons and jets, as well as the lepton reconstruction and
 2080 selection efficiency. Some smaller uncertainties, such as trigger efficiency and pile-up
 2081 correction, are also considered. Table 6.9 lists the major systematic components from
 2082 leptons and jets for signal and major background processes in $\ell\ell\ell'\ell'$ channel. The to-
 2083 tal uncertainties for sources from electron, muon and jet respectively, as well as the sum
 2084 (quadratic sum) of them are also summarized in this table.

name	EW- $Z Z jj$	QCD qq -initial	QCD gg
nominal yield	20.61	76.69	13.10
EG_RESOLUTION_ALL	$\pm^{0.00\%}_{0.03\%}$	$\pm^{0.02\%}_{0.04\%}$	$\pm^{0.01\%}_{1.41\%}$
EG_SCALE_ALL	$\pm^{0.03\%}_{0.05\%}$	-0.04%	$\pm^{0.01\%}_{0.06\%}$
EL_EFF_ID_TOTAL_1NPCOR_PLUS_UNCOR	$\pm^{2.66\%}_{2.58\%}$	$\pm^{2.60\%}_{2.53\%}$	$\pm^{2.65\%}_{2.57\%}$
EL_EFF_Iso_TOTAL_1NPCOR_PLUS_UNCOR	$\pm 0.70\%$	$\pm 0.47\%$	$\pm 0.42\%$
EL_EFF_Reco_TOTAL_1NPCOR_PLUS_UNCOR	$\pm 0.55\%$	$\pm 0.55\%$	$\pm 0.63\%$
JET_EtaIntercalibration_NonClosure	-0.01%	-0.03%	0%
JET_GroupedNP_1	$\pm 1.97\%$	$\pm^{11.82\%}_{10.14\%}$	$\pm^{16.21\%}_{12.92\%}$
JET_GroupedNP_2	$\pm 0.23\%$	$\pm 1.26\%$	+5.3%
JET_GroupedNP_3	$\pm 0.55\%$	$\pm 2.94\%$	$\pm^{3.14\%}_{0.12\%}$
JET_JER_SINGLE_NP	0.11%	+5.47%	+6.31%
JET_JvtEfficiency	$\pm 0.04\%$	$\pm 0.12\%$	$\pm 0.15\%$
MUON_EFF_ISO_STAT	$\pm 0.09\%$	$\pm 0.08\%$	$\pm 0.07\%$
MUON_EFF_ISO_SYS	$\pm 0.54\%$	$\pm 0.55\%$	$\pm 0.56\%$
MUON_EFF_RECO_STAT	$\pm 0.15\%$	$\pm 0.19\%$	$\pm 0.15\%$
MUON_EFF_RECO_STAT_LOWPT	$\pm 0.06\%$	$\pm 0.02\%$	$\pm 0.03\%$
MUON_EFF_TTVA_STAT	$\pm 0.06\%$	$\pm 0.07\%$	$\pm 0.06\%$
MUON_EFF_TTVA_SYS	$\pm 0.03\%$	$\pm 0.4\%$	$\pm 0.03\%$
MUON_ID	$\pm 0.03\%$	$\pm 0.02\%$	<0.001%
MUON_MS	-0.05%	$\pm^{0.04\%}_{0.01\%}$	<0.001%
MUON_SAGITTA_RESBIAS	$\pm 0.01\%$	$\pm 0.02\%$	<0.001%
MUON_SAGITTA_RHO	+1.13%	-0.73%	$\pm 1.00\%$
MUON_SCALE	$\pm 0.02\%$	$\pm^{0.03\%}_{0.02\%}$	<0.001%
PRW_DATASF	$\pm 0.5\%$	$\pm^{0.42\%}_{1.02\%}$	$\pm^{2.17\%}_{1.46\%}$
Electron Exp.	$\pm^{2.8\%}_{2.7\%}$	$\pm^{2.70\%}_{2.62\%}$	$\pm^{2.75\%}_{2.64\%}$
Muon Exp.	$\pm 1.3\%$	$\pm 1.3\%$	$\pm 1.04\%$
Jet Exp.	$\pm 2.0\%$	$\pm^{13.39\%}_{10.64\%}$	$\pm^{18.54\%}_{13.57\%}$
Total experimental uncertainties	$\pm^{3.7\%}_{4.0\%}$	$\pm^{13.72\%}_{11.11\%}$	$\pm^{18.90\%}_{13.57\%}$

Table 6.9 Experimental systematic uncertainties in $\ell\ell\ell'\ell'$ channel with the luminosity of 139 fb^{-1} . The “Electron Exp.”, “Muon Exp.” and “Jet Exp.” represent the quadrature of the respective sources from electron, muon, and jets.

2085 In addition, the uncertainty of the combined 2015 to 2018 integrated luminosity is
 2086 1.7%^[93] in ATLAS experiment, obtained using the LUCID-2 detector^[94] for the primary
 2087 luminosity measurements.

2088 On top of them, a systematic uncertainty for MD distribution with different pile-up
 2089 ($\langle\mu\rangle$) is also considered for QCD- $Z Z jj$ background by comparing the distributions be-

tween events with low and high pile-up conditions. A boundary of $\langle\mu\rangle = 33$ is used to defined low/high pile-up according to the average $\langle\mu\rangle$ for signal (about 34.5) and QCD background (about 33). Figure 6.8 shows the MD distribution in SR (left) and QCD CR (right) in two different PU conditions, the difference as function of MD is then taken into account as additional shape uncertainty for statistical fit.

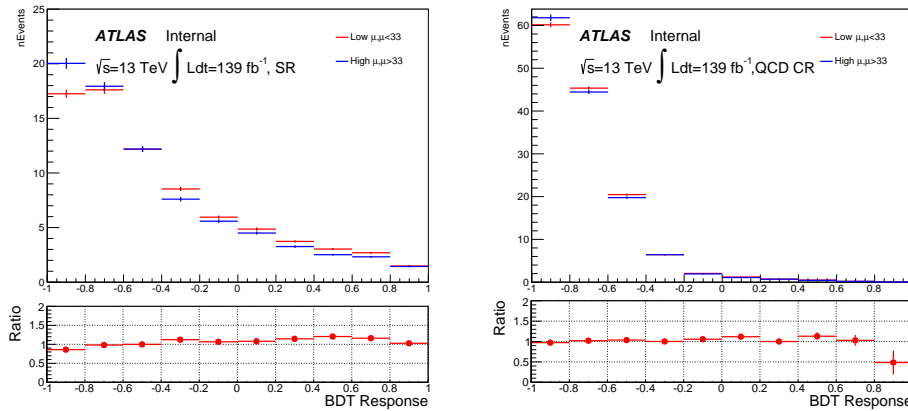


Fig. 6.8 MD distribution for QCD- $Z Z jj$ process in low and high pile-up events for SR (left) and CR (right).

Moreover, a conservative uncertainty is assigned to QCD- $Z Z jj$ process by comparing the sample modelled by SHERPA generator (nominal) with MADGRAPH5_aMC@NLO. The MD shape difference for both SR (left) and QCD CR (right) are shown in figure 6.9. The modelling uncertainty is then calculated from the envelop between nominal and alternative samples as function of MD as one additional shape uncertainty.

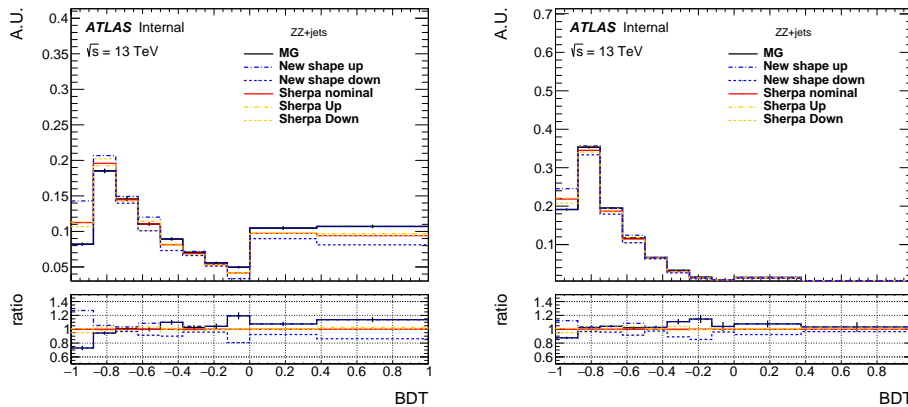


Fig. 6.9 MD shape difference for QCD $q\bar{q} \rightarrow ZZ$ background between different SHERPA theoretical uncertainties and sample from MADGRAPH5_aMC@NLO on SR (left) and CR (right).

2100 6.6 Measurement of fiducial cross section

2101 The fiducial cross section for inclusive $Z Z j j$ production, including both EW and
 2102 QCD components, is then measured. The definition of fiducial volume, which is used for
 2103 cross section measurement, follows closely to the detector-level selection but use physics
 2104 objects at particle-level, which are reconstructed in simulation from stable final-state par-
 2105 ticles, prior to their interactions with the detector.

2106 For electrons and muons, QED final-state radiation is for the most part recovered by
 2107 adding the four-momenta of surrounding photons that are not originating from hadrons
 2108 and within an angular distance $\Delta R < 0.1$ to the lepton four-momentum, called lepton
 2109 “dressing” at truth level. Particle-level jets are built with anti- k_T algorithm with radius
 2110 parameter $R = 0.4$ using all final-state particles except leptons and neutrinos as inputs.
 2111 Comparing to the events selection at detector-level in section 6.3, at particle-level, the se-
 2112 lected dilepton pair mass required is relaxed to be within 60 to 120 GeV for the reasons
 2113 of reducing the migration effect, as well as being more compatibility with CMS publica-
 2114 tion^[78]. All other kinematic selections are the same as the definition at detector-level.

2115 6.6.1 Calculation of C-factor

2116 C-factor is defined as the ratio between the number of selected events at detector-level
 2117 and the number of particle-level events in fiducial volume (FV):

$$C = \frac{N_{\text{detector-level}}}{N_{\text{FV}}} \quad (6.5)$$

2118 The value of C-factor for each $Z Z j j$ process are calculated from each individual simula-
 2119 tion samples as listed in table 6.10 together with their systematics.

Process	C	ΔC (stats.)	ΔC (sys.)	ΔC (theo.)
EWK $Z Z j j$	0.663	± 0.002	$\pm^{0.032}_{0.031}$	NA
QCD $q\bar{q} \rightarrow Z Z$	0.702	± 0.003	$\pm^{0.061}_{0.051}$	$\pm^{0.015}_{0.018}$
QCD $gg \rightarrow Z Z$	0.741	± 0.021	$\pm^{0.143}_{0.072}$	± 0.002

Table 6.10 C Factor of different $Z Z j j$ processes.

2120 Then the C from different processes are combined together to be used as inputs for
 2121 cross section calculation:

$$C = \sum_i \frac{N_{\text{FV}}^i}{\sum_j N_{\text{FV}}^j} \times C_i = 0.699 \pm 0.003(\text{stats.}) \pm^{0.011}_{0.013} (\text{theo.}) \pm 0.028(\text{exp.}) \quad (6.6)$$

2122 The stats. refers to the statistical uncertainty from MC simulation statistics. The theo. and

2123 exp. denote the theoretical and experimental uncertainties described in section 6.5.

2124 **6.6.2 Result of fiducial cross section**

2125 The cross section in fiducial volume is computed as:

$$\sigma^{FV} = \frac{N_{data} - N_{bkg}}{C \times Lumi} \quad (6.7)$$

2126 where N_{data} and N_{bkg} denote the number of events selected from detector-level selection
2127 from data and sum of backgrounds, and C is the C-factor calculated above, Lumi represents
2128 the integrated luminosity of data from 2015 to 2018 of 139 fb^{-1} . Table 6.11 shows the
2129 fiducial cross section for $\ell\ell\ell'\ell'$ final state measured from equation 6.7, as well as the
2130 predicted cross section measured from MC simulation directly.

Measured fiducial σ [fb]	Predicted fiducial σ [fb]
$1.27 \pm 0.12(\text{stat}) \pm 0.02(\text{theo}) \pm 0.07(\text{exp}) \pm 0.01(\text{bkg}) \pm 0.03(\text{lumi})$	$1.14 \pm 0.04(\text{stat}) \pm 0.20(\text{theo})$

Table 6.11 Measured and predicted fiducial cross-sections in $\ell\ell\ell'\ell' jj$ final-state. Uncertainties due to different sources are presented.

2131 The measured cross section has a total uncertainty of 11%, and is found to be compat-
2132 ible with SM prediction. This measurement is still dominant by data statistic.

2133 **6.7 Search for EW- $ZZjj$**

2134 **6.7.1 MD discriminant**

2135 To further separate the EW- $ZZjj$ component from QCD- $ZZjj$, a MD based on
2136 Gradient Boosted Decision Tree (BDT) algorithm^[95] is trained with simulated events
2137 via TMVA framework^[69]. Training is performed between EW (signal) and QCD (back-
2138 ground) processes. Twelve event kinematic variables sensitive to the characteristics of the
2139 EW signal are used as input features in training. Table 6.12 lists those input variables with
2140 the order of their importance in BDT response provided by TMVA tool. One can see the
2141 jet-related information provides larger sensitivity. Then the MD distributions in both SR
2142 and QCD CR region are used for statistical fit.

2143 **6.7.2 Fitting procedure**

2144 A profile likelihood fit is performed on MD discriminant to extract the EW- $ZZjj$
2145 signal from backgrounds. The binning of MD distributions in SR is optimized to maximize

Rank	Variables	Description
1	m_{jj}	Dijet invariant mass
2	p_T^{j1}	p_T of the leading jet
3	p_T^{j2}	p_T of the sub-leading jet
4	$\frac{p_T(ZZjj)}{H_T(ZZjj)}$	p_T of the $Z Z jj$ system divided by the scalar p_T sum of Z bosons and two jets
5	$y_{j1} \times y_{j2}$	Product of jet rapidities
6	Δy_{jj}	Rapidity difference between two jets
7	Y_{Z2}^*	Rapidity of the second Z boson
8	Y_{Z1}^*	Rapidity of the Z boson reconstructed from the lepton pair with the mass closer to the Z boson mass
9	p_T^{ZZ}	p_T of 4l system
10	m_{ZZ}	Invariant mass of 4l system
11	p_T^{Z1}	p_T of the Z boson reconstructed from the lepton pair with the mass closer to the Z boson mass
12	$p_T^{\ell3}$	p_T of the third lepton

Table 6.12 Input features for the training of MD.

the sensitivity for detecting EW signal. The normalization of QCD- $Z Z jj$ production (μ_{QCD}^{III}) in $\ell\ell\ell'\ell'$ channel is determined by data from simultaneously fit in SR and QCD CR as described in section 6.4. The signal strength of EW- $Z Z jj$ production (μ_{EW}) is taken as parameter of interest and floated in the fit. The effects of the uncertainties related to normalizations and shapes described previously in section 6.5 of background processes in the MD distribution are all taken into account.

In most case, a common nuisance parameter is used for each source of systematic in all bins and all categories. The statistical uncertainties for simulated samples are uncorrelated among all bins, and the background uncertainties only applied to their corresponding backgrounds. Furthermore, to be more conservative, the generator modelling uncertainty for QCD- $Z Z jj$ production mentioned in section 6.5 is separated to be two nuisance pa-

2157 parameters in low and high MD region.

2158 **6.7.3 Result of fit**

2159 The results of fitting to $\ell\ell\ell'\ell'$ final state are presented in table 6.13. To drive expected
 2160 results, the observed data is used for QCD CR to extract normalization factor of QCD
 2161 component (μ_{QCD}^{III}), while in SR, asimov data built from background prediction and signal
 2162 model with SM assumed cross section is used.

	μ_{EW}	$\mu_{QCD}^{\ell\ell\ell'jj}$	Significance Obs. (Exp.)
$\ell\ell\ell'jj$	1.54 ± 0.42	0.95 ± 0.22	$5.48 (3.90) \sigma$

Table 6.13 Observed μ_{EW} and $\mu_{QCD}^{\ell\ell\ell'jj}$, as well as the observed and expected significance from the individual $\ell\ell\ell'\ell'$ channel. The full set of systematic uncertainties are included.

2163 As a conclusion, the background-only hypothesis is rejected at 5.5σ (3.9σ) for ob-
 2164 served (expected) data, which leads to the observation of EW- $ZZjj$ production.

2165 Figure 6.10 shows the post-fit MD distributions for $\ell\ell\ell'\ell'$ channel in SR (left) and
 2166 QCD CR (right). The EW- $ZZjj$ cross section measured in $\ell\ell\ell'\ell'$ channel is extracted
 to be 0.94 ± 0.26 fb.

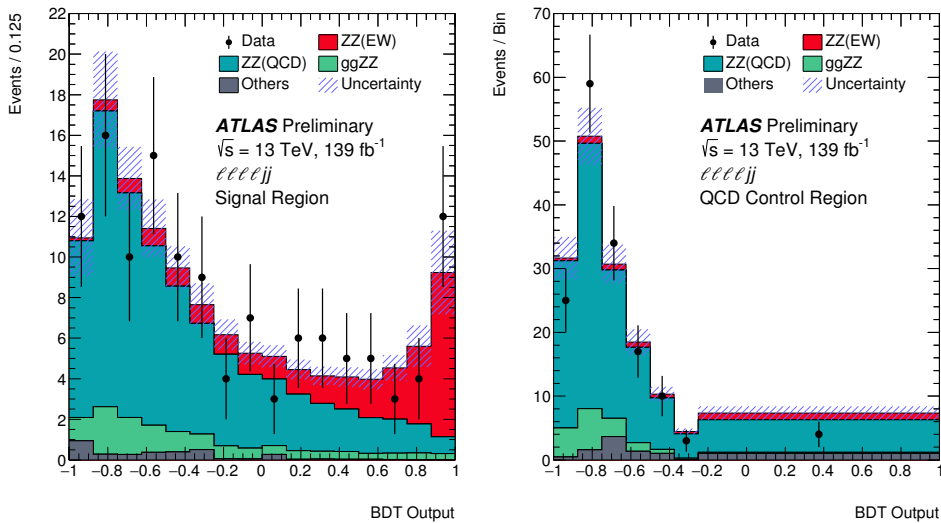


Fig. 6.10 Observed and post-fit expected multivariate discriminant distributions after the statistical fit in the $\ell\ell\ell'\ell'$ SR (left) and QCD CR (right). The error bands include the experimental and theoretical uncertainties, as well as the uncertainties in μ_{EW} and $\mu_{QCD}^{\ell\ell\ell'jj}$. The error bars on the data points show the statistical uncertainty on data.

2167

2168 Figure 6.11 shows the m_{jj} distribution in SR (left) and QCD CR (right), where the
 2169 normalization of EW and QCD processes are scaled according to their observed value in
 2170 table 6.13. High m_{jj} region is more sensitive for EW- $ZZjj$ events detection from this

2171 figure. Figure 6.12 shows the spectrum of invariant mass of $\ell\ell\ell'\ell'$ system (m_{ZZ}) in SR
 2172 also with the normalization of EW and QCD processes scaled.

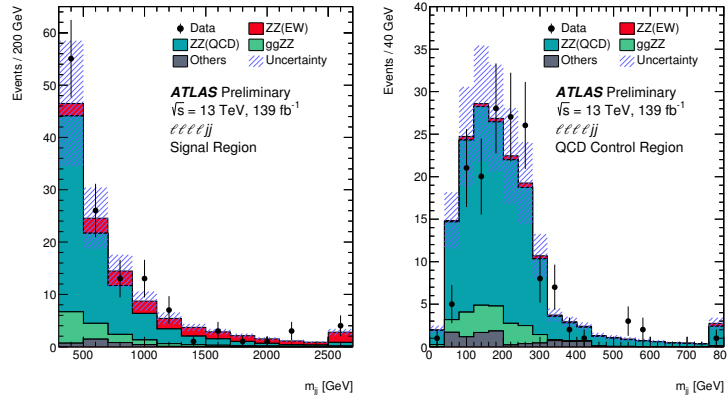


Fig. 6.11 Observed and post-fit expected m_{jj} distributions in SR (left) and QCD CR (right). The error bands include the expected experimental and theoretical uncertainties. The error bars on the data points show the statistical uncertainty. The contributions from the QCD and EW production of $Z Z jj$ events are scaled by 0.96 and 1.35, respectively, corresponding to the observed normalization factors in the statistical fit. The last bin includes the overflow events.

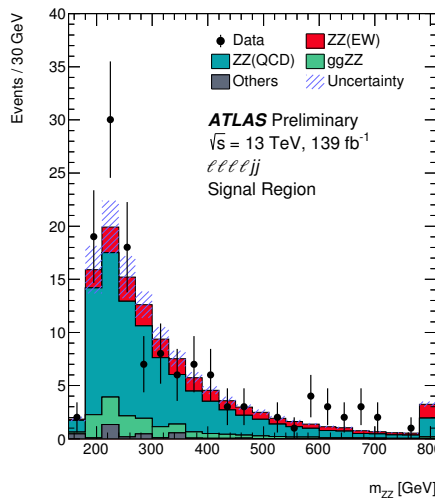


Fig. 6.12 Observed and post-fit expected m_{ZZ} spectrum in SR. The error bands include the expected experimental and theoretical uncertainties. The error bars on the data points show the statistical uncertainty. The contributions from the QCD and EW production of $Z Z jj$ events are scaled by 0.96 and 1.35, respectively, corresponding to the observed normalization factors in the statistical fit. The last bin includes the overflow events.

2173 Figure 6.13 is the display of one event candidate of EW- $Z Z jj$ production in $2e2\mu$
 2174 final state with two jets in forward and backward region.

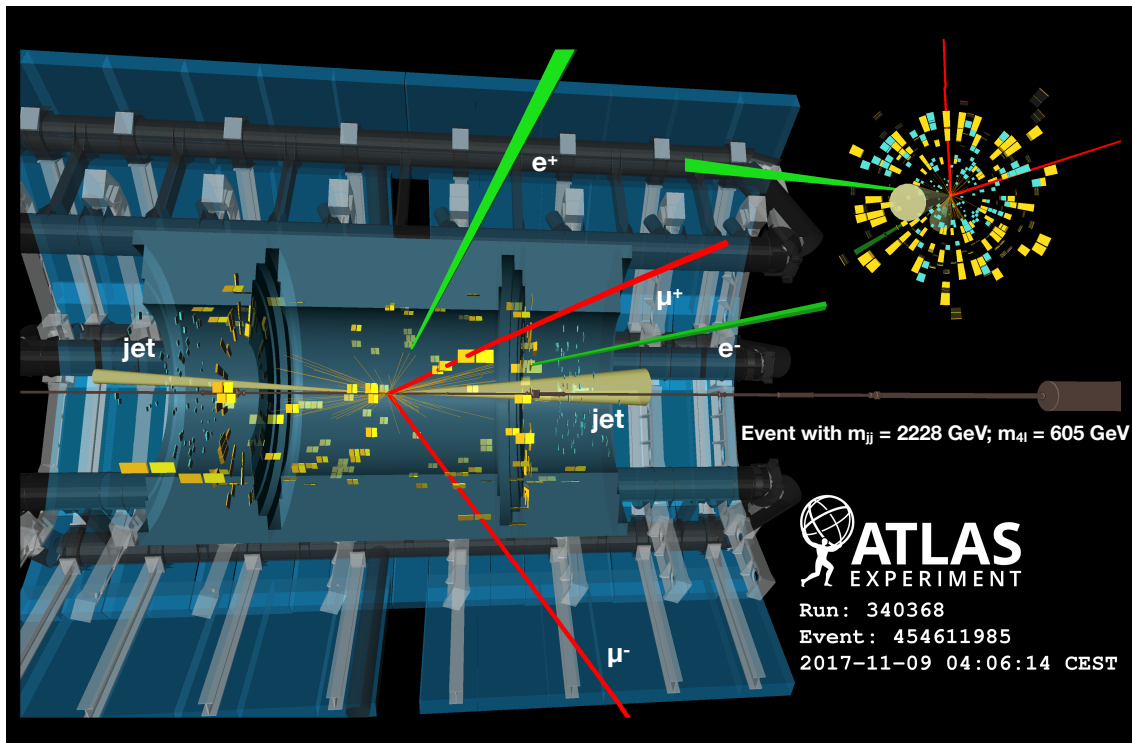


Fig. 6.13 Display of an event candidate of EW- $Z Z jj$ production in $2e2\mu$ channel in last MD bin ($0.875 < \text{MD} < 1.0$). The invariant mass of the di-jet (four-lepton) system is 2228 (605) GeV.

2175 6.8 Prospect study of EW- $Z Z jj$ production in HL-LHC

2176 The High-Luminosity Large Hadron Collider (HL-LHC) project aims to increase the
 2177 luminosity by a factor of 10 beyond the LHC's design value to increase the potential for
 2178 discoveries after 2025. The expected luminosity will reach 3000 fb^{-1} with the centre-of-
 2179 mass energy of 14 TeV.

2180 As introduced in previous sections, with full run-2 data of 139 fb^{-1} collected by AT-
 2181 LAS detector at the LHC, the EW- $Z Z jj$ production is the last channel of observation for
 2182 VBS processes with massive bosons due to its very low cross section in $Z Z$ channel. So
 2183 we expect that this channel will benefit significantly from the increased luminosity at the
 2184 HL-LHC, and can be studied in great details for this known mechanism.

2185 In this section, a prospective study is performed for EW- $Z Z jj$ production at the HL-
 2186 LHC in the $\ell\ell\ell'\ell'$ channel. The study uses 3000 fb^{-1} of simulated pp collision data at a
 2187 centre-of-mass energy of 14 TeV as expected to be recorded by the ATLAS detector at the
 2188 HL-LHC. All simulated events are produced at particle-level, and the detector effects of
 2189 leptons and jets reconstruction and identification are estimated by corrections assuming
 2190 the mean number of interactions per bunch crossing ($\langle\mu\rangle$) of 200.

2191 6.8.1 The ATLAS detector at HL-LHC

2192 As the expectation of HL-LHC, the new Inner Tracker (ITk)^[96] will extend the tracking
2193 acceptance capability of ATLAS detector to pseudorapidity ($|\eta|$) up to 4.0. By including
2194 a forward muon trigger, the upgraded Muon Spectrometer^[97] is also expected to provide
2195 muon identification capabilities to $|\eta|$ up to 4.0. In addition, the new high granularity tim-
2196 ing detector (HGTD)^[98] designed to mitigate the pile-up (PU) effects is also expected to be
2197 installed in the forward region of $2.4 < |\eta| < 4.0$. More details of expected performance
2198 of the upgraded ATLAS detector at the HL-LHC has been reported in Ref.^[99].

2199 6.8.2 Simulation

2200 The analysis is performed using particle-level events. The samples are generated at
2201 $\sqrt{s} = 14$ TeV. The signal in this analysis is EW- $ZZjj$ process, while only the domi-
2202 nant irreducible background of QCD- $ZZjj$ is considered. Both signal and background
2203 are generated using SHERPA with the NNPDF3.0NNLO PDF set. The signal sample is
2204 modelled with two jets at Matrix Element (ME) level. The background is generated with
2205 up to one (three) outgoing partons at NLO (LO) in pQCD. As a quick study, other minor
2206 backgrounds such as fake backgrounds from $Z+jets$ and top-quark processes, as well as
2207 Diboson without 4l final-state and Triboson processes are not considered in this analysis.
2208 Furthermore, for hard scattering events, the pile-up collisions are set with a mean value of
2209 200 interactions per bunch crossing. Signal and background yields are then scaled to an
2210 integrated luminosity of 3000 fb^{-1} as expected at the HL-LHC.

2211 6.8.3 Event selection

2212 The analysis selection follows closely to the one in ATLAS run-2 analysis as described
2213 in section 6.3. Here are some changes according to the expectation of the HL-LHC sce-
2214 nario for ATLAS detector:

- 2215 • Extend the lepton (both electron and muon) identification to $|\eta| < 4.0$
2216 • Pile-up (PU) jet suppression is applied with a PU rejection factor of 50 for all PU
2217 jets in the region of $|\eta| < 3.8$, based on the expected ATLAS detector performance
2218 at the HL-LHC.
2219 • The jets are required to have $p_T > 30$ (70) GeV in the $|\eta| < 3.8$ ($3.8 < |\eta| < 4.5$)
2220 region.
2221 • For two selected jets, tighten the m_{jj} requirement to be $m_{jj} > 600$ GeV, and require
2222 $\Delta\eta_{jj} > 2$.

2223 In addition, a fiducial volume, used to study the expected precision of the cross-section

2224 measurements, is defined at particle-level with the same kinematic requirements listed
2225 above.

2226 Table 6.14 summarized the number of selected signal and background events nor-
2227 malized to 3000 fb^{-1} . In addition to the *baseline* selection listed above, to compare the
2228 different detector scenarios at the HL-LHC, two alternative selections are also studied:

- 2229 1. Reduce the lepton η region to 2.7, to understand the effect due to forward lepton
2230 reconstruction and identification with the upgraded ATLAS detector.
2231 2. Only apply the PU jet suppression with region $|\eta| < 2.4$, to measure the improve-
2232 ment of *baseline* by extending the rejection range of PU jets at the HL-LHC with
2233 the installation of HGTD.

Selection	$N_{\text{EW-ZZjj}}$	$N_{\text{QCD-ZZjj}}$	$N_{\text{EW-ZZjj}} / \sqrt{N_{\text{QCD-ZZjj}}}$
Baseline	432 ± 21	1402 ± 37	11.54 ± 0.58
Leptons with $ \eta < 2.7$	373 ± 19	1058 ± 33	11.46 ± 0.62
PU jet suppression only in $ \eta < 2.4$	536 ± 23	15470 ± 120	4.31 ± 0.19

**Table 6.14 Comparison of event yields for signal ($N_{\text{EW-ZZjj}}$) and background ($N_{\text{QCD-ZZjj}}$) pro-
cesses, and expected significance of EW- $Z Z jj$ processes, normalized to 3000 fb^{-1}
data at 14 TeV, with baseline and alternative selections. Uncertainties in the table
refer to expected data statistical uncertainty at 14 TeV with 3000 fb^{-1} .**

2234 From this table, one can see the extended track coverage increases the $\ell\ell\ell'\ell' jj$ events
2235 by 15 to 30%, via improving the lepton efficiency. But the significance of searching for
2236 EW- $Z Z jj$ process does not improve so much due to the large increment of background
2237 events.

2238 Figure 6.14 shows the kinematic distributions of di-jet invariant mass (m_{jj}), the $Z Z$
2239 invariant mass (m_{ZZ}) and the ϕ separation of two Z bosons ($|\Delta\phi(Z Z)|$) as well as the
2240 centrality of the $Z Z$ system. The $Z Z$ centrality is defined as:

$$Z Z \text{ centrality} = \frac{|y_{ZZ} - (y_{j1} + y_{j2})/2|}{|y_{j1} - y_{j2}|} \quad (6.8)$$

2241 To measure the event yield, the top panel shows the stack distribution for EW- and QCD-
2242 $Z Z jj$ processes, while bottom panel is the ratio between two processes.

2243 6.8.4 Systematics

2244 According to studies in section 6.5, the dominant systematic in $\ell\ell\ell'\ell'$ channel is from
2245 theoretical systematic for QCD- $Z Z jj$ background process. Different sizes of systematics
2246 have been studied, at a factor of 5, 10 and 30% on background modelling. The 5% un-

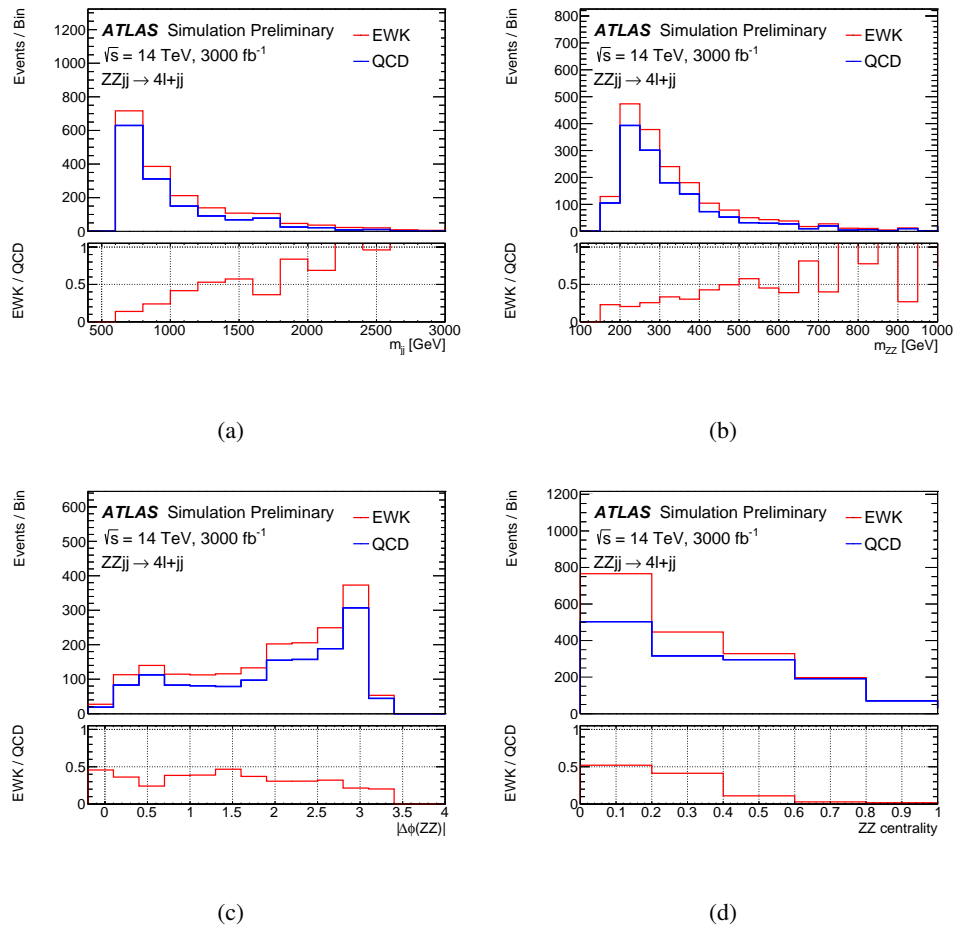


Fig. 6.14 Detector-level distributions of EW- and QCD- $Z Z_{jj}$ processes with selected events in defined phase space at 14 TeV of (a) m_{jj} , (b) m_{ZZ} , (c) $|\Delta\phi(ZZ)|$, (d) ZZ centrality, normalized to 3000 fb^{-1} .

certainty is an optimal estimation when there is enough data events from QCD-enriched control region at the HL-LHC that can be used to constrain the theoretical normalization on QCD- $Z Z_{jj}$ process. The 30% one is a conservative estimation, in which the uncertainties are directly calculated from different PDF sets and QCD renormalization and factorization scales, following recommendation from the PDF4LHC mentioned in section 6.5.

For experimental sources, the jet systematics have been checked following the setting provided by the HL-LHC in Ref.^[99], and the uncertainties are within 5% level, which is smaller than run-2 measurement at 10%. Figure 6.15 depicts the up and down variations for jet uncertainty provided by the HL-LHC performance tool as function of dijet invariant mass (m_{jj}). Therefore, a conservative 5% uncertainty is used as experimental uncertainty.

Since the final result relies greatly on the uncertainties, especially the theoretical uncertainties on QCD- $Z Z_{jj}$ production. So results with different uncertainty conditions

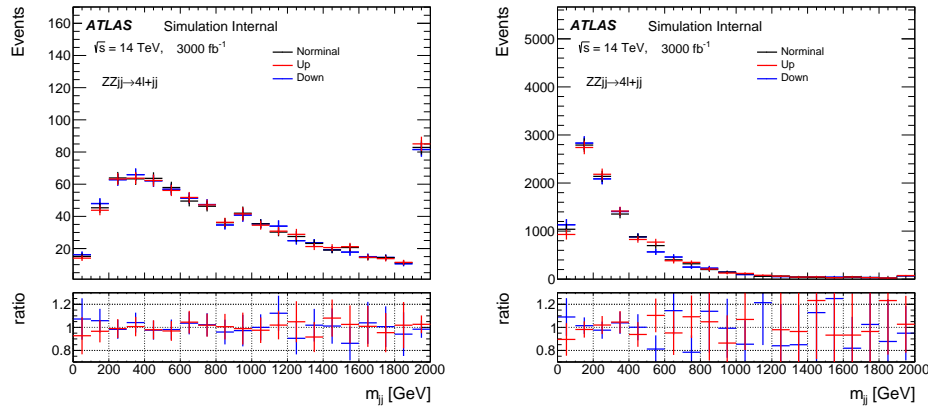


Fig. 6.15 Jet variations on m_{jj} distribution for EW- $Z Z jj$ (left) and QCD- $Z Z jj$ (right) processes with luminosity of 3000 fb^{-1} at 14 TeV. Upgrade Performance Function is used to extract the uncertainties with *baseline* setting.

are shown as below:

- The case with statistical uncertainty of simulated samples only.
- The case with statistical and experimental uncertainties (5%)
- The case with statistical, experimental and additional theoretical uncertainties at 5%, 10% and 30% levels respectively.

Three different sources of uncertainties are treated as uncorrelated and summed up quadratically.

6.8.5 Results

In this analysis, instead of a statistical fit, the expected significance of EW- $Z Z jj$ production is calculated as:

$$\text{Significance} = \frac{S}{\sqrt{\sigma(B)_{stat.}^2 + \sigma(B)_{syst.}^2}}, \quad (6.9)$$

where S presents the number of selected signal events, and $\sigma(B)_{stat.}$ and $\sigma(B)_{syst.}$ denote the statistical and systematic (exp. + theo.) uncertainties from background processes. The statistical uncertainty is computed from expected data yield with an integrated luminosity of 3000 fb^{-1} .

Based on baseline selection of $m_{jj} > 600 \text{ GeV}$, an additional scan over different m_{jj} cuts is also performed with a step of 50 GeV under different systematic conditions, as shown in figure 6.16.

In addition, the expected differential cross section of EW- $Z Z jj$ process is measured in the defined phase space at 14 TeV, as a function of m_{ZZ} and m_{jj} , shown in figure 6.17.

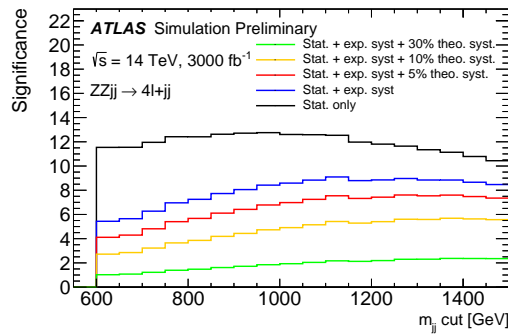


Fig. 6.16 The expected significance of EW- $Z Z_{jj}$ processes as a function of different m_{jj} cut with 3000 fb^{-1} , under conditions of different sizes of theoretical uncertainties on the QCD- $Z Z_{jj}$ background modelling. The statistical uncertainty is estimated from expected data yield at 14 TeV with 3000 fb^{-1} . Different uncertainties are summed up quadratically.

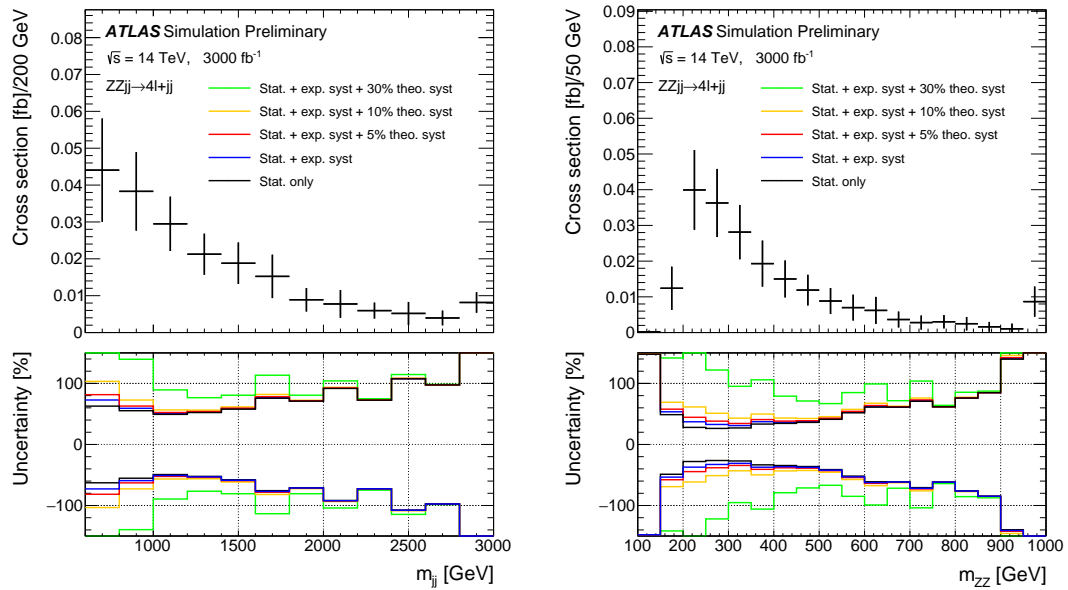


Fig. 6.17 The projected differential cross-sections at 14 TeV for the EW- $Z Z_{jj}$ processes as a function of m_{jj} (left) and m_{ZZ} (right). The top panel shows measurement with statistical only case, where statistical uncertainty is estimated from expected data yield at 14 TeV with 3000 fb^{-1} . The bottom panel shows impact of different sizes of systematic uncertainties.

2279 The expected differential cross sections are calculated as:

$$\sigma = \frac{N_{pseudo-data} - N_{QCD-ZZjj}}{L * C_{EW-ZZjj}} \quad (6.10)$$

$$C_{EW-ZZjj} = \frac{N_{EW-ZZjj}^{det.}}{N_{EW-ZZjj}^{part.}}$$

2280 where $N_{pseudo-data}$ denotes the expected number of data events with 3000 fb^{-1} luminosity
 2281 at 14 TeV, and $N_{QCD-ZZjj}$ and $N_{EW-ZZjj}$ are the number of predicted events of QCD-
 2282 $ZZjj$ and EW- $ZZjj$ processes in particle-level. The $C_{EW-ZZjj}$ factor represents the
 2283 detector efficiency for EW- $ZZjj$ processes introduced in section 6.6.1. The interference
 2284 between EW- and QCD- $ZZjj$ processes is ignored due to its minor contribution.

2285 The value of expected integrated cross section as well as its uncertainty under different
 2286 systematic conditions are shown in table 6.15 with 3000 fb^{-1} luminosity at 14 TeV. The
 2287 statistical uncertainty is at 10% level when with such large luminosity. The result is dom-
 2288 inated by systematics and can reach 100% level when theoretical modelling uncertainty is
 30% for QCD- $ZZjj$ processes.

	Cross section [fb]	Stat. only	Plus exp.	Plus 5% theo.	Plus 10% theo.	Plus 30% theo.
EW- $ZZjj$	0.21	± 0.02	± 0.04	± 0.05	± 0.08	± 0.21

Table 6.15 Summary of expected cross-section measured with different theoretical uncertainties. The statistical uncertainty is computed from expected data yield with 3000 fb^{-1} at 14 TeV. Different uncertainties are treated as uncorrelated and summed quadratically.

2289

2290 **6.9 Conclusion**

2291 The fiducial cross section for inclusive $ZZjj$ production is measured in this section,
2292 with a total relative uncertainty of 11% for the $\ell\ell\ell'\ell'$ final state, and found to be com-
2293 patible with the SM prediction. The observation of electroweak production of two jets in
2294 association with a Z -boson pair decay to $\ell\ell\ell'\ell'$ final state using 139 fb^{-1} of 13 TeV pp
2295 collision data collected by ATLAS experiment at the LHC is presented in this section.
2296 The search for electroweak production of two jets in association with a Z -boson pair is
2297 based on multivariate discriminants (MD) to enhance the separation between the signal
2298 and backgrounds. In $\ell\ell\ell'\ell'$ final state, the background-only hypothesis is rejected with
2299 an observed (expected) significance of 5.5 (3.9) σ , which gives the first observation of
2300 electroweak production in $ZZjj$ channel.

2301 In addition, the prospective study for the EW- $ZZjj$ production at the HL-LHC in
2302 the $\ell\ell\ell'\ell'$ channel, using 3000 fb^{-1} simulated pp collision data at a centre-of-mass
2303 energy of 14 TeV has been presented. The precision of the expected measurements of the
2304 integrated and differential cross sections as a function of dijet or $\ell\ell\ell'\ell'$ invariant mass are
2305 shown. Under the assumption of theoretical uncertainty for the QCD- $ZZjj$ processes and
2306 experimental uncertainty for jets being constraint at 5% level respectively, with statistical
2307 uncertainty in 3000 fb^{-1} being considered, the observation of the EW- $ZZjj$ process can
2308 reach a significance of 7 σ .

2309 **Chapter 7 Search for heavy resonances decaying into**
2310 **a pair of Z bosons in $\ell\ell\ell'\ell'$ final state using pp**
2311 **collision data collected by ATLAS detector from 2015 to**
2312 **2018**

2313 **7.1 Introduction**

2314 A new particle was discovered by the ATLAS and CMS Collaborations at the LHC^[3-4]
2315 in 2012. Both two experiments have confirmed that the properties including spin, cou-
2316 plings and parity of this new particle are consistent with Higgs boson predicted in the
2317 Standard Model (SM), which is an important milestone in understanding of the mecha-
2318 nism of EWSB. Nevertheless, the possibility that this newly discoved particle is just a part
2319 of the extended Higgs sector as predicted by various extensions in the SM cannot be ruled
2320 out. There are many models predicted the existence of new heavy resonances decaying
2321 into dibosons, such as a heavy spin-0 neutral Higgs boson^[100] and the two-Higgs-doublet
2322 models (2HDM)^[6], as well as the spin-2 Kaluza–Klein (KK) excitations of the graviton
2323 (G_{KK})^[101].

2324 Though with smaller branching ratio comparing to semileptonic or fully hadronic de-
2325 cay channels, the $\ell\ell\ell'\ell'$ final state has its unique sensitivity in mass range smaller than
2326 1 TeV region due to its good mass resolution and relative smaller experimental and the-
2327 oretical systematics. This section presents the search for heavy resonance decaying into
2328 a pair of Z bosons to the $\ell\ell\ell'\ell'$ final state, in which ℓ denotes to either an electron
2329 or a muon. Several signal hypotheses are considered. The first hypothesis is a heavy
2330 Higgs boson (spin-0 resonance) under the narrow-width approximation (NWA). Then as
2331 several theoretical models prefer non-negligible natural widths, the models under large-
2332 width approximation (LWA), assuming widths of 1%, 5%, 10% and 15% of the resonance
2333 mass, are also studied. In addition, the graviton excitations (spin-2 resonance) under the
2334 Randall–Sundrum model are also searched. It is assumed that the heavy resonance is
2335 produced predominantly via the gluon-gluon Fusion (ggF) and the Vector Boson Fusion
2336 (VBF) productions, but with the unknown ratio of two production rates. So the results are
2337 separated for ggF and VBF production modes. To gain more sensitivity, the $\ell\ell\ell'\ell'$ events
2338 are classified into ggF- and VBF-enriched categories. Moreover, for the NWA model, the
2339 categorizations are studied under both cut-based and multivariate (MVA) -based methods,
2340 the details of categorization are shown in following sections.

2341 The search uses the four-lepton invariant mass in the range of 200 GeV to 2000 GeV for
 2342 signal hypothesis of spin-0 resonance under the NWA model, and from 400 GeV to
 2343 2000 GeV for the one under the LWA models. And the spin-2 graviton signals are searched
 2344 in the mass range from 600 GeV to 2000 GeV. The data collected by ATLAS detector at
 2345 the LHC from 2015 to 2018 at the centre-of-mass energy of 13 TeV is used. In case of no
 2346 excess, upper limits on the production rate of different signal hypotheses are computed
 2347 from statistical fits to m_{4l} distribution.

2348

7.2 Data and MC samples

2349

7.2.1 Data samples

2350 The data used in this analysis are collected by ATLAS detector at the centre-of-mass
 2351 energy of 13 TeV during the years of 2015 to 2018. Only events passing the latest Good
 2352 Run List (GRL) released by the Data Quality group from ATLAS experiment as listed in
 2353 section 6.2.1 corresponding to an integrated luminosity of $139.0 \pm 2.4 \text{ fb}^{-1}$ are used.
 2354 Table 7.1 listed the recorded integrated luminosity, average and peak pile-up of each year's
 data.

Table 7.1 Summary of the recorded integrated luminosity (lumi), average and peak pile-up (PU) of data from 2015 to 2018.

Year	recorded integrated lumi	lumi after GRL	average PU	peak PU
2015	3.86 fb^{-1}	36.2 fb^{-1}	13.4	28.1
2016	35.6 fb^{-1}		25.1	52.2
2017	46.9 fb^{-1}	44.3 fb^{-1}	37.8	79.8
2018	60.6 fb^{-1}	58.5 fb^{-1}	36.1	88.6

2355

7.2.2 Background MC simulations

2356 Background processes considered in this analysis include ZZ ($q\bar{q} \rightarrow ZZ$, $gg \rightarrow ZZ$), triboson (WWZ , WZZ , ZZZ), $Z+jets$ and top-quark ($t\bar{t}$, ttV) processes.

2357 The QCD $q\bar{q} \rightarrow ZZ$ process is modelled using SHERPA 2.2.2^[81] with the
 2358 NNPDF3.0NNLO^[82] PDF, where events with up to one (three) outgoing partons are gen-
 2359 erated at NLO (LO) in pQCD. The production of ZZ from the gluon-gluon initial state
 2360 with a four-fermion loop or with an exchange of the Higgs boson, which has an order of α_S^4
 2361 in QCD, is not included in this SHERPA simulation. So a separate gg induced ZZ sample
 2362 including the continuum background, the SM Higgs boson, and the interference contri-
 2363 bution is modelled using SHERPA 2.2.2 with the NNPDF3.0NNLO PDF set, and with an
 2364 2365

2366 additional 1.7 k-factor^[83] being applied. The EW- $ZZjj$ production is simulated using
2367 SHERPA 2.2.2 with the NNPDF3.0NNLO PDF, and the $ZZZ \rightarrow \ell\ell\ell'\ell'qq$ process is
2368 also taken into account in this sample.

2369 The $Z+jets$ events are generated using SHERPA 2.2.2 with the NNPDF3.0NNLO PDF,
2370 in which the ME is calculated for up to two partons with next-to-leading-order (NLO)
2371 accuracy in pQCD and up to four partons with LO accuracy. The $Z+jets$ events are
2372 normalized using the next-to-next-to-leading-order (NNLO) cross section. The triboson
2373 processes with full leptonic decays and at least four prompt charged leptons are generated
2374 using SHERPA 2.1.1. For top-quark pair ($t\bar{t}$) production and the single top-quark produc-
2375 tions in t -channel, s -channel and Wt -channel, the PowHEG-Box v2 is used with the CT10
2376 PDF. The productions of $t\bar{t}$ in association with Z boson(s) ($t\bar{t}Z$) is modelled with MAD-
2377 GRAPH5_aMC@NLO.

2378

7.2.3 Signal MC simulations

2379 One model considered in this analysis is heavy spin-0 resonance under the Narrow
2380 Width Approximation (NWA) simulated using PowHEG-Box v2 MC event generator with
2381 the CT10 PDF. The gluon-gluon fusion (ggF) production mode and vector-boson fusion
2382 (VBF) production mode are calculated separately with matrix elements up to NLO in
2383 QCD. The PowHEG-Box is interfaced to PYTHIA8 for parton showering, and for decaying
2384 the Higgs boson into the $H \rightarrow ZZ \rightarrow \ell\ell\ell'\ell'$ final states. Events of NWA signal are
2385 generated at mass points between 200 GeV to 2000 GeV using the step of 100 (200) GeV up
2386 to (above) 1 TeV in both ggF and VBF production modes.

2387 In addition, heavy Higgs boson events under the Large Width Approximation (LWA)
2388 with widths of 1%, 5%, 10% and 15% of the boson mass are generated using MAD-
2389 GRAPH5_aMC@NLO 2.3.2 interfaced to PYTHIA8. Only ggF production is consid-
2390 ered. Mass points between 400 GeV to 2000 GeV are simulated with the step of 100
2391 (200) GeV up to (above) 1 TeV. To describe jet multiplicity, MADGRAPH5_aMC@NLO is
2392 used to simulated process of $pp \rightarrow H + \geq 2\text{jets}$ at NLO in QCD with the FxFx merging
2393 scheme^[102].

2394 Spin-2 Kaluza–Klein (KK) gravitons (G_{KK}) from the Bulk Randall–Sundrum
2395 model^[103] are also studies in this analysis. Events are generated by MAD-
2396 GRAPH5_aMC@NLO at LO in QCD, which is then interfaced to PYTHIA8 for parton
2397 showering. The G_{KK} -gluon coupling $k/\overline{M}_{\text{Planck}}$, where k is the curvature scale of the
2398 extra dimension and $\overline{M}_{\text{Planck}}$ is the reduced Planck mass, is set to 1. The width of the
2399 resonance is correlated with the coupling $k/\overline{M}_{\text{Planck}}$ and in this configuration is around

2400 6% of its mass. The mass of the G_{KK} is the only free parameter in this simplified model.
2401 Mass points between 600 GeV to 2 TeV with 200 GeV spacing were generated.

2402

7.3 Analysis selections

2403

7.3.1 Objects selection

2404 Similar to VBSZZ analysis in section 6.3, the selection of this analysis relies on the
2405 definition of multiple objects: *electrons*, *Muons*, and *jets*. Details of definitions for each
2406 object are described as below:

2407 **Electron:** As described in section 4.2.3, electrons are reconstructed from energy
2408 deposits in the EM calorimeter matched to a track in the inner detector. The electron
2409 candidates satisfying the *Loose* criterion valuing by the likelihood-based (LH) method
2410 are selected, with a selection efficiency ranging from 90% for transverse momentum
2411 $p_T = 20$ GeV to 96% for $p_T > 60$ GeV. In addition, the electrons are required to have
2412 $p_T > 7$ GeV, $|\eta| < 2.47$ and $|z_0 \sin\theta| < 0.5$ mm.

2413 **Muon:** To increase the acceptance range in reco-level for $\ell\ell\ell'\ell'$ channel, all four
2414 types of muons (CB, ST, CT, ME muons, described in section 4.2.4) are used. The CT
2415 muons are required to pass $p_T > 15$ GeV and $|\eta| < 0.1$, while the ST muons are also
2416 limited in $|\eta| < 0.1$ region. The ME muons are only used in the region of $2.5 < |\eta| < 2.7$.
2417 And at most one CT, ST or ME muon is allowed in one $\ell\ell\ell'\ell'$ quadruplet. The Muon
2418 candidates are required to pass $p_T > 5$ GeV and $|\eta| < 2.7$, and satisfy the *Loose* identifi-
2419 cation criterion with an efficiency of at least 98.5%. The impact parameter requirements
2420 of $|d_0| < 1$ mm and $|z_0 \sin\theta| < 0.5$ mm are further applied.

2421 **Jets:** Jets are clustered using the anti- k_t algorithm with radius parameter $R =$
2422 0.4 implemented in the FASTJET package as described in section 4.2.5. The ‘particle
2423 flow’ (PFlow) objects^[104], which combines measurements from both the tracker and the
2424 calorimeter, are used as inputs to the FASTJET package. The energy deposited in the
2425 calorimeter by all charged particles is removed, and the jet reconstruction is performed on
2426 an ensemble of PFlow objects consisting of the remaining calorimeter energy and tracks
2427 which are matched to the hard interaction. This improves the accuracy of the charged-
2428 hadron measurement, while retaining the calorimeter measurements of neutral-particle
2429 energies. Compared to only using topological clusters, jets reconstructed with the particle
2430 flow algorithm with $p_T > 30$ GeV have approximately 10% better transverse momentum
2431 resolution. The jets used in this analysis are then required to have $p_T > 30$ GeV and
2432 $|\eta| < 4.5$. To further reduce the effects of pile-up jets, a jet vertex tagger (JVT) is applied

2433 to jets with $p_T < 60$ GeV and $|\eta| < 2.4$.

2434 **Overlap removal:** As the selected jet and lepton candidates can be reconstructed
 2435 from same detector information, an overlap-removal procedure is applied. For electron
 2436 and muon sharing the same ID track, the electron is selected in the case that the muon is
 2437 calorimeter-tagged and does not have a MS track, or is a segment-tagged muon, otherwise
 2438 the muon is selected. The jet overlapping with electron (muon) within a cone of size of
 2439 $\Delta R \equiv \sqrt{(\Delta\eta)^2 + (\Delta\phi)^2} = 0.2(0.1)$ are removed.

2440 **7.3.2 Event selection**

2441 First of all, the four-lepton events are required to pass single or multi-lepton triggers.
 2442 Due to the increasing of peak luminosity and pile-up, the p_T and E_T thresholds of triggers
 2443 increase slightly during the data-taking periods from 2015 to 2018. Table 7.2 summarizes
 2444 the triggers used for $\ell\ell\ell'\ell'$ channel. The overall trigger efficiency for selected signal
 2445 events passing final selection is around 98%.

**Table 7.2 Summary of the p_T (E_T) trigger thresholds (in GeV) employed for the muon (electron)
 trigger selection in the year of 2015, 2016, 2017, and 2018.**

Trigger item	Trigger threshold			
	2015	2016	2017	2018
single muon	$\mu 20; \mu 50; \mu 60$	$\mu 24; \mu 26; \mu 40; \mu 50$	$\mu 26; \mu 50; \mu 60$	$\mu 26; \mu 50; \mu 60$
single electron	$e 24; e 60; e 120$	$e 26; e 60; e 140; e 300$	$e 26; e 60; e 140; e 300$	$e 26; e 60; e 140; e 300$
dimuon	$2\mu 10; \mu 18_{-\mu 8}$	$2\mu 10; 2\mu 14; \mu 22_{-\mu 8}$	$2\mu 14; \mu 22_{-\mu 8}$	$2\mu 14; \mu 22_{-\mu 8}$
dielectron	$2e 12$	$2e 15; 2e 17$	$2e 17; 2e 24$	$2e 17; 2e 24$
electron-muon	$e 24_{-\mu 8}$	$e 24_{-\mu 8}; e 26_{-\mu 8}$ $e 17_{-\mu 14}; e 7_{-\mu 24}; 2e 12_{-\mu 10}; e 12_{-\mu 10}$	$e 26_{-\mu 8}$	$e 26_{-\mu 8}$
trimuon	$\mu 18_{-2\mu 4}$	$\mu 11_{-2\mu 4}; \mu 6_{-2\mu 4}; \mu 20_{-2\mu 4}; 3\mu 4$ $3\mu 6$	$4\mu 4; \mu 20_{-2\mu 4}; 3\mu 4$	$\mu 20_{-2\mu 4}$
trilepton	$e 17_{-2e 9}$	$e 17_{-2e 9}; e 17_{-2e 10}$	$e 24_{-2e 12}$	$e 24_{-2e 12}$

2446 The $\ell\ell\ell'\ell'$ quadruplets are formed by two opposite-sign, same-flavour (OSSF) lepton
 2447 pairs ($\ell^+\ell^-$). The p_T threshold of first three leading leptons are required to be 20, 15 and
 2448 10 GeV. If there are more than one combination of lepton pairing in quadruplet, the pairing
 2449 is selected by keeping it with the mass of lepton pairs closest (leading pair, refers as m_{12})
 2450 and second closest (sub-leading pair, refers as m_{34}) to Z boson mass. The mass of leading
 2451 pair is required to satisfy $50 < m_{12} < 106$ GeV, while the sub-leading pair is required to
 2452 be less than 115 GeV and larger than 50 GeV.

2453 The two lepton pairs in quadruplet are required to have angular separation with $\Delta R >$
 2454 0.1. To suppress the contribution from $J/\psi \rightarrow \ell\ell$ decays, for 4 μ and 4 e quadruplets,
 2455 the events are rejected if any opposite-sign same-flavour lepton pair is found with mass

2456 below 5 GeV. If there are more than one quadruplets from different channels in event at
 2457 this point, the one with highest expected signal rate is selected in the order of 4μ , $2e2\mu$,
 2458 $4e$. The transverse impact-parameter significance ($|d_0|/\sigma_{d_0}$) for muons (electrons) is then
 2459 required to be smaller than 3 (5) to suppress the backgrounds from heavy-flavour hadrons.

2460 In addition, the track- and calorimeter- based isolation criteria is required for all elec-
 2461 trons and muons to further suppress the reducible backgrounds of $Z+jets$ and $t\bar{t}$. For
 2462 lepton isolation selection, the two track- and calorimeter- based variables, $E_T^{topocone}$ and
 2463 $p_T^{varcone}$ as described in section 4.2.4 (section 4.2.3) for muons (electrons), are vulnerable
 2464 to pileup. For track-based variable, this is because of additional tracks in the event. The
 2465 definition of $p_T^{varcone}$ attempts to limit the tracks used in the calculation to those from the
 2466 vertex via a loose cut of $|z_0 \sin(\theta)| < 3$, which proved to be too loose in new pile-up
 2467 regime 2017 and 2018 datasets. So new track-based variable is used, by adding a require-
 2468 ment that the track be used in determining the vertex, or that, if not, it both pass the cut on
 2469 $|z_0 \sin(\theta)|$ and not be used in determining any other vertex, which makes the track-based
 2470 variable to be more isolation-robust in the high pile-up regime. The new variable is named
 2471 as `ptvarcone[cone]_TightTTVA_pt[pT cut]`, where [cone] is the cone size and [p_T cut] is
 2472 the cutoff for including tracks in the calculation.

2473 For calorimeter-based variable, the calculation of $E_T^{topocone}$ corrects the pile-up effects
 2474 by subtracting an average pileup contribution computed over the whole detector. But with
 2475 the increasing of energy density of pile-up events, the root mean square (RMS) of $E_T^{topocone}$
 2476 variable increases, which leads to the increment of possibility that the pile-up fluctuations
 2477 are not be accounted for correctly. One possible solution is that use particle-flow (PFlow)
 2478 method to calculate the calorimeter isolation. As part of PFlow reconstruction process,
 2479 it assigns the clusters to tracks which improves the track-cluster association for better de-
 2480 termination of the raw value of the E_T in the cone. And using PFlow jets to calculate the
 2481 pileup correction provides a further improvement. So a resulting variable named `neflow-`
 2482 `isol[cone]` is used. Finally, a requirement of isolation, called *FixedCutPFlowLoose*, which
 2483 gives better performance in high piup-up condition is applied to electrons and muons as:
 2484
$$(\max(\text{ptcone20_TightTTVA_pt500}, \text{ptvarcone30_TightTTVA_pt500}) + 0.4 \times \text{neflow-} \\ 2485 \text{isol20}) / p_T < 0.16$$

2486 On the top of impact parameter cut and lepton isolation cut, the four-lepton candidates
 2487 are also required to originate from a common vertex to reduce $Z+jets$ and $t\bar{t}$ backgrounds.
 2488 This is ensured by applying a vertex fit χ^2 cut of 4 ID tracks of lepton candidates satisfying
 2489 $\chi^2/N_{dof} < 6$ (9) for events in 4μ ($4e$ and $2e2\mu$) channel(s).

2490 To improve the mass resolution, the QED process of final state radiation (FSR) pho-

2491 tons in Z boson decays are taken into account in the reconstruction of Z bosons. The
2492 four-momentum of any reconstructed photon that is consistent with having been radiated
2493 from lepton(s) in leading pair are added into final state. Moreover, the four-momenta of
2494 leptons in both (leading and sub-leading) pairs are recomputed by performing a Z -mass-
2495 constrained kinematic fit, which uses a Breit–Wigner Z boson line-shape and Gaussian
2496 function with width set to the expected lepton resolution per lepton to model the momen-
2497 tum response function. The Z -mass-constrained mass improves the $m_{4\ell}$ resolution by up
2498 to 15% depending on m_H .

2499 In summary, table 7.3 lists a comprehensive object and event level selection as de-
2500 scribed above. Table 7.4 to 7.7 shows the cutflow of NWA ggF and VBF signal at the
2501 mass points of 600 and 1000 GeV as examples.

2502

7.3.3 Event categorizations

2503 To improve the sensitivity of search in both VBF and ggF production mode in NWA
2504 model, events are classified into the VBF- and ggF- enriched categories. With the statistic
2505 increasing in full run-2 data, a multivariate (MVA) based classifier has been studied for
2506 NWA signal, while in the meantime the traditional cut-based classifier is also used as a
2507 model-independent result for all three (NWA, LWA, graviton) models.

2508

1. Cut-based categorization

2509 There are four categories in total: one VBF-enriched category and three ggF-enriched
2510 categories. The categorization is defined based on kinematic cuts:

- 2511 • VBF-CBA-enriched category: Events have at least two selected jets as defined in
2512 section 7.3.1, with the two leading jets being separated by $|\Delta\eta_{jj}| > 3.3$ and invariant
2513 mass satisfying $m_{jj} > 400$ GeV;
- 2514 • ggF-CBA-enriched categories: The remaining events that are not classified into
2515 VBF-enriched category. Then events are categorized into three channels based on
2516 lepton-flavor, namely ggF_2e2μ, ggF_4e and ggF_4μ.

2517

2. MVA-based categorization

2518 In order to target different production modes, two types of classifiers, one dedicate to
2519 VBF production while the other one for ggF, have been trained using deep neural network
2520 technique. Details of two classifiers are described as below:

2521

DNN models

2522 Figure 7.1 shows the architecture of VBF (left) and ggF (right) network. The VBF
2523 network includes three parts: two recurrent neural networks (RNNs) and one multilayer
2524 perceptron (MLP). The ggF network consists of one RNN and one MLP.

Table 7.3 Summary of the object and event selection requirements.

Physics Objects	
ELECTRONS	
Loose Likelihood quality electrons with hit in innermost layer, $E_T > 7$ GeV and $ \eta < 2.47$	
Interaction point constraint: $ z_0 \cdot \sin \theta < 0.5$ mm (if ID track is available)	
MUONS	
Loose identification with $p_T > 5$ GeV and $ \eta < 2.7$	
Calo-tagged muons with $p_T > 15$ GeV and $ \eta < 0.1$, segment-tagged muons with $ \eta < 0.1$	
Stand-alone and silicon-associated forward restricted to the $2.5 < \eta < 2.7$ region	
Combined, stand-alone (with ID hits if available) and segment-tagged muons with $p_T > 5$ GeV	
Interaction point constraint: $ d_0 < 1$ mm and $ z_0 \cdot \sin \theta < 0.5$ mm (if ID track is available)	
JETS	
anti- k_T jets with <i>bad-lose</i> identification, $p_T > 30$ GeV and $ \eta < 4.5$	
OVERLAP REMOVAL	
Jets within $\Delta R < 0.2$ of an electron or $\Delta R < 0.1$ of a muon are removed	
VERTEX	
At least one collision vertex with at least two associated track	
PRIMARY VERTEX	
Vertex with the largest p_T^2 sum	
Event Selection	
QUADRUPLET	- Require at least one quadruplet of leptons consisting of two pairs of same-flavour opposite-charge leptons fulfilling the following requirements:
SELECTION	<ul style="list-style-type: none"> - p_T thresholds for three leading leptons in the quadruplet: 20, 15 and 10 GeV - Maximum one calo-tagged or stand-alone muon or silicon-associated forward per quadruplet - Leading di-lepton mass requirement: $50 < m_{12} < 106$ GeV - Sub-leading di-lepton mass requirement: $50 < m_{34} < 115$ GeV - $\Delta R(\ell, \ell') > 0.10$ for all leptons in the quadruplet - Remove quadruplet if alternative same-flavour opposite-charge di-lepton gives $m_{\ell\ell} < 5$ GeV - Keep all quadruplets passing the above selection
ISOLATION	<ul style="list-style-type: none"> - Contribution from the other leptons of the quadruplet is subtracted - FixedCutPFlowLoose WP for all leptons
IMPACT	- Apply impact parameter significance cut to all leptons of the quadruplet
PARAMETER	- For electrons: $d_0/\sigma_{d_0} < 5$
SIGNIFICANCE	- For muons: $d_0/\sigma_{d_0} < 3$
BEST	- If more than one quadruplet has been selected, choose the quadruplet
QUADRUPLET	with highest Higgs decay ME according to channel: 4μ , $2e2\mu$, $2\mu2e$ and $4e$
VERTEX	- Require a common vertex for the leptons:
SELECTION	- $\chi^2/\text{ndof} < 5$ for 4μ and < 9 for others decay channels

Table 7.4 Cutflow table for a narrow-width ggF signal sample at $m_H = 600$ GeV. N_{event} denotes the number of events selected after each cut is applied, normalized to 139 fb^{-1} , according to the expected upper limit on the cross section. The acceptances (the proportion of events selected relative to the initial number of events) are also included.

	N_{event}	$N_{\text{event}}/\text{BR}(ZZ \rightarrow \ell\ell\ell'\ell')$	Acc. [%]	Acc. · $\text{BR}(ZZ \rightarrow \ell\ell\ell'\ell') \cdot 1000$
Initial	17.902	3 964.3	100.00	4.516
Lepton selection	6.247	1 383.4	34.90	1.576
SFOS	5.758	1 275.1	32.16	1.453
Kinematic cuts	5.754	1 274.2	32.14	1.452
Z_1 Mass	5.726	1 267.9	31.98	1.444
Z_2 Mass	5.112	1 132.0	28.56	1.290
J/ψ Veto	5.111	1 131.9	28.55	1.289
ΔR	5.111	1 131.7	28.55	1.289
Isolation	4.864	1 077.0	27.17	1.227
Impact parameters	4.796	1 062.1	26.79	1.210
Vertex requirement	4.786	1 059.8	26.73	1.207
Trigger	4.783	1 059.1	26.72	1.207
“Badjet” veto	4.763	1 054.7	26.61	1.201

Table 7.5 Cutflow table for a narrow-width ggF signal sample at $m_H = 1000$ GeV. N_{event} denotes the number of events selected after each cut is applied, normalized to 139 fb^{-1} , according to the expected upper limit on the cross section. The acceptances (the proportion of events selected relative to the initial number of events) are also included.

	N_{event}	$N_{\text{event}}/\text{BR}(ZZ \rightarrow \ell\ell\ell'\ell')$	Acc. [%]	Acc. · $\text{BR}(ZZ \rightarrow \ell\ell\ell'\ell') \cdot 1000$
Initial	5.603	1 240.8	100.00	4.516
Lepton selection	2.141	474.1	38.21	1.725
SFOS	1.944	430.5	34.70	1.567
Kinematic cuts	1.943	430.3	34.68	1.566
Z_1 Mass	1.932	427.8	34.48	1.557
Z_2 Mass	1.715	379.7	30.61	1.382
J/ψ Veto	1.715	379.7	30.60	1.382
ΔR	1.714	379.6	30.60	1.382
Isolation	1.640	363.2	29.27	1.322
Impact parameters	1.620	358.6	28.90	1.305
Vertex requirement	1.616	357.8	28.84	1.302
Trigger	1.615	357.7	28.83	1.302
“Badjet” veto	1.609	356.2	28.71	1.297

Table 7.6 Cutflow table for a narrow-width VBF signal sample at $m_H = 600$ GeV. N_{event} denotes the number of events selected after each cut is applied, normalized to 139 fb^{-1} , according to the expected upper limit on the cross section. The acceptances (the proportion of events selected relative to the initial number of events) are also included.

	N_{event}	$N_{\text{event}}/\text{BR}(ZZ \rightarrow \ell\ell\ell'\ell')$	Acc. [%]	Acc. · $\text{BR}(ZZ \rightarrow \ell\ell\ell'\ell') \cdot 1000$
Initial	12.143	2 688.9	100.00	4.516
Lepton selection	4.307	953.7	35.47	1.602
SFOS	3.975	880.2	32.74	1.478
Kinematic cuts	3.972	879.6	32.71	1.477
Z_1 Mass	3.953	875.4	32.56	1.470
Z_2 Mass	3.545	785.0	29.19	1.318
J/ψ Veto	3.545	785.0	29.19	1.318
ΔR	3.544	784.9	29.19	1.318
Isolation	3.418	756.9	28.15	1.271
Impact parameters	3.368	745.9	27.74	1.253
Vertex requirement	3.362	744.5	27.69	1.250
Trigger	3.360	744.0	27.67	1.250
“Badjet” veto	3.340	739.7	27.51	1.242

Table 7.7 Cutflow table for a narrow-width VBF signal sample at $m_H = 1000$ GeV. N_{event} denotes the number of events selected after each cut is applied, normalized to 139 fb^{-1} , according to the expected upper limit on the cross section. The acceptances (the proportion of events selected relative to the initial number of events) are also included.

	N_{event}	$N_{\text{event}}/\text{BR}(ZZ \rightarrow \ell\ell\ell'\ell')$	Acc. [%]	Acc. · $\text{BR}(ZZ \rightarrow \ell\ell\ell'\ell') \cdot 1000$
Initial	3.827	847.4	100.00	4.516
Lepton selection	1.474	326.5	38.53	1.740
SFOS	1.351	299.1	35.30	1.594
Kinematic cuts	1.350	299.0	35.28	1.593
Z_1 Mass	1.341	297.0	35.04	1.583
Z_2 Mass	1.195	264.6	31.23	1.410
J/ψ Veto	1.195	264.6	31.23	1.410
ΔR	1.195	264.6	31.22	1.410
Isolation	1.161	257.1	30.34	1.370
Impact parameters	1.148	254.1	29.99	1.354
Vertex requirement	1.146	253.8	29.95	1.352
Trigger	1.145	253.6	29.93	1.352
“Badjet” veto	1.139	252.2	29.77	1.344

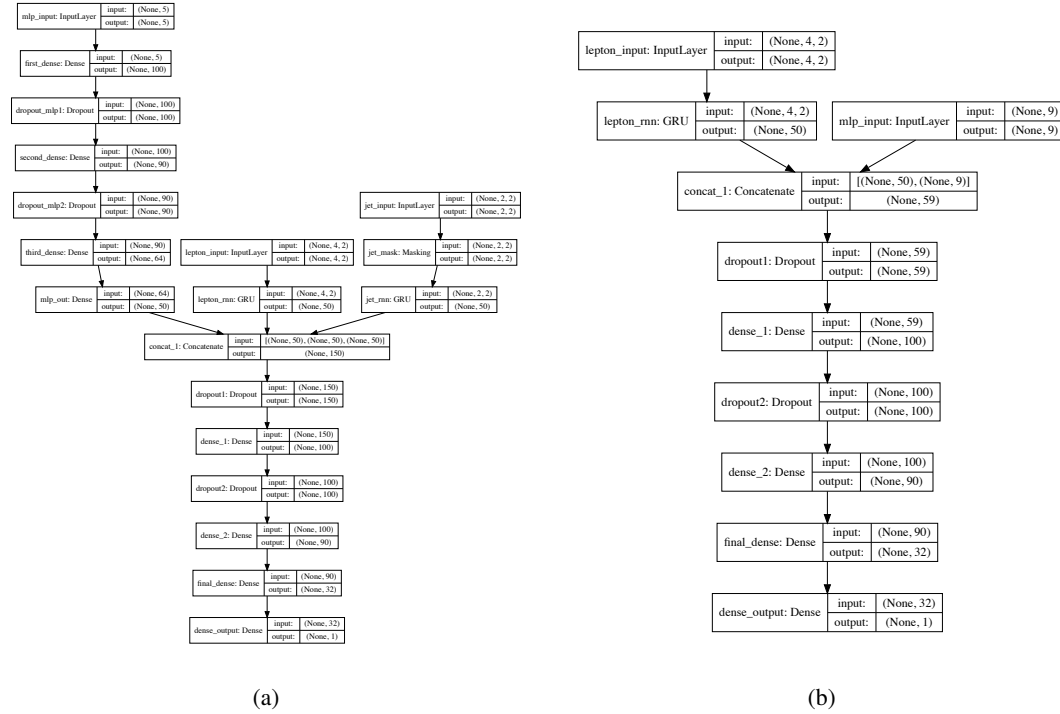


Fig. 7.1 (a) VBF DNN architecture diagram. (b) ggF DNN architecture.

For training, the VBF and ggF signal samples at the masses of 200, 300, 400, 500, 600, 700, 800, 900, 1000, 1200, 1400 GeV are used with positive label. The VBF (ggF) signals are only used for VBF (ggF) classifier. The background including simulated samples of QCD and EW $q\bar{q} \rightarrow ZZ$ processes as well as $gg \rightarrow ZZ$ process summed according to their cross section are assigned with negative labels. In addition to the selections described in section 7.3.2, the events used for VBF network are required to have $N_{\text{jets}} \geq 2$, while $N_{\text{jets}} < 2$ is required for events in ggF network.

In order to assign equivalent importance to signals with different mass assumptions, during the training, signal events are reweighted to follow the $m_{4\ell}$ distribution from background, as shown in figure 7.2 (figure 7.3) before (left) and after(right) reweighting for VBF (ggF) samples.

Input features

Table 7.8 (table 7.9) lists the input features used for VBF (ggF) network during the training. For VBF network, one RNN (the other one) takes the p_T and η of p_T -ordered four leptons (two leading jets) as input features, which intends to study the time relationship from particle decay between leptons (jets). For ggF network, the only one RNN model takes the p_T and η of p_T -ordered four leptons as inputs.

Evaluation of models

Figure 7.4 shows the output of “ggF-classifier” and “VBF-classifier” for data, SM

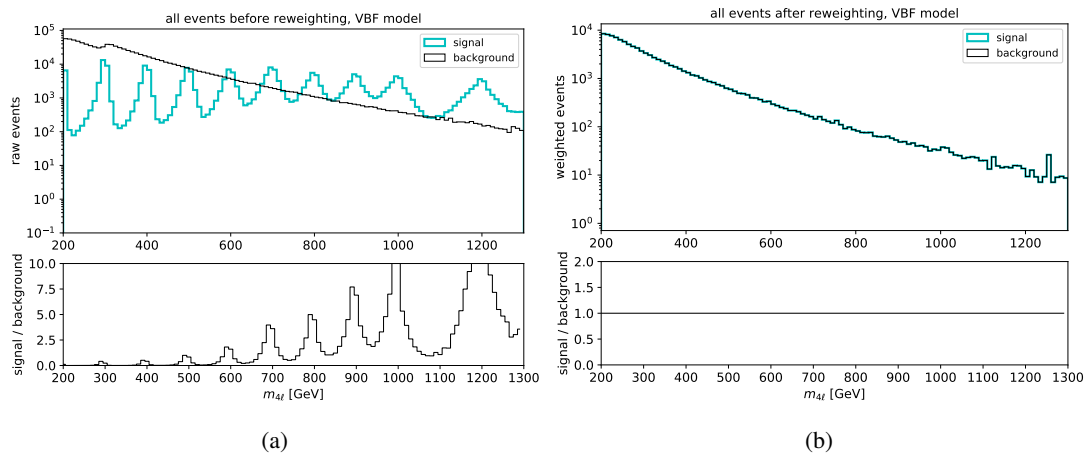


Fig. 7.2 (a) $m_{4\ell}$ distribution of raw (unweighted) training events for VBF signal (blue) and background (black); (b) $m_{4\ell}$ distribution of weighted VBF signal (blue) and background (black) used at training time.

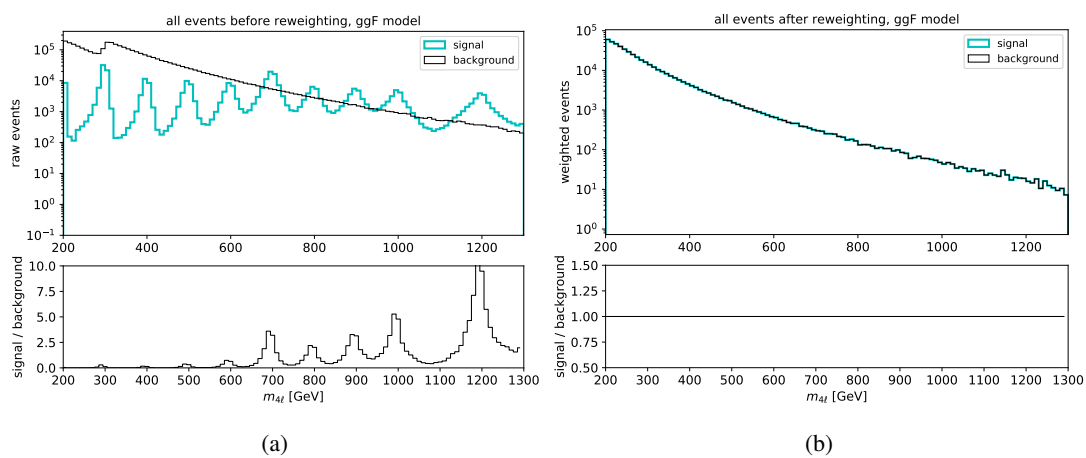


Fig. 7.3 (a) $m_{4\ell}$ distribution of raw (unweighted) training events for ggF signal (blue) and background (black); (b) $m_{4\ell}$ distribution of weighted ggF signal (blue) and background (black) used at training time.

Table 7.8 Input features used in the “VBF-classifier” for the $\ell\ell\ell'\ell'$ analysis. The RNN stands for the recurrent neural network and MLP for the multilayer perceptron.

Model	Inputs	Description
RNN	$p_T^{j0,j1}$	transverse momenta of the two leading jets
	$\eta^{j0,j1}$	pseudorapidity of the two leading jets
	$p_T^{\ell0,\ell1,\ell2,\ell3}$	transverse momenta of the four leptons
	$\eta^{\ell0,\ell1,\ell2,\ell3}$	pseudorapidity of the four leptons
MLP	$m_{4\ell}$	invariant mass of the four lepton system
	m_{jj}	invariant mass of the two leading jet system
	p_T^{jj}	transverse momentum of the two leading jet system
	$\Delta\eta_{H,j}$	difference in pseudorapidity between the four lepton system and the leading jet
	$\min\Delta R_{jZ}$	minimum distance between one of the two lepton pairs and a jet

2544 backgrounds and an example signal at 600 GeV. The ggF and VBF signals cross section
 2545 are set to be one hundred times of their observed upper limit described in section 7.7.3 for
 2546 ggF output and fifty times of the observed upper limit for VBF output for best visibility.

2547 Then the optimal cut at output score from each classifier is chosen based on an overall
 2548 good performance of classifier to have a large significance improvement while retaining
 2549 a high signal efficiency. Figure 7.5 shows the significance improvements of MVA-based
 2550 cuts when comparing with cut-based one at different VBF (left) and ggF (right) mass
 2551 samples, where the significance is calculated as:

$$Z = \sqrt{2 \left(n \ln \left[\frac{nb + \sigma^2}{b^2 + n\sigma^2} \right] - \frac{b^2}{\sigma^2} \ln \left[1 + \frac{\sigma^2(n-b)}{b(b+\sigma^2)} \right] \right)} \quad (7.1)$$

2552 Cut at 0.5 (0.8) for VBF (ggF) classifier is chosen as shown in solid lines.

2553 Then the events passing VBF classifier are categorized into VBF-MVA-enriched category.
 2554 Otherwise, the events failing VBF classifier but passing ggF classifier are categorized into ggF-MVA-high category, which is further split into 3 channels. All remaining
 2555 events are sorted into one additional ggF-MVA-low category. Thus there are five categories defined in MVA-based categorization. In summary, cuts applied in categorization
 2556 are defined as follow, and these different phase spaces are also illustrated in figure 7.6.

- 2557
- VBF-MVA-enriched category: Events have at least two selected jets ($N_{\text{jets}} \geq 2$),
 2558 and with $DNN_{\text{VBF}} > 0.8$;

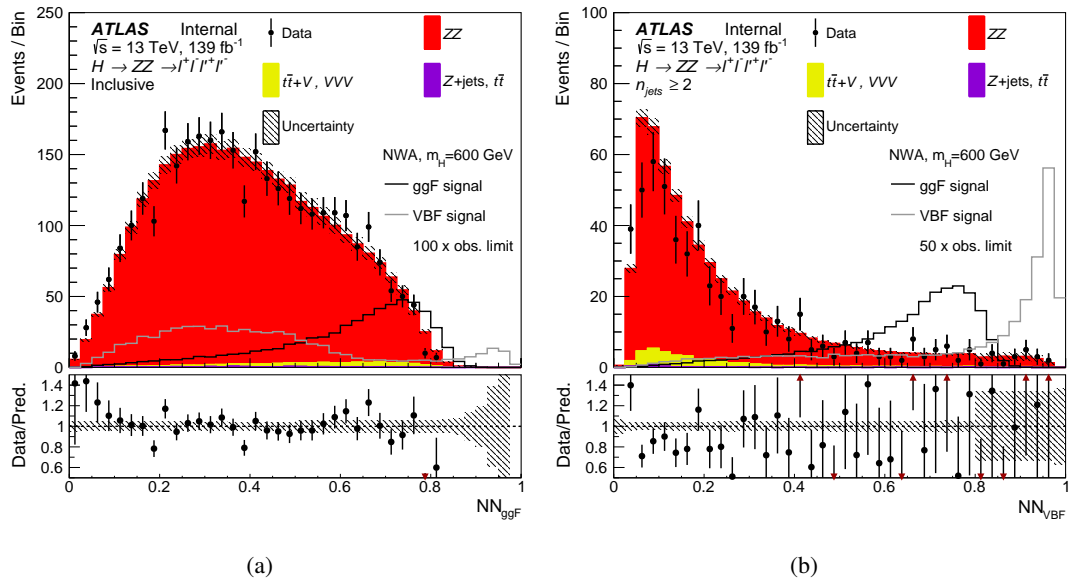


Fig. 7.4 The output score of “ggF-classifier” (a) and “VBF-classifier” (b) with the events passing the common event selections for the data, the SM backgrounds and an example of a NWA signal with a mass of 600 GeV. For the “VBF-classifier”, an additional requirement of at least two jets in the event is applied. The signals cross section are set to one hundred times of the observed limit for the “ggF-classifier” and fifty times of the observed limit for the “VBF -classifier”. The ZZ backgrounds are scaled by the normalisation factors shown in Table 7.15. The lower panels show the ratio of data to prediction. Only statistical and experimental systematic uncertainties are included.

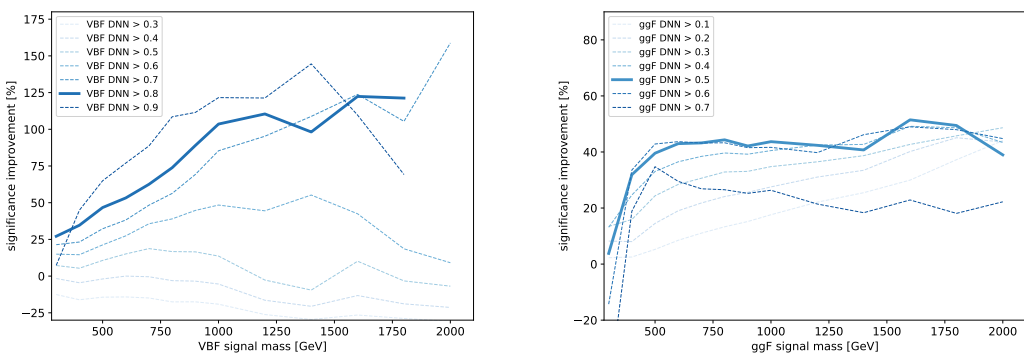


Fig. 7.5 Significance improvements of the MVA-based over the cut-based categorization of the VBF (ggF) category for VBF (ggF) signal samples from 300 to 2000 GeV for seven different cuts on the VBF (ggF) output score. The optimal cut of 0.8 (0.5) for VBF (ggF) score is chosen as the solid line, while other alternative cuts are plotted with dashed lines. For VBF category, results at 2000 GeV for cuts of 0.8 and 0.9 are missing due to a lack of background events passing this tight selection.

Table 7.9 Input features used in the “ggF-classifier” for the $\ell\ell\ell'\ell'$ analysis. The RNN stands for the recurrent neural network and MLP for the multilayer perceptron.

Model	Inputs	Description
RNN	$p_T^{\ell 0,\ell 1,\ell 2,\ell 3}$	transverse momenta of the four leptons
	$\eta^{\ell 0,\ell 1,\ell 2,\ell 3}$	pseudorapidity of the four leptons
MLP	$m_{4\ell}$	invariant mass of the four lepton system
	$p_T^{4\ell}$	transverse momentum of the four lepton system
	$\eta^{4\ell}$	pseudorapidity of the four lepton system
	$\cos \theta^*$	production angle of the leading Z defined in the four lepton rest frame
	$\cos \theta_1$	angle between the negative final state lepton and the direction of flight of leading Z in the Z rest frame
	$\cos \theta_2$	angle between the negative final state lepton and the direction of flight of sub-leading Z in the Z rest frame
	Φ	angle between the decay planes of the four final state leptons expressed in the four lepton rest frame
	p_T^{j0}	transverse momentum of the leading jet
	η^{j0}	pseudorapidity of the leading jet

- 2561 • ggF-MVA-high categories: ($N_{\text{jets}} \geq 2 \ \&\& \ DNN_{\text{VBF}} \leq 0.8 \ \&\& \ DNN_{\text{ggF}} >$
 2562 $0.5) || (N_{\text{jets}} < 2 \ \&\& \ DNN_{\text{ggF}} > 0.5);$
 2563 • ggF-MVA-low category: All remaining events that fail VBF and ggF cuts men-
 2564 tioned above.

2565 7.3.4 Signal acceptance

2566 The signal acceptance is defined as the ratio of events passing all analysis selection in
 2567 each category to the total number of simulated events in whole phase space. In denom-
 2568 inator, the events with τ final states are not taken into account. And the contribution of
 2569 τ -lepton decay to electrons and muons final states is found to be negligible.

2570 Figure 7.7 and 7.8 show the acceptance of NWA signals in DNN- and Cut- based
 2571 categorization, estimated by merging the three signal MC campaigns, mc16a, mc16d and
 2572 mc16e. A 3-rd order polynomial fit is applied for each category.

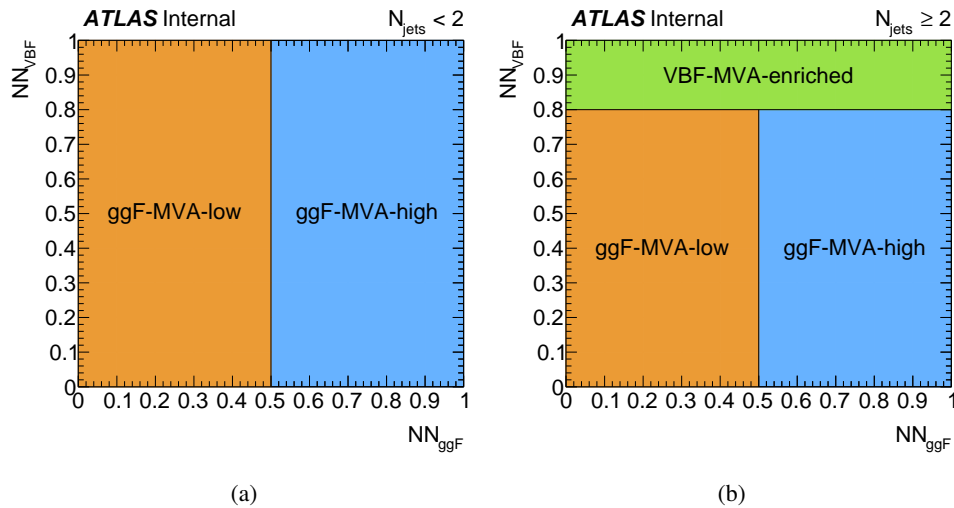


Fig. 7.6 Illustration of the MVA-based VBF and ggF event classification for events with (a) $N_{\text{jets}} < 2$ and (b) $N_{\text{jets}} \geq 2$.

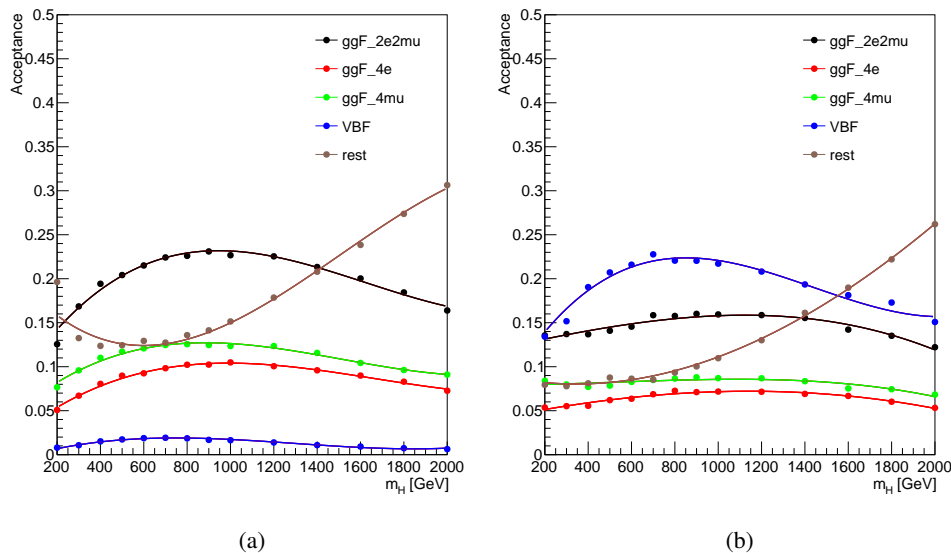


Fig. 7.7 NWA acceptance as a function of m_H for the MVA-based categorization for the samples of (a) ggF production; (b) VBF production.

2573 7.4 Background estimation

2574 In this analysis, 97% of total expected background events are from irreducible ZZ
 2575 backgrounds, which includes about 86% quark-antiquark annihilation ($q\bar{q} \rightarrow ZZ$), 10%
 2576 of gluon-induced production ($gg \rightarrow ZZ$) and around 1% of EW vector boson scattering
 2577 ($q\bar{q} \rightarrow ZZ$ EW) contribution. For $q\bar{q} \rightarrow ZZ$ EW, although it has small contribution
 2578 in total background events after analysis selection, it's important for VBF category with
 2579 about 16% contribution.

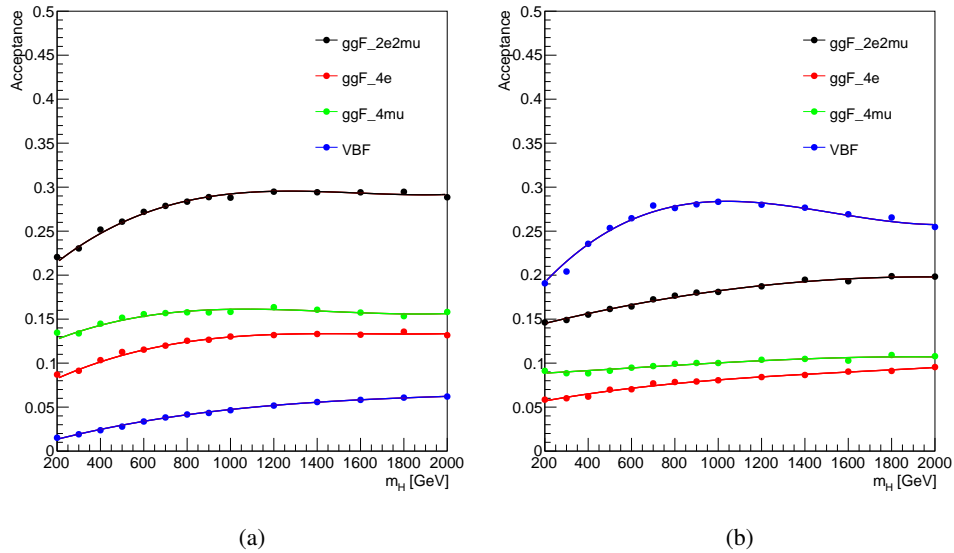


Fig. 7.8 NWA acceptance as a function of m_H for the Cut-based categorization for the samples of (a) ggF production mode; (b) VBF production mode.

2580 In addition to irreducible backgrounds, events from $Z+jets$ and $t\bar{t}$ processes, represent
 2581 as reducible backgrounds, contribute at a few percent level and can be measured using data
 2582 driven method that will be described briefly later. Additional background called ‘Others’,
 2583 including ttV and triple-V (VVV) processes, has tiny contribution and is estimated from
 2584 MC simulation directly.

2585 7.4.1 Irreducible backgrounds

2586 The Irreducible backgrounds have events with four prompt leptons. The normalization
 2587 of two dominant backgrounds $q\bar{q} \rightarrow ZZ$ and $gg \rightarrow ZZ$ are taken from data by statistical
 2588 fit, and the normalization of small $q\bar{q} \rightarrow ZZ$ EW background is measured directly from
 2589 MC simulation.

2590 The $m_{4\ell}$ shapes of all three background components are taken from MC samples and
 2591 then parameterized by an empirical function for each of them in each category respectively.
 2592 Details of background modellings are illustrated as below:

2593 The empirical function used for background parameterization is:

$$f(m_{4\ell}) = C_0 H(m_0 - m_{4\ell}) f_1(m_{4\ell}) + H(m_{4\ell} - m_0) f_2(m_{4\ell}), \quad (7.2)$$

where,

$$f_1(x) = \left(\frac{x - a_4}{a_3} \right)^{a_1-1} \left(1 + \frac{x - a_4}{a_3} \right)^{-a_1-a_2},$$

$$f_2(x) = \exp \left[b_0 \left(\frac{x - b_4}{b_3} \right)^{b_1-1} \left(1 + \frac{x - b_4}{b_3} \right)^{-b_1-b_2} \right],$$

$$C_0 = \frac{f_2(m_0)}{f_1(m_0)}.$$

The function consists of two parts, the first part f_1 describes the $m_{4\ell}$ spectrum in low mass region where both Z bosons decay on-shell, while the second one f_2 covers distribution at high mass tail. The transition between the low- and high- mass parts is presented in function 7.2 by the Heaviside step function $H(x)$ at the transition point m_0 . The m_0 is chosen to optimize the smoothness of the function, and practically $m_0 = 260$ (350) GeV is used for $q\bar{q} \rightarrow ZZ$ ($gg \rightarrow ZZ$ and $q\bar{q} \rightarrow ZZ$ EW). Besides, the continuity of two functions at m_0 is ensured by the factor C_0 applied to f_1 . The coefficients a_i in f_1 and b_i in f_2 are shape parameters obtained by fitting to $m_{4\ell}$ distribution from each MC simulated sample.

Figure 7.9 to 7.11 shows the fitting results of $q\bar{q} \rightarrow ZZ$, $gg \rightarrow ZZ$, $q\bar{q} \rightarrow ZZ$ EW backgrounds in four cut-based categories (ggF-CBA-enriched- $2e2\mu$, ggF-CBA-enriched- $4e$, ggF-CBA-enriched- 4μ and VBF-CBA-enriched). Figure 7.12 to 7.14 shows the fitting results of those backgrounds in five MVA-based categories (ggF-MVA-high- $2e2\mu$, ggF-MVA-high- $4e$, ggF-MVA-high- 4μ , ggF-MVA-low and VBF-MVA-enriched).

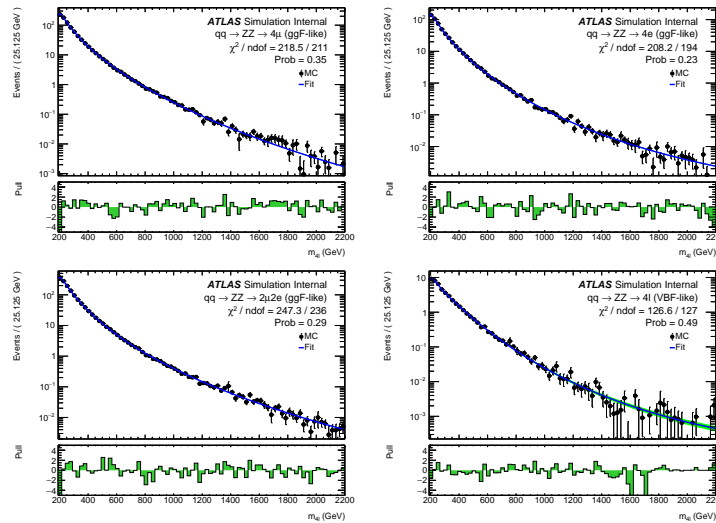


Fig. 7.9 Distributions of the $m_{4\ell}$ invariant mass fit projections of the $q\bar{q} \rightarrow ZZ$ background samples for the 4μ , $4e$ and $2\mu2e$ final states in the ggF-CBA-enriched category, and the 4ℓ inclusive VBF-CBA-enriched category. Cut-based categorization is used.

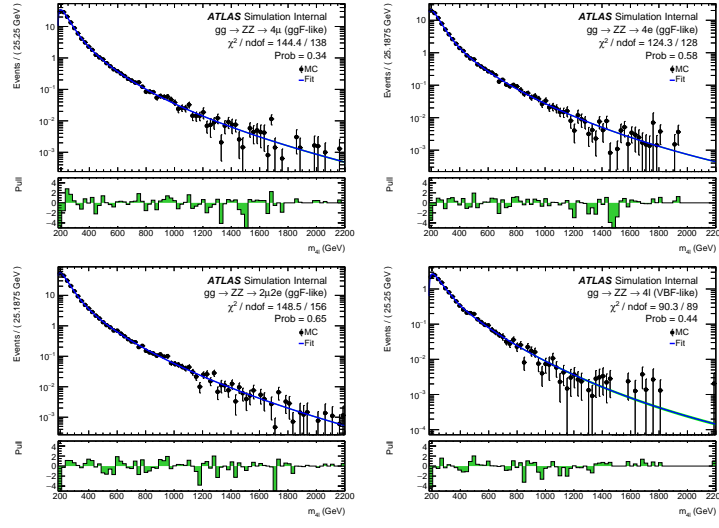


Fig. 7.10 Distributions of the $m_{4\ell}$ invariant mass fit projections of the $gg \rightarrow ZZ$ background samples for the 4μ , $4e$ and $2\mu 2e$ final states in the ggF-CBA-enriched category, and the 4ℓ inclusive VBF-CBA-enriched category. Cut-based categorization is used.

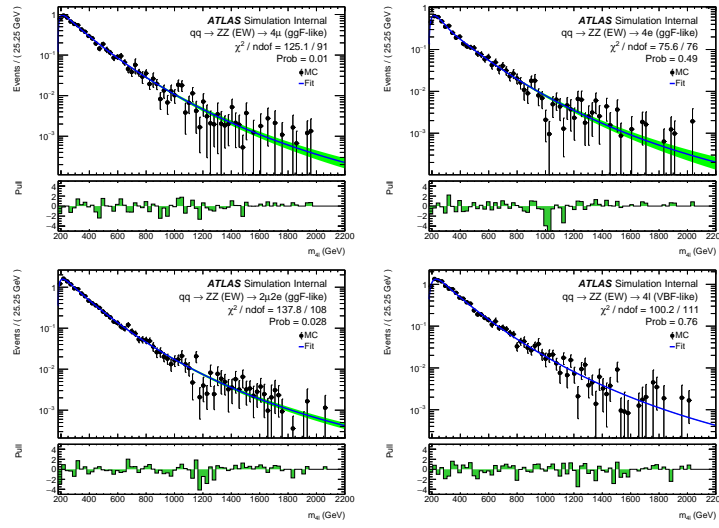


Fig. 7.11 Distributions of the $m_{4\ell}$ invariant mass fit projections of the $q\bar{q} \rightarrow ZZ$ (EW) background samples for the 4μ , $4e$ and $2\mu 2e$ final states in the ggF-CBA-enriched category, and the 4ℓ inclusive VBF-CBA-enriched category. Cut-based categorization is used.

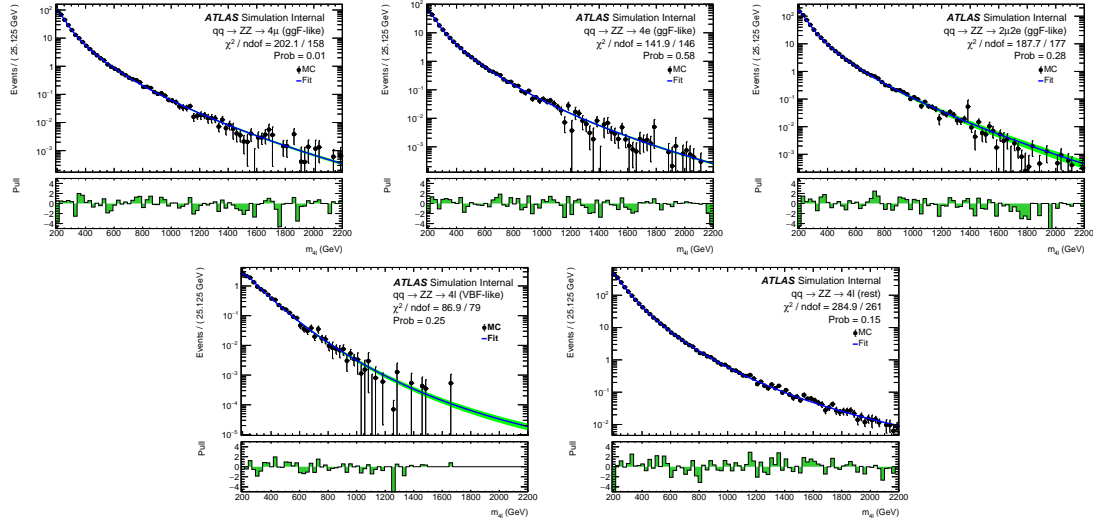


Fig. 7.12 Distributions of the $m_{4\ell}$ invariant mass fit projections of the $q\bar{q} \rightarrow ZZ$ background samples for the 4μ , $4e$ and $2\mu2e$ final states in the ggF-MVA-high category, the 4ℓ inclusive ggF-MVA-low category and VBF-MVA-enriched category. DNN-based categorization is used.

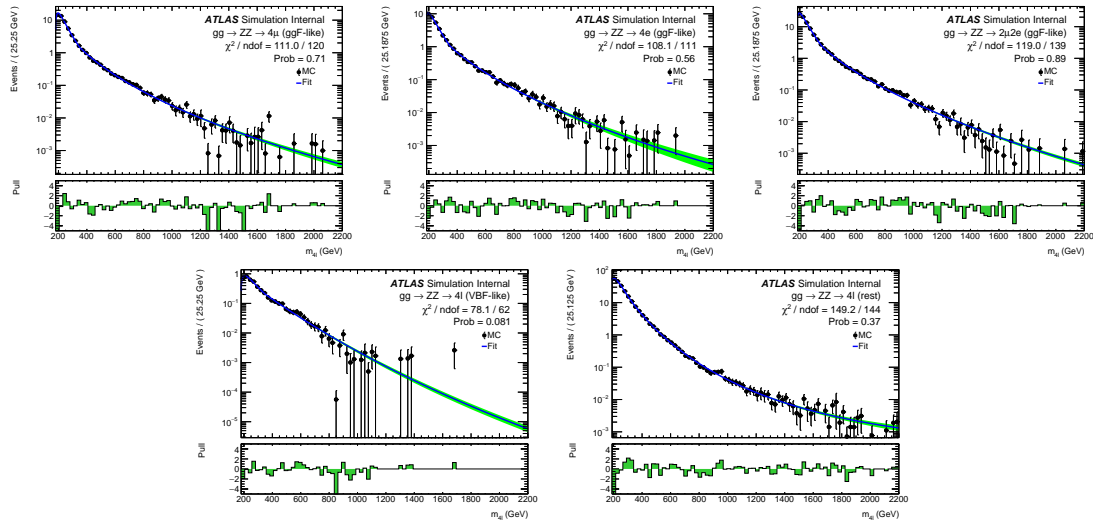


Fig. 7.13 Distributions of the $m_{4\ell}$ invariant mass fit projections of the $gg \rightarrow ZZ$ background samples for the 4μ , $4e$ and $2\mu2e$ final states in the ggF-MVA-high category, the 4ℓ inclusive ggF-MVA-low category and VBF-MVA-enriched category. DNN-based categorization is used.

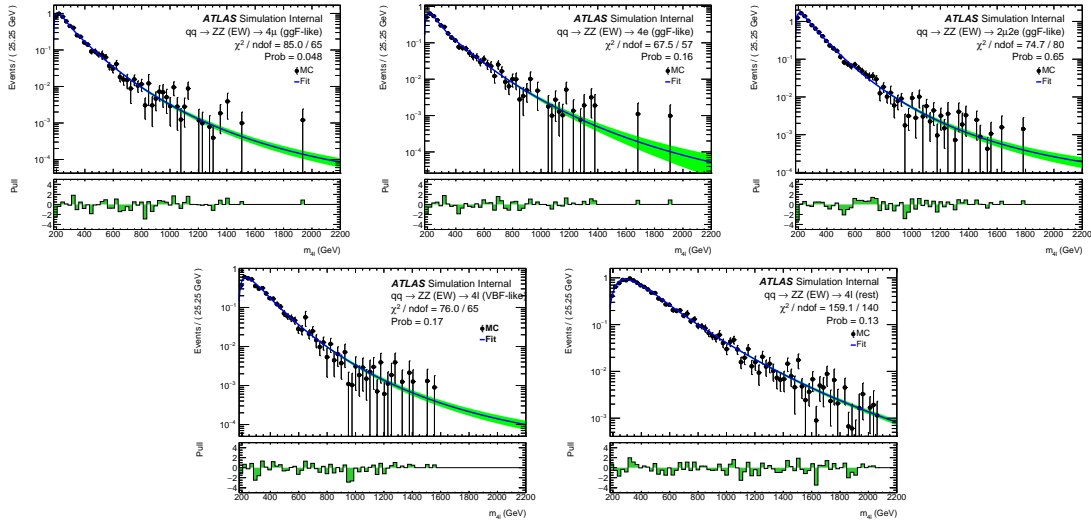


Fig. 7.14 Distributions of the $m_{4\ell}$ invariant mass fit projections of the $q\bar{q} \rightarrow ZZ$ (EW) background samples for the 4μ , $4e$ and $2\mu2e$ final states in the ggF-MVA-high category, the 4ℓ inclusive ggF-MVA-low category and VBF-MVA-enriched category. DNN-based categorization is used.

2608 7.4.2 Reducible backgrounds

2609 Similar as section 6.4, the reducible backgrounds include $Z+jets$ (consists of both
 2610 heavy- and light-flavour jets), top quark pair, and WZ production, which contain fake
 2611 and non-isolated leptons. The simulations are not very robust in terms of the selection
 2612 efficiencies. Thus, the data-driven method is applied to estimate the normalization of
 2613 those processes in different control regions (CRs). The estimations in this analysis are
 2614 performed separately for $\ell\ell + \mu\mu$ and $\ell\ell + ee$ final states, with slightly different approaches
 2615 for “muon” and “electron” backgrounds.

2616 The “electron” backgrounds mostly come from process of a Z boson with light-flavour
 2617 jets ($Z+LF$) misidentified as electrons. The large contribution of “muon” backgrounds
 2618 come from heavy-flavour jets produced in association with a Z boson ($Z+HF$) or in the
 2619 decays of top quark. The estimations are done following the common H4l studies without
 2620 a specific $m_{4\ell}$ range requirement^[105], and then the corresponding fraction of event yield
 2621 in $m_{4\ell} > 200$ GeV is calculated from MC simulation.

2622 $\ell\ell + \mu\mu$ final states

2623 The normalizations of “muon” backgrounds are extracted from simultaneous fits of
 2624 the leading lepton pair’s invariant mass (m_{12}) in four orthogonal CRs:

- 2625 • **Inverted d_0 CR:** this CR is formed by inverting the d_0 selection for at least one
 2626 lepton in subleading lepton pair while the leptons in leading pair are required to
 2627 pass all standard selection. This CR enhances $Z+HF$ and $t\bar{t}$ as leptons from heavy-

- flavour hadronic decays are characterised by large d_0 .
- $e\mu + \mu\mu$ **CR**: this CR is formed using an opposite-charge different-flavour dilepton in leading pair. It aims to enhance $t\bar{t}$ background as the leading lepton pair cannot come from Z boson decay.
 - **Inverted isolation CR**: in this CR, leptons in leading pair are required to satisfy all standard analysis selection, while for leptons in subleading pair, they are required to pass d_0 selection but have at least one of them failing isolation selection. This CR enhances the events from $Z+LF$ processes while suppress $Z+HF$ by d_0 cut.
 - **Same-sign CR**: in this CR, the leptons in subleading pair are required to have same-charge, while the leading pair still passes standard selection. This CR is not dominant by any specific background since all reducible backgrounds could have sizable contribution in it.

The fit results of normalizations are then propagated to signal region (SR) by applying transfer factors to account the difference of selection efficiencies between SR and CRs.

The transfer factors are computed using $Z + \mu$ MC samples.

$\ell\ell + ee$ final states

The “electron” backgrounds are estimated in $3\ell + X$ CR, where X denotes the lower p_T electron in the subleading pair. The selection and identification criterias for X are relaxed , while other three leptons must satisfy the standard selection. In this case, X could be a light-flavour jet, a photon conversion or an electron from heavy-flavour hadron decay. Moreover, the subleading pair is required to have same charge dilepton to ensure the orthogonality to the signal region. The normalization of backgrounds are obtained based on a fit to the number of hits in the innermost ID layer in CR, and the transfer factors are computed from $Z + e$ simulated sample.

The $m_{4\ell}$ shapes of reducible backgrounds are obtained from MC simulation in signal region, and then smoothed by an one-dimensional kernel estimation, which models the input data as a superposition of Gaussian kernels, one for each data point with contributing $1/N$ to total integral N ^[106]. The difference from using different smoothing strength (ρ) in kernel estimation is taken into account as additional shape uncertainties for these reducible backgrounds.

7.5 Signal modelling

The parameterization of $m_{4\ell}$ distributions based on simulated samples for signals are described in this section. Several signal models are studied, including heavy Higgs like

2661 narrow-width signal (NWA) and large-width signal (LWA), as well as the modelling of
2662 Randall-Sundrum graviton (RSG) signal.

2663 7.5.1 Modelling of narrow-width signal

2664 For narrow-width (NWA) signal, the $m_{4\ell}$ width is totally determined by detector reso-
2665 lution, which is modelled by the sum of a Crystal Ball (C) function^[107-108] and a Gaussian
2666 (G) function:

$$P_s(m_{4\ell}) = f_C \cdot C(m_{4\ell}; \mu, \sigma_C, \alpha_C, n_C) + (1 - f_C) \cdot G(m_{4\ell}; \mu, \sigma_G) \quad (7.3)$$

2667 The two functions share the same central value μ , while the resolution parameters, σ_C
2668 and σ_G , are different. In the Crystal Ball function, the parameters α_C and n_C model the
2669 shape of non-Gaussian tail, and the fraction parameter f_C is used to ensure the relative
2670 normalization between two functions.

2671 The parameters are obtained by fitting to signal MC simulations combining the mc16a,
2672 mc16d and mc16e campaigns for each category at each mass points from 200 GeV to
2673 2000 GeV respectively, and the shape of ggF and VBF signals are found to be similar.
2674 Figure 7.15 shows the $m_{4\ell}$ distribution and fitted curves for ggF production at mass from
2675 200 GeV to 2000 GeV in $2e2\mu$ channel as examples.

2676 Then the $C + G$ parameters are fitted with a polynomial function as the function of
2677 generated mass points (m_H), as an example shown in figure 7.16 for $2e2\mu$ channel. The
2678 fitting quality can be measured by the Pearson's χ^2 , which is within 3 (2) for $2e2\mu$ ($4e$ and
2679 4μ) channel.

2680 In addition, possible difference on the signal yield extracted from parameterization and
2681 MC simulation is studied. Figure 7.17 shows this difference by computing $\frac{N_{\text{reco}} - N_{\text{fit}}}{N_{\text{fit}}}$, where
2682 N_{reco} denotes the total number of reconstructed events observed from MC simulation at
2683 that mass point and N_{fit} depicts the number of events obtained from the fitted PDF. The
2684 differences are treated as an additional systematic uncertainty with the value of 2% (1%)
2685 for $2e2\mu$ ($4e$ and 4μ) channel in statistical fit.

2686 In summary, the final interpolated signal shapes for the ggF production mode are
2687 shown together in figure 7.18 for mass points with step of 100 GeV from 200 GeV to
2688 3000 GeV.

2689 7.5.2 Modelling of large-width signal

2690 The $m_{4\ell}$ shape of heavy Higgs model in large-width (LWA) hypothesis can be de-
2691 scribed by a convolution of a truth distribution and a resolution from detector effect. The

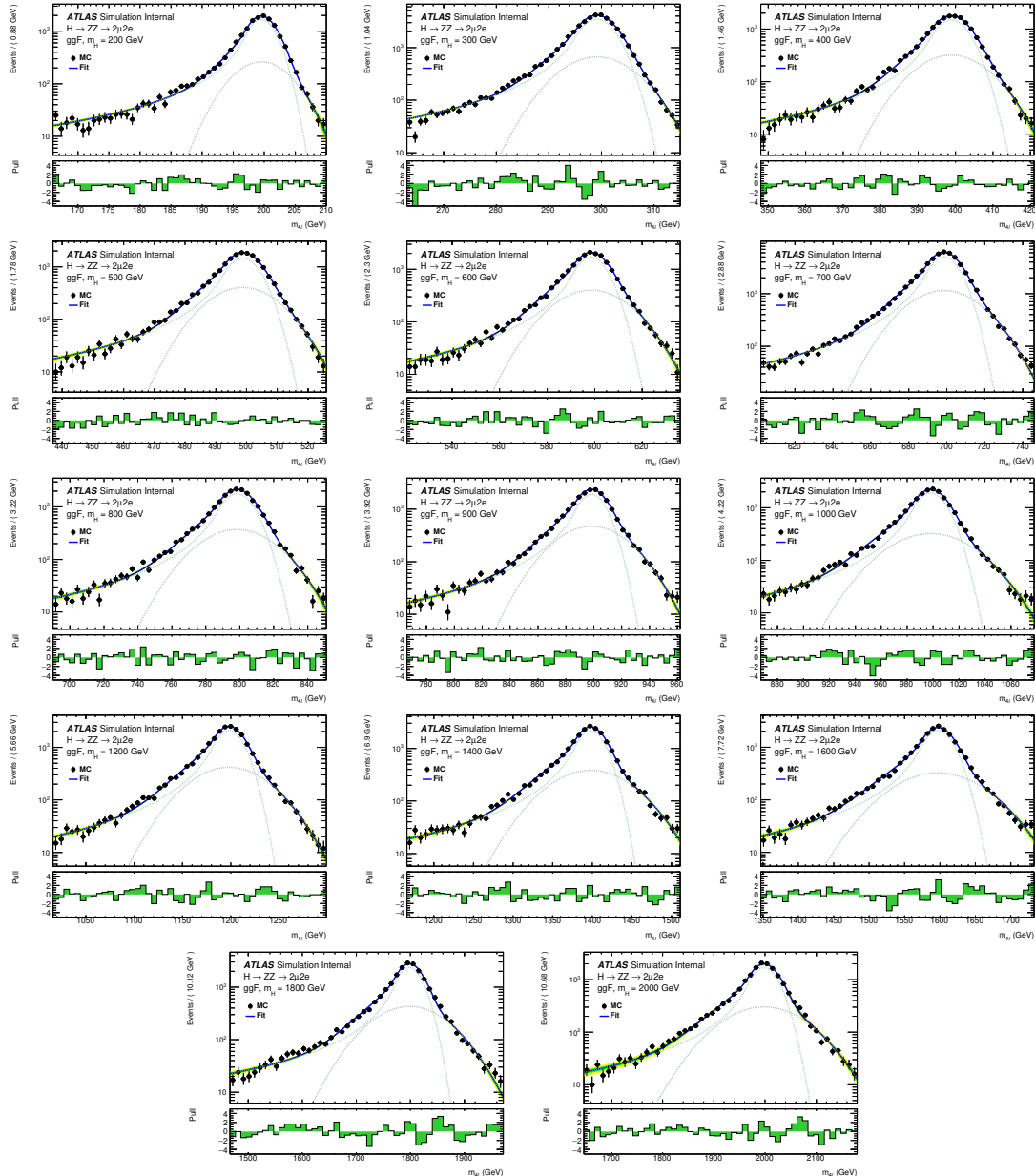


Fig. 7.15 Distributions of the $m_{2\mu 2e}$ and fit projection for signal samples between 200 to 3000 GeV for ggF production mode. Three MC campaigns, mc16a, mc16d and mc16e, are combined. The lower panel in each plot shows the pull distribution.

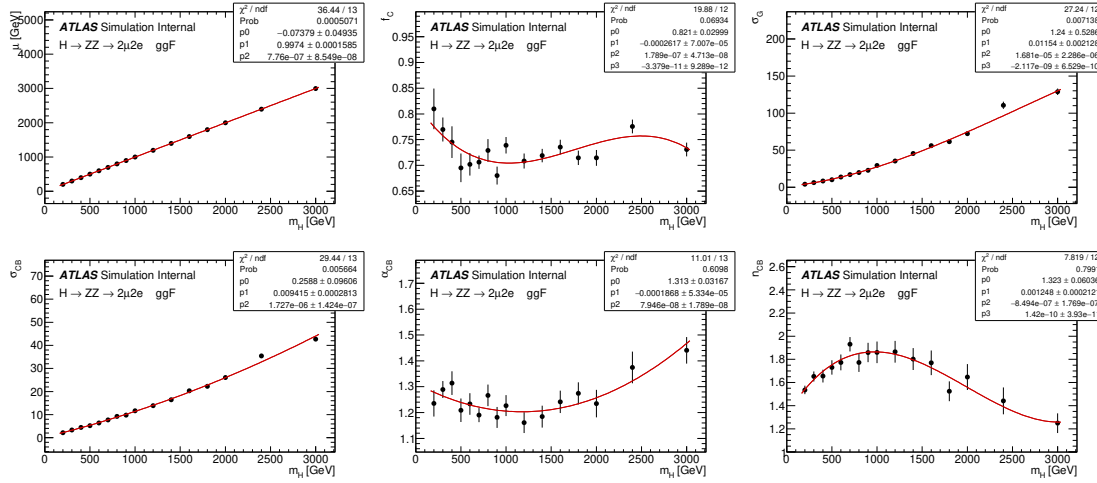


Fig. 7.16 Polynomial fits of the parameters μ , f_c , σ_G , σ_C , n_c and α_c for the signal $\mathcal{C} + \mathcal{G}$ model in the $2\mu 2e$ channel as a function of m_H for the ggF production mode. The combination of the mc16a, mc16d and mc16e MC campaigns is used.

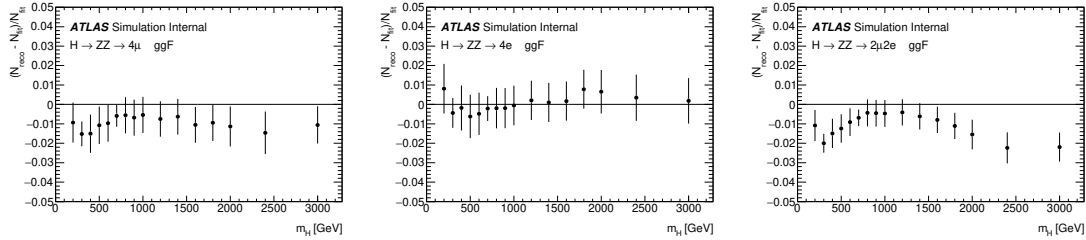


Fig. 7.17 The difference between MC simulation and parameterization of 4μ (left), $4e$ (middle) and $2\mu 2e$ (right) for the ggF production mode. The combination of the mc16a, mc16d and mc16e MC campaigns is used.

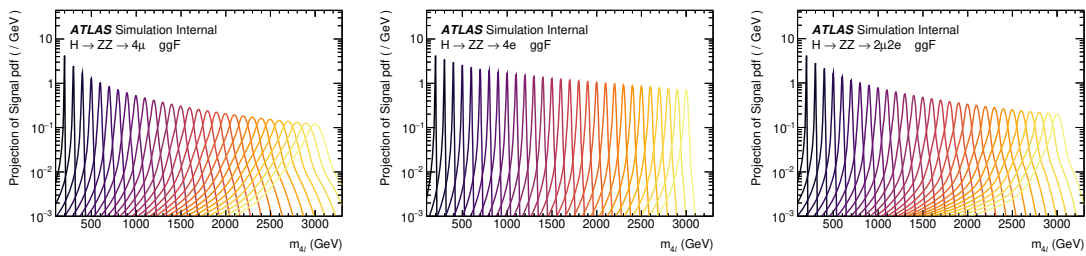


Fig. 7.18 The final signal shapes for the ggF production mode, interpolated from the polynomial fit parameters.

detector resolution effect is the one modelled by the function described in NWA parameterization, as in NWA model the truth level width is negligible.

The differential parton cross section for the heavy Higgs model can be written as^[109]:

$$\sigma_{gg \rightarrow H \rightarrow ZZ}(s) = \frac{1}{2s} \int d\Omega |A_{gg \rightarrow H}(s, \Omega)|^2 \frac{1}{|s - s_H|^2} |A_{H \rightarrow ZZ}(s, \Omega)|^2 \quad (7.4)$$

where $A_{gg \rightarrow H}(s, \Omega)$ and $A_{H \rightarrow ZZ}(s, \Omega)$ are corresponding Higgs production and decay amplitudes, and $\frac{1}{|s - s_H|}$ denotes the Higgs propagator and Ω represents the phase space of the process.

Using the definition of a partial width,

$$\Gamma_{H \rightarrow F}(s) = \frac{1}{2\sqrt{s}} \int d\Omega |A_{H \rightarrow F}(s, \Omega)|^2 \quad (7.5)$$

the parton cross section can be rewritten as,

$$\sigma_{gg \rightarrow H \rightarrow ZZ}(s) = 2 \frac{1}{|s - s_H|^2} \times \Gamma_{H \rightarrow gg}(s) \times \Gamma_{H \rightarrow ZZ}(s) \quad (7.6)$$

with the components computed in Ref^[109-110]:

$$\begin{aligned} \frac{1}{s - s_H} &= \frac{1 + i \cdot \bar{\Gamma}_H / \bar{m}_H}{s - \bar{m}_H^2 + i \cdot s \cdot \bar{\Gamma}_H / \bar{m}_H} \\ \bar{m}_H &= \sqrt{\bar{\Gamma}_H^2 + m_H^2} \\ \bar{\Gamma}_H &= \bar{m}_H \cdot \frac{\Gamma_H}{m_H} \end{aligned} \quad (7.7)$$

$$\Gamma_{H \rightarrow ZZ}(s) = C \cdot s^{\frac{3}{2}} \cdot \left[1 - \frac{4m_Z^2}{s} + \frac{3}{4} \left(\frac{4m_Z^2}{s} \right)^2 \right] \cdot \left[1 - \frac{4m_Z^2}{s} \right]^{\frac{1}{2}} \quad (7.8)$$

$$\begin{aligned} \Gamma_{H \rightarrow gg}(s) &= C \cdot s^{\frac{3}{2}} \cdot |A_t(\tau_t)|^2 \\ A_t(\tau) &= 2 \frac{\tau + (\tau - 1)f(\tau)}{\tau^2} \\ \tau_t &= \frac{s}{4m_t^2} \\ f(\tau) &= \begin{cases} \arcsin^2(\sqrt{\tau}), & \tau \leq 1 \\ -\frac{1}{4} \left[\log \frac{1+\sqrt{1-\tau^{-1}}}{1-\sqrt{1-\tau^{-1}}} - i\pi \right]^2, & \tau > 1 \end{cases} \end{aligned} \quad (7.9)$$

where m_f stands for the mass of a fermion f , and Γ_H denotes an assumed total width of the heavy Higgs boson.

At the LHC, the $m_{4\ell}$ line shape can be defined by a hadron cross section that is derived from equation 7.6 by multiplication with gluon-gluon luminosity \mathcal{L}_{gg} described in^[11]. Meanwhile, the cross section is rewritten as a function of $m_{4\ell}$ instead of s , which will give an extra power of mass dependence in the formula:

$$\sigma_{pp \rightarrow H \rightarrow ZZ}(m_{4\ell}) = 2 \cdot m_{4\ell} \cdot \mathcal{L}_{gg} \cdot \frac{1}{|s - s_H|^2} \cdot \Gamma_{H \rightarrow gg}(m_{4\ell}^2) \cdot \Gamma_{H \rightarrow ZZ}(m_{4\ell}^2) \quad (7.10)$$

The analytical shapes of truth level $m_{4\ell}$ distribution of gg2VV MC samples is shown on figure 7.19.

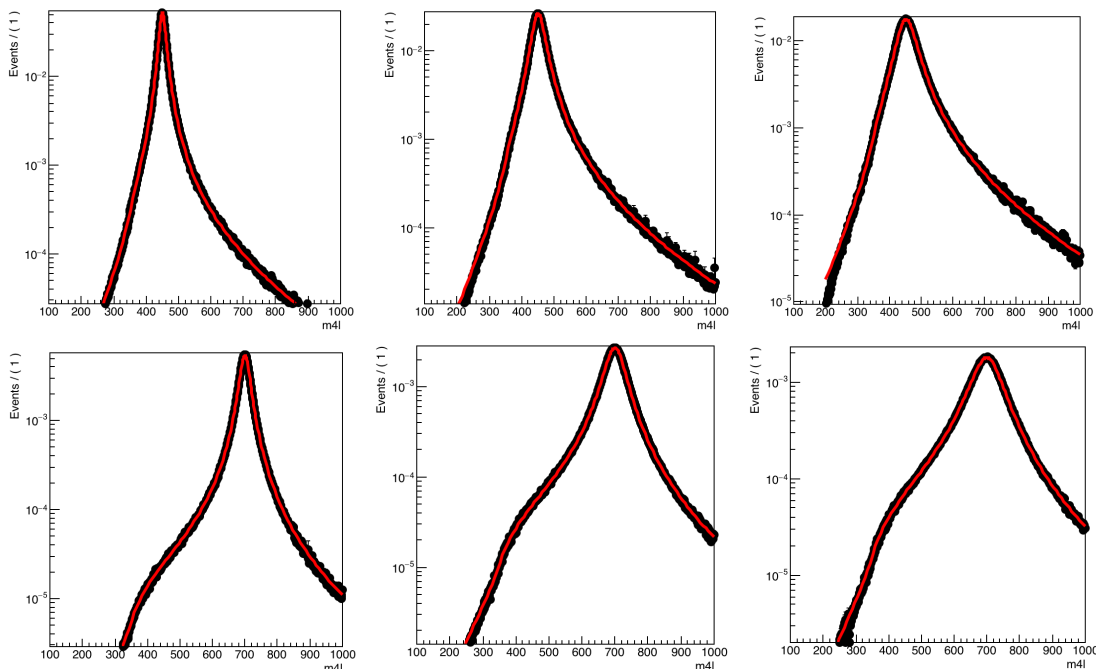


Fig. 7.19 Comparison of the analytical shape to a truth $m_{4\ell}$ distribution of gg2VV MC samples for $m_H = 450$ GeV (top), 700 GeV (bottom) and width equal to 5% (left), 10% (middle), 15% (right) of the mass.

The reconstruction level signal shape can then be modelled by the analytical truth shape convoluted with detector effects modelled in section 7.5.1. A comparison between the modelled shape and reconstruction level MC simulation for signal mass above 400 GeV (for ggF production in $2e2\mu$ channel as an example) are shown in figure 7.20, the shapes are well compatible between each other. This modelling is not valid for lower masses due to the rapid change of detector resolution.

7.5.3 Modelling of interference

There are three processes sharing the same gg initial state and ZZ final state:

- The SM $gg \rightarrow ZZ$ process with an amplitude A_B

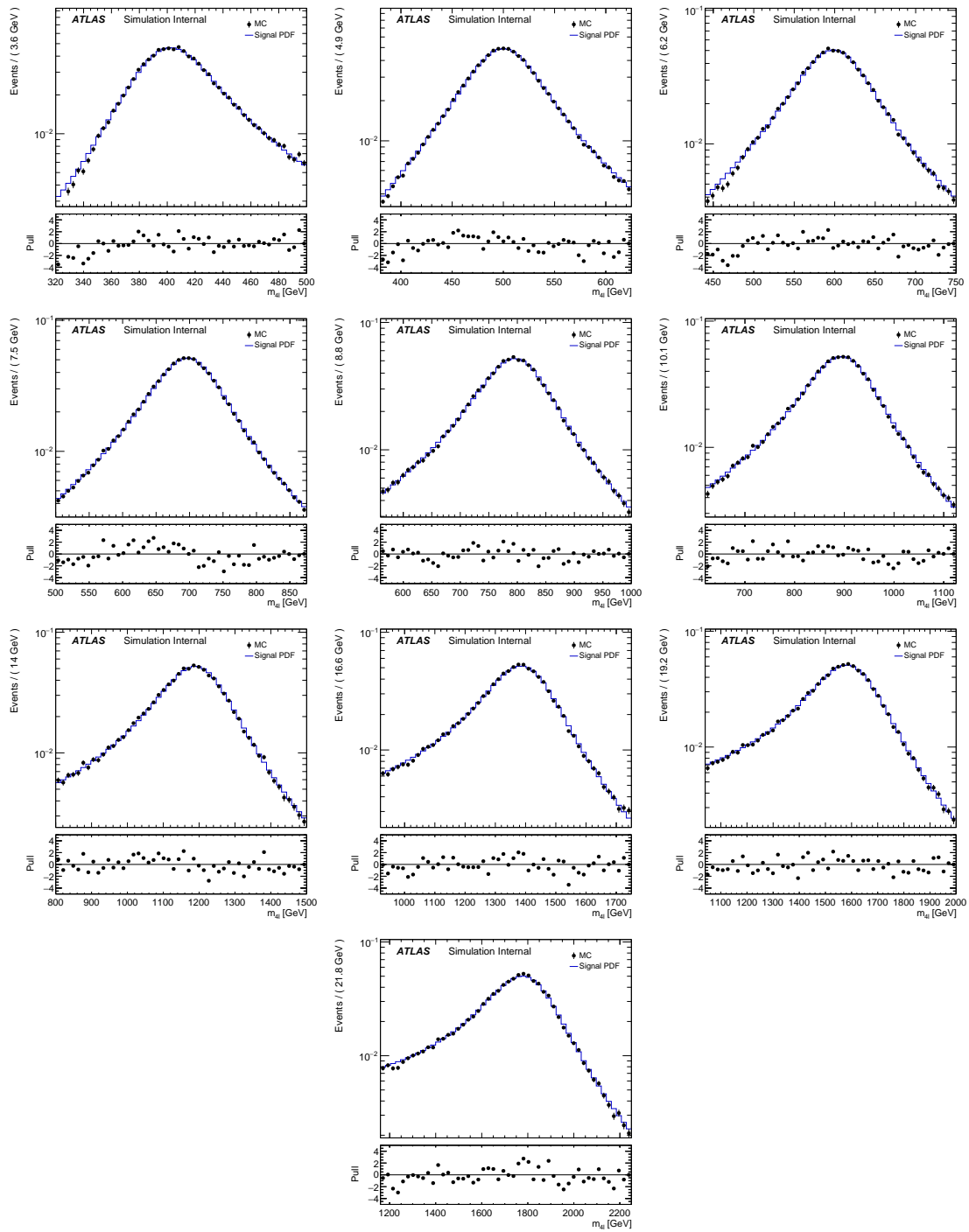


Fig. 7.20 Comparison between the analytical shape convoluted with detector effects and the reconstructed $m_{2\mu 2e}$ MC distribution for mass points ranging from 400 to 1800 GeV and width equal to 15% of the mass.

- The SM (light) Higgs at mass of around 125 GeV with an amplitude A_h
 - The BSM heavy Higgs we are searching in this analysis with an amplitude A_H
- The three processes can interfere with each other due to the same initial and final states.
- The parton cross section for these processes can be written as:

$$\begin{aligned}
 \sigma_{gg \rightarrow (X) \rightarrow ZZ}(s) &= \frac{1}{2s} \int d\Omega |A_h(s, \Omega) + A_H(s, \Omega) + A_B(s, \Omega)|^2 \\
 &= \frac{1}{2s} \int d\Omega \left(|A_h(s, \Omega)|^2 + |A_H(s, \Omega)|^2 + |A_B(s, \Omega)|^2 \right) + \\
 &\quad + \frac{1}{s} \int d\Omega \left(\text{Re} [A_h(s, \Omega) \cdot A_B^*(s, \Omega)] \right. \\
 &\quad \left. + \text{Re} [A_H(s, \Omega) \cdot A_B^*(s, \Omega)] + \text{Re} [A_H(s, \Omega) \cdot A_h^*(s, \Omega)] \right) \\
 &\quad + \frac{1}{s} \text{Re} \left[\frac{1}{s - s_H} \int d\Omega \cdot A_H^P(s, \Omega) \cdot A_H^D(s, \Omega) \cdot A_B^*(s, \Omega) \right] \\
 &\quad + \frac{1}{s} \int d\Omega \cdot \text{Re} \left[A_H^P(s, \Omega) \cdot \frac{1}{s - s_H} \cdot A_H^D(s, \Omega) \cdot A_h^{P*}(s, \Omega) \cdot \frac{1}{(s - s_h)^*} \cdot A_h^{D*}(s, \Omega) \right]
 \end{aligned} \tag{7.11}$$

The first term in equation 7.11 denotes the on-shell SM Higgs contribution, which is negligible in this analysis. The second term corresponds to the heavy Higgs contribution, whose line shape has been described in previous section. The third term is the $gg \rightarrow ZZ$ continuum process, while the forth term is the interference between SM Higgs and $gg \rightarrow ZZ$ continuum. The fifth and sixth terms are the interferences between heavy Higgs and $gg \rightarrow ZZ$ continuum (H-B), and between heavy Higgs and SM Higgs (H-h) that we are interested in. More details about the parameterization of these two interferences are described as below.

1. Interference between heavy Higgs and $gg \rightarrow ZZ$ continuum

The parton cross section of this interference term has been written down in equation 7.11. By assuming that this function has a smooth behaviour, it can be replaced with complex polynomial:

$$\int d\Omega \cdot A_H^P(s, \Omega) \cdot A_H^D(s, \Omega) \cdot A_B^*(s, \Omega) \approx (a_0 + a_1 \cdot \sqrt{s} + \dots) + i \cdot (b_0 + b_1 \cdot \sqrt{s} + \dots) \tag{7.12}$$

The parameters a_i and b_i can be extracted by fitting to the $m_{4\ell}$ distribution from truth level MC simulation after analysis selection. Since the signal mass and width does not enter into this function, the parameters should be independent for every tested signal hypothesis.

Same as description for equation 7.10, the parton cross section can be transformed

2738 into a hadron cross section as a function of $m_{4\ell}$:

$$\sigma_{pp}(m_{4\ell}) = \mathcal{L}_{gg} \cdot \frac{1}{m_{4\ell}} \cdot \text{Re} \left[\frac{1}{s - s_H} \cdot ((a_0 + a_1 \cdot m_{4\ell} + \dots) + i \cdot (b_0 + b_1 \cdot m_{4\ell} + \dots)) \right] \quad (7.13)$$

2739 where the propagators are shown in equation 7.7.

2740 Figure 7.21 shows the distributions of interference function obtained by simultaneous
2741 fitting to $m_{4\ell}$ shape from truth level H-B interference simulation at different mass in $2e2\mu$
2742 channel as an example.

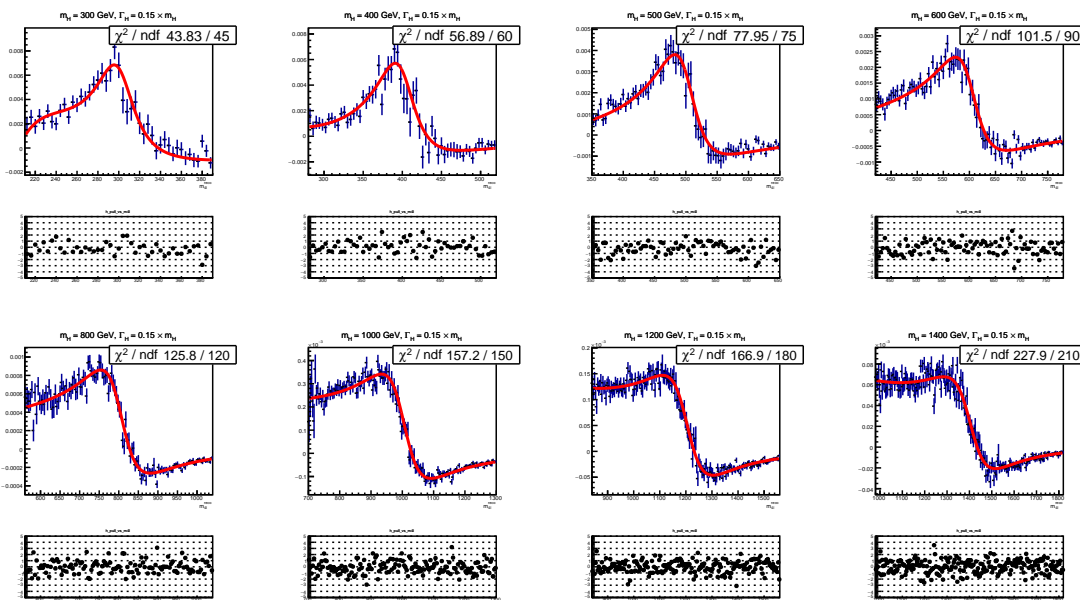


Fig. 7.21 The interference (H-B) model fitted to the truth $m_{4\ell}$ MC distribution after signal region selection for $2\mu2e$ channel.

2743 2. Interference between heavy Higgs and SM Higgs

2744 The parton cross section of this interference term has been written down in equa-
2745 tion 7.11. By assuming the production and decay amplitudes are the same for heavy Higgs
2746 boson and SM Higgs boson, the cross section function can be simplified to:

$$\sigma_{gg}(s) = \frac{1}{s} \int d\Omega \cdot \text{Re} \left[\frac{1}{s - s_H} \cdot \frac{1}{(s - s_h)^*} \right] \cdot |A_{gg \rightarrow H}(s, \Omega)|^2 |A_{H \rightarrow ZZ}(s, \Omega)|^2 \quad (7.14)$$

2747 Taking into account Equation 7.5:

$$\sigma_{gg}(s) = 4 \cdot \text{Re} \left[\frac{1}{s - s_H} \cdot \frac{1}{(s - s_h)^*} \right] \cdot \Gamma_{H \rightarrow gg}(s) \cdot \Gamma_{H \rightarrow ZZ}(s) \quad (7.15)$$

2748 where the propagators are described in equation 7.7, and the partial widths are de-
2749 scribed in equations 7.8 and 7.9.

2750 Same as previous procedure, the parton cross section can be transformed to a hadron
 2751 cross section as a function of $m_{4\ell}$:

$$\sigma_{pp}(m_{4\ell}) = 4 \cdot m_{4\ell} \cdot \mathcal{L}_{gg} \cdot \text{Re} \left[\frac{1}{s - s_H} \cdot \frac{1}{(s - s_h)^*} \right] \cdot \Gamma_{H \rightarrow gg}(m_{4\ell}) \cdot \Gamma_{H \rightarrow ZZ}(m_{4\ell}) \quad (7.16)$$

2752 The modelling procedure of interference is the same as the way for large-width signal
 2753 described in section 7.5.2. The truth line shape is measured as analytical function from
 2754 equation 7.16, and then convolute with detector effect from NWA parameterization to get
 2755 the reconstruction level shape.

2756 For LWA signal model, these two interferences are carefully token into account, and
 2757 the integration of the pure LWA signal with the interferences is used for further studies.
 2758 Figure 7.22 shows the signal model for large-width scenario at mass points of 400 GeV,
 2759 600 GeV, 800 GeV, for three different signal widths: 5%, 10%, 15%, with and without
 2760 interference. Additionally, the contribution of the interference between heavy Higgs and
 2761 SM Higgs (H-h) is shown together with the one between heavy Higgs and SM $gg \rightarrow$
 2762 ZZ background (H-b). One can see the interference effect on signal shape becomes less
 2763 important when going to higher mass.

2764 7.5.4 Modelling of spin-2 RS Graviton signal

2765 The search for Randall-Sundrum (RS) graviton is performed in mass region between
 2766 600 to 2000 GeV. The width of resonance is determined by the $k/\overline{M}_{\text{Planck}}$, which, as
 2767 mentioned in section 7.2.3, is set to be 1. In this configuration, the width of signal is
 2768 expected to be about 6% of its mass.

The reconstructed $m_{4\ell}$ lineshape of graviton is also built by convolving the truth-level lineshape with a detector resolution function, where the detector resolution effect is modelled by a Gaussian + Crystal Ball function, whose parameters are taken from the NWA signal parameterization in section 7.5.1. And for truth-level shape, for graviton, it's modelled as the product of a relativistic Breit-Wigner (RBW) term, a term corresponding to the squared matrix element of the production process and a parton luminosity term \mathcal{L} as given in [112]. So the truth lineshape of $m_{4\ell}$ is token from:

$$m_{4\ell}^{\text{Truth}} \sim \mathcal{L}_{gg} \cdot s^2 \cdot \frac{s(1+s)(1+2s+2s^2)}{(s^2 - m_G^2)^2 + m_G^2 \Gamma^2}$$

2769 The truth-level signal model is extracted by fitting to MC simulation at truth-level with
 2770 the mass m_G and width Γ parameters floating at each mass points respectively. And then

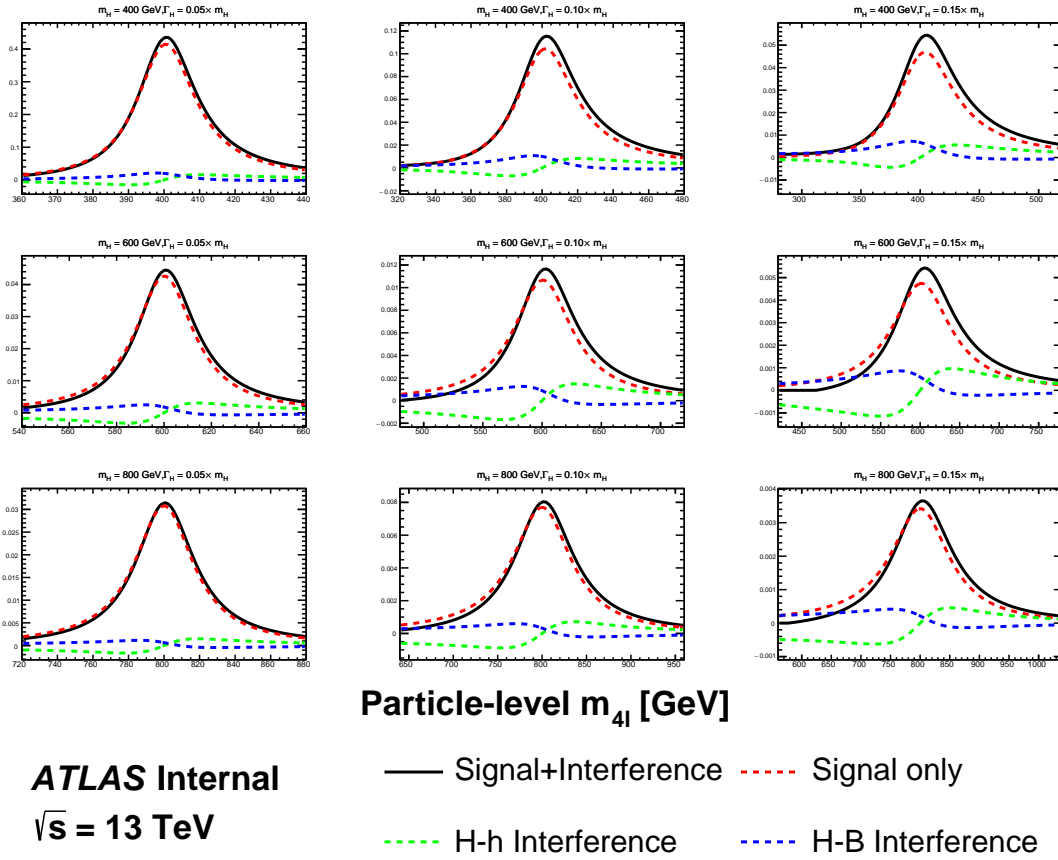


Fig. 7.22 The signal modelling for the large-width scenario at m_H of 400 GeV (top), 600 GeV (middle) and 800 GeV (bottom), as well as three different signal width: 5% (left), 10% (middle) and 15% (right). The contribution of the interference between heavy Higgs and SM Higgs (H - h) is shown together with the one between heavy Higgs and SM $gg \rightarrow ZZ$ background (H - b).

the two parameters are parameterized as the function of m_H by a linear fit as shown in figure 7.23.

The final signal model is obtained by convolving the truth-level lineshape with the detector resolution function. To verify the result, figure 7.24 compares the $m_{4\ell}$ lineshape from parameterization with the one observed from reconstructed-level MC simulation in $2e2\mu$ channel at masses of 600 GeV, 1600 GeV and 2000 GeV as examples.

7.6 Systematic uncertainties

This section describes the sources and value of theoretical and experimental systematic uncertainties considered in this analysis. In addition, as mentioned in previous sections, the uncertainties of irreducible background modelling, reducible background shape smoothing procedure and signal yield difference between simulation and parameterization

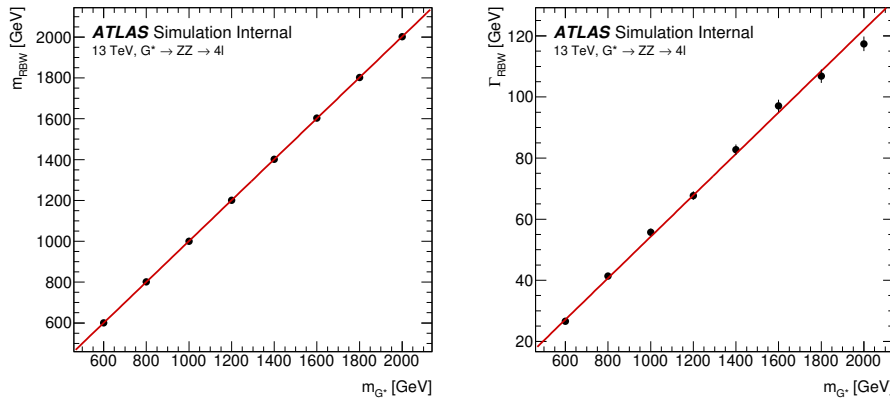


Fig. 7.23 Fitted parameters of the graviton RBW, m_{RBW} and Γ_{RBW} , as a function of the graviton resonance mass, m_G .

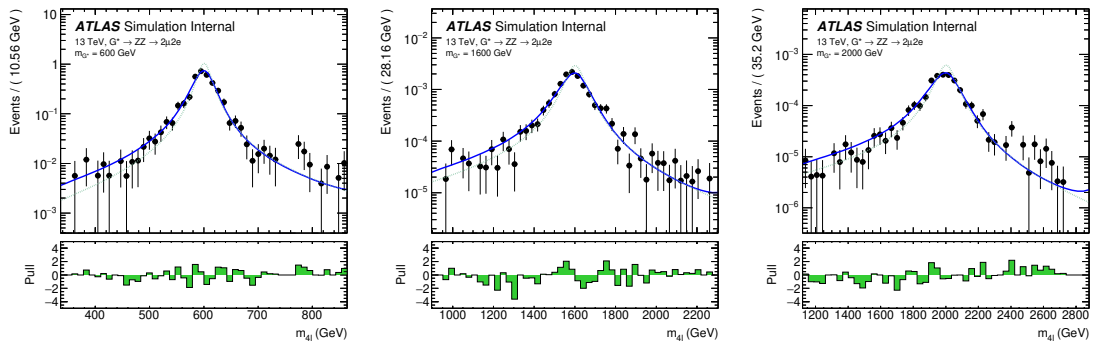


Fig. 7.24 Reconstructed m_{4l} distributions in the $2\mu 2e$ channel with the final signal model superimposed for each RS graviton signal sample at masses of 600 GeV, 1600 GeV and 2000 GeV. The lower panel in each plot shows the pull distribution. The dashed green lines show the truth-level graviton signal models for reference.

2782 are all taken into account.

7.6.1 Theoretical uncertainties

2784 The theoretical modelling uncertainties include the PDF variations, missing QCD
 2785 higher-order corrections via the variations of factorisation and renormalization scales, and
 2786 the parton showering uncertainties.

1. Theoretical uncertainties for signal

2788 The PDF, QCD scale and parton showering uncertainties affecting the acceptance difference originating from analysis selection for signal are taken into account in different categories. The acceptance uncertainties are calculated on the acceptance factor which 2790 extrapolates from the fiducial space to the full phase space by a simple ratio:

$$A = \frac{N_{fiducial}}{N_{total}} \quad (7.17)$$

2792 For PDF uncertainties, the standard derivations of 100 PDF replicas of NNPDF3.0
 2793 NNLO, as well as comparison to two external PDF sets: MMHT2014 NNLO, CT14
 2794 NNLO are considered. For missing QCD higher-order corrections, the effects are studied
 2795 with truth events by comparing weights corresponding to variations of the renormalization
 2796 and factorization scale factors, up and down by a factor of two, and the envelop of different
 2797 variations is used. The parton showering uncertainties are estimated by comparing events
 2798 with different setting via PYTHIA8.

2799 Systematic uncertainties are studied for both cut- and MVA- based event categorizations, in two different categories: the inclusive ggF-CBA-enriched and VBF-CBA-enriched category for cut-based analysis and in three different categories: inclusive ggF-MVA-high, ggF-MVA-low and VBF-MVA-enriched category for MVA-based one. This section shows the MVA-based results as an example.

2804 Table 7.10 and 7.11 show the theoretical uncertainties mentioned above for ggF and
 2805 VBF signal respectively in MVA-based categorization.

Table 7.10 Summary of acceptance uncertainties of PDF, QCD scale and parton shower variations for ggF production. The MVA-based categorization is used.

Categories	PDF	QCD Scale	Parton Shower
ggF-MVA-high	0.40%	0.06%	2.03%
ggF-MVA-low	0.56%	0.07%	4.86%
VBF-MVA-enriched	0.53%	0.09%	3.43%

Table 7.11 Summary of acceptance uncertainties of PDF, QCD scale and parton shower variations for VBF production. The MVA-based categorization is used.

Categories	PDF	QCD Scale	Parton Shower
ggF-MVA-high	0.18%	1.20%	0.41%
ggF-MVA-low	0.43%	0.26%	0.36%
VBF-MVA-enriched	0.23%	3.19%	0.85%

2806 **2. Theoretical uncertainties for SM background processes**

2807 The theoretical uncertainties of irreducible ZZ backgrounds are considered in terms
 2808 of both the variations of shape of $m_{4\ell}$ distributions and the acceptance originating from
 2809 the event selection.

2810 The PDF and QCD scale uncertainties are considered by using the same method as
 2811 described for signal. The parton showering uncertainties for those SHERPA samples are
 2812 evaluated by varying the resummation scale by a factor of 2, changing the CKKW setting
 2813 and using different showering option, following the PMG recommendation in ref.^[113],
 2814 and the quadratic sum between the uncertainties in different kinds of showering option

2815 is taken as final result of uncertainties. Moreover, the shape uncertainty associated with
2816 electroweak higher-order correction for $q\bar{q} \rightarrow ZZ$ process is also taken into account.

2817 Same as for signals, these theoretical uncertainties for irreducible backgrounds are
2818 studied for both cut- and MVA- based event categorizations. The value of shape uncer-
2819 tainties vary from less than 1% at low mass region to 50% at high mass tail due to large
2820 statistic fluctuation. As for the acceptance uncertainties, the values vary from about 1%
2821 for PDF variations to 40% for parton showering variations. The VBF category has relative
2822 larger uncertainties.

2823 Table 7.12 summarizes the acceptance uncertainties of PDF, QCD scale, and parton
2824 showering variations for the dominant background: $q\bar{q} \rightarrow ZZ$.

**Table 7.12 Summary of acceptance uncertainties of PDF, scale, and parton showering varia-
tions for QCD $q\bar{q} \rightarrow ZZ$ background. The MVA-based categorization is used.**

Categories	PDF	QCD Scale	Parton showering
ggF-MVA-high	1.15%	10.16 %	3.71%
ggF-MVA-low	1.04%	3.26 %	3.80%
VBF-MVA-enriched	2.91%	27.90 %	23.82%

2825

7.6.2 Experimental systematics

2826 The signal and background predictions used in this analysis are also affected by vari-
2827 ous sources of experimental systematic uncertainties. Similar as described in section 6.5.2,
2828 the dominant experimental uncertainties in this analysis come from the energy/momentum
2829 scales and reconstruction and identification efficiencies of the leptons and jets, as well as
2830 the luminosity uncertainty. The systematic uncertainties are calculated using the recom-
2831 mendations from the Combined Performance (CP) groups of ATLAS experiment. Ta-
2832 ble 7.13 summarizes the experimental systematics considered in this analysis that affect
2833 either the normalization of total event yield or the shape of $m_{4\ell}$ distribution. The impact
2834 of those systematics in statistical fit are studied in section 7.7.

2835

7.7 Results in $\ell\ell\ell'\ell'$ channel

2836 The statistical treatment in searching for heavy resonances in $ZZ \rightarrow \ell\ell\ell'\ell'$ final state
2837 is described in this section. Results are presented in both cut- and MVA- based analysis.

2838 7.7.1 Statistical procedure

2839 The upper limits on heavy resonances are obtained using the unbinned profile likelihood fits. $m_{4\ell}$ is the discriminant. The likelihood function is a product of a Poisson term
 2840 representing the probability of observing n events and a weighted sum of both signal and
 2841 background probability distribution functions (PDFs) evaluated at all observed events.

$$L(x_1..x_n|\sigma_{ggF}, \sigma_{VBF}) = \text{Pois}(n|S_{ggF} + S_{VBF} + B) \left[\prod_{i=1}^n \frac{S_{ggF}f_{ggF}(x_i) + S_{VBF}f_{VBF}(x_i) + Bf_B(x_i)}{S_{ggF} + S_{VBF} + B} \right] \quad (7.18)$$

2843 where f_X s are the probability distribution functions of signal and backgrounds modelled
 2844 in section 7.5 and 7.4, S_X and B are the normalizations of signal and sum of backgrounds.

2845 The parameters of interest (POI) in the search is σ_{ggF} (and σ_{VBF} only for NWA signal),
 2846 which is the cross section of signal model in ggF (and VBF) production mode. In the case
 2847 of there are two POIs, when testing one POI, the other one is profiled along with other
 2848 nuisance parameters (except left unconstrained) during the minimization. These POIs
 2849 enter the likelihood inside the expected signal yields S_{ggF} and S_{VBF} as:

$$S_{ggF(VBF)} = \sigma_{ggF(VBF)} \times BR(S \rightarrow ZZ) \times A \times C \times \int \mathcal{L} \quad (7.19)$$

2850 where $A \times C$ is the signal acceptance as parameterized in 7.3.4, and $\int \mathcal{L} = 139 \text{ fb}^{-1}$ is the
 2851 integrated luminosity of the dataset.

2852 The dependence of the expected number of signal and background events (normaliza-
 2853 tions) and the shape of the PDFs on the systematic uncertainties measured in section 7.6
 2854 is described by a set of nuisance parameters (NPs) θ_i . The Gaussian constraints are ap-
 2855 plied to those NPs. The constraints are implemented as additional ‘penalty’ terms added
 2856 to the likelihood which increase the negative log-likelihood when any nuisance parameter
 2857 is shifted from its nominal value. The final likelihood function $L(\sigma_{ggF}, \sigma_{VBF}, m_H, \theta_i)$ is
 2858 therefore a function of $\sigma_{ggF}, \sigma_{VBF}, m_H$, and θ_i .

2859 Furthermore, the normalization of SM background $pp \rightarrow ZZ$, including both $q\bar{q} \rightarrow$
 2860 ZZ and $gg \rightarrow ZZ$, is a free parameter (μ_{ZZ}) and profiled during the minimization.
 2861 Floating ZZ normalization in fit takes the advantage of reducing the dependence on the-
 2862 ory predictions and their associated uncertainties, especially given that the increased data
 2863 luminosity would provide precise determination of the SM ZZ background rate.

2864 At the end, the upper limit on production cross-section $\sigma_{ggF(VBF)}$ at a given heavy
 2865 resonance model is obtained by setting the mass of signal m_H parameter as constant at the
 2866 desired value, and maximising the likelihood function with respect to nuisance parameters.

2867 The CL_s ^[114] method is used to obtain exclusion limits.

2868 7.7.2 For to likelihood function under background-only hypothesis for
2869 MVA-based analysis

2870 Both MVA- and cut-based analysis are studied by performing likelihood fit to the
2871 (pseudo-) data under the background-only hypothesis and under different signal models.
2872 Due to the same background estimation and modelling procedures, as well as the same
2873 method of systematic measurements, this section only shows the results of background-
2874 only fits for MVA-based analysis under the model of heavy Higgs resonance with narrow-
2875 width as an example. The final results of interpretation in both MVA- and cut- based
2876 analysis in all signal models described in section 7.5 will be measured in next section.

2877 First of all, table 7.14 summarized the expected and observed number of events for
2878 region of $m_{4\ell} > 200$ GeV together with their systematic uncertainties after background-
2879 only fit. The post-fit $m_{4\ell}$ spectrum in each category is shown in figure 7.25.

2880 To inspect the likelihood model, pulls and constraints as well as the correlation matrix
2881 of NPs are studied by performing a background only fit. Figure 7.26 shows the pulls and
2882 constraints when fitting to pseudo-data (top) and observed data (bottom). Figure 7.27
2883 shows the correlation matrix, only for NPs with correlation between each others greater
2884 than 0.1 when fitting to pseudo-data. The normalization of ZZ background is taken from
2885 data for one category each, as shown in table 7.15.

2886 The impact of a systematic uncertainty on the result depends on the production mode
2887 and the mass hypothesis. To check the impact of systematic uncertainties on expected sig-
2888 nal sensitivity, a NP ranking study is performed using signal injected Asimov data with
2889 the injected cross section close to 95% CLs upper limit at the masses of 400 GeV and
2890 1000 GeV. The results are shown in table 7.16. For ggF production, at lower masses, the
2891 systematic uncertainties of parton showering variation for signal, the luminosity uncer-
2892 tainty, and the parametrization of signal acceptance dominate, while at higher masses, the
2893 shape uncertainties from PDF variation for ZZ ($q\bar{q} \rightarrow ZZ$ and $gg \rightarrow ZZ$) background
2894 become important, as also seen in VBF production mode. In addition for VBF, jet related
2895 uncertainties become more important comparing to ggF production. Moreover, the domi-
2896 nate uncertainties include the acceptance uncertainty from QCD scale variation for signal
2897 and the luminosity uncertainty.

2898 7.7.3 Interpretations

2899 1. Spin-0 resonance with NWA

2900 In the absence of a specific model, the ratio of ggF and VBF production mode is un-
2901 known for this additional heavy scalar. For this reason, the fits for ggF and VBF processes

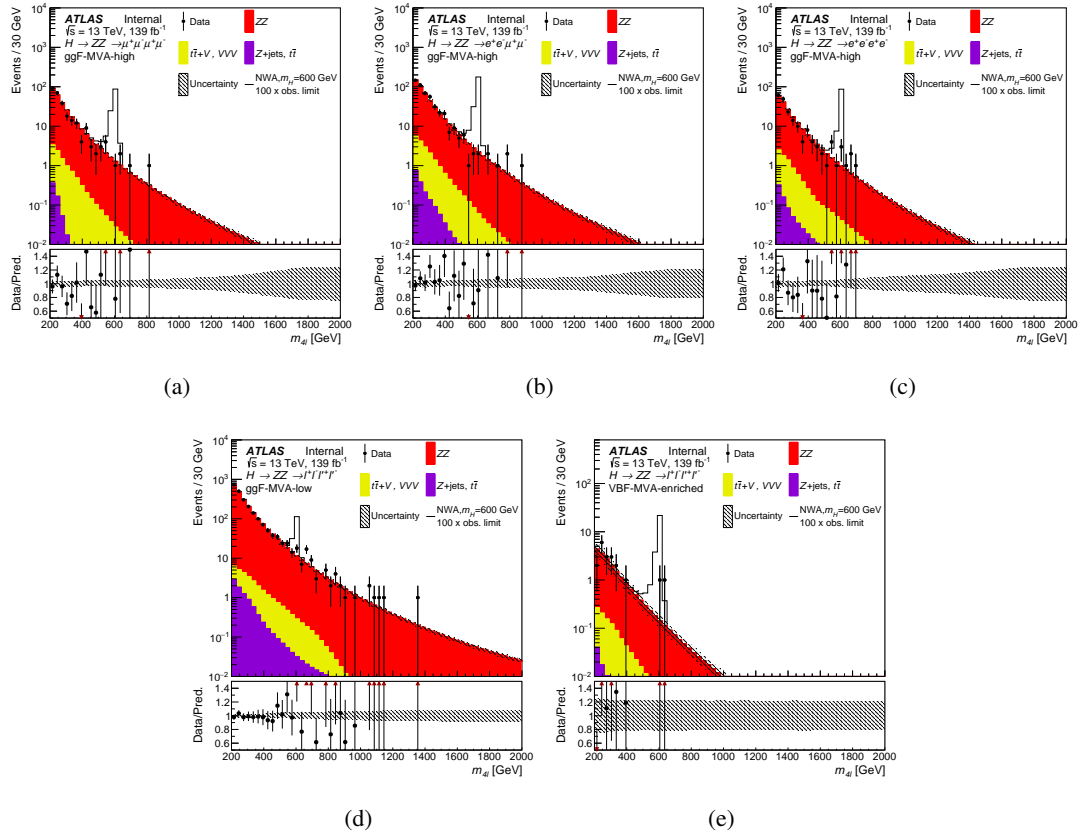


Fig. 7.25 Distribution of the four-lepton invariant mass $m_{4\ell}$ in the $\ell\ell\ell'\ell'$ search for (a), (b), (c) the ggF-MVA-high categories, (d) the ggF-MVA-low category and (e) the VBF-MVA-enriched category. The backgrounds are determined from a combined likelihood fit to the data under the background-only hypothesis. The simulated signal at 600 GeV is normalized to a cross section corresponding to one hundred times the observed upper limit given in section 7.7.3. The error bars on the data points indicate the statistical uncertainty, while the systematic uncertainty in the prediction is shown by the hatched band. The lower panels show the ratio of data to prediction.

are done separately, and in each case the cross section of the untested process is allowed to be a free parameter in the statistical fit. The observed and expected upper limit at 95% confidence level (CL) on the $\sigma \times BR(H \rightarrow ZZ)$ of a narrow scalar resonance for both ggF (left) and VBF (right) production mode with the integrated luminosity of 139 fb^{-1} is shown in figure 7.28 (7.29) for MVA- (cut-) based analysis. No excess over 2σ is found.

2. Spin-0 resonance with LWA

In the case of LWA model, only ggF production mode is studied. The interference between the heavy scalar and SM Higgs boson ($H-h$), as well as the heavy scalar and SM $gg \rightarrow ZZ$ continuum background ($H-B$) as modelled in section 7.5.3 are taken into account. The upper limit at 95% confidence level (CL) on ggF cross section times branch ratio ($\sigma_{ggF} \times BR(H \rightarrow ZZ)$) is shown in figure 7.30 for a width of 1, 5, 10 and 15% of

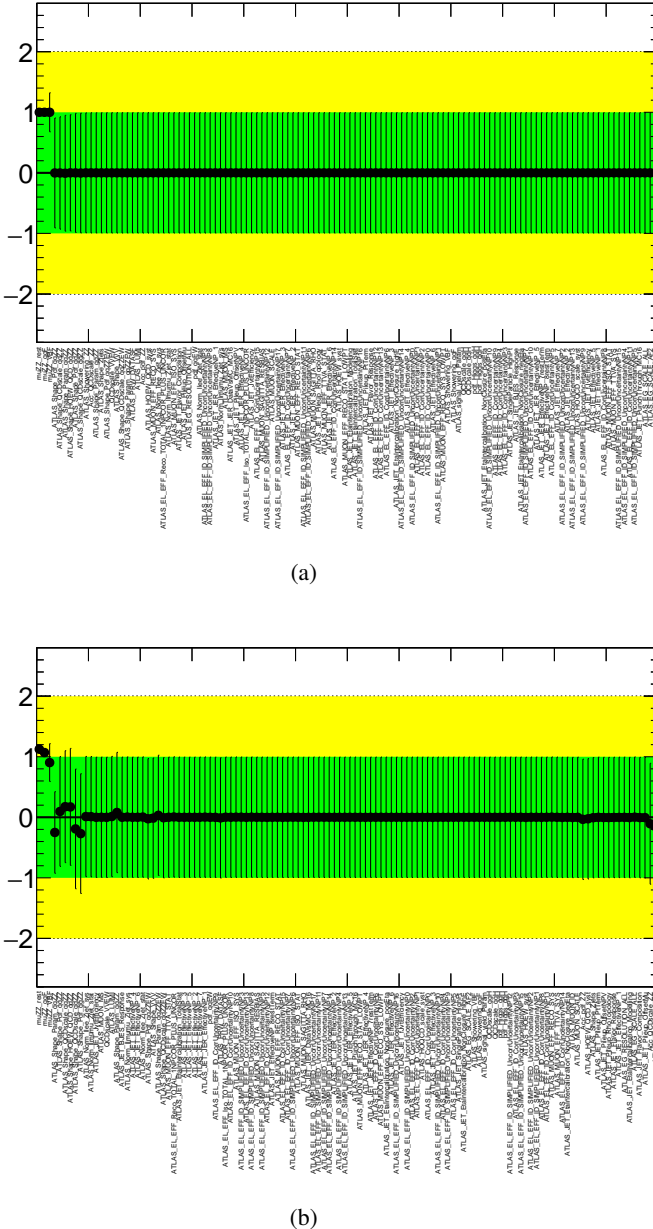
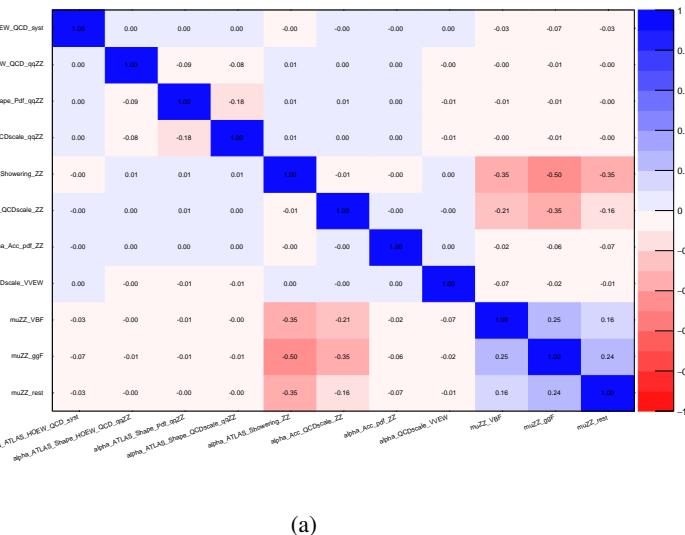


Fig. 7.26 Pulls and constraints of nuisance parameters after a background only fit to (a) Asimov data and (b) observed data in the $\ell\ell\ell'\ell'$ channel. The Asimov data is generated with background data only, and the observed data includes datasets from 2015 to 2018.

2913 m_H .

2914 3. Spin-2 RS Graviton resonance

2915 The observed and expected 95% upper limit on the cross section times branching ratio
 2916 for RS Graviton (RSG) scenario is shown in figure 7.31. Same as LWA case, only $4e$,
 2917 4μ and $2e2\mu$ channel of ggF production mode are used. On top of the expected and ob-
 2918 served upper limits in this model, a predicted cross section as function of mass provided
 2919 by theorist is also shown in the figure. Comparing with the observed result provided by
 2920 $ZZ \rightarrow \ell\ell\ell'\ell'$ decay, this spin-2 graviton is excluded up to a mass of 1500 GeV.



(a)

Fig. 7.27 Correlation of nuisance parameters after a background only fit to Asimov data in the $\ell\ell\ell'\ell'$ channel. The Asimov data is generated with background data only.

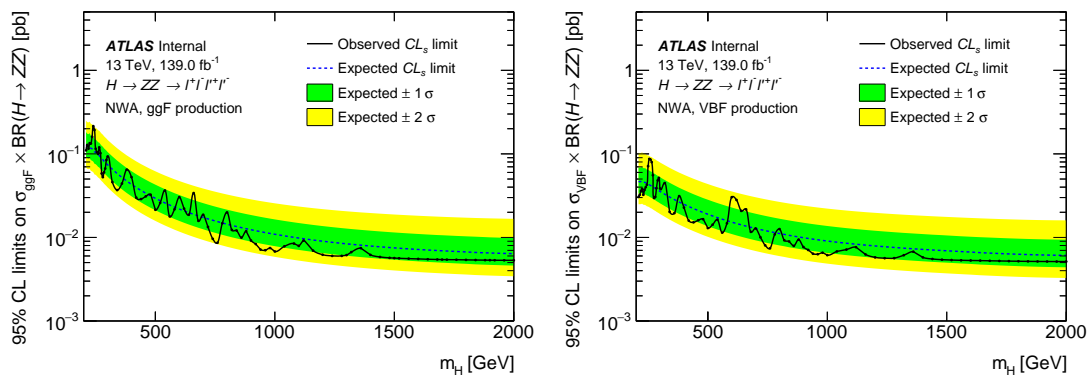


Fig. 7.28 The expected and observed upper limits at 95% CL on $\sigma \times BR(H \rightarrow ZZ)$ using the MVA-based analysis for ggF (left) and VBF (right) production. The green and yellow bands represent the $\pm 1\sigma$ and $\pm 2\sigma$ uncertainties in the expected limits.

4. Summary of interpretation

As a summary, figure 7.32 shows the comparison of expected and observed 95% CL upper limits between different models described above.

Figure 7.33 compares the expected 95% CL upper limits as a function of the NWA resonance mass in this analysis with full run-2 data and the one in previous publication^[115] with the integrated luminosity of 36.1 fb^{-1} . With a significant increase of integrated luminosity and an improved analysis strategy, comparing to the previous publication, the expected sensitivities of searching for narrow-width heavy resonance reduce by up to 70% in MVA-based analysis, where 50% of reduction is due to luminosity increase while other improvement mainly comes from inviting multivariate method.

Figure 7.34 shows the display of one candidate event passing analysis selection in

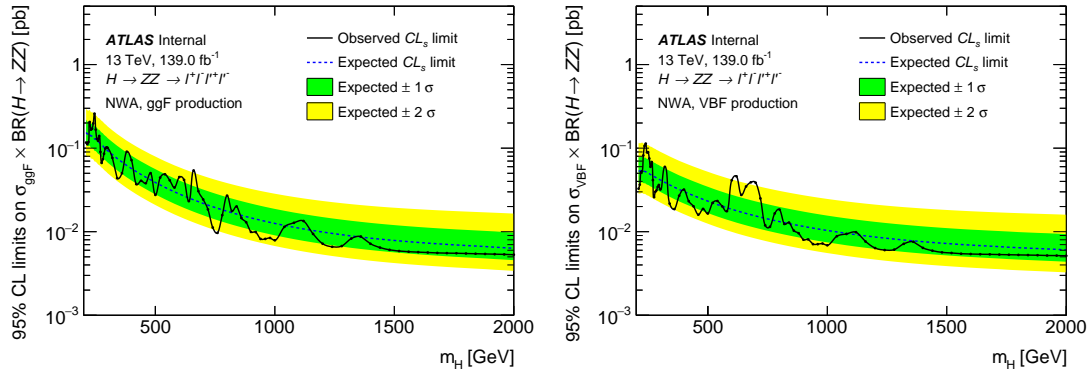


Fig. 7.29 The expected and observed upper limits at 95% CL on $\sigma \times BR(H \rightarrow ZZ)$ using the cut-based analysis for ggF (left) and VBF (right) production. The green and yellow bands represent the $\pm 1\sigma$ and $\pm 2\sigma$ uncertainties in the expected limits.

2932 four-muon final state with four-muon invariant mass of 1.34 TeV.

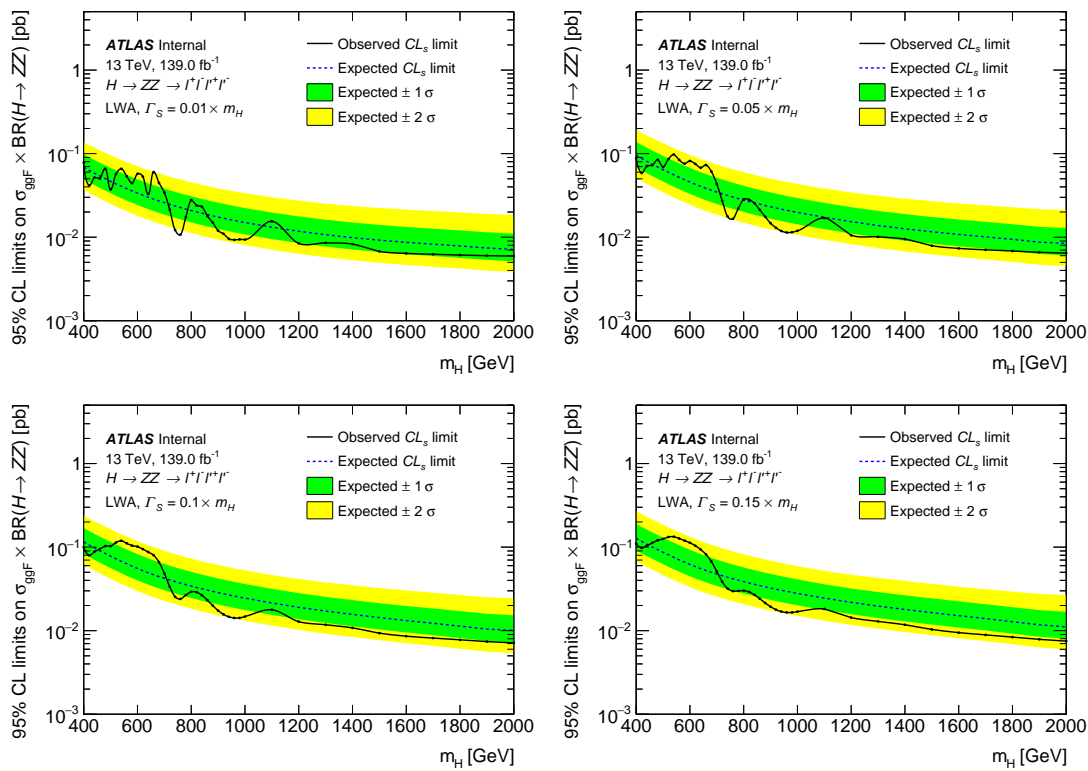


Fig. 7.30 The upper limits at 95% confidence level on $\sigma_{ggF} \times BR(H \rightarrow ZZ)$ as a function of the heavy resonance mass m_H for the ggF production mode with an intrinsic width of 1% (top left), 5% (top right), 10% (bottom left) and 15% (bottom right) for both the case where interference with Standard Model processes is considered. The green and yellow bands represent the $\pm 1\sigma$ and $\pm 2\sigma$ uncertainties in the expected limits.

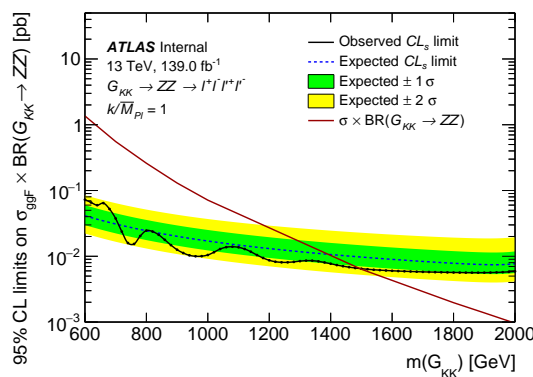


Fig. 7.31 The upper limits at 95% confidence level on $\sigma_{ggF} \times BR(G_{KK} \rightarrow ZZ)$ as a function of the heavy resonance mass $m(G_{KK})$ for the ggF production mode in RS Graviton model. The green and yellow bands represent the $\pm 1\sigma$ and $\pm 2\sigma$ uncertainties in the expected limits.

Table 7.13 A list of the experimental systematics considered in this analysis. The NPs have been separated by whether they only affect the normalisation (left column) or if they affect the shape (right column) of the $m_{4\ell}$ distribution. They are further subdivided into the primary objects that they affect.

Normalisation NPs	Shape NPs
Electrons	
EL_EFF_ID_CorrUncertaintyNP [0–15]	EG_RESOLUTION_ALL
EL_EFF_ID_SIMPLIFIED_UncorrUncertaintyNP [0–17]	EG_SCALE_ALLCORR
EL_EFF_Iso_TOTAL_1NPCOR_PLUS_UNCOR	EG_SCALE_E4SCINTILLATOR
EL_EFF_Reco_TOTAL_1NPCOR_PLUS_UNCOR	EG_SCALE_LARCALIB_EXTRA2015
	EG_SCALE_LARTEMPERATURE_EXT
	EG_SCALE_LARTEMPERATURE_EX
Muons	
MUON_EFF_ISO_STAT	MUON_ID
MUON_EFF_ISO_SYS	MUON_MS
MUON_EFF_RECO_STAT	MUON_SAGITTA_RESBIAS
MUON_EFF_RECO_STAT_LOWPT	MUON_SAGITTA_RHO
MUON_EFF_RECO_SYS	MUON_SCALE
MUON_EFF_RECO_SYS_LOWPT	
MUON_EFF_TTVA_STAT	
MUON_EFF_TTVA_SYS	
Jets	
	JET_BJES_Response
	JET_EffectiveNP_[1–7]
	JET_EffectiveNP_8restTerm
	JET_EtaIntercalibration_Mod
	JET_EtaIntercalibration_Non
	JET_EtaIntercalibration_Non
	JET_EtaIntercalibration_Non
	JET_EtaIntercalibration_Tot
	JET_Flavor_Composition
	JET_Flavor_Response
	JET_JER_DataVsMC
	JET_JER_EffectiveNP_[1–6]
	JET_JER_EffectiveNP_7restTer
	JET_Pileup_OffsetMu
	JET_Pileup_OffsetNPV
	JET_Pileup_PtTerm
	JET_Pileup_RhoTopology
	JET_PunchThrough_MC16
	JET_SingleParticle_HighPt
Other	
HOEW_QCD_syst	
HOEW_syst	
HOQCD_scale_syst	
PRW_DATASF	

Table 7.14 Expected and observed numbers of events for $m_{4\ell} > 200$ GeV, together with their systematic uncertainties, for three MVA-based categories. The expected number of events, as well as their uncertainties, are obtained from a likelihood fit to the data under the background-only hypothesis. The uncertainties of the ZZ normalisation factors, presented in table 7.15, are also taken into account.

Process	VBF-enriched category	ggF-enriched categories			the “rest” category
		4 μ channel	2e2 μ channel	4e channel	
$q\bar{q} \rightarrow ZZ$	11 ± 4	232 ± 10	389 ± 17	154 ± 7	2008 ± 47
$gg \rightarrow ZZ$	3 ± 2	37 ± 6	64 ± 10	26 ± 4	247 ± 19
ZZ (EW)	4.1 ± 0.4	4.5 ± 0.2	7.5 ± 0.4	3 ± 0.2	14.3 ± 0.7
$Z+jets, t\bar{t}$	0.08 ± 0.02	0.6 ± 0.1	1.7 ± 0.4	0.8 ± 0.1	8.8 ± 2.1
$t\bar{t}V, VVV$	0.97 ± 0.1	9.8 ± 0.2	17.5 ± 0.4	7.8 ± 0.2	21.9 ± 0.5
Total background	19 ± 4.5	285 ± 11.7	479 ± 19.7	192 ± 8.1	2301 ± 50.7
Observed	19	271	493	191	2301

Table 7.15 ZZ normalization factor in each category, obtained from a likelihood fit to the data under the background-only hypothesis.

Normalization factor	Fitted value
$\mu_{ZZ}^{ggF-MVA-high}$	1.07 ± 0.047
$\mu_{ZZ}^{ggF-MVA-low}$	1.12 ± 0.026
$\mu_{ZZ}^{VBF-MVA-enriched}$	0.91 ± 0.314

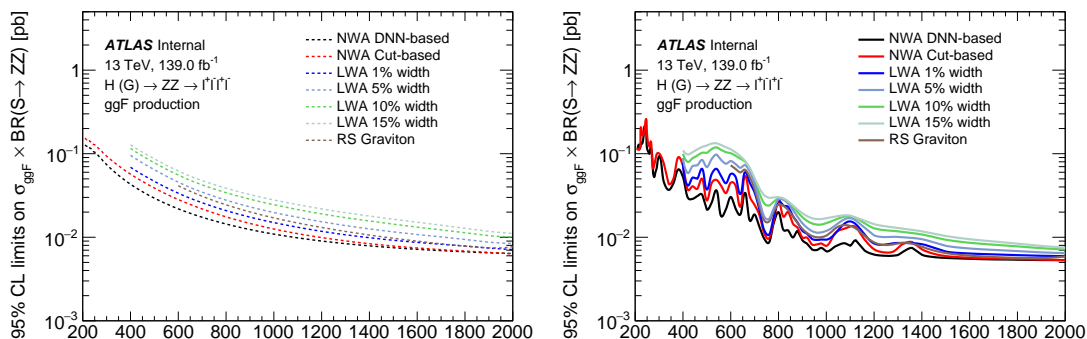


Fig. 7.32 The expected (left) and observed (right) upper limits at 95% confidence level on $\sigma \times BR(S \rightarrow ZZ)$ for ggF production mode at different assumptions.

Table 7.16 Impact of the leading systematic uncertainties, the data statistic uncertainties, as well as the total uncertainties on the predicted signal event yield with the cross section times branching ratio being set to the expected upper limit, expressed as a percentage of the signal yield for the ggF (left) and VBF (right) production modes at $m_H = 400$ and 1000 GeV.

ggF production		VBF production	
Systematic source	Impact [%]	Systematic source	Impact [%]
$m_H = 400$ GeV			
Parton showering of ggF	2.3	QCD scale of VBF	2.7
Luminosity	1.8	Jet flavor composition	2.5
PDF of $q\bar{q} \rightarrow ZZ$	1.6	Luminosity	1.8
Signal yield parameterization	1.4	Jet energy scale (in-su calibration)	1.6
Data stat. uncertainty	48	Data stat. uncertainty	57
Total Uncertainty	49	Total Uncertainty	58
$m_H = 1000$ GeV			
PDF of $q\bar{q} \rightarrow ZZ$	2.5	QCD scale of VBF	2.3
Parton showering of ggF	2.4	PDF of $q\bar{q} \rightarrow ZZ$	2.2
PDF of $gg \rightarrow ZZ$	1.9	Luminosity	1.8
Luminosity	1.8	PDF of $gg \rightarrow ZZ$	1.6
Data stat. uncertainty	84	Data stat. uncertainty	92
Total Uncertainty	86	Total Uncertainty	93

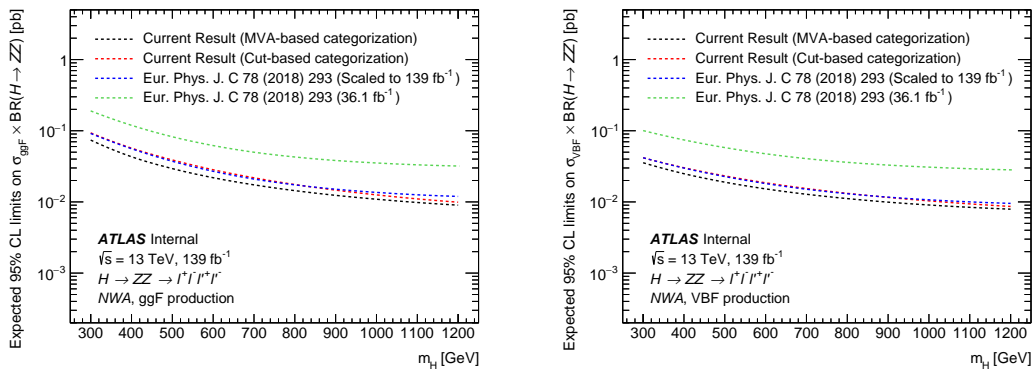


Fig. 7.33 Comparisons of the expected upper limits at 95% CL on the cross section times branching ratio as a function of the heavy resonance mass m_H for the ggF production mode (left) and for the VBF production mode (right) in the case of the NWA. The expected limits from the previous publication are shown in the green dashed line and are projected to the 139 fb^{-1} as shown in the blue dashed line. In addition, the current results based on either cut-based categorisation or the multivariate-based categorisation are shown in red and black lines.

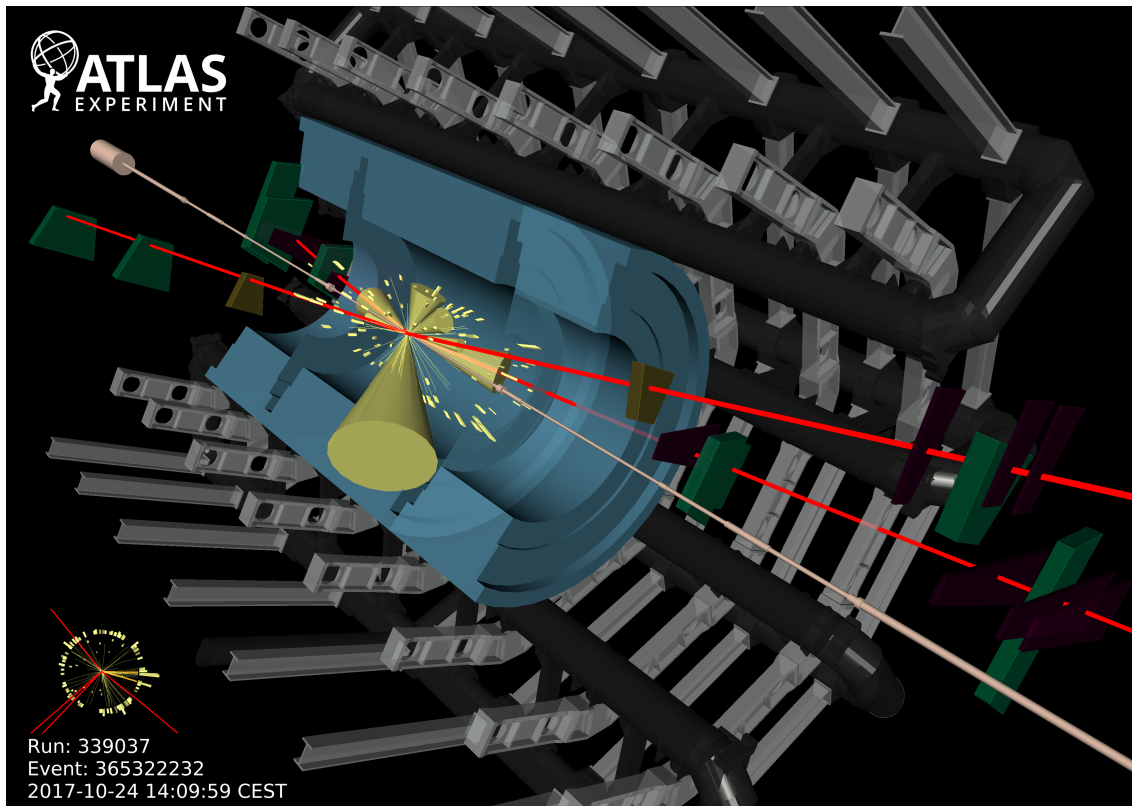


Fig. 7.34 Display of one candidate event in 4μ final state with the mass of 1.35 TeV.

2933 7.8 Conclusion

2934 Searches of heavy resonances decaying into a pair of Z boson to $\ell\ell\ell'\ell'$ final state
2935 are performed using 139 fb^{-1} of 13 TeV pp collision data collected by ATLAS experiment
2936 at the LHC. The results are interpreted as 95% CL upper limits on the production cross
2937 section of a spin-0 and spin-2 resonances under different theoretical models. The search
2938 range of the hypothetical resonances is between 200 GeV to 2000 GeV depending on the
2939 signal model.

2940 The spin-0 resonance is assumed to be a heavy Higgs like scalar produced predom-
2941 inantly from gluon–gluon fusion (ggF) and vector-boson fusion (VBF) decays, and it is
2942 studied under both the narrow-width approximation and with the large-width assumption.
2943 For narrow-width approximation, limits on cross section of heavy scalar decaying into
2944 two Z bosons are set separately for ggF and VBF production modes, under DNN- and
2945 cut- based analysis. In DNN-based analysis, the 95% CL upper limit range is from 215 fb
2946 at $m_H = 240 \text{ GeV}$ to 5.3 fb at $m_H = 2000 \text{ GeV}$ for ggF production mode, and from 87 fb
2947 at $m_H = 255 \text{ GeV}$ to 5.1 fb at $m_H = 1960 \text{ GeV}$ for VBF production mode. In cut-based
2948 analysis, the 95% CL upper limit range is from 259 fb at $m_H = 245 \text{ GeV}$ to 5.3 fb at
2949 $m_H = 2000 \text{ GeV}$ for ggF production mode, and from 113 fb at $m_H = 240 \text{ GeV}$ to 5.1 fb
2950 at $m_H = 2000 \text{ GeV}$ for VBF production mode. DNN-based analysis gains about 20% im-
2951 provement on upper limits at lower mass region comparing to the cut-based analysis, while
2952 for mass above 1500 GeV, both analyses perform closely. For large-width approximation,
2953 limits are studied on ggF production rate at four different widths assumptions: 1%, 5%,
2954 10% and 15% of resonance’s mass, with the interference between the heavy scalar and the
2955 SM Higgs boson as well as the heavy scalar and the SM $gg \rightarrow ZZ$ continuum background
2956 taken into account. The maximum and minimum of upper limits are obtained as 78 fb at
2957 $m_H = 400 \text{ GeV}$ to 5.9 fb at $m_H = 2000 \text{ GeV}$ for 1% width; 98 fb at $m_H = 540 \text{ GeV}$ to 6.4
2958 fb at $m_H = 2000 \text{ GeV}$ for 5% width; 119 fb at $m_H = 540 \text{ GeV}$ to 7.1 fb at $m_H = 2000 \text{ GeV}$
2959 for 10% width; 133 fb at $m_H = 540 \text{ GeV}$ to 7.5 fb at $m_H = 2000 \text{ GeV}$ for 15% width. Last
2960 but not least, the framework of the Randall–Sundrum model with a graviton excitation
2961 spin-2 resonance with $m(G_{KK}) < 1500 \text{ GeV}$ is excluded at 95% CL.

2962

Chapter 8 Summary

2963 On December 3rd, 2018, the LHC finished its second run (run-2) after three fantastic
2964 years. Thanks to run-2 with largely increased statistic, we now know the masses of the
2965 Higgs boson, top quark and W boson to considerably greater precision. And also confirm
2966 the Standard Model as a stable theory.

2967 In this dissertation, various physics processes in $ZZ \rightarrow \ell\ell\ell'\ell'$ final state are studied,
2968 taking the advantage of full run-2 pp collision data in the LHC. Using this signature,
2969 we measured the fiducial cross section of ZZ production to $\ell\ell\ell'\ell' jj$ channel in SM,
2970 which is an important physics process and major background in many analysis with ZZ
2971 production, eg. Higgs analysis (HZZ). In addition, we searched the electroweak ZZ
2972 production via vector boson scattering in associated with 2-jet process in $\ell\ell\ell'\ell'$ final
2973 state. In the meantime, the searches of heavy resonances decaying into a pair of Z bosons
2974 to $\ell\ell\ell'\ell'$ final state for several different hypothetical resonances are conducted in this
2975 dissertation. The results of several analyses are summarized as below:

2976 **Measurement of fiducial cross section of ZZ production in $\ell\ell\ell'\ell' jj$ final state**

2977 The fiducial cross section of inclusive SM $ZZ \rightarrow \ell\ell\ell'\ell'$ production is measured to
2978 be:

$$\sigma_{ZZ \rightarrow \ell\ell\ell'\ell'}^{fid} = 1.27 \pm 0.12(stat) \pm 0.02(theo) \pm 0.07(exp) \pm 0.01(bkg) \pm 0.03(lumi) \quad (8.1)$$

2979 which is found to be compatible with the SM prediction. The ZZ cross section is calcu-
2980 lated with up to one (three) outgoing partons at NLO (LO) using **SHERPA** 2.2.2 for QCD
2981 production, and in LO using **MADGRAPH5_aMC@NLO** 2.6.1 for EW production. The
2982 total uncertainty is 11%, the analysis is still data static dominant (data statistic uncertainty
2983 is about 9.5%).

2984 **Observation of electroweak ZZ production in $\ell\ell\ell'\ell' jj$ final state**

2985 Thanks to the largely increased data statistic collected by ATLAS experiment in the
2986 LHC run-2, the electroweak ZZ production (EW- $ZZjj$) to $\ell\ell\ell'\ell'$ channel in associ-
2987 ation with two jets is observed with a significant deviation from the background-only
2988 hypothesis. The signal strength of EW- $ZZjj$ production, the normalization of QCD-
2989 $ZZjj$ production, as well as the observed and expected statistical significance measured

2990 in $\ell\ell\ell'\ell' jj$ channel are found to be:

$$\begin{aligned}\mu_{\text{EW}} &= 1.54 \pm 0.42 \\ \mu_{\text{QCD}} &= 0.95 \pm 0.22\end{aligned}\quad (8.2)$$

Obs. (Exp.) Significance = 5.48 (3.90) σ

2991 Then in this dissertation, the differential cross section and expected significance of
 2992 EW- $ZZjj$ production, using 3000 fb^{-1} simulated pp collision data at a centre-of-mass
 2993 energy of 14 TeV to be recorded by ATLAS experiment at the HL-LHC, are studied via
 2994 simulations. The HL-LHC will for sure give us more opportunity to probe rare process
 2995 like $ZZ \rightarrow \ell\ell\ell'\ell'$ in the future.

2996 Searches of heavy ZZ resonances in $\ell\ell\ell'\ell'$ final state

2997 Searches of heavy ZZ resonances are performed in four-lepton invariant mass $m_{4\ell}$
 2998 range from 200 GeV to 2000 GeV. Data are found to agree with the background-only
 2999 hypothesis, and 95% CL upper limits are set on the production rate under the models of:

- 3000 • Spin-0 heavy Higgs under narrow-width approximation (NWA).

3001 Search range is from 200 GeV to 2000 GeV.

3002 In DNN-based analysis, the limits are range from 215 fb at $m_H = 240$ GeV to 5.3
 3003 fb at $m_H = 2000$ GeV for ggF production mode, and from 87 fb at $m_H = 255$ GeV
 3004 to 5.1 fb at $m_H = 1960$ GeV for VBF production mode.

3005 The DNN-based analysis is found to be at most 20% better than cut-based results.

- 3006 • Spin-0 heavy Higgs under large-width approximation (LWA) with the width of 1,
 3007 5, 10, 15% of its mass.

3008 Search range is from 400 GeV to 2000 GeV, and only ggF production is studied.

3009 The maximum and minimum of upper limits are obtained as 78 fb at $m_H = 400$ GeV
 3010 to 5.9 fb at $m_H = 2000$ GeV for 1% width; 98 fb at $m_H = 540$ GeV to 6.4 fb at $m_H =$
 3011 2000 GeV for 5% width; 119 fb at $m_H = 540$ GeV to 7.1 fb at $m_H = 2000$ GeV for
 3012 10% width; 133 fb at $m_H = 540$ GeV to 7.5 fb at $m_H = 2000$ GeV for 15% width.

- 3013 • Spin-2 graviton excitation under the Randall–Sundrum model.

3014 Search range is from 600 GeV to 2000 GeV, and only ggF production is studied.

3015 The maximum and minimum of limits are 73 fb at $m_H = 600$ GeV and 5.6 fb
 3016 at $m_H = 1880$ GeV for ggF production mode. And the mass of graviton below
 3017 1500 GeV is excluded comparing the observed results with theoretical prediction.

3018

3019 In summary, the $ZZ \rightarrow \ell\ell\ell'\ell'$ production presented in this dissertation are consis-
 3020 tent with SM prediction. This result completes the observation of weak boson scattering

3021 for massive bosons, which is a new milestone reached in the study of electroweak symme-
3022 try breaking. In the meantime, no indication of new physics is observed. We are looking
3023 forward the HL-LHC, with greatly increased luminosity and higher centre-of-mass energy,
3024 which should enhance the sensitivity for new physics search and precise measurement for
3025 rare process like $\ell\ell\ell'\ell'$ final state.

3026

Bibliography

- 3027 [1] LANGACKER P. Introduction to the Standard Model and Electroweak Physics[C/OL]//
3028 Proceedings of Theoretical Advanced Study Institute in Elementary Particle Physics on The
3029 dawn of the LHC era (TASI 2008): Boulder, USA, June 2-27, 2008. 2010: 3-48. DOI:
3030 [10.1142/9789812838360_0001](https://doi.org/10.1142/9789812838360_0001).
- 3031 [2] PICH A. Electroweak Symmetry Breaking and the Higgs Boson[J/OL]. Acta Phys. Polon.,
3032 2016, B47:151. DOI: [10.5506/APhysPolB.47.151](https://doi.org/10.5506/APhysPolB.47.151).
- 3033 [3] Observation of a new particle in the search for the standard model higgs boson with the atlas
3034 detector at the lhc[J/OL]. Physics Letters B, 2012, 716(1):1 - 29. <http://www.sciencedirect.com/science/article/pii/S037026931200857X>. DOI: <https://doi.org/10.1016/j.physletb.2012.08.020>.
- 3036 [4] Observation of a new boson at a mass of 125 gev with the cms experiment at the lhc[J/OL].
3037 Physics Letters B, 2012, 716(1):30 - 61. <http://www.sciencedirect.com/science/article/pii/S0370269312008581>. DOI: <https://doi.org/10.1016/j.physletb.2012.08.021>.
- 3039 [5] PROFUMO S, RAMSEY-MUSOLF M J, SHAUGHNESSY G. Singlet higgs phenomenology
3040 and the electroweak phase transition[J/OL]. Journal of High Energy Physics, 2007, 2007(08):
3041 010-010. <https://doi.org/10.1088%2F1126-6708%2F2007%2F08%2F010>. DOI: [10.1088/1126-6708/2007/08/010](https://doi.org/10.1088/1126-6708/2007/08/010).
- 3043 [6] BRANCO G, FERREIRA P, LAVOURA L, et al. Theory and phenomenology of two-higgs-
3044 doublet models[J/OL]. Physics Reports, 2012, 516(1):1 - 102. <http://www.sciencedirect.com/science/article/pii/S0370157312000695>. DOI: <https://doi.org/10.1016/j.physrep.2012.02.002>.
- 3046 [7] DREMIN I M. Soft and hard processes in QCD[J/OL]. JETP Lett., 2005, 81:307-310. DOI:
3047 [10.1134/I.1944068](https://doi.org/10.1134/I.1944068).
- 3048 [8] WOMERSLEY J. QCD at the Tevatron: Status and prospects[C/OL]//Proceedings, 5th Inter-
3049 national Symposium on Radiative Corrections - RADCOR 2000. 2000. <http://www.slac.stanford.edu/econf/C000911/>.
- 3051 [9] LIN H W, et al. Parton distributions and lattice QCD calculations: a community white paper
3052 [J/OL]. Prog. Part. Nucl. Phys., 2018, 100:107-160. DOI: [10.1016/j.ppnp.2018.01.007](https://doi.org/10.1016/j.ppnp.2018.01.007).
- 3053 [10] COLLINS J C, SOPER D E, STERMAN G F. Factorization of Hard Processes in QCD[J/OL].
3054 Adv. Ser. Direct. High Energy Phys., 1989, 5:1-91. DOI: [10.1142/9789814503266_0001](https://doi.org/10.1142/9789814503266_0001).
- 3055 [11] STIRLING W J. Perturbative QCD[J/OL]. 2000(CERN-OPEN-2000-296):40 p. <https://cds.cern.ch/record/1194745>. DOI: [10.5170/CERN-2000-007.305](https://doi.org/10.5170/CERN-2000-007.305).
- 3057 [12] GROJEAN C. Higgs Physics[J/OL]. 2017(arXiv:1708.00794):143-158. 12 p. <https://cds.cern.ch/record/2243593>. DOI: [10.5170/CERN-2016-005.143](https://doi.org/10.5170/CERN-2016-005.143).

Bibliography

- 3059 [13] Cern yellow reports: Monographs: Handbook of LHC Higgs Cross Sections: 4. Deciphering
3060 the Nature of the Higgs Sector[M/OL]. 2016. <https://cds.cern.ch/record/2227475>. DOI: [10.23731/CYRM-2017-002](https://doi.org/10.23731/CYRM-2017-002).
- 3062 [14] HEINEMEYER S. Cern yellow reports: Monographs: Handbook of LHC Higgs Cross Sec-
3063 tions: 3. Higgs Properties: Report of the LHC Higgs Cross Section Working Group[M/OL].
3064 2013. <https://cds.cern.ch/record/1559921>. DOI: [10.5170/CERN-2013-004](https://doi.org/10.5170/CERN-2013-004).
- 3065 [15] CHANG J, CHEUNG K, LU C T, et al. *ww* scattering in the era of post-higgs-boson discovery
3066 [J/OL]. Phys. Rev. D, 2013, 87:093005. <https://link.aps.org/doi/10.1103/PhysRevD.87.093005>.
- 3067 [16] BRUNING O S, COLLIER P, LEBRUN P, et al. LHC Design Report Vol.1: The LHC Main
3068 Ring[J]. 2004.
- 3069 [17] BUNING O, COLLIER P, LEBRUN P, et al. LHC Design Report. 2. The LHC infrastructure
3070 and general services[J]. 2004.
- 3071 [18] BENEDIKT M, COLLIER P, MERTENS V, et al. LHC Design Report. 3. The LHC injector
3072 chain[J]. 2004.
- 3073 [19] EVANS L, BRYANT P. LHC machine[J/OL]. Journal of Instrumentation, 2008, 3(08):S08001-
3074 S08001. <https://doi.org/10.1088%2F1748-0221%2F3%2F08%2Fs08001>. DOI: [10.1088/1748-0221/3/08/s08001](https://doi.org/10.1088/1748-0221/3/08/s08001).
- 3076 [20] MOBS E. The CERN accelerator complex. Complexe des accélérateurs du CERN[J/OL]. 2016.
3077 <https://cds.cern.ch/record/2197559>.
- 3078 [21] COLLABORATION A. The ATLAS experiment at the CERN large hadron collider[J/OL].
3079 Journal of Instrumentation, 2008, 3(08):S08003-S08003. <https://doi.org/10.1088%2F1748-0221%2F3%2F08%2Fs08003>. DOI: [10.1088/1748-0221/3/08/s08003](https://doi.org/10.1088/1748-0221/3/08/s08003).
- 3081 [22] PEREZ G. Unitarization models for vector boson scattering at the lhc[D/OL]. 2018. DOI:
3082 [10.5445/IR/1000082199](https://doi.org/10.5445/IR/1000082199).
- 3083 [23] PEQUENAO J. Computer generated image of the whole ATLAS detector[Z/OL]. 2008. <https://cds.cern.ch/record/1095924>.
- 3085 [24] MCFAYDEN J. The lhc and atlas detector. in: Third generation susy and $t^-t + z$ productin.
3086 [D/OL]. 2014. DOI: [10.1007/978-3-319-07191-6_2](https://doi.org/10.1007/978-3-319-07191-6_2).
- 3087 [25] COLLABRATION A. Operation and performance of the ATLAS semiconductor tracker. Op-
3088 eration and performance of the ATLAS semiconductor tracker[J/OL]. JINST, 2014, 9(CERN-
3089 PH-EP-2014-049. CERN-PH-EP-2014-049):P08009. 80 p. <https://cds.cern.ch/record/1698966>.
3090 DOI: [10.1088/1748-0221/9/08/P08009](https://doi.org/10.1088/1748-0221/9/08/P08009).
- 3091 [26] ATLAS pixel detector electronics and sensors[J/OL]. Journal of Instrumentation, 2008, 3(07):
3092 P07007-P07007. <https://doi.org/10.1088%2F1748-0221%2F3%2F07%2Fp07007>. DOI: [10.1088/1748-0221/3/07/p07007](https://doi.org/10.1088/1748-0221/3/07/p07007).

Bibliography

- 3094 [27] MULLIER G. The upgraded pixel detector of the atlas experiment for run-2 at the large hadron
3095 collider[J/OL]. Journal of Instrumentation, 2016, 11:C02061-C02061. DOI: [10.1088/1748-0221/11/02/C02061](https://doi.org/10.1088/1748-0221/11/02/C02061).
- 3097 [28] The silicon microstrip sensors of the atlas semiconductor tracker[J/OL]. Nuclear Instruments
3098 and Methods in Physics Research Section A: Accelerators, Spectrometers, Detectors and Asso-
3099 ciated Equipment, 2007, 578(1):98 - 118. <http://www.sciencedirect.com/science/article/pii/S0168900207007644>. DOI: <https://doi.org/10.1016/j.nima.2007.04.157>.
- 3101 [29] SULTAN D M S. Development of small-pitch, thin 3d sensors for pixel detector upgrades at
3102 hl-lhc[D/OL]. 2017. DOI: [10.13140/RG.2.2.36253.82403/1](https://doi.org/10.13140/RG.2.2.36253.82403/1).
- 3103 [30] The ATLAS transition radiation tracker (TRT) proportional drift tube: design and performance
3104 [J/OL]. Journal of Instrumentation, 2008, 3(02):P02013-P02013. <https://doi.org/10.1088%2F1748-0221%2F3%2F02%2Fp02013>. DOI: [10.1088/1748-0221/3/02/p02013](https://doi.org/10.1088/1748-0221/3/02/p02013).
- 3106 [31] BUCHANAN N, CHEN L, GINGRICH D, et al. Design and implementation of the front end
3107 board for the readout of the atlas liquid argon calorimeters[J/OL]. Journal of Instrumentation,
3108 2008, 3:P03004. DOI: [10.1088/1748-0221/3/03/P03004](https://doi.org/10.1088/1748-0221/3/03/P03004).
- 3109 [32] Technical design report atlas: ATLAS liquid-argon calorimeter: Technical Design Report
3110 [M/OL]. Geneva: CERN, 1996. <https://cds.cern.ch/record/331061>.
- 3111 [33] AAD G, ABBOTT B, ABDALLAH J, et al. Readiness of the atlas tile calorimeter for lhc
3112 collisions[J]. European Physical Journal C, 2010.
- 3113 [34] Technical design report atlas: ATLAS muon spectrometer: Technical Design Report[M/OL].
3114 Geneva: CERN, 1997. <https://cds.cern.ch/record/331068>.
- 3115 [35] SLIWA K. "ATLAS Overview and Main Results"[C]//Proceedings, International School on
3116 High Energy Physics : Workshop on High Energy Physics in the near Future. (LISHEP 2013):
3117 Rio de Janeiro, Brazil, March 17-24, 2013. 2013.
- 3118 [36] RUIZ-MARTINEZ A, COLLABORATION A. The Run-2 ATLAS Trigger System: ATL-DAQ-
3119 PROC-2016-003[R/OL]. Geneva: CERN, 2016. <https://cds.cern.ch/record/2133909>. DOI:
3120 [10.1088/1742-6596/762/1/012003](https://doi.org/10.1088/1742-6596/762/1/012003).
- 3121 [37] PÁSZTOR G. The Upgrade of the ATLAS Electron and Photon Triggers towards LHC Run 2 and
3122 their Performance: ATL-DAQ-PROC-2015-053. arXiv:1511.00334[R/OL]. Geneva: CERN,
3123 2015. <https://cds.cern.ch/record/2063746>.
- 3124 [38] COLLABORATION A. Atlas computing: Technical design report[R/OL]. Geneva: CERN.
3125 <http://atlas-computing.web.cern.ch/atlas-computing/packages/athenaCore/athenaCore.php>.
- 3126 [39] AAD G, et al. The ATLAS Simulation Infrastructure[J/OL]. Eur. Phys. J., 2010, C70:823-874.
3127 DOI: [10.1140/epjc/s10052-010-1429-9](https://doi.org/10.1140/epjc/s10052-010-1429-9).
- 3128 [40] HOCHÉ S. Introduction to parton-shower event generators[C/OL]//Proceedings, Theoretical

Bibliography

- 3129 Advanced Study Institute in Elementary Particle Physics: Journeys Through the Precision Fron-
3130 tier: Amplitudes for Colliders (TASI 2014): Boulder, Colorado, June 2-27, 2014. 2015: 235-
3131 295. DOI: [10.1142/9789814678766_0005](https://doi.org/10.1142/9789814678766_0005).
- 3132 [41] GLEISBERG T, HöCHE S, KRAUSS F, et al. Event generation with SHERPA 1.1[J/OL]. Journal
3133 of High Energy Physics, 2009, 2009(02):007-007. <https://doi.org/10.1088%2F1126-6708%2F2009%2F02%2F007>. DOI: [10.1088/1126-6708/2009/02/007](https://doi.org/10.1088/1126-6708/2009/02/007).
- 3135 [42] BÄHR M, GIESEKE S, GIGG M A, et al. Herwig++ physics and manual[J/OL]. The European
3136 Physical Journal C, 2008, 58(4):639-707. <https://doi.org/10.1140/epjc/s10052-008-0798-9>.
- 3137 [43] NASON P. A New method for combining NLO QCD with shower Monte Carlo algorithms
3138 [J/OL]. JHEP, 2004, 11:040. DOI: [10.1088/1126-6708/2004/11/040](https://doi.org/10.1088/1126-6708/2004/11/040).
- 3139 [44] FRIXIONE S, WEBBER B R. Matching NLO QCD computations and parton shower simula-
3140 tions[J/OL]. Journal of High Energy Physics, 2002, 2002(06):029-029. <https://doi.org/10.1088%2F1126-6708%2F2002%2F06%2F029>. DOI: [10.1088/1126-6708/2002/06/029](https://doi.org/10.1088/1126-6708/2002/06/029).
- 3142 [45] SJOSTRAND T, MRENNNA S, SKANDS P Z. A Brief Introduction to PYTHIA 8.1[J/OL].
3143 Comput. Phys. Commun., 2008, 178:852-867. DOI: [10.1016/j.cpc.2008.01.036](https://doi.org/10.1016/j.cpc.2008.01.036).
- 3144 [46] BARBERIO E, et al. The Geant4-Based ATLAS Fast Electromagnetic Shower Simulation
3145 [C/OL]//Astroparticle, particle and space physics, detectors and medical physics applications.
3146 Proceedings, 10th Conference, ICATPP 2007, Como, Italy, October 8-12, 2007. 2008: 802-
3147 806. <http://cdsweb.cern.ch/record/1064665/files/soft-conf-2007-002.pdf>. DOI: [10.1142/9789812819093_0133](https://doi.org/10.1142/9789812819093_0133).
- 3149 [47] RICHTER-WAS E, FROIDEVAUX D, POGGIOLI L. ATLFAST 2.0 a fast simulation package
3150 for ATLAS: ATL-PHYS-98-131[R/OL]. Geneva: CERN, 1998. <https://cds.cern.ch/record/683751>.
- 3152 [48] EDMONDS K, FLEISCHMANN S, LENZ T, et al. The Fast ATLAS Track Simulation (FA-
3153 TRAS): ATL-SOFT-PUB-2008-001. ATL-COM-SOFT-2008-002[R/OL]. Geneva: CERN,
3154 2008. <https://cds.cern.ch/record/1091969>.
- 3155 [49] BOYD J T, COSTA M J, TONOYAN A, et al. Commissioning of the ATLAS reconstruction
3156 software with first data[J/OL]. Journal of Physics: Conference Series, 2010, 219(3):032059.
3157 <https://doi.org/10.1088%2F1742-6596%2F219%2F3%2F032059>. DOI: [10.1088/1742-6596/219/3/032059](https://doi.org/10.1088/1742-6596/219/3/032059).
- 3159 [50] CORNELISSEN T, ELSING M, FLEISCHMANN S, et al. Concepts, Design and Implemen-
3160 tation of the ATLAS New Tracking (NEWT): ATL-SOFT-PUB-2007-007. ATL-COM-SOFT-
3161 2007-002[R/OL]. Geneva: CERN, 2007. <https://cds.cern.ch/record/1020106>.
- 3162 [51] AAD G, et al. Muon reconstruction performance of the ATLAS detector in proton-proton col-
3163 lision data at $\sqrt{s} = 13$ TeV[J/OL]. Eur. Phys. J., 2016, C76(5):292. DOI: [10.1140/epjc/s10052-016-3990-0](https://doi.org/10.1140/epjc/s10052-016-3990-0).

- 3164 016-4120-y.
- 3165 [52] ILLINGWORTH J, KITTLER J. A survey of the hough transform[J/OL]. Computer Vision,
3166 Graphics, and Image Processing, 1988, 44(1):87 - 116. <http://www.sciencedirect.com/science/article/pii/S0734189X88800331>. DOI: [https://doi.org/10.1016/S0734-189X\(88\)80033-1](https://doi.org/10.1016/S0734-189X(88)80033-1).
- 3167 [53] Vertex Reconstruction Performance of the ATLAS Detector at 13 TeV: ATL-PHYS-PUB-2015-
3169 026[R/OL]. Geneva: CERN, 2015. <https://cds.cern.ch/record/2037717>.
- 3170 [54] AABOUD M, et al. Reconstruction of primary vertices at the ATLAS experiment in Run 1
3171 proton-proton collisions at the LHC[J/OL]. Eur. Phys. J., 2017, C77(5):332. DOI: <10.1140/epjc/s10052-017-4887-5>.
- 3173 [55] Electron efficiency measurements with the ATLAS detector using the 2015 LHC proton-proton
3174 collision data: ATLAS-CONF-2016-024[R/OL]. Geneva: CERN, 2016. <https://cds.cern.ch/reCORD/2157687>.
- 3176 [56] LAMPL W, LAPLACE S, LELAS D, et al. Calorimeter Clustering Algorithms: Description
3177 and Performance: ATL-LARG-PUB-2008-002. ATL-COM-LARG-2008-003[R/OL]. Geneva:
3178 CERN, 2008. <https://cds.cern.ch/record/1099735>.
- 3179 [57] CORNELISSEN T G, ELSING M, GAVRILENKO I, et al. The global χ^2 track fitter in ATLAS
3180 [J/OL]. Journal of Physics: Conference Series, 2008, 119(3):032013. <https://doi.org/10.1088%2F1742-6596%2F119%2F3%2F032013>. DOI: <10.1088/1742-6596/119/3/032013>.
- 3182 [58] Electron efficiency measurements with the ATLAS detector using the 2012 LHC proton-proton
3183 collision data: ATLAS-CONF-2014-032[R/OL]. Geneva: CERN, 2014. <http://cds.cern.ch/reCORD/1706245>.
- 3185 [59] LIMPER M. Track and vertex reconstruction in the ATLAS inner detector[D/OL]. 2009. <http://cds.cern.ch/record/1202457>.
- 3187 [60] AAD G, et al. Topological cell clustering in the ATLAS calorimeters and its performance in
3188 LHC Run 1[J/OL]. Eur. Phys. J., 2017, C77:490. DOI: <10.1140/epjc/s10052-017-5004-5>.
- 3189 [61] ZHENG Z. Identification of very-low transverse momentum muons with the ATLAS experi-
3190 ment: ATL-MUON-PROC-2018-018[R/OL]. Geneva: CERN, 2018. <https://cds.cern.ch/reCORD/2649299>.
- 3192 [62] CACCIARI M, SALAM G P. Pileup subtraction using jet areas[J/OL]. Physics Letters B, 2008,
3193 659(1):119 - 126. <http://www.sciencedirect.com/science/article/pii/S0370269307011094>. DOI:
3194 <https://doi.org/10.1016/j.physletb.2007.09.077>.
- 3195 [63] CACCIARI M, SALAM G P, SOYEZ G. The anti-ktjet clustering algorithm[J/OL]. Journal of
3196 High Energy Physics, 2008, 2008(04):063-063. <https://doi.org/10.1088%2F1126-6708%2F2008%2F04%2F063>. DOI: <10.1088/1126-6708/2008/04/063>.
- 3198 [64] CACCIARI M, SALAM G P, SOYEZ G. Fastjet user manual[J/OL]. The European Physical

Bibliography

- 3199 Journal C, 2012, 72(3):1896. <https://doi.org/10.1140/epjc/s10052-012-1896-2>.
- 3200 [65] AAD G, et al. Jet energy measurement and its systematic uncertainty in proton-proton collisions
3201 at $\sqrt{s} = 7$ TeV with the ATLAS detector[J/OL]. Eur. Phys. J., 2015, C75:17. DOI: [10.1140/epjc/s10052-014-3190-y](https://doi.org/10.1140/epjc/s10052-014-3190-y).
- 3203 [66] AABOUD M, et al. Jet energy scale measurements and their systematic uncertainties in proton-
3204 proton collisions at $\sqrt{s} = 13$ TeV with the ATLAS detector[J/OL]. Phys. Rev., 2017, D96(7):
3205 072002. DOI: [10.1103/PhysRevD.96.072002](https://doi.org/10.1103/PhysRevD.96.072002).
- 3206 [67] Optimisation of the ATLAS *b*-tagging performance for the 2016 LHC Run: ATL-PHYS-PUB-
3207 2016-012[R/OL]. Geneva: CERN, 2016. <https://cds.cern.ch/record/2160731>.
- 3208 [68] PIACQUADIO G, WEISER C. A new inclusive secondary vertex algorithm for b-jet tagging in
3209 ATLAS[J/OL]. Journal of Physics: Conference Series, 2008, 119(3):032032. [https://doi.org/10.1088/1742-6596/119/3/032032](https://doi.org/10.1088%2F1742-6596%2F119%2F3%2F032032). DOI: [10.1088/1742-6596/119/3/032032](https://doi.org/10.1088/1742-6596/119/3/032032).
- 3211 [69] SPECKMAYER P, HÖCKER A, STELZER J, et al. The toolkit for multivariate data analysis,
3212 TMVA 4[J/OL]. Journal of Physics: Conference Series, 2010, 219(3):032057. [https://doi.org/10.1088/1742-6596/219/3/032057](https://doi.org/10.1088%2F1742-6596%2F219%2F3%2F032057). DOI: [10.1088/1742-6596/219/3/032057](https://doi.org/10.1088/1742-6596/219/3/032057).
- 3214 [70] Performance of missing transverse momentum reconstruction with the atlas detector using
3215 proton–proton collisions at $\sqrt{s}=13\text{TeV}$ [J/OL]. The European Physical Journal C, 2018, 78(11):903. <https://doi.org/10.1140/epjc/s10052-018-6288-9>.
- 3217 [71] LEE B W, QUIGG C, THACKER H B. The Strength of Weak Interactions at Very High-
3218 Energies and the Higgs Boson Mass[J/OL]. Phys. Rev. Lett., 1977, 38:883-885. DOI: [10.1103/PhysRevLett.38.883](https://doi.org/10.1103/PhysRevLett.38.883).
- 3220 [72] CHANOWITZ M S, GAILLARD M K. The TeV Physics of Strongly Interacting W's and Z's
3221 [J/OL]. Nucl. Phys., 1985, B261:379-431. DOI: [10.1016/0550-3213\(85\)90580-2](https://doi.org/10.1016/0550-3213(85)90580-2).
- 3222 [73] SZLEPER M. The Higgs boson and the physics of WW scattering before and after Higgs
3223 discovery[J]. 2014.
- 3224 [74] Evidence for electroweak production of $W^\pm W^\pm jj$ in pp collisions at $\sqrt{s} = 8$ TeV with the
3225 atlas detector[J/OL]. Phys. Rev. Lett., 2014, 113:141803. <https://link.aps.org/doi/10.1103/PhysRevLett.113.141803>.
- 3227 [75] Observation of electroweak production of a same-sign w boson pair in association with two jets
3228 in pp collisions at $\sqrt{s} = 13$ TeV with the atlas detector[J/OL]. Phys. Rev. Lett., 2019, 123:
3229 161801. <https://link.aps.org/doi/10.1103/PhysRevLett.123.161801>.
- 3230 [76] SIRUNYAN A M, et al. Observation of electroweak production of same-sign W boson pairs
3231 in the two jet and two same-sign lepton final state in proton-proton collisions at $\sqrt{s} = 13$ TeV
3232 [J/OL]. Phys. Rev. Lett., 2018, 120(8):081801. DOI: [10.1103/PhysRevLett.120.081801](https://doi.org/10.1103/PhysRevLett.120.081801).
- 3233 [77] Observation of electroweak $w\pm z$ boson pair production in association with two jets in pp col-

Bibliography

- 3234 lisions at s=13 tev with the atlas detector[J/OL]. Physics Letters B, 2019, 793:469 - 492.
3235 <http://www.sciencedirect.com/science/article/pii/S0370269319303211>. DOI: <https://doi.org/10.1016/j.physletb.2019.05.012>.
- 3237 [78] Measurement of vector boson scattering and constraints on anomalous quartic couplings from
3238 events with four leptons and two jets in proton–proton collisions at s=13 tev[J/OL]. Physics
3239 Letters B, 2017, 774:682 - 705. <http://www.sciencedirect.com/science/article/pii/S0370269317308328>. DOI: <https://doi.org/10.1016/j.physletb.2017.10.020>.
- 3241 [79] ALWALL J, FREDERIX R, FRIXIONE S, et al. The automated computation of tree-level and
3242 next-to-leading order differential cross sections, and their matching to parton shower simulations
3243 [J/OL]. JHEP, 2014, 07:079. DOI: [10.1007/JHEP07\(2014\)079](https://doi.org/10.1007/JHEP07(2014)079).
- 3244 [80] BALL R D, et al. Parton distributions with LHC data[J/OL]. Nucl. Phys. B, 2013, 867:244-289.
3245 DOI: [10.1016/j.nuclphysb.2012.10.003](https://doi.org/10.1016/j.nuclphysb.2012.10.003).
- 3246 [81] GLEISBERG T, HÖCHE S, KRAUSS F, et al. Event generation with SHERPA 1.1[J/OL].
3247 JHEP, 2009, 02:007. DOI: [10.1088/1126-6708/2009/02/007](https://doi.org/10.1088/1126-6708/2009/02/007).
- 3248 [82] BALL R D, et al. Parton distributions for the LHC run II[J/OL]. JHEP, 2015, 04:040. DOI:
3249 [10.1007/JHEP04\(2015\)040](https://doi.org/10.1007/JHEP04(2015)040).
- 3250 [83] CAOLA F, MELNIKOV K, RÖNTSCH R, et al. Qcd corrections to zz production in gluon
3251 fusion at the lhc[J/OL]. Phys. Rev. D, 2015, 92:094028. <https://link.aps.org/doi/10.1103/PhysRevD.92.094028>.
- 3253 [84] FRIXIONE S, RIDOLFI G, NASON P. A positive-weight next-to-leading-order Monte Carlo
3254 for heavy flavour hadroproduction[J/OL]. JHEP, 2007, 09:126. DOI: [10.1088/1126-6708/2007/09/126](https://doi.org/10.1088/1126-6708/2007/09/126).
- 3256 [85] LAI H L, et al. New parton distributions for collider physics[J/OL]. Phys. Rev. D, 2010, 82:
3257 074024. DOI: [10.1103/PhysRevD.82.074024](https://doi.org/10.1103/PhysRevD.82.074024).
- 3258 [86] ALIOLI S, NASON P, OLEARI C, et al. NLO single-top production matched with shower in
3259 POWHEG: s- and t-channel contributions[J/OL]. JHEP, 2009, 09:111. DOI: [10.1088/1126-6708/2009/09/111](https://doi.org/10.1088/1126-6708/2009/09/111).
- 3261 [87] FREDERIX R, RE E, TORRIELLI P. Single-top t-channel hadroproduction in the four-flavour
3262 scheme with POWHEG and aMC@NLO[J/OL]. JHEP, 2012, 09:130. DOI: [10.1007/JHEP09\(2012\)130](https://doi.org/10.1007/JHEP09(2012)130).
- 3264 [88] RE E. Single-top Wt-channel production matched with parton showers using the POWHEG
3265 method[J/OL]. Eur. Phys. J. C, 2011, 71:1547. DOI: [10.1140/epjc/s10052-011-1547-z](https://doi.org/10.1140/epjc/s10052-011-1547-z).
- 3266 [89] COLLABORATION A. ATLAS Pythia 8 tunes to 7 TeV data[M/OL]. 2014. <https://cds.cern.ch/record/1966419>.
- 3268 [90] ATLAS Collaboration. Performance of pile-up mitigation techniques for jets in pp collisions at

Bibliography

- 3269 $\sqrt{s} = 8$ TeV using the ATLAS detector[J/OL]. Eur. Phys. J. C, 2016, 76:581. DOI: [10.1140/epjc/s10052-016-4395-z](https://doi.org/10.1140/epjc/s10052-016-4395-z).
- 3270
- 3271 [91] BELLM J, et al. Herwig 7.0/Herwig++ 3.0 release note[J/OL]. Eur. Phys. J. C, 2016, 76(4): 196. DOI: [10.1140/epjc/s10052-016-4018-8](https://doi.org/10.1140/epjc/s10052-016-4018-8).
- 3272
- 3273 [92] BAHR M, et al. Herwig++ Physics and Manual[J/OL]. Eur. Phys. J. C, 2008, 58:639-707. DOI: [10.1140/epjc/s10052-008-0798-9](https://doi.org/10.1140/epjc/s10052-008-0798-9).
- 3274
- 3275 [93] Luminosity determination in pp collisions at $\sqrt{s} = 13$ TeV using the ATLAS detector at the 3276 LHC: ATLAS-CONF-2019-021[R/OL]. Geneva: CERN, 2019. <http://cds.cern.ch/record/2677054>.
- 3277
- 3278 [94] The new LUCID-2 detector for luminosity measurement and monitoring in ATLAS[J/OL]. Journal 3279 of Instrumentation, 2018, 13(07):P07017-P07017. [https://doi.org/10.1088/1748-0221/13/07/p07017](https://doi.org/10.1088%2F1748-0221%2F13%2F07%2Fp07017). DOI: [10.1088/1748-0221/13/07/p07017](https://doi.org/10.1088/1748-0221/13/07/p07017).
- 3280
- 3281 [95] COADOU Y. Boosted decision trees and applications[J/OL]. EPJ Web of Conferences, 2013, 3282 55:02004-. DOI: [10.1051/epjconf/20135502004](https://doi.org/10.1051/epjconf/20135502004).
- 3283
- 3284 [96] COLLABORATION A. Technical Design Report for the ATLAS Inner Tracker Pixel Detector: 3285 CERN-LHCC-2017-021. ATLAS-TDR-030[R/OL]. Geneva: CERN, 2017. <https://cds.cern.ch/record/2285585>.
- 3286
- 3287 [97] COLLABORATION A. Technical Design Report for the Phase-II Upgrade of the ATLAS Muon 3288 Spectrometer: CERN-LHCC-2017-017. ATLAS-TDR-026[R/OL]. Geneva: CERN, 2017. <https://cds.cern.ch/record/2285580>.
- 3289
- 3290 [98] COLLABORATION A. Technical Proposal: A High-Granularity Timing Detector for the ATLAS 3291 Phase-II Upgrade: CERN-LHCC-2018-023. LHCC-P-012[R/OL]. Geneva: CERN, 2018. <https://cds.cern.ch/record/2623663>.
- 3292
- 3293 [99] Expected performance for an upgraded ATLAS detector at High-Luminosity LHC: ATL-PHYS- 3294 PUB-2016-026[R/OL]. Geneva: CERN, 2016. <https://cds.cern.ch/record/2223839>.
- 3295
- 3296 [100] HILL A, VAN DER BIJ J J. Strongly interacting singlet-doublet higgs model[J/OL]. Phys. Rev. 3297 D, 1987, 36:3463-3473. <https://link.aps.org/doi/10.1103/PhysRevD.36.3463>.
- 3298
- 3299 [101] DAVOUDIASL H, HEWETT J, RIZZO T. Bulk gauge fields in the randall–sundrum 3300 model1work supported by the department of energy, contract de-ac03-76sf00515.1[J/OL]. 3301 Physics Letters B, 2000, 473(1):43 - 49. <http://www.sciencedirect.com/science/article/pii/S0370269399014306>. DOI: [https://doi.org/10.1016/S0370-2693\(99\)01430-6](https://doi.org/10.1016/S0370-2693(99)01430-6).
- 3302
- 3303 [102] FREDERIX R, FRIXIONE S. Merging meets matching in MC@NLO[J/OL]. JHEP, 2012, 12: 061. DOI: [10.1007/JHEP12\(2012\)061](https://doi.org/10.1007/JHEP12(2012)061).
- 3304
- 3305 [103] AGASHE K, DAVOUDIASL H, PEREZ G, et al. Warped Gravitons at the LHC and Beyond 3306 [J/OL]. Phys.Rev., 2007, D76:036006. DOI: [10.1103/PhysRevD.76.036006](https://doi.org/10.1103/PhysRevD.76.036006).

Bibliography

- 3304 [104] ATLAS Collaboration. Jet reconstruction and performance using particle flow with the ATLAS
3305 Detector[J/OL]. Eur. Phys. J. C, 2017, 77:466. DOI: [10.1140/epjc/s10052-017-5031-2](https://doi.org/10.1140/epjc/s10052-017-5031-2).
- 3306 [105] Measurements of higgs boson production and couplings in the four-lepton channel in pp col-
3307 lisions at center-of-mass energies of 7 and 8 tev with the atlas detector[J/OL]. Phys. Rev. D,
3308 2015, 91:012006. <https://link.aps.org/doi/10.1103/PhysRevD.91.012006>.
- 3309 [106] CRANMER K S. Kernel estimation in high-energy physics[J/OL]. Comput. Phys. Commun.,
3310 2001, 136:198-207. DOI: [10.1016/S0010-4655\(00\)00243-5](https://doi.org/10.1016/S0010-4655(00)00243-5).
- 3311 [107] OREGLIA M. A Study of the Reactions $\psi' \rightarrow \gamma\gamma\psi$ [M/OL]. SLAC, 1980. <https://www.slac.stanford.edu/cgi-wrap/getdoc/slac-r-236.pdf>.
- 3313 [108] GAISER J. Charmonium Spectroscopy From Radiative Decays of the J/ψ and ψ' [M/OL].
3314 SLAC, 1982. <https://www.slac.stanford.edu/cgi-wrap/getdoc/slac-r-255.pdf>.
- 3315 [109] GORIA S, PASSARINO G, ROSCO D. The Higgs Boson Lineshape[J/OL]. Nucl.Phys., 2012,
3316 B864:530-579. DOI: [10.1016/j.nuclphysb.2012.07.006](https://doi.org/10.1016/j.nuclphysb.2012.07.006).
- 3317 [110] SPIRA M, DJOUADI A, GRAUDENZ D, et al. Higgs boson production at the LHC[J]. Nucl.
3318 Phys., 1995, B 453:17-82.
- 3319 [111] BALL R D, et al. Parton Distribution Benchmarking with LHC Data[J/OL]. JHEP, 2013, 04:
3320 125. DOI: [10.1007/JHEP04\(2013\)125](https://doi.org/10.1007/JHEP04(2013)125).
- 3321 [112] BIJNENS J, EEROLA P, MAUL M, et al. Qcd signatures of narrow graviton resonances in
3322 hadron colliders[J/OL]. Physics Letters B, 2001, 503(3-4):341-348. DOI: [10.1016/s0370-2693\(01\)00238-6](https://doi.org/10.1016/s0370-2693(01)00238-6).
- 3324 [113] ATLAS Collaboration. PMG Systematic Uncertainty Recipes[EB/OL]. <https://twiki.cern.ch/twiki/bin/view/AtlasProtected/PmgSystematicUncertaintyRecipes>.
- 3326 [114] READ A L. Presentation of search results: The CL(s) technique[J]. J. Phys. G, 2002, 28:
3327 2693-2704.
- 3328 [115] AABOUD M, et al. Search for heavy ZZ resonances in the $\ell^+\ell^-\ell^+\ell^-$ and $\ell^+\ell^-v\bar{v}$ final states
3329 using proton–proton collisions at $\sqrt{s} = 13$ TeV with the ATLAS detector[J/OL]. Eur. Phys. J.
3330 C, 2018, 78(4):293. DOI: [10.1140/epjc/s10052-018-5686-3](https://doi.org/10.1140/epjc/s10052-018-5686-3).